ADVANCING THE USE OF THE DAMAGE RATING INDEX (DRI) FOR EVALUATION OF CONCRETE AFFECTED BY INTERNAL SWELLING REACTIONS (ISR)

CASSANDRA TROTTIER

Thesis submitted to the University of Ottawa
in partial Fulfillment of the requirements for the
Doctorate in Philosophy

Department of Civil Engineering
Faculty of Engineering
University of Ottawa

Abstract

The damage rating index (DRI) is a microscopy tool and methodology used to identify deterioration caused by internal swelling reactions (ISR) in concrete. The DRI was initially developed to evaluate concrete affected by alkali-aggregate reaction (AAR) and has since begun to be employed for other types of ISR. It utilizes a point-count method to count distinct petrographic and distress features across a surface, providing insight into the type, extent, and pattern of deterioration. This study addresses research gaps related to the DRI’s ability to distinguish between ISR mechanisms, the connection between microscopy and mechanical responses, operator variability, and the use of technology for more efficient data collection. This thesis is paper-based and includes five papers aimed at addressing the identified research gaps. The first topic is divided into two papers, with the first exploring the tool's adaptability by modifying the counting method to better describe deterioration due to delayed ettringite formation (DEF). The study illustrates the enhanced capability of the DRI to characterize DEF-induced deterioration more effectively. The second paper assesses the counting method in relation to mechanical responses. The second topic and third paper investigates the relationship between distress features and mechanical responses. The research employs linear regression through detailed analysis, establishing significant correlations that provide valuable insights into the engineering implications of distress features observed under microscopy. The third topic is variability, and the fourth paper presents an approach for autonomous operator training aimed at improving skill acquisition and reducing variability. This approach proposes a robust training framework, demonstrating promising results in standardizing operator performance. The final topic and fifth paper evaluate a technique for assessing the outcomes of automating the collection of distress feature counts via images. The study compares the accuracy and efficiency of operator-based versus machine-based data collection, highlighting the advantages of automation in terms of consistency and speed. The combined findings from these studies offer a comprehensive understanding of the DRI's adaptability to ISR mechanisms, distress feature analysis, autonomous training methodologies, and automated evaluation techniques. Future research can build upon these findings and approaches to further innovate and refine the use of the DRI in engineering practices.

Keywords: *concrete durability, concrete deterioration, stereomicroscopy, alkali-aggregate reaction (AAR), alkali-silica reaction (ASR), internal swelling reaction (ISR), point-count data, damage rating index (DRI), operator calibration, automation*.

This thesis is dedicated to Abigail, Nicholas and Marc.

"Some people know what they want to do, and some of us will always search for who we want to be". -CT

Acknowledgements

It is at the end of a long journey that you realize you were never alone. The support I have received has been a blessing. I must first thank Marc, my life partner, for being by my side the entire time, listening to my endless stories about the DRI and sharing this significant accomplishment with me. I would not have been able to do this without you. Merci mille fois, merci.

Thank you to my family for supporting all my crazy ambitions over the years. I’m grateful to my parents, Chantal and Alain, who taught me the importance of a strong work ethic, that hard work always pays off, and the value of lending a helping hand. To my sister Stéphanie, my niece and nephew, and my brother-in-law Shane, thank you for ensuring I took time off to be with family. A special thanks to Mimi for being the supportive grandmother she is, and to my in-laws for inspiring me to pursue university studies.

I would like to extend a special thank you to my bestie, Crystal. She never misses a phone call to listen to me panic about things that may not matter anymore, always ensuring that I don’t spiral out of control and helping me see the funny side of everything, even in the most difficult situations times.

I don’t think "thank you" sufficiently expresses my gratitude for my thesis supervisor, Dr. Leandro F.M. Sanchez. This doesn’t signify the end of a chapter but rather the commencement of limitless opportunities. Thank you for believing in me from day one and giving a chance to someone who never knew they could reach this point. I can’t begin to list the opportunities I've had under your guidance, from travelling internationally for the first time to collaborate with my dear colleague Francisco Locati, to completely trusting me to take the lead in organizing ICAAR 2024. These challenges have shaped the person I am today, and I would not change a thing.

Naturally, I would like to thank my colleagues from uOttawa, particularly the OG µStructure gang. You all took me in during my undergrad, and I truly felt a sense of belonging among you. Mayra de Grazia, you may not realize the impact you have had on me with your kindness and willingness to share your knowledge, but I want you to know that you are an inspiration, and the passion you have is contagious.

Gamal Elnabelsy and Muslim Majeed have been more than just laboratory technical support over the years. I will always be grateful for the morning coffees, sweets, treats, and history lessons that enriched my understanding of this world.

The AAR community for the various venues available to contribute to research and science. My gratitude goes to Benoît Fournier for encouraging me to continue studying the DRI and for trusting me with this daunting task. Andreas Leemann, thank you for the fruitful collaboration that began with a directed study. Lastly, I want to thank Isabel Fernandes for agreeing to be an evaluator of my thesis and for her continued support.

I owe an endless supply of thanks to the Vanier Scholarship (Natural Sciences and Engineering Research Council of Canada - NSERC). Financial freedom allowed me to remove a layer of stress and discover my potential as a researcher and knowledge sharer.

Table of Contents

List of Figures

List of Tables

List of symbols and abbreviations

AAR	Alkali-Aggregate Reaction
ACR	Alkali-Carbonate Reaction
AI	Artificial Intelligence
AIC	Akaike Information Criterion
ASR	Alkali-Silica Reaction
ASTM	American Society for Testing and Materials
β_0	Intercept coefficient in linear regression
β_i	Variable *i* coefficient in linear regression
CI	Confidence Interval
C_3A	Tricalcium Aluminate
CAD	Coarse Aggregate Debonded
CCA	Closed Crack in the Aggregate
CCP	Crack in the Cement Paste
CCPG	Crack in the Cement Paste with Gel
CCP_{RP}	Crack in the Cement Paste with Reaction Product
CD	Crack Density
CNN	Convolutional Neural Network
CO_2	Carbon Dioxide
CPT	Concrete Prism Test
CSA	Canadian Standards Association
CSH	Calcium Silicate Hydrate
DAP	Disaggregated or corroded particle
Debon	Debonded or dislodged aggregate
DEF	Delayed Ettringite Formation
DEF+ASR	DEF combined with ASR
DRI	Damage Rating Index
E	Modulus of Elasticity
EST	Estimated values
f_c	Compressive strength
f_c'	Design Compressive strength
f_t	Tensile strength
FT+ASR	FT combined with ASR
GT	Ground Truth
GU	General Use
HA	Hysteresis Area
HP	High Purity
IQR	Interquartile Range
ISR	Internal Swelling Reaction
k	Number of count categories

KOH	Potassium Hydroxide
ML	Machine Learning
n or N	Number of analyzed squares
$Na_2O_{eq.}$	Equivalent Sodium Hydroxide
NaOH	Sodium Hydroxide
NLI	Nonlinearity Index
NM	New Mexico
o_e	Expected counts
o_i	Observed counts
OCA	Open Crack in the Aggregate
OCAG	Open Crack in the Aggregate with Gel
OCA_{RP}	Open Crack in the Aggregate with Reaction Product
PDI	Plastic Deformation Index
PNG	Portable Network Graphic
R^2	Coefficient of Determination
RBG	Red Blue Green
RH	Relative Humidity
ROI	Region of Interest
SD	Standard Deviation
SDI	Stiffness Damage Index
SDT	Stiffness Damage Test
Tx or TX	Texas
UV	Ultraviolet
$\Delta l/l\%$	Length change
$\Delta v/v\%$	Volumetric change
SPR	Springhill
X_i	DRI number until square *i*

Chapter 1: Introduction

1.1.Synopsis

Internal swelling reactions (ISR) are among the most severe mechanisms of concrete deterioration affecting critical infrastructure worldwide [1–3]. Alkali-aggregate reaction (AAR), delayed ettringite formation (DEF), and freezing and thawing (FT) constitute ISR mechanisms, which result in an expansive phenomenon that develops and leads to internal and external cracking, reduction of load capacity (i.e., public safety concerns), and significant deformations that impact the serviceability and accessibility of the structure (e.g., operation of doors and flood gates, dilation joint alignment, uneven sidewalk surfaces, etc.). Effective maintenance and repair of concrete affected by ISR necessitate an examination of the current condition of the concrete material to determine the cause and extent of damage, as well as the potential for further deterioration. In Canada, AAR has prompted investigations across several provinces [4–10], the establishment of material testing and reactive aggregate usage standards (CSA A23.2-27A), and the development of condition assessment tools such as the stiffness damage test (SDT) and the damage rating index (DRI) [11–15]. While the parameters of the SDT have been extensively studied for integration into engineering practice [12,16,17], work remains to be done for the DRI due to several factors, such as time constraints, subjectivity in result interpretation, and a lack of conceptual understanding of the method as an engineering tool. Consequently, the DRI, a microscopy tool developed in Canada in the 90s [13], enables an operator to identify the cause and extent of damage to concrete using a stereomicroscope. The DRI was initially introduced as a petrographic tool and continues to be utilized as such [18–20], while it has more recently found application in engineering practice [10,11,21–25]. Through a point counting method, all distress features (i.e., cracks categorized by location, type, and whether filled with reaction product) are classified and counted in 1 cm by 1 cm squares on the surface of a sawn and polished concrete core, weighted using pre-determined factors based on the severity of these features relative to the damage, and normalized over 100 cm^2. The DRI generates a wealth of valuable information, such as a numerical score for direct comparisons, bar charts of the weighted and unweighted normalized counts (the latter being for the extended version of the DRI [15,26]), heatmaps to visualize the distribution of the deterioration [27,28], and, most importantly, correlations with volumetric expansions [14,29–31]. Therefore, a multi-level assessment was developed to characterize the cause and extent of damage based on SDT outputs, mechanical property losses, and the DRI number for ISR [21]. However, the DRI number alone does not capture the various patterns generated by AAR, DEF, and/or FT at different levels of deterioration. Therefore, this work addresses the limitations associated with using the DRI in engineering practice for a better understanding and determination of ISR-induced deterioration in concrete. Reliable, accessible, and practical evaluation tools to assess concrete deterioration are crucial for accurately investigating critical infrastructure affected by ISR.

1.2.Research objectives

The main objectives of this research are as follows and illustrated in Figure 1.1:

1. Adaptability: Apply the DRI tool to concrete affected by mechanisms other than ASR, such as delayed ettringite formation (DEF).
2. Subjectivity: Reduce the subjectivity of the DRI outputs by correlating the distress features with expansion and mechanical responses to better understand the role of each distress feature for a given ISR extent of damage.

3. Accessibility: Improve the DRI tool's accessibility for scientific and engineering practitioners by establishing an autonomous operator training and calibration protocol by defining the ranges of expected values obtained by experienced operators.

4. Ingenuity: Propose a universal evaluation technique of machine learning outputs to understand better the distress feature count distributions, capturing the extent of AAR damage and better selecting training datasets.

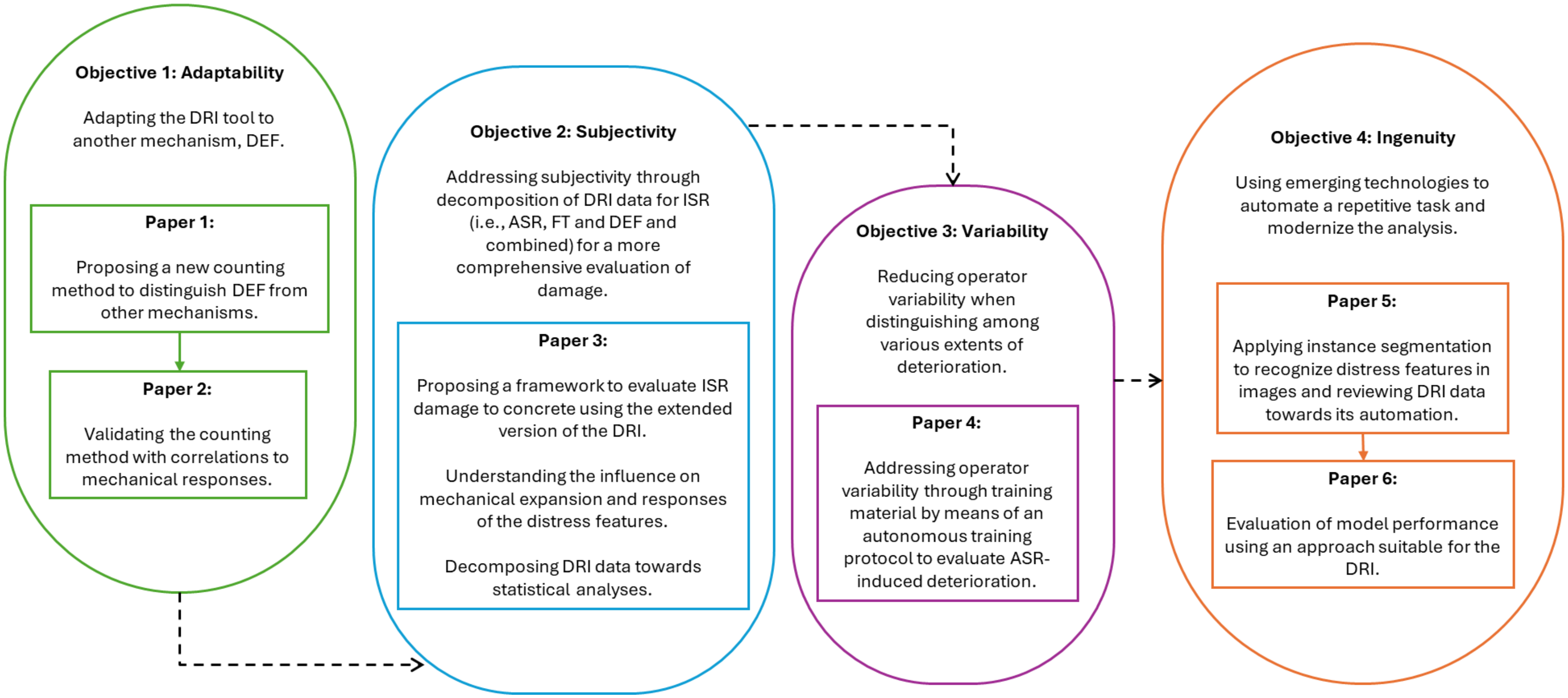

Figure 1.1. PhD Thesis objective organization.

1.3.Thesis organization

This thesis will be divided into 10 chapters. Chapter 1 introduces the research gaps regarding the evaluation of damage to concrete caused by internal swelling reactions (ISR) using the damage rating index (DRI) as an evaluation tool.

Chapter 2 will follow with a comprehensive literature review on using the damage rating index (DRI) since its development to understand how engineering practitioners can adopt it to evaluate damage to concrete objectively. Chapter 2 will raise the questions that have prompted this research program, such as "*How do you address/consider the variability when conducting the analysis?*" "*How do you draw objective conclusions from the results?*" and "*How can we adopt the DRI as an engineering tool?*". This chapter begins with an insight into how durability and preservation are paths towards sustainable approaches, followed by an overview of internal swelling reactions such as alkali-aggregate reaction (AAR), delayed ettringite formation (DEF), and freezing and thawing (FT), along with the current methods used to diagnose their damage to concrete. The core of the literature review is captured by a critical review of the DRI since its development.

Chapter 3 demonstrates the research methodology and experimental program associated with the subsequent chapters 4 through 10.

Chapter 4 presents a peer-reviewed conference paper that has been presented at the 1st Interdisciplinary Symposium on Smart & Sustainable Infrastructures (ISSSI 2023) international conference in conjunction with the 77th RILEM Annual Week (*Réunion Internationale des Laboratoires et Experts des Matériaux, systèmes de construction et ouvrages*) and was published with Springer entitled *"Capturing internal swelling reactions (ISR) damage in concrete through the damage rating index (DRI)"*. This chapter highlights the methodology adopted to distinguish

DEF from ASR through the counting procedure. The adaptability of the DRI tool was further presented at the *29^{e} Colloque sur la progression de la recherche québécoise sur les ouvrages d'art* where the constructive feedback from operators in other academic institutions and practitioners in the industry was well received. The presentation was entitled *"L'évaluation de béton atteint par les réactions de gonflement interne"*.

Chapter 5 presents a peer-reviewed conference paper entitled *"Evaluation of damage due to DEF through the multi-level assessment"* published by the 17th International Conference on Alkali-Aggregate Reaction in Concrete (ICAAR) via Springer. This chapter assesses the damage characteristics caused by DEF in comparison to mechanical responses to validate the counting method proposed in Chapter 4.

Chapter 6 presents a journal paper to be submitted to Cement and Concrete Research, in which the distress features noted in the DRI methodology are evaluated against expansion and mechanical responses to distinguish their roles in ISR-induced concrete deterioration. This paper also addresses variability within a sample, establishes confidence intervals for the total counts of each distress feature based on the extent of ISR deterioration, and breaks down the DRI data to better understand the contribution of the count distribution to the extent of deterioration.

Chapter 7 presents a technical letter from RILEM that has been accepted for submission, acting as a guide for operator calibration. Due to the significant demand for training in the damage rating index's (DRI) methodology, this work was developed to function as an independent training protocol. Alongside creating this paper, a workshop was organized as a pre-conference event for ICAAR. This workshop received support through co-sponsorship from RILEM's Educational Activities Committee (EAC) PhD Course program and ACI (American Concrete Institute).

Chapter 8 presents a peer-reviewed conference paper entitled *"Reviewing the damage rating index (DRI) concept towards its automation"* published at the 17th International Conference on Alkali-Aggregate Reaction in Concrete (ICAAR) via Springer. This work follows a feasibility study on the automation of DRI using machine learning [32], which yielded promising results. However, a new approach was necessary because of the large volume of new training data required. Therefore, this project is ongoing in collaboration with Englobe Corp.

Chapter 9 presents a peer-reviewed journal paper submitted to Cement that outlines a proposed method for interpreting DRI data collected through its automated version. This method facilitates more efficient visual and statistical comparisons, enabling multidisciplinary efforts to achieve a common metric for evaluating a machine learning model's performance.

Chapter 10 summarizes the findings of this research program and provides insights into further studies and steps necessary to advance the use of the DRI in engineering practice.

1.4. References

[1] V.E. Saouma, ed., Diagnosis & Prognosis of AAR Affected Structures: State-of-the-Art Report of the RILEM Technical Committee 259-ISR, Springer International Publishing, Cham, 2021. https://doi.org/10.1007/978-3-030-44014-5.

[2] L.F.M. Sanchez, Internal Swelling Reactions in Concrete: Mechanisms and Condition Assessment, 1st ed., CRC Press, Boca Raton, 2024. https://doi.org/10.1201/9781003188155.

[3] I. Sims, A. Poole, eds., Alkali-aggregate reaction in concrete: a world review, CRC Press, Taylor & Francis Group, a Balkema book, Boca Raton London New York Leiden, 2017.

[4] M.D.A. Thomas, K.J. Folliard, J.H. Ideker, North America (USA and Canada), in: Alkali-Aggregate Reaction in Concrete: A World Review, 1st ed., Taylor & Francis Group, London, UK, 2013: pp. 467–491.

[5] C. Rogers, P.E. Grattan-Bellew, R.D. Hooton, J. Ryell, M.D. Thomas, Alkali-aggregate reactions in Ontario, Can. J. Civ. Eng. 27 (2000) 246–260. https://doi.org/10.1139/l99-073.

[6] D. Bragg, Alkali-aggregate reactivity in Newfoundland, Canada, Can. J. Civ. Eng. 27 (2000) 192–203. https://doi.org/10.1139/l99-067.

[7] M.-A. Bérubé, B. Durand, D. Vézina, B. Fournier, Alkali-aggregate reactivity in Québec (Canada), Canadian Journal of Civil Engineering 27 (2000) 226. https://doi.org/10.1139/cjce-27-2-226.

[8] The Jacques Cartier and Champlain Bridges Incorporated, Deconstruction of the original Champlain Bridge, Ponts Jacques Cartier - Champlain Bridges (2023).

https://jacquescartierchamplain.ca/en/major-projects/deconstruction-of-the-original-champlain-bridge/deconstruction-site/history/ (accessed August 1, 2023).

[9] L.F.M. Sanchez, B. Fournier, D. Mitchell, J. Bastien, Condition assessment of an ASR-affected overpass after nearly 50 years in service, Construction and Building Materials 236 (2020) 117554. https://doi.org/10.1016/j.conbuildmat.2019.117554.

[10] M. Khaleghi-Esfahani, B. Fournier, B. Bissonnette, P.-L. Fecteau, D. Conciatori, S. Khani, Diagnostic and Prognostic Assessments on a 50 Year-Old Bridge Subjected to Severe Environmental and In-Service Conditions, in: L.F.M. Sanchez, C. Trottier (Eds.), Proceedings of the 17th International Conference on Alkali-Aggregate Reaction in Concrete, Springer Nature Switzerland, Cham, 2024: pp. 597–605. https://doi.org/10.1007/978-3-031-59419-9_69.

[11] M.-A. Bérubé, N. Smaoui, B. Fournier, B. Bissonnette, B. Durand, Evaluation of the expansion attained to date by concrete affected by alkali–silica reaction. Part III: Application to existing structures, Can. J. Civ. Eng. 32 (2005) 463–479. https://doi.org/10.1139/l04-104.

[12] L.F.M. Sanchez, B. Fournier, M. Jolin, J. Bastien, D. Mitchell, Practical use of the Stiffness Damage Test (SDT) for assessing damage in concrete infrastructure affected by alkali-silica reaction, Construction and Building Materials 125 (2016) 1178–1188. https://doi.org/10.1016/j.conbuildmat.2016.08.101.

[13] P.E. Grattan-Bellew, A. Danay, Comparison of laboratory and field evaluation of alkali-silica reaction in large dams, in: Collection / Collection : NRC Publications Archive / Archives des publications du CNRC, 1992: pp. 1–25.

[14] V. Villeneuve, Détermination de l’endommagement du béton par méthode pétrographique quantitative, Master’s Thesis., Université Laval, 2011.

[15] L.F.M. Sanchez, B. Fournier, M. Jolin, J. Duchesne, Reliable quantification of AAR damage through assessment of the Damage Rating Index (DRI), Cement and Concrete Research 67 (2015) 74–92. https://doi.org/10.1016/j.cemconres.2014.08.002.

[16] L.F.M. Sanchez, B. Fournier, M. Jolin, J. Bastien, Evaluation of the Stiffness Damage Test (SDT) as a tool for assessing damage in concrete due to alkali-silica reaction (ASR): Input parameters and variability of the test responses, Construction and Building Materials 77 (2015) 20–32. https://doi.org/10.1016/j.conbuildmat.2014.11.071.

[17] L.F.M. Sanchez, B. Fournier, M. Jolin, J. Bastien, Evaluation of the stiffness damage test (SDT) as a tool for assessing damage in concrete due to ASR Test loading and output responses for concretes incorporating fine or coarse reactive aggregates, Cement and Concrete Research 56 (2014) 213–229.

[18] C.A. MacDonald, M. Piersanti, M. Shehata, J. Magnan, Use of the damage rating index (dri) to evaluate level of deterioration due to alkali-silica reaction in 34-year old concrete from the Sudbury area, in: 17th Euroseminar on Microscopy Applied to Building Materials, Toronto, Canada, 2019.

[19] F. Shrimer, Use of the Damage Rating Index as Input for Service Life Prediction in Alkali-Silica Reaction Affected Concrete, in: D. Cong, D. Broton (Eds.), Advances in Cement Analysis and Concrete Petrography, ASTM International, 100 Barr Harbor Drive, PO Box C700, West Conshohocken, PA 19428-2959, 2019: pp. 89–104. https://doi.org/10.1520/STP161320180246.

[20] M. Champagne, J. Lindgård, B. Fournier, B. Bissonnette, Profiling the internal damage within an ASR-affected dam component with the Damage Rating Index (DRI), in: 16th International Conference on Alkali-Aggregate Reaction, Lisboa, Portugal, 2022.

[21] L.F.M. Sanchez, T. Drimalas, B. Fournier, D. Mitchell, J. Bastien, Comprehensive damage assessment in concrete affected by different internal swelling reaction (ISR) mechanisms, Cement and Concrete Research 107 (2018) 284–303. https://doi.org/10.1016/j.cemconres.2018.02.017.

[22] R.-P. Martin, L. Sanchez, B. Fournier, F. Toutlemonde, Evaluation of different techniques for the diagnosis & prognosis of Internal Swelling Reaction (ISR) mechanisms in concrete, Construction and Building Materials 156 (2017) 956–964. https://doi.org/10.1016/j.conbuildmat.2017.09.047.

[23] H. Ahmed, A. Zahedi, L.F.M. Sanchez, P.-L. Fecteau, Condition assessment of ASR-affected reinforced concrete columns after nearly 20 years in service, Construction & Building Materials 347 (2022) 128570. https://doi.org/10.1016/j.conbuildmat.2022.128570.

[24] N.P. Hasparyk, S.C. Kuperman, Revisiting Concrete Structures from a Hydroelectric Power Plant Affected by ASR in Brazil, with a New Diagnose of Coupled Attack (ASR + DEF), in: L.F.M. Sanchez, C. Trottier (Eds.), Proceedings of the 17th International Conference on Alkali-Aggregate Reaction in Concrete, Springer Nature Switzerland, Cham, 2024: pp. 400–410. https://doi.org/10.1007/978-3-031-59349-9_46.

[25] R.H.R.Q. Melo, N.P. Hasparyk, F. Tiecher, Assessment of Concrete Impairments over Time Triggered by DEF, Journal of Materials in Civil Engineering 35 (2023). https://doi.org/10.1061/JMCEE7.MTENG-15041.

[26] L. Sanchez, B. Fournier, M. Jolin, M.A.B. Bedoya, J. Bastien, J. Duchesne, Use of Damage Rating Index to Quantify Alkali-Silica Reaction Damage in Concrete: Fine versus Coarse Aggregate, ACI Materials Journal 113 (2016). https://doi.org/10.14359/51688983.

[27] A. Zahedi, L. Saliba, L.F.M. Sanchez, A.J. Boyd, Reliability of the damage rating index to assess the condition of concrete affected by external sulfate attack, Magazine of Concrete Research 75 (2023) 135–148. https://doi.org/10.1680/jmacr.22.00061.

[28] M. Champagne, Applying the damage rating index for the spatial damage assessment in concrete specimens affected by alkali-silica reaction (ASR), Master's Thesis., Université Laval, 2020.

[29] P. Rivard, B. Fournier, G. Ballivy, The Damage Rating Index Method for ASR Affected Concrete—A Critical Review of Petrographic Features of Deterioration and Evaluation Criteria, Cement, Concrete, Aggr. 24 (2002) 11228. https://doi.org/10.1520/CCA10531J.

[30] M.-A. Bérubé, B. Fournier, T. Côté, Using the damage rating index for assessing the expansion of concrete affected by freeze-thaw, sulphate attack, or ASR, in: 14th International Conference on Alkali-Aggregate Reaction, Austin, Texas, USA, 2012.

[31] L.F.M. Sanchez, T. Drimalas, B. Fournier, Assessing condition of concrete affected by internal swelling reactions (ISR) through the Damage Rating Index (DRI), Cement 1–2 (2020) 100001. https://doi.org/10.1016/j.cement.2020.100001.

[32] A. Bezerra, The Use of Artificial Intelligence for Assessing Damage in Concrete Affected by Alkali-Silica Reaction (ASR), Master's Thesis., University of Ottawa, 2020.

Chapter 2: Literature review

2.1.Durability: The key to a sustainable future

Concrete is recognized as the most widely used building material worldwide. Its consumption signifies economic growth, as a significant portion of critical infrastructure is constructed using concrete. The mass of existing concrete can now be compared to global biomass [1]. However, concrete production considerably impacts the environment; cement production alone accounts for 26% of CO_2 emissions from the global industrial sector [2]. While society depends on reliable infrastructure to ensure the smooth movement of people, goods, energy, resources, and information, sustainability initiatives in the concrete industry aim to produce concrete materials that emit lower CO_2 levels to address climate change. For instance, electrification has been investigated as an alternative to fossil fuels for energy; however, it significantly affects the environment and communities where infrastructure, such as dams, is located [3]. Additionally, natural resources are becoming scarce in urban centres, where mining and exploitation in remote regions further obstruct societal progress. The Canadian federal government has invested in the maintenance and repair of existing infrastructure, translating into a preservation initiative for a more sustainable future by reducing the need for new concrete production and minimizing the disposal of unused concrete in landfills. Recycling concrete remains a challenge within the circular economy due to the lack of a Canadian standard protocol guiding practitioners on mixture proportioning and the non-urgent need to decrease landfill space in such a vast country. Therefore, our duty as civil engineering practitioners and academics is to ensure that existing infrastructure continues to serve the public safely and ethically. However, concrete deterioration caused by an active mechanism—where conditions such as temperature, relative humidity, and chemical composition accelerate the deterioration—poses a considerable challenge for owners/operators of critical infrastructure. These mechanisms cause irreversible damage that shortens the service life of concrete, with available strategies limited to mitigation (i.e., reducing the kinetics) and rehabilitation (i.e., external measures to fully or partially restore the lost mechanical performance of the affected element). Although demolition and rebuilding with better-performing materials may seem like the most viable option when repair costs exceed those of alternatives—such as with Montréal's Champlain Bridge [4,5]—in other cases, demolition leads to immeasurable disruptions and consequences for society and the environment, as demonstrated with the Mactaquac Dam in Fredericton, where the "Mactaquac Life Achievement Project" is currently being implemented to achieve the intended 100-year service life [6]. Furthermore, extending the service life through design by 50% can reduce cumulative CO2 emissions by 14% [7]. Conversely, the challenges arising from the decreased service life of a given concrete due to persistent distress mechanisms require additional resources.

Another approach to fostering a more sustainable concrete industry is the implementation of circular economy strategies [8]. The primary objectives of this approach are to reduce overall consumption and divert waste from landfills. This suggests that maintenance, repair, and rehabilitation become essential tasks to ensure that the concrete in the field meets the purpose for which it was designed and operates within the intended timeframe (i.e., service life). However, remedial measures may only be effective when the cause and extent of the damage are known; thus, their effectiveness depends on a thorough, accurate, and complete diagnosis that requires the proper tools to deliver such results. Access to reliable diagnostic tools is beneficial for preserving concrete rather than opting for demolition. Although recycling (or downcycling, in the case of concrete reduced to aggregate) is a common strategy in a circular economy, recycled concrete affected by internal swelling reactions (ISR) presents numerous challenges that can hinder its potential for further use [9,10]. Furthermore, Canadian standards do not explicitly guide mix-designers to use recycled concrete (CSA A23.1:19, 2019, clause 8.11.2.2.2.2 and Annex O [11]). Moreover, the emergence of new, more "sustainable" concrete materials highlights a gap in field performance data necessary to evaluate their durability. It is crucial to understand the impact of distress mechanisms in these new materials and the durability testing methods, as some knowledge may be transferred from conventional concrete to these innovative materials. Nonetheless, the tools currently employed to evaluate the damage to conventional concrete must offer a satisfactory level of certainty concerning their field performance to be considered reliable diagnostic instruments, thereby ensuring the durability of these innovative materials.

2.2. Overview of typical internal swelling reactions (ISR) in concrete

2.2.1. Alkali-aggregate reaction (AAR)

Alkali-aggregate reaction (AAR) is present around the world and one of the leading cause for early deterioration of concrete infrastructure [12]. There are two types of AAR in concrete: a) alkali-silica reaction (ASR) which involves reactive silica in the aggregate and b) alkali-carbonate reaction (ACR) involving carbonate rock aggregates; the latter being less understood and less common on the field. ASR therefore consists of a chemical reaction between unstable silica mineral phases from the aggregates and the alkalis (Na^+, K^+, OH^-) from the concrete pore solution resulting in a secondary reaction product formed that swells upon water intake. This secondary reaction product is often referred to as "silica gel". The secondary reaction product exerts a pressure greater than that of the tensile resistance of concrete resulting in cracking of the concrete (Figure 9.1.1).

Figure 2.1. ASR-affected concrete retaining wall next to an on-ramp in Québec.

On the other hand, ACR entails carbonate rock aggregate in which the process of dedolomitization (Equation 2.1) is observed where the dolomite is transformed into calcite and brucite in an alkaline environment. The damaging effects of ACR therefore remain unknown yet, ACR can be characterized by dark rims on the aggregate's boundary and a white carbonate halo around the aggregate in the cement paste (Figure 2.2a). Dedolomitization (Figure 2.2b) is considered as a harmless process by some researchers [13–15] although the so-called ACR can cause expansion [16]. ACR has devasted regions nearby Kingston, Ontario for which the quarries containing such reactive carbonate rock have since been closed. This reaction is said to not cause expansion nor expansion related cracks [14] while it is believed that the mechanism causing cracks in such concrete is the presence of ASR gel [14,17].

$$\underset{\text{dolomite}}{CaMg(CO_3)_2} + 2OH^-{}_{aq} \longrightarrow \underset{\text{brucite}}{Mg(OH)_2} + \underset{\text{calcite}}{CaCO_3} + CO_3^{2-}{}_{aq} \quad \text{Eq. 2.1}$$

a) b)

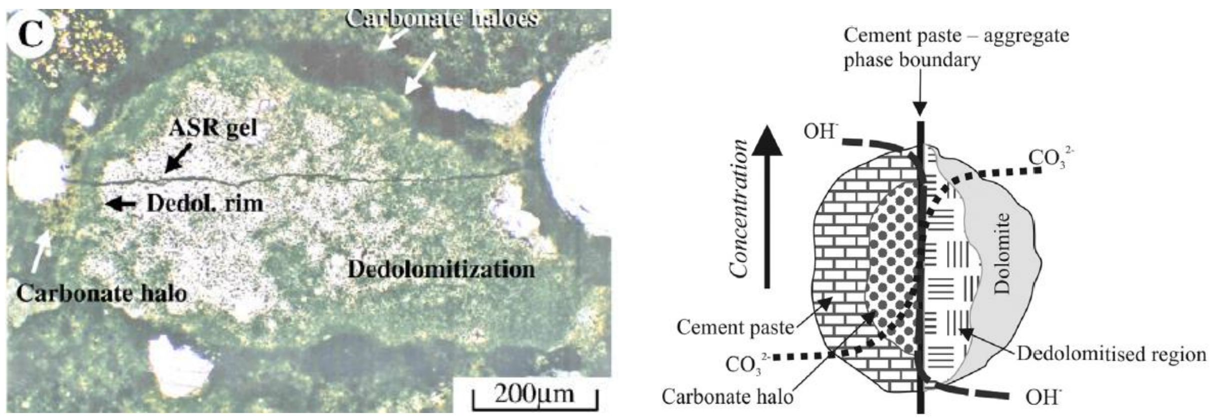

Figure 2.2. The so-called ACR in concrete as represented by a) Katayama [14] with the inclusion of ASR and b) Štukovnik et al. (2019) without ASR.

2.2.2. Delayed ettringite formation (DEF)

Delayed ettringite formation (DEF) is a form of internal sulphate attack in which cracks in the concrete's cement paste are generally observed accompanied by ettringite crystals filling such gaps without an external source of sulphates (i.e., external sulphate attack). Ettringite is one of cement's (i.e., Portland cement) primary hydration products; the others being Portlandite and CSH. Ettringite plays an important role in controlling concrete's stiffening; the transition between the fresh to hardened state [18]. Ettringite can appear in voids (Figure 2.3) and cracks yet doesn't indicate damage since it can dissolve and recrystalize in such locations when exposed to long periods of moisture [18,19]; this form of ettringite is referred to as *secondary ettringite* and is considered as harmless [20].

a) b)

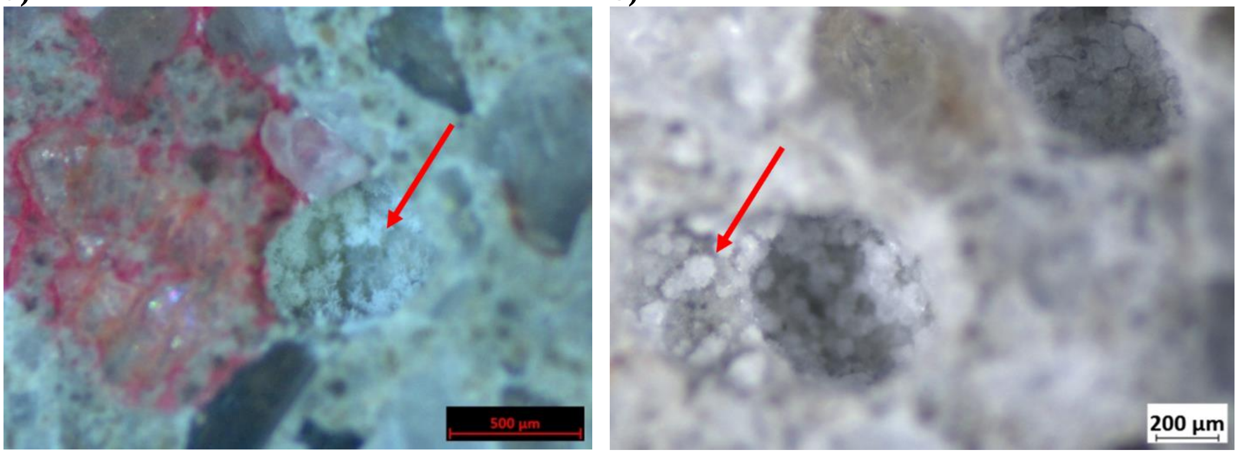

Figure 2.3. Micrographs of concrete presenting ettringite needles in void from concrete extracted from: a) a bridge in Brazil and b) jersey barriers from Atlanta, USA.

However, when internal temperatures reach above approximately 65°C [19,20], the conditions prevent the ettringite from forming and as the temperature reduces, the ettringite forms in the stiff concrete hence the term "*delayed ettringite formation*". The elevated temperatures can be produced in steam-cured concrete, mass concrete, casting in high heat weather, excess of cement, and certain cement physical and chemical leading to high hydration heat after which the ettringite crystals grow under humid conditions [20]. Some researchers state that due to the excessive heat required for DEF to occur, there is a homogeneous paste expansion detaching it from the aggregate causing the gaps where ettringite later fills meanwhile others believe the formation of the crystals cause the cracking [21–25]. Nevertheless, the characteristics of damage to concrete due to DEF remain as cracks at the aggregate-paste interface and cracks in the bulk cement paste.

DEF is also often found in combination with ASR on the field as a decrease in alkalis consumed by ASR favours ettringite formation [23,26]. The challenge faced when assessing such combined mechanisms is the determination of the contribution of the distinct mechanisms. Moreover, leaching of alkalis at a concrete's surface could induce heterogenous damage where more evidence of DEF or ASR could be observed at different locations. Nevertheless, an understanding of the damage caused by DEF as captured through the DRI is necessary before attempting to decouple the combined mechanisms. Thus, this work only focuses on single mechanisms.

2.2.3. Freezing and thawing (FT)

In addition to the combination of DEF with ASR, concrete can experience freezing and thawing (FT) either independently or alongside ASR when exposed to severe climates such as those found in Canada. This typically results in deterioration, which is characterized by cracks in the cement paste (see Figure 2.4a). The deterioration process due to FT often begins with moisture infiltrating the surface, causing layers of concrete near the surface to delaminate sequentially (refer to Figure 2.4b). Concurrently, the inner regions of the concrete are subject to uneven pressures within the void system of the cement paste, leading to cracks forming around these voids. Cracks resulting from FT are usually located at the interface between the aggregate and paste, extending into the cement paste [27,28]. FT-related deterioration further weakens the aggregate-paste interface, where the micromechanical properties are most adversely affected [29]. This is consistent with the crack propagation model described by [30], as shown in Figure 2.4c. There is a lack of extensive research on the combined impacts of FT and ASR [27,31–34]. Nevertheless, Gong et al. (2020) explored the effects of FT and ASR, particularly when one distress mechanism was triggered before the other. Their modelling indicated that FT continues to affect the concrete even as ASR reaction products accumulate in the entrained air voids, thereby reducing the overall effectiveness of air entrainment [32].

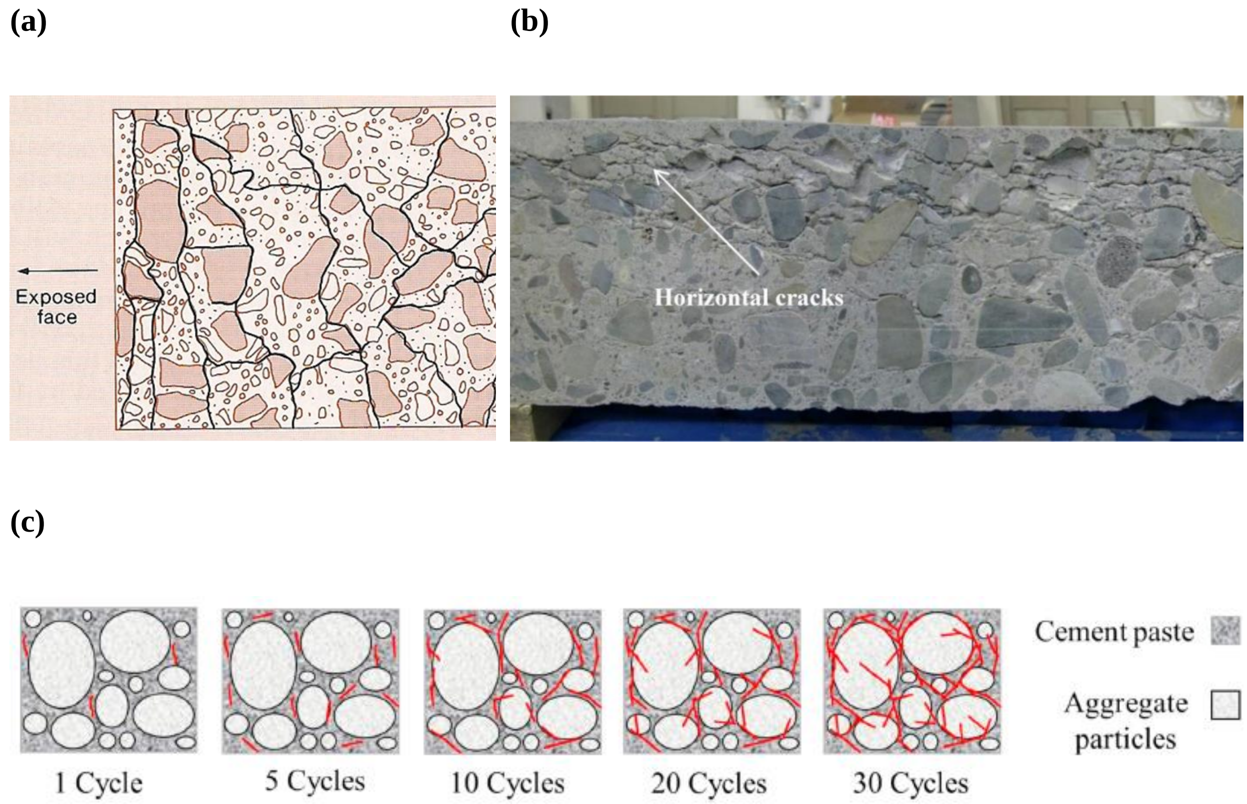

Figure 2.4. FT crack pattern: (a) as by [35], (b) from a cross section of a 40 year of canal wall exposed to water and soil (top and bottom of the image, respectively) [36], and (c) as a descriptive crack propagation model [30].

However, it is crucial to comprehend the damage inflicted by DEF and FT, as revealed through stereomicroscopy, before attempting to separate their intertwined mechanisms. There has been a noticeable rise in instances where ASR has been pinpointed as the main cause of ISR damage when utilizing a multi-level assessment [27,37–41]. Yet, given the extensive research focused on diagnosing ASR in comparison to DEF and FT, there are ongoing concerns about the risk of misdiagnosis, especially in cases involving multiple mechanisms. Thus, gaining a clearer insight into distinguishing DEF and FT from other mechanisms using visualization tools that illustrate the damage's spread and pattern in the concrete is vital, particularly during the early and intermediate stages.

2.3. Tools used to diagnose the cause of damage and evaluate its extent

2.3.2. Qualitative evaluation of damage through microscopy

Microscopy is currently used to diagnose secondary reaction products from AAR, DEF, or other mechanisms producing a secondary reaction product. The secondary reaction products are detected through optical microscopy or SEM, which can be combined with EDS/EDX to determine the chemical composition of the observed minerals. Petrography involves producing thin sections approximately 30 microns thick, after which the sections are examined using optical microscopy to distinguish the minerals. Conversely, SEM can be used for either thin sections or small mounted sections (thicker than 30 microns, depending on the capacity of the equipment used for preparation and analysis). Microscopy serves as a tool to characterize the observed concrete products and examine areas where damage has occurred. However, such equipment and testing protocols necessitate experienced petrographers to prepare or validate sample preparation and conduct the diagnosis. Furthermore, the analysis is limited to the size of the samples that the equipment can accommodate, meaning multiple sample sets may be required to assess the extent of damage, depending on the magnification used. Nevertheless, properly characterizing secondary reaction products remains crucial to a complete diagnosis. Figure 2.5 illustrates the secondary reaction products associated with ASR and DEF.

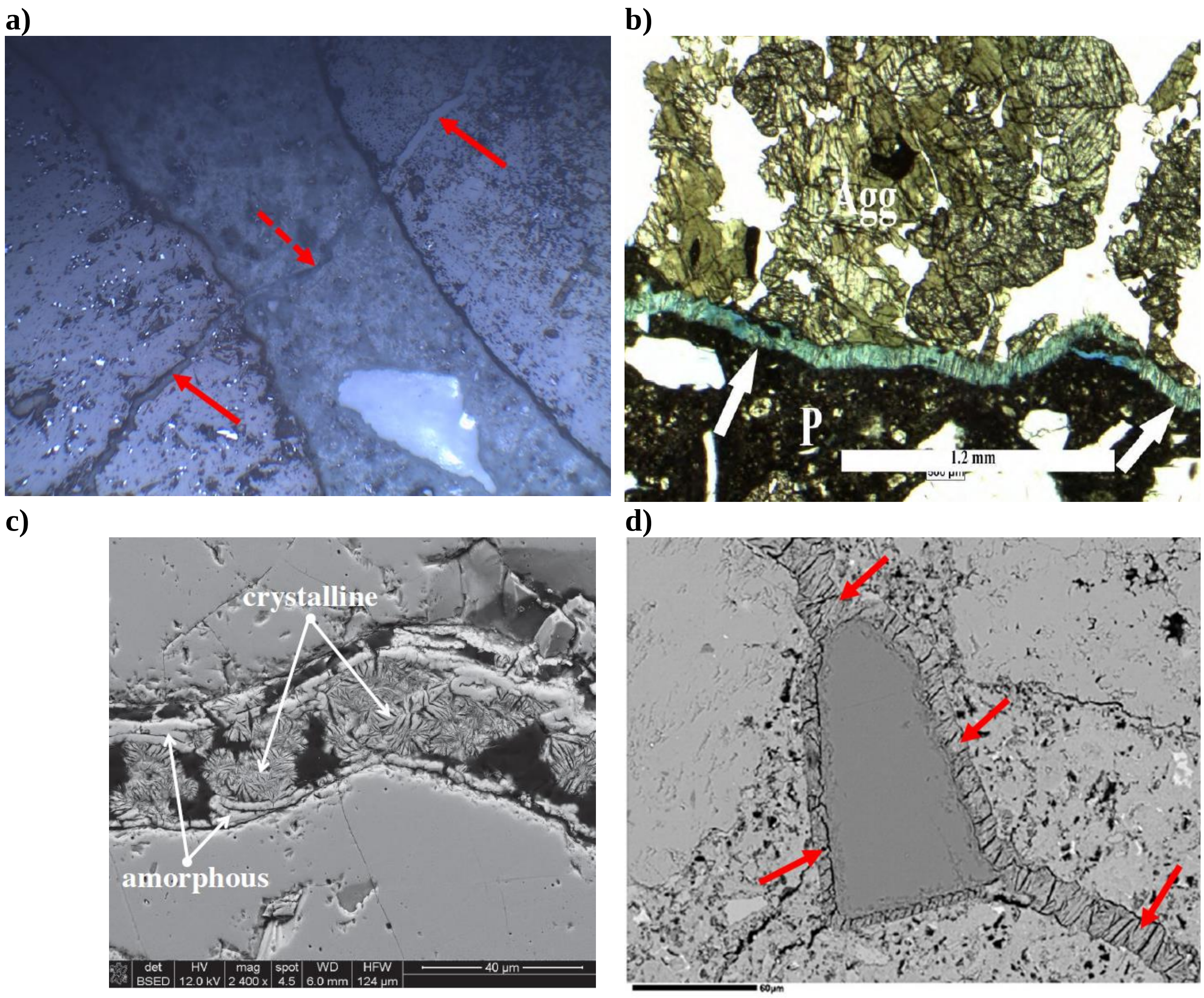

Figure 2.5. Micrographs captured with: a) optical microscopy under reflected light where the solid arrows highlight a crack filled with ASR secondary reaction product in the aggregates while the dashed arrow highlights a crack filled with ASR secondary reaction product in the cement paste (field of view of 2 mm), b) optical microscopy under natural light where the ettringite is highlighted by a blue epoxy (scale bar represents 1.2 mm) [42], c) SEM in BSE mode where both crystalline and amorphous ASR secondary product is highlighted (scale bar represents 40 microns) [43], and d) SEM in BSE mode where red arrows highlight ettringite filled crack surrounding the dark grey aggregate particle (black bar shows scale of 60 microns) [23].

The petrographic and distress features commonly observed as indicators of AAR (ASR and ACR) and DEF differ significantly from one another, making the diagnosis of each mechanism feasible through stereomicroscopy. DEF exhibits detached or dislodged aggregate particles [23,44–46], cracks that are partially or completely filled with ettringite [23], and cracks surrounding the aggregate that are either partially or completely encompassing it [22]. In contrast, ASR-affected concrete shows opaque crystalline “silica gel” made up of silicon, sodium, potassium, and calcium in the aggregate's cracks, along with amorphous “silica gel” that has a more translucent colour visible in cracks within the cement paste, which has a higher calcium content [47]. This change in the characteristics of the ASR secondary reaction product indicates damage progression, as cracks typically initiate in the aggregate and gradually extend toward the cement paste as the damage increases, as illustrated in Figure 2.6a [48]. Additionally, the so-called “reaction rims” can be observed, where the outer edge of the reactive particles darkens (Figure 2.6b), and “silica gel” can be found in voids of the concrete (Figures 2.6c and d), which represent petrographic features. However, the distinction between features that indicate the presence of ASR and those that signify ASR damage should be classified into petrographic versus distress features, respectively.

a)

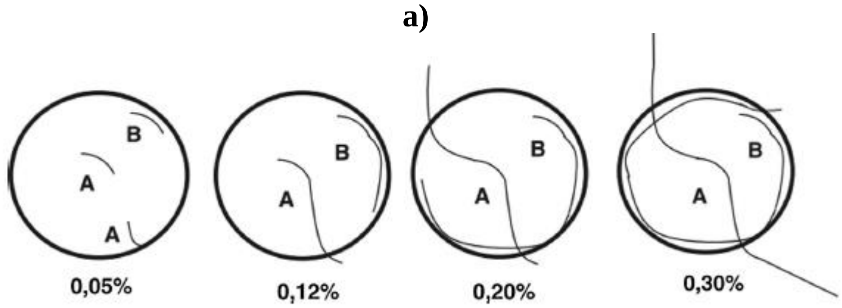

b) **c)**

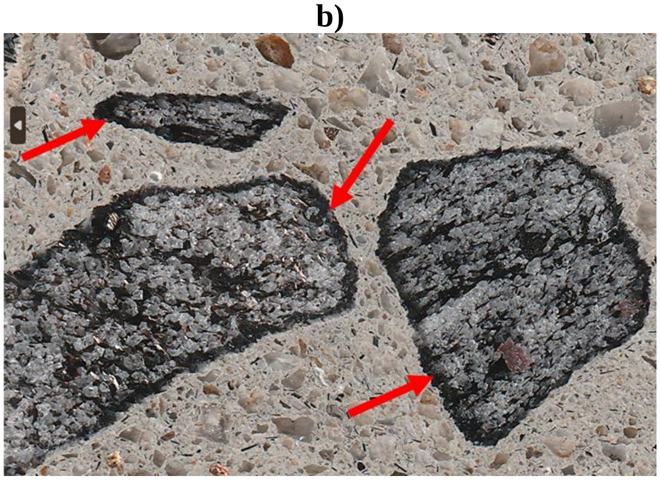

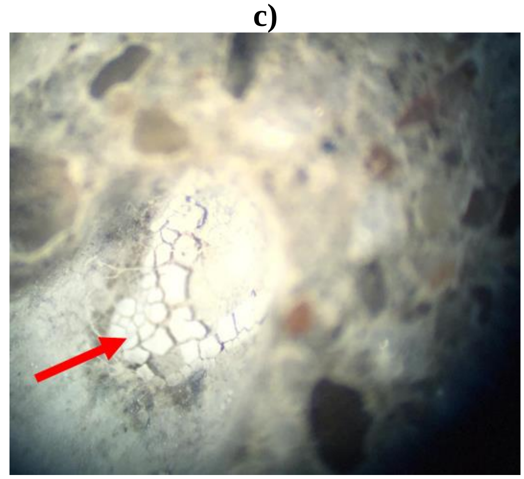

d)

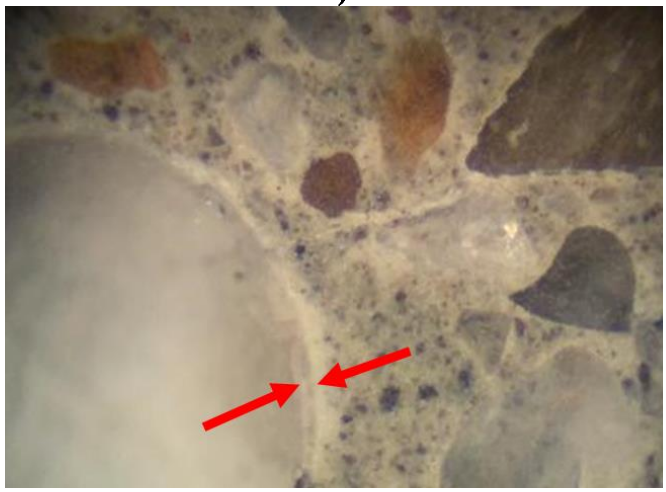

Figure 2.6. a) Qualitative model of crack propagation in ASR-affected CC with sharp cracks - A and onion skin cracks – B as per [48], b) micrographs of concrete affected by ASR presenting c) reaction rims, desiccated "silica gel", and d) "silica gel" lining a void.

However, a qualitative crack propagation model for DEF is not yet available outside this thesis's scope, even though models that demonstrate cracking patterns exist for various distress mechanisms in more deteriorated concrete (i.e., a more advanced stage of damage), as shown in Figure 2.7. Crack progression aids in characterizing the level of damage, thus complementing the deterioration assessment, although it can be challenging to examine through qualitative microscopy. Consequently, the next section of this literature review will introduce image analysis as a methodology to capture crack propagation and patterns, attempting to quantify the damage.

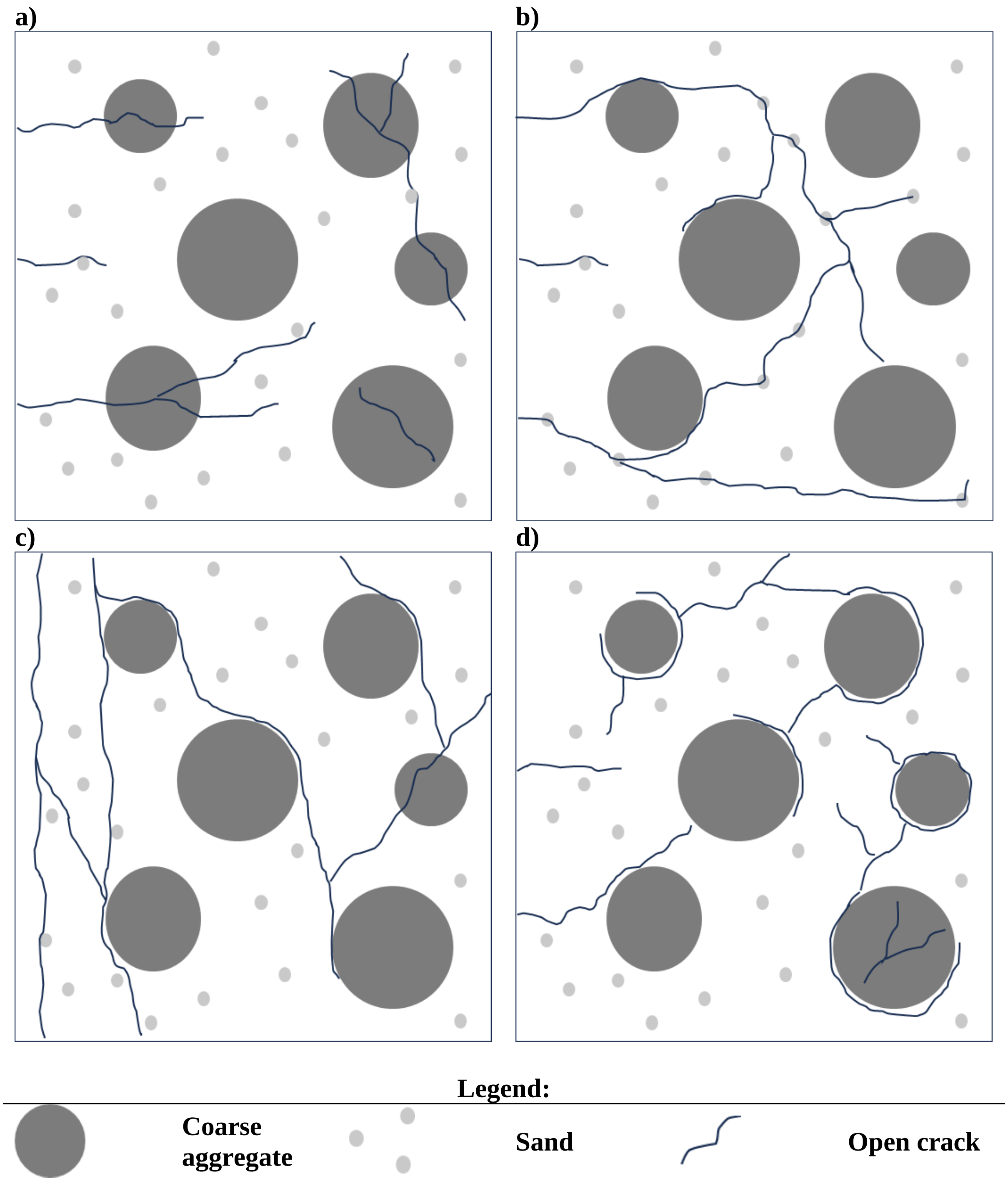

Figure 2.7. A crack pattern in concrete affected by a) ASR reactive coarse aggregate, b) ASR reactive sand, freezing and thawing cycles, and d) DEF. The concrete's surface is shown on the left-hand side. Adapted from [35].

2.3.3. *Image analysis: a step towards quantitative assessment of deterioration*

Many techniques have been developed over recent decades to understand the implications of distress features, specifically cracks, and their propagation throughout the material at a larger scale (i.e., mesoscale). Although all flaws and cracks compromise the quality of concrete, distinguishing between distress features/cracks that represent the measured mechanical damage is necessary. Techniques utilizing image analysis to quantify the characteristics of observed cracks at the mesoscale (e.g., extent, orientation, length, widths, and density) have proven effective in providing insight into the extent of the damage. By employing readily available open-source software such as ImageJ, Fiji, and NIH Image [49,50], analysis time may be reduced through the creation of a subroutine to eliminate unwanted artifacts in the analysis (i.e., voids filled with dye or fluorescent material when analyzing cracks). Furthermore, image analysis has begun quantifying the deterioration caused by ISRs based on observed or selected parameters. In an earlier study, Rivard et al. (2000) identified the lengths of cracks and their orientation as indicators of the extent of damage caused by ASR, using image analysis on laboratory-made specimens measuring 75 by 75 by 300 mm at 20x magnification. However, they noted that the aggregate influences the damage indicator (i.e., Potsdam sandstone shows a better correlation between crack density and expansion) [51]. Later, Lindgård et al. (2012) developed the concept of 'cracking intensity' to correlate the area of cracks with prism expansion induced by ASR, using a larger analysis surface (i.e., 70 mm by 280 mm) to provide characteristics such as cracking extent and pattern, thereby highlighting the necessity of using a surface area large enough to represent the concrete element [52]. In the absence of a reaction product, determining the cause of cracking can be challenging when employing other microscopy methods; therefore, image analysis may be better suited for these types of damage. In a study measuring damage from freezing and thawing, Li et al. (2014)

correlated crack characteristics such as crack length density (i.e., total length over the analyzed area) and crack area density with mechanical damage for both air-entrained and non-air-entrained concrete mixtures using image analysis at 40x magnification [28]. Although image analysis provides valuable insights at a scale more representative of induced mechanical degradation, selecting crack characteristics as a damage indicator when the damage level remains a challenge emphasizes the importance of combining tools to evaluate damage from unknown distress mechanisms. The following section presents the multi-level assessment, which integrates mechanical and microscopy tools to evaluate and measure the damage caused by ISR.

2.3.4. Multi-level assessment

Concrete in service may not show signs of deterioration for several years, particularly if the deterioration stems from an ISR such as AAR and DEF, where damage propagates from within the concrete. The multi-level assessment protocol was developed to evaluate and quantify the extent of damage caused by ISR, facilitating informed decision-making regarding mitigation, repair, and rehabilitation strategies. The following section will provide an overview of the concept behind the stiffness damage test (SDT) and a brief introduction to the damage rating index (DRI), with a more comprehensive review to be presented in Section 2.4.

- *<u>The stiffness damage test (SDT)</u>*

The stiffness damage test (SDT) is a mechanical cyclical loading test that measures the amount of damage (i.e., cracks) within the concrete by evaluating the energy released into the system. Initially, a loading/unloading test under compression was developed to assess rock cores [53], where the impact of cracks in a solid material was analyzed via stress-strain curves. Following this research, Chrisp et al. (1993) created the initial version of the SDT to quantify damage to concrete caused by ASR while preserving the specimen (the non-destructive nature of the SDT) for future testing after a designated period under accelerated exposure conditions [54]. They discovered that the parameters best-describing damage varied based on the damage level, typically unknown during a diagnostic evaluation. The influence of crack orientation was also captured through the SDT and stress-strain curves (Figure 2.8). The modulus of elasticity was observed to vary because of crack orientation, and the hysteresis loop is largest when cracks are more perpendicular to the test load direction. The non-linearity index (NLI) was introduced to indicate the principal direction of the cracks, where an NLI below unity signifies cracks oriented parallel to the test loading direction; conversely, an NLI above unity indicates cracks perpendicular to the test loading direction. This parameter was further corroborated by [55], demonstrating the previously mentioned trend for cores extracted from reinforced concrete blocks, where an NLI below unity was found for cores oriented parallel to the reinforcements (i.e., longitudinal), with cracks aligned to the loading direction, becoming more pronounced with an increase in expansion represented by a lower NLI.

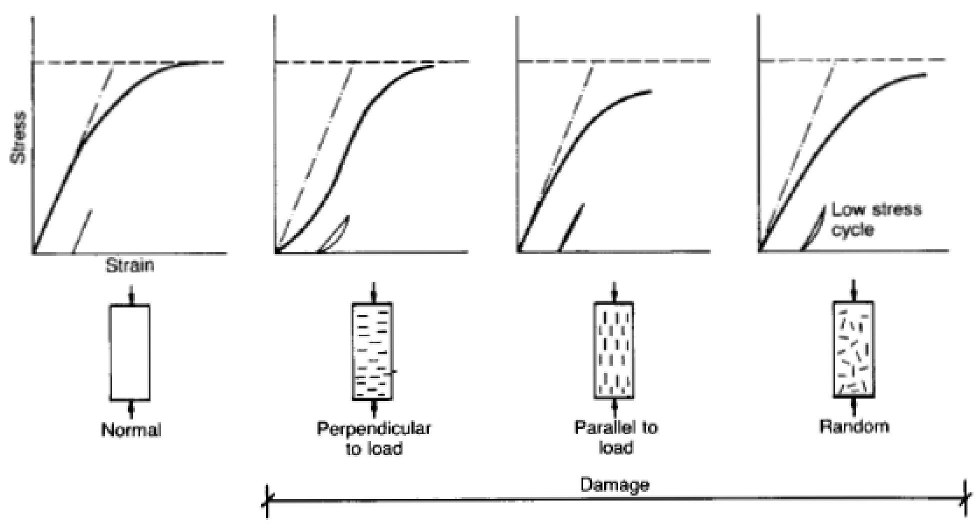

Figure 2.8. SDT and stress-strain response based on crack orientation [54].

Given concerns about differences between laboratory-made specimens and cores taken from actual structures, a three-part study was undertaken to assess the SDT's effectiveness in quantifying damage to concrete, following a scalable sequence: i) laboratory-made cylindrical specimens measuring 10 cm by 20 cm, ii) blocks and slabs created in the lab and subjected to various controlled conditions, and iii) cores extracted from multiple structures affected by ASR [38,56,57]. A modified version of the SDT was applied, increasing the test load to 10 MPa instead of the 5.5 MPa suggested by Chrisp et al., as a load of 10 MPa could close the cracks caused by ASR, yielding statistically reliable results. It was established that the SDT is more effective in quantifying ASR damage from cores taken from laboratory-made concrete blocks and in-service structures than from surface cracking and petrographic examinations. However, while the cause of the deterioration was known, it did not eliminate the need for microscopy. Furthermore, the modulus of elasticity, an important mechanical property in structural concrete, shows less diagnostic significance concerning its loss as expansion increases due to its convergence with increasing expansion. Smaoui et al. (2004) indicate that the two SDT parameters most valuable for assessing concrete expansion are the area of the hysteresis loop, which represents the energy dissipated during the first loading-unloading cycle, and the plastic axial deformation accumulated over the five cycles. This results in a coefficient of determination (R^2) greater than 0.83 when plotted against expansion, except for one instance where $R^2=0.27$; this is attributed to the precision of the deformation measurement equipment when analyzing low values of deformation [56]. Meanwhile, the variability of the results for plastic deformation remained minimal, even for those low values, which had higher uncertainty due to measurement precision, regardless of the type of reactive aggregate. Moreover, due to the experimental variability, a sample size of 3 is advised, particularly for cores extracted from structures to account for the material's heterogeneity under varying conditions. Figure 2.9 illustrates the output for sound concrete compared to damaged concrete.

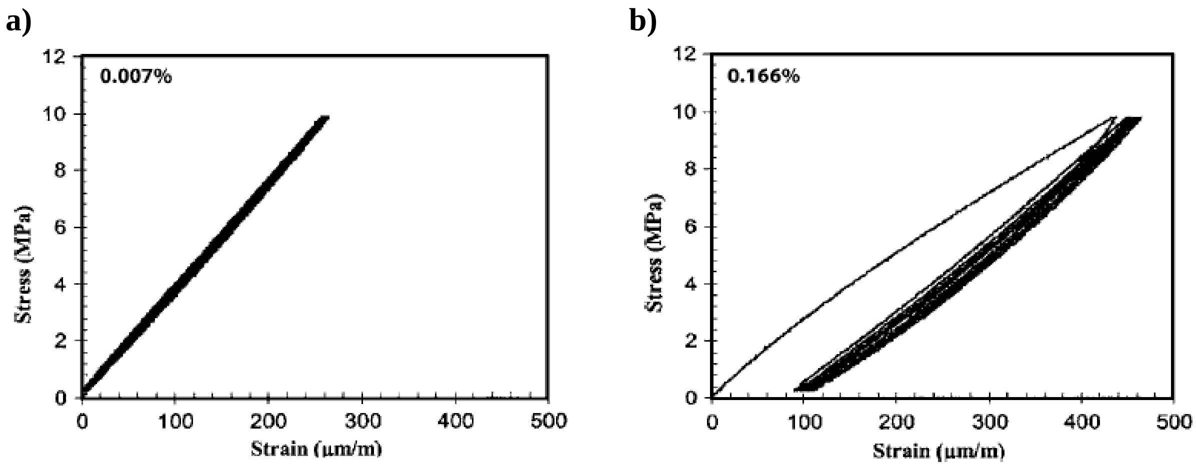

Figure 2.9. SDT stress-strain response for a) sound concrete and b) damaged concrete [56].

Sanchez et al. (2014, 2015, 2016) then advanced the developments on the SDT as an evaluation tool with a diagnostic character by comparing all the input/output parameters and proposing indices to quantify damage, irrespective of the type and initial strength properties of the conventional concrete [45–47]. One of the proposed input parameters that showed strong correlations with the level of damage was the test load of 40% of the maximum compressive strength of sound concrete or concrete that exhibited a low amount of damage, thus maintaining the non-destructive nature of the test by keeping the load within the elastic range of the material while also providing minimal variability [45]. Nonetheless, it was noted that for high levels of damage, the SDT may exhibit a destructive character [45], which was addressed by adjusting the load in another study [48]. Furthermore, specimen and core characteristics (i.e., aspect ratio, humidity conditions, end preparation, and core location), along with loading rate, were evaluated to better define the input parameters and their effects on the outcomes of the SDT [45].

The aforementioned indices represent the energy dissipated into the system relative to the total energy, specifically the stiffness damage index (SDI) and the plastic deformation relative to the total deformation as the plastic deformation index (PDI). The SDI (Equation 2.2) measures the energy used to close the cracks, indicating the loss of physical integrity, while the PDI (Equation

2.3) assesses the unrecoverable deformation. Meanwhile, the non-linearity index (NLI) indicates crack direction (Equation 2.4). An illustration of the SDT outputs is shown in Figure 2.10.

$$SDI = \frac{\sum_{i=1}^{5} SI_i}{\sum_{i=1}^{5}(SI_i + SII_i)} \quad \text{Eq. 2.2}$$

$$PDI = \frac{DI}{DII} \quad \text{Eq. 2.3}$$

$$NLI = \frac{secant\ of\ half\ maximum\ \ of\ first\ load\ cycle}{secant\ at\ maximum\ of\ first\ load\ cycle} \quad \text{Eq. 2.4}$$

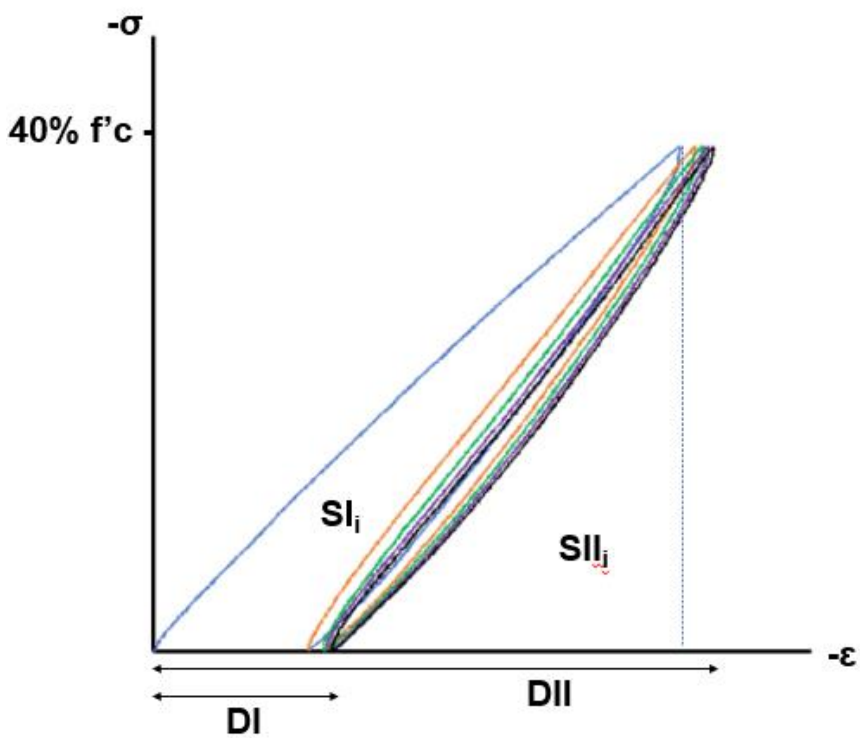

Figure 2.10. Illustration of SDT outputs.

The NLI is, therefore, used to illustrate the principal direction of the cracks. An NLI below one indicates cracks parallel to the test loading direction, while an NLI above one denotes cracks perpendicular to the test loading direction. This parameter was further verified by [55], which demonstrated the aforementioned trend for cores extracted from reinforced concrete blocks. An

NLI below one was observed for cores taken in the direction parallel to the reinforcements (i.e., longitudinal), where cracks are parallel to the loading direction. Their effect becomes more pronounced with an increase in expansion, represented by a lower NLI (Figure 2.11).

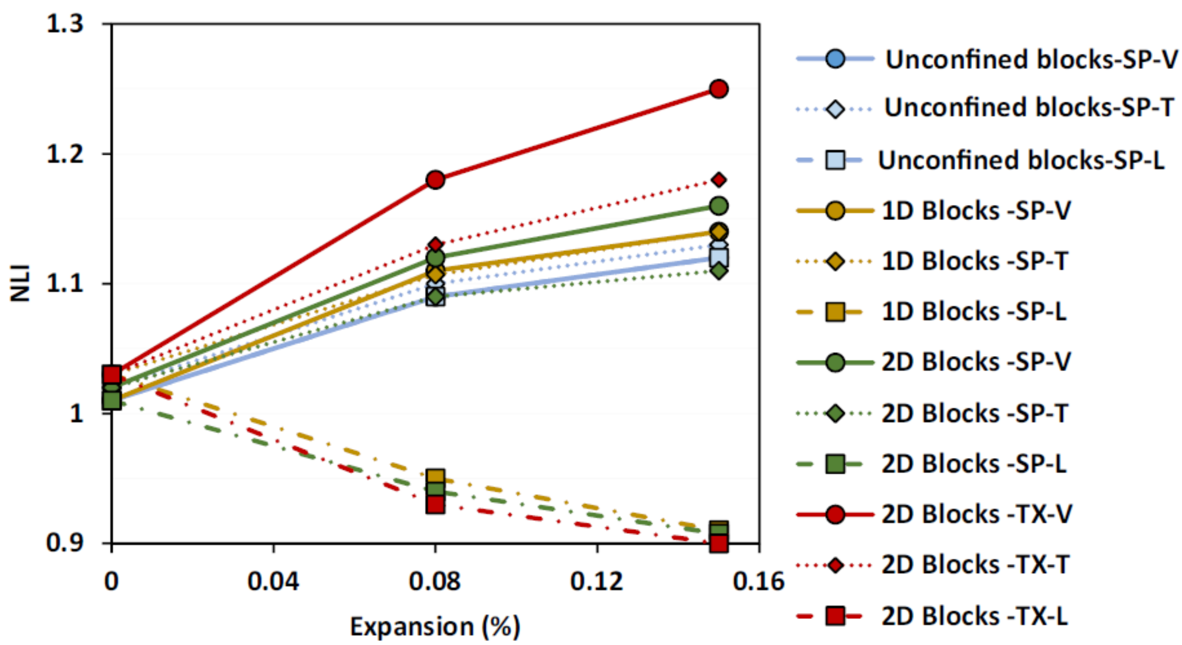

Figure 2.11. NLI vs deterioration level for various crack orientations [55].

The contributions to improving the diagnostic capabilities of the SDT led to the elimination of subjectivity in interpreting the results obtained and aided in quantifying the level of damage to the concrete. The SDT has since been employed for various distress mechanisms and has proven more adaptable to ISR mechanisms [44,58–60]. Alongside the development of the SDT for ASR applications, researchers have utilized the SDT to assess damage caused by fire [61–63]. However, to consider the multi-level assessment as a comprehensive tool package for the reliable diagnosis of unknown damage, both the SDT and DRI must fulfil specific reliability criteria to evaluate the cause and extent of damage.

- *The damage rating index (DRI)*

The following presents a general overview of the method, as a thorough critical review is provided in Section 2.4. The damage rating index (DRI) is a semi-quantitative microscopy tool that employs a stereomicroscope at 15-16x magnification, while the petrographer/operator counts petrographic and distress features in the field of view of 1 cm by 1 cm on the surface of a polished and reflective concrete section (Figure 2.12). Each count is multiplied by a weighting factor that indicates the importance of the petrographic and distress feature concerning the overall observable and measurable damage. The sum of all counts is normalized to 100 cm^2 for comparative purposes and accounts for differences in core or specimen sizes. Due to the various types of feature counts, bar charts are generated to visualize the importance of certain features and their advancements as damage.

To prepare concrete cores (or specimens if made in a laboratory) for DRI analysis, the cores/specimens are cut in half along their axis using a masonry saw fitted with a diamond blade (notched when used without coolant, and un-notched when used with coolant such as water). One-half of the core/specimen is ground flat using a coarse grit material (either a powder or an impregnated disk), while the other half can be used for additional tests (i.e., chemical characterization). The flattened surface is polished with a descending series of powders or impregnated disks until a highly reflective surface is achieved. A grid of 1 cm by 1 cm squares is placed or drawn on the completed surface to delineate the fields of view during the analysis and prevent overlapping counts. Using a stereomicroscope at 15-16x magnification (depending on equipment availability), assembled with oblique and/or ring lights, the petrographer/operator counts and tabulates the observable petrographic/distress features in each square of the grid.

Consequently, the counts are categorized based on their petrographic/distress features and location (i.e., within the aggregate or cement paste).

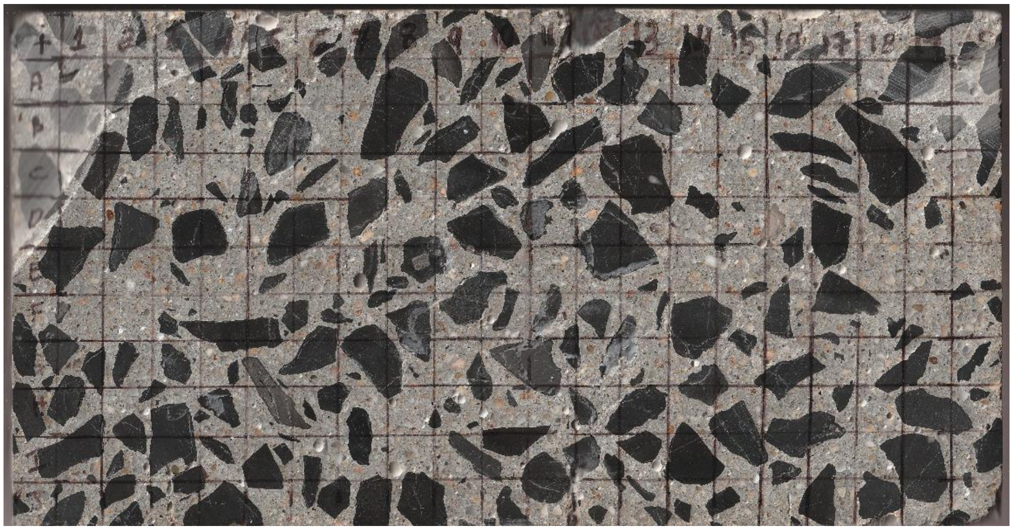

Figure 2.12. Surface preparation for DRI analysis.

Since the DRI was developed in 1992 by Grattan-Bellew [64], modifications have been made to the method to reduce variability [46] and ensure correlation with the observed level of damage represented by an expansion level (Δl/l%) [38,45,48,56,57,64–69]. Moreover, recent studies have shown that the DRI number, when combined with other tools such as the SDT, alongside compressive and tensile strength losses and reductions in modulus of elasticity, can provide a more reliable diagnosis of the extent of damage in laboratory-made specimens and cores extracted from concrete elements, regardless of the type of reactive aggregate used [70,71]. These multi-level evaluations have also been utilized for structures affected by ASR [27,37] and other mechanisms [30,58–60]. Despite ongoing advancements aimed at creating more reliable and practical condition assessments through multi-level evaluations, these methods remain non-standardized to date, and their global adoption, particularly the DRI, has been limited. Generally, mechanical tools are more readily adopted by engineering practitioners, while microscopy is perceived more as a petrographic tool. The following section reviews the concept of the DRI by examining its development and evolving use over the past decades.

2.4. The damage rating index (DRI): a critical review

2.4.2. The original developments

This section offers a thorough and comprehensive review of the Damage Rating Index (DRI), addressing its limited application and constraints regarding its acceptability for evaluating the cause and extent of damage to concrete. This review aims to highlight the underlying reasons for these reservations about using the DRI as a tool for assessing the cause and extent of ISR damage.

The DRI was significantly influenced by a method developed by [72], as noted in [65], wherein three orthogonal thin sections measuring 10 cm by 10 cm in total (i.e., normalized to 100 cm^2) are sawn from concrete to represent the anisotropic and heterogeneous nature of concrete. Features within a 1 cm^2 grid were counted at 50x magnification. Sims et al. (1992) highlighted that for a method to remain objective when analyzing various types of concrete, the procedure must facilitate comparison and establish the relative extent of damage to the concrete. However, the researchers indicated that the absence of a standard approach and reference material complicates correlating the observations with other properties [72]. Furthermore, the method was developed to enhance the sensitivity of microscopy analysis in AAR diagnosis by employing a point-counting technique, as microscopy is visual and its results can be qualitative and subjective. The number of occurrences of the microscopic features associated with ASR observed in concrete was then recorded and normalized to 100 cm^2. Table 2.1 provides a summary of the microscopic features counted using this method, including how these can be differentiated and a description, thus guiding the operator towards a systematic approach using a finite variety of pre-determined features that are considered significant.

Table 2.1. Pre-determined petrographic features, as per Sims et al. 1992 used for objective analysis of ASR-affected concrete.

Microscopic feature	Optional differentiation	Description
ASR Reaction site	* Aggregate particle size * Type of constituent * Porosity of particle	Position associated with an aggregate particle where reaction is occurring, gel is being generated and microcracks are being propagated.
ASR Gel Deposits	* Located in cracks * Located in voids * Altered * Layered	Discrete deposits of gel product remote# from the reaction site; may be altered (eg. carbonated) or have developed a texture.
Cracks & Microcracks	* Cracks or microcracks * Open, closed or filled * Peripheral or radiating * Traversing cement paste, aggregate or both	Microcracks are <10μm wide. Cracks and microcracks might be single or ramifying, peripheral to aggregate or radiating away from a remote# reaction site.
Fractured Aggregate	* Aggregate particle size * Type of constituent * Porosity of particle	Internally fractured aggregate particles: not a reaction site but possibly caused by ASR.
Densified cement paste	* Absence or abundance of portlandite * Isolated patches or bordering cracks	Areas of darkened cement paste which might be gel impregnated and in which $Ca(OH)_2$ might have become depleted.

Situated in a different grid square.

The point-counting technique used for cracks in networks is illustrated in Figure 2.13, where the crack network is divided into segments and nodes. The point counts can be calculated by tallying all 16 segments and subtracting the 8 nodes to arrive at a total of 8 cracks. In practice, this technique is less obvious; therefore, cracks are often counted beginning from one segment tip (starting point) and following the crack until all ends have been addressed (endpoints), which results in the same number of cracks. Sims et al. (1992) further proposed using indices to describe the level of progress achieved thus far or to predict further development and stated that surfaces larger than 200 cm^2 were considered impractical [72].

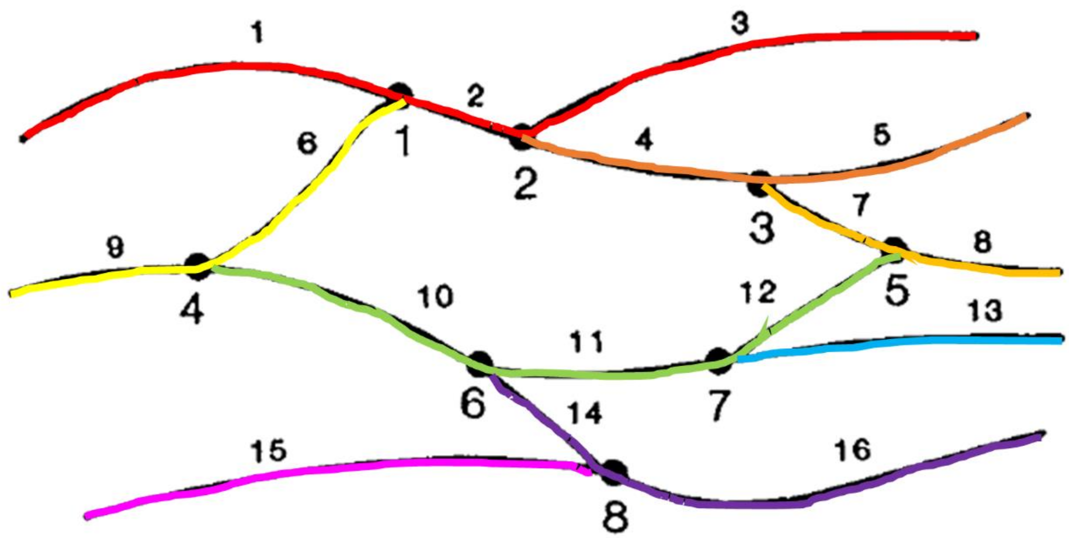

Figure 2.13: Point-count method using nodes and segments in a crack network. Colours highlight counts of segments used in practice during point counts for the DRI. Adapted from [72].

Afterwards, Grattan-Bellew [54] developed the DRI to address the cost of sample preparation for the thin sections used in the method proposed by Sims et al. (1992), the fragility of thin sections leading to cracks that resemble undistinguishable damage, and the lengthy and costly analysis time required when large aggregates are incorporated into concrete (such as in dams), where larger surface areas are necessary for representativeness. The DRI has frequently faced criticism within the ISR community as a method for quantifying damage in concrete, mainly due to its time-consuming procedures and the high variability among its operators. Consequently, the nature of the DRI has been modified since its proposal as a method for evaluating damage, adjusting both the petrographic/distress features counted and the applied weighting factors, which are presented hereafter.

Initially, the DRI was developed to assess ASR generated by the coarse aggregate in concrete dams; therefore, the counted petrographic/distress features were based on observable ASR characteristics [64]. Weighting factors (Table 2) were applied to those counts somewhat arbitrarily. The lowest factor was assigned to closed cracks in the aggregate (i.e., 0.25) as these features may have been caused by natural or manufacturing processes (i.e., rock weathering, extraction, crushing, sieving, etc.). Other features were selected to highlight ASR when additional distress mechanisms were observed. The applied weighting factors increased with damage severity (that is, extension into the cement paste). For example, a crack in the coarse aggregate containing gel (i.e., a reaction product formed within the aggregate because of ASR, with a weighting factor of 2) had a lower weighting factor compared to a crack in the cement paste with gel (i.e., a factor of 4), indicating the progression of ASR damage. Conversely, cement paste cracks without gel were assigned a weighting factor of 2, as they may represent other distress mechanisms unrelated to ASR, such as shrinkage, freezing and thawing, or sulphate attack. This method, therefore, biased the identification towards ASR while still underscoring other distress mechanisms through their counts.

The use of the DRI, however, was still limited due to its high variability, stemming from the nature of the observed petrographic features and the operator's ability to distinguish and identify them as ASR features. This includes the presence of substances like polishing abrasives or other residues in cracks that could be misidentified as gel. Consequently, this limitation restricted its use to experienced petrographers rather than operators. However, Dunbar and Grattan-Bellew (1995) reported a covariance of 16.6% among three operators using the same equipment and analyzing the same concrete surface, which was deemed acceptable, while others achieved a covariance of 22% after a one-hour training session [73], as noted in [46]. Evidently, variability decreases with experience; however, other circumstances influence the outcomes of the DRI and will be discussed further in the following sections.

2.4.3. Modifications and current method

The degree of damage is often defined by the level of expansion achieved through concrete swelling, which measures the change in length or volume relative to its initial length or volume measurement ($\Delta l/l\%$ or $\Delta v/v\%$). Consequently, many authors attempt to correlate the Damage Rating Index (DRI) with the level of expansion obtained in laboratory-made specimens, leading to the use of the DRI to assess the expansion level when it is unknown (i.e., as part of the diagnostic process to determine the extent of the damage). To begin correlating petrographic/distress features to ASR damage, Rivard et al. (2002) examined various features concerning the achieved expansion of concrete prisms produced in a laboratory and cores extracted from reinforced and plain concrete blocks. They proposed removing the reaction rim and the air voids filled with gel from the counted features, as these indicate the presence of ASR rather than damage to the concrete. However, since both features are signs of ASR, they should still be noted during an investigation into the cause of the damage. This distinction consequently begins to differentiate petrographic features from distress features, with the latter being more representative of the concrete deterioration due to ASR, as observed through mechanical testing methods.

Several works have proposed modifying or adding weighting factors and changing grid sizes to better represent damage caused by ASR through the DRI [64,74–76]. In 2011, the DRI procedure was revised [46] by altering the petrographic and distress features to focus on those that best represent ASR damage. Consequently, distress features and their associated weighting factors were adjusted to tackle the variability issues observed from misinterpreting reaction products versus other substances, the consequences of sample preparation (i.e., the removal of reaction products), and to more accurately reflect the significance of the petrographic features regarding the damage. This new set of distress features and factors (Table 2.3, further introduced in the subsequent section) has reduced the overall variability among petrographers and operators to below 20% in an intra-laboratory analysis. The following will, therefore, outline the rationale behind the proposed weighting factors from the petrographic perspective and their impact on the losses in mechanical properties and durability.

The petrographic perspective

The weighting factor of 0.25 remains for closed cracks in the aggregate (CCA) since they are less likely to represent any ASR damage but are still considered, as they can serve as reactive sites acting as fast-track channels and may open later in the reaction stages. For the open cracks in the aggregates, whether or not they contain reaction products (i.e., OCA and OCA_{RP}, respectively), a factor of 2 has been chosen to account for the possibility of reaction product removal and to minimize interpretation issues. It is worth noting that the coarser fraction of sand particles (i.e., down to 1 mm in size) is now also considered, as previously verified by [48]. Thus far, only the coarse aggregates have been included in the DRI analysis, and incorporating finer particles broadens the application of the DRI to encompass ASR-reactive sands. However, this does not restrict the counts to this size; in some instances, cracks can be observed in smaller sand particles, including secondary reaction products and extensions into the cement paste, thus representing an advanced ASR stage. Moreover, aggregates may have been cut such that only a small portion is visible (i.e., the tip of an elongated particle). Cracks observed in the cement paste, whether associated with reaction products or not (i.e., CCP and CCP_{RP}, respectively), are then assigned a weighting factor of 3 to reflect the severity of the damage through its extension into the cement paste when stemming from the aggregate. However, a crack in the cement paste may not be related to ASR yet can still significantly impact the mechanical and durability properties of the concrete; therefore, the highest weighting factor is considered appropriate. For instance, a crack in the cement paste originating from an aggregate will then be counted as two cracks with a total weight of 5 (i.e., 1 OCA x 2 + 1 CCP x 3 = 5). In all cases, cracks, regardless of size, are to be counted because if they are found in abundance, their effect on the result will be significant. Conversely, if their occurrence is less frequent, their impact would be diluted in the result. Villeneuve (2011) further confirmed the removal of voids filled with secondary reaction products and reaction rims in the aggregate, as they greatly influenced variability [46]. Nevertheless, such petrographic features may not necessarily indicate damage within the concrete; for example, ettringite needles in a void do not imply DEF or other forms of sulphate attack and, therefore, are not counted as a distressing feature but rather as a petrographic feature to further enhance the analysis.

In the literature, some works refer to the reaction product as "gel," as indicated by the “G” in “OCAG and CCPG." This terminology is reasonable when evaluating concrete affected by ASR; however, it may further limit the use of the DRI for other mechanisms. Therefore, the notation “RP” will henceforth be used to signify that a crack is filled with a reaction product (i.e., OCA_{RP} and CCP_{RP}). Additionally, it remains unclear in the literature throughout the developments of the DRI why a CCP or debonded/dislodged aggregate (referred to as CAD/Debon where cracks are located in the coarse aggregate-paste interface) would be assigned a weighting factor of 3 when not associated with ASR. One explanation may be that the factors were selected in reference to ASR to depict the evolution of the damage, where a CCP or CAD/Debon resulting from ASR is considered another, more severe stage of damage—namely, that the damage has propagated from the aggregate to the cement paste. For DEF, a crack in the interface represents the beginning of damage that simultaneously diminishes both the modulus of elasticity and compressive strength; therefore, a weighting factor of 3 can be justified but needs to be verified through mechanical losses. Moreover, CCPs are inherently linked to decreased durability, as openings on the surface of concrete may facilitate the ingress of harmful agents and expedite deterioration from within. An initial attempt to correlate the loss in mechanical properties with the DRI was made, finding that a sharper decrease in the modulus of elasticity is observed for DEF-affected concrete [29], which justifies the weighting factor of 3 for debonded aggregates. However, no studies have been conducted to correlate cracks present in the aggregate-paste interface caused by DEF with losses in modulus of elasticity. Based on the DRI guide developed at Université Laval [70], a crack in the aggregate-paste interface is considered as a debonded aggregate when 50% of the interface is met with a crack; yet, it is not clear how to account for this crack regarding counts when extending into the bulk cement paste. Further work is necessary to adopt the DRI for DEF.

In addition, a corroded/disaggregated particle (DAP) previously proposed by [74,75] consists of a factor of 2, as it affects the integrity of the aggregate and is the most indicative of ASR, although occurrences are rare. The optimized weighting factors were then verified using a wide range of reactive aggregates, which showed that DRI increases with expansion for laboratory-made specimens [32,60], highlighting the diagnostic potential of the DRI. Table 2.3 describes the pre-defined list of petrographic/distress features, along with the associated weighting factors from the original version and its most recent iteration development. It should be noted that the features with the suffix -RP were previously introduced as “with gel”; however, this limits the DRI’s usage to

ASR, and Debon henceforth indicates the debonded aggregate to clarify that examinations extend beyond the coarse aggregate.

Table 2.2. Petrographic/distress features as per the DRI and their weighting factors.

Petrographic/distress feature	**Original weighting factor [64]**	**Optimized weighting factor [46]**	**Type of feature**
Crack in the aggregate	0.25	-	Distress
Closed crack in the aggregate (CCA)	-	0.25	Distress
Opened crack in the aggregate (OCA)	-	2	Distress
Opened crack in the aggregate with reaction product (OCA_{RP})*	2	2	Distress+ petrographic
Corroded/debonded aggregate	-	2	Distress
Reaction rim in aggregate	0.5	-	Petrographic
Crack in the cement paste (CCP)	2	3	Distress
Crack in the cement paste with reaction (CCP_{RP})	4	3	Distress+ petrographic
Air voir lined/filled with gel	0.5	-	Petrographic
De-bonded aggregates (Debon)	3	3	Distress

Mechanical property and durability loss

The relationship between distress features and losses in mechanical properties is seldom explored in the literature. Figures 2.14a and 2.14b further illustrate the correlation between the DRI and the modulus of elasticity and SDI, indicating that the weighting factors chosen for calculating the DRI correspond to the damage in concrete [45]. Although the correlation between the DRI and expansion is more frequently presented in the literature, expansion may not directly correlate to damage, even though damage increases with expansion. Additionally, varying slopes are observed in Figure 2.14, particularly in Figure 2.14b, suggesting that one single linear regression may not accurately represent the relationship between DRI and other variables that measure damage. Furthermore, a reduced stiffness is generally associated with damage to the aggregate (and/or the aggregate/paste interface, which acts as a bridge transferring stresses to the aggregate). Therefore, a weighting factor of 2 for cracks in the aggregate is appropriate for open cracks. In contrast, for cracks in the cement paste, a weighting factor of 3 is supported by tensile strength reduction testing, where concrete affected by freezing and thawing (labelled FT) demonstrates the greatest loss. Moreover, cracks located only in the aggregate-paste interface simultaneously affect both the aggregate and cement paste by impairing the transfer of stresses from the cement paste to the aggregate, thereby reducing the modulus of elasticity and compressive and tensile strengths. Hence, a weighting factor of 3 for such cracks is justified. Concerns regarding the DRI's capability to characterize damage were raised due to the absence of a count for cracks extending from the aggregate to the cement paste [77]. However, as aforementioned, such cracks would consist of 2 with a total weighted count of 5 (i.e., 1 OCA x 2 + 1 CCP x 3 = 5).

a)

b)

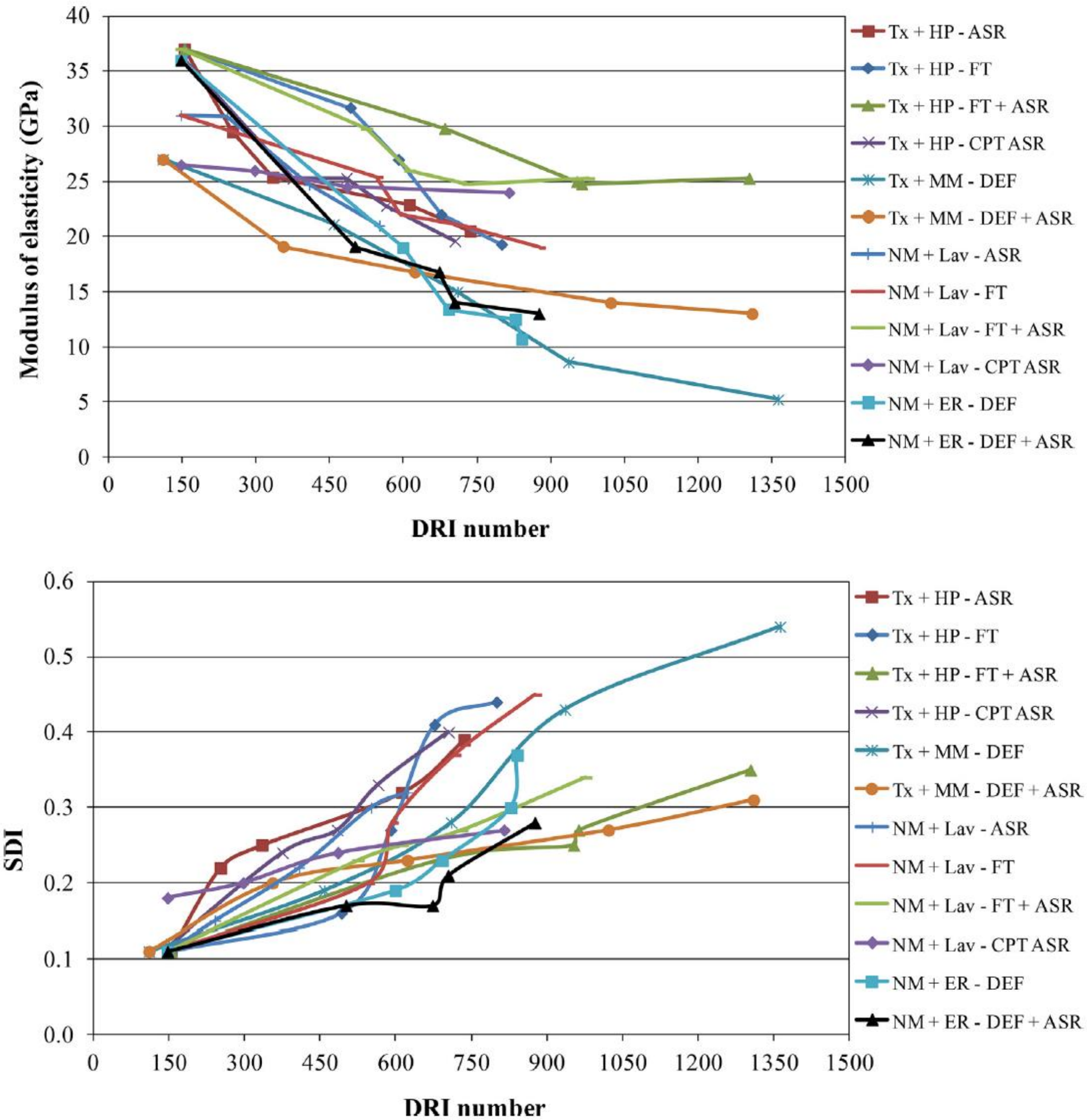

Figure 2.14. Mechanical response as a function of DRI for a) modulus of elasticity and b) SDI, an SDT output parameter [45].

2.4.4. Factors influencing DRI outcomes

- *<u>Sample preparation</u>*

From previous studies, the sample preparation procedure can vary from using water (i.e., uncontrolled or controlled water flow) with polishing powders or disks of various sizes/grit sequences attached to a hand-held polisher or a rotating table. The time needed to achieve the desired surface quality varies based on the aforementioned factors and the concrete itself (i.e., type of aggregate, strength of cement paste, degree of damage, etc.), with "harder" concrete taking more time to polish compared to "softer" concrete. Additionally, some polishing disks require a specific amount of water to reduce friction heat, allowing for efficient use of the disks while extending their lifespan. The criticism of excessive water usage in concrete sample preparation, especially for ISR which involves a reaction product, stems from the fact that water can wash out the desired petrographic features (i.e., reaction products) either fully or partially. Grattan-Bellew and Mitchell (2006) (information extracted from [46]) compared DRI values for ASR-affected concrete specimens (using the original weighting factors) across various polishing techniques and found that dry polishing with disks resulted in the lowest DRI values, followed by wet polishing using polishing powders on a rotating table, while wet polishing with disks produced the highest DRI values (i.e., 115-150, 263, and 361, respectively) [73], indicating the influence of sample preparation on the variability of DRI results. While the use of water could lead to ASR gel washout from observable cracks, fewer cracks with gel should logically result in a lower DRI number (i.e., the weighting factors used for this analysis when "gel" is encountered in cracks are 2 and 4 as opposed to 0.25 and 2 for the aggregate and cement paste, respectively). However, using water may create a more reflective surface, allowing more features to be observed. On the other hand, polishing powder is often trapped in voids or open cracks, decreasing their apparent counts due to the uncertainty in distinguishing trapped powder residue from "gel" within cracks and voids. Furthermore, stereomicroscopes can have a magnification of 15x or 16x based on the model, which is not likely to increase variability; however, the type of light (i.e., colour, ring vs oblique goose-necks), light intensity, position, and the incident angle of the incoming light wave/ray (i.e., highlighting cracks while minimizing shadow artifacts) used to create the visible image from the reflective surface can impact variability. It is crucial to note that different laboratories worldwide may use locally available equipment to gather data for calculating DRI, which may enhance that variability. Nonetheless, establishing a calibration procedure or metric is necessary to promote the use of DRI in condition assessment rather than standardizing the microscope and its setup, which could reduce accessibility to the DRI tool.

- *Combined types of damage*

In addition, concrete in service can be subjected to a multitude of conditions from environmental factors and micro-climates, loading, reinforcement, and confinement, among others, as well as various distress mechanisms. Some distress mechanisms may be active or may have occurred in the early stages of the concrete's life (i.e., shrinkage, loading cracks, etc.) which might compromise the concrete's durability and further accelerate active ISR mechanisms through the ingress of harmful agents (i.e., water, chlorides, carbonation, etc.). In such cases, the cracks that were not caused by an active ISR mechanism can be counted but do not signify the damage caused by ISR. However, the distinction between these cracks is not clear. A researcher [78] noted that mechanical cracks could not be distinguished from those produced due to ASR through the DRI. Sims et al. (1992) also mentioned that identifying ASR features is relatively straightforward, yet the resultant damage becomes more challenging when other mechanisms are involved [72]. Furthermore, the DRI for sound concrete is not negligible due to aggregate features in the form of closed cracks resulting from rock weathering/processing, as well as minor cracks in the cement paste. Nevertheless, the cracks in the aggregate may act as reactive sites to further develop ASR if the aggregate is reactive. Thus, they contribute to the DRI with a small attributable weighting factor to account for their less significant impact on the overall results and mechanical property loss [46,48]. Furthermore, [79] indicated that for 45 MPa concrete, more cracks were observed compared to 25 and 35 MPa concrete at low damage levels, highlighting the DRI's ability to capture such differences. Yet, understanding how to further incorporate compressive strength and other variables in crack counts remains a crucial aspect of the overall condition assessment challenge.

- *Damage distribution*

Damage homogeneity or heterogeneity can be observed during the analysis of the surface, which could significantly influence the outcomes of the DRI. The DRI number, as a simple indicator, does not capture the cause of the damage or its spread. However, when the cause is known and the damage is visualized as homogeneous throughout the analyzed surface, the DRI provides insight into the extent of the damage. In field concrete, this may not be true, as the cause and extent of the damage are often unknown, and the spread of damage varies with respect to the depth from which the core was extracted. For example, more "gel" was observed at greater depths during petrographic examinations [80]. In harsh climates such as Canada, evidence of freezing and thawing can further contribute to the heterogeneity of the damage [27]. Moreover, within the same structure, differences can be observed; in some cases, one mechanism may be triggered, while in another location within the same structure, a different mechanism may be more apparent [23]. Meanwhile, for the same type of damage, various degrees can be observed. This was evident for a core extracted from the entire thickness of a dam, which produced a damage profile relative to depth [81]. It was further noted that damage heterogeneity within the material could induce variability in testing results [79]. Nonetheless, it is expected that to obtain a reliable quantitative and objective assessment of damage to concrete, the damage should be homogeneous in each core or specimen in order to be considered a representative specimen.

- *The human factor*

Furthermore, some discrepancies were observed when evaluating the damage (represented by expansion) using the DRI with the original weighting factors that considered signs of ASR. Thus, as the DRI number and degree of damage increased, the concrete was mechanically assessed to be at a lower level of damage, highlighting the necessity to adjust the weighting factors [76]. Following the intra-laboratory study conducted by [46], the variability among the group of operators was found to be below 20% after adhering to a detailed training and procedure. However, this study was carried out within a single laboratory, using the same sample preparation techniques and equipment. An inter-laboratory study for the DRI tool has yet to be conducted, which impedes its standardization. Nonetheless, it remains a significant challenge to consider and address every parameter that may influence the outcomes of the DRI, thus underscoring the need for an approach to develop a calibration procedure to adapt the tool for various scenarios, ensure transparency, and account for the variabilities that will arise.

2.4.5. Adapting the DRI tool for engineering purposes

- *Using the DRI to capture distress mechanisms other than ASR*

In the literature, the DRI has primarily been employed for evaluating ASR, either by indicating its presence or semi-quantifying the damage caused. Consequently, the terminology used to describe the DRI has been biased towards ASR. For instance, it often specifies whether there is “gel” in a crack rather than a reaction product and further states that the method was developed to assess ASR in concrete [57] rather than being developed by ASR but not limited to it. More recently, DEF damage has been assessed using the DRI [44–46,59,60] with the current weighting factors, whereas it was previously utilized to distinguish DEF with the original weighting factors [42,82].

Others have applied the current weighting factors to evaluate distress mechanisms, such as freezing and thawing, and external sulphate attack, which were also assessed through the DRI [30,44,83]. Figure 15 illustrates the distinction between various types of distress mechanisms through the bar charts created while gathering counts for the DRI calculation. It is evident that the damage caused by ASR, when compared to DEF for similar DRI values (i.e., ~ 500 and 600, respectively), shows larger orange bars for the concrete affected by DEF. According to [45], for ASR+DEF, there appear to be more open cracks in the aggregate and fewer in the cement paste; therefore, the pattern has changed, but the overall number of such cracks remains the same, as illustrated in Figure 15. One may observe arrows indicating similar expansion levels; however, the observed features differ significantly, with larger orange bars shown for DEF-affected concrete compared to ASR and likewise for freeze-thaw-affected concrete. Nevertheless, defining the ranges of values per distress feature representing a significant difference between types and levels of damage remains essential for objective results interpretation.

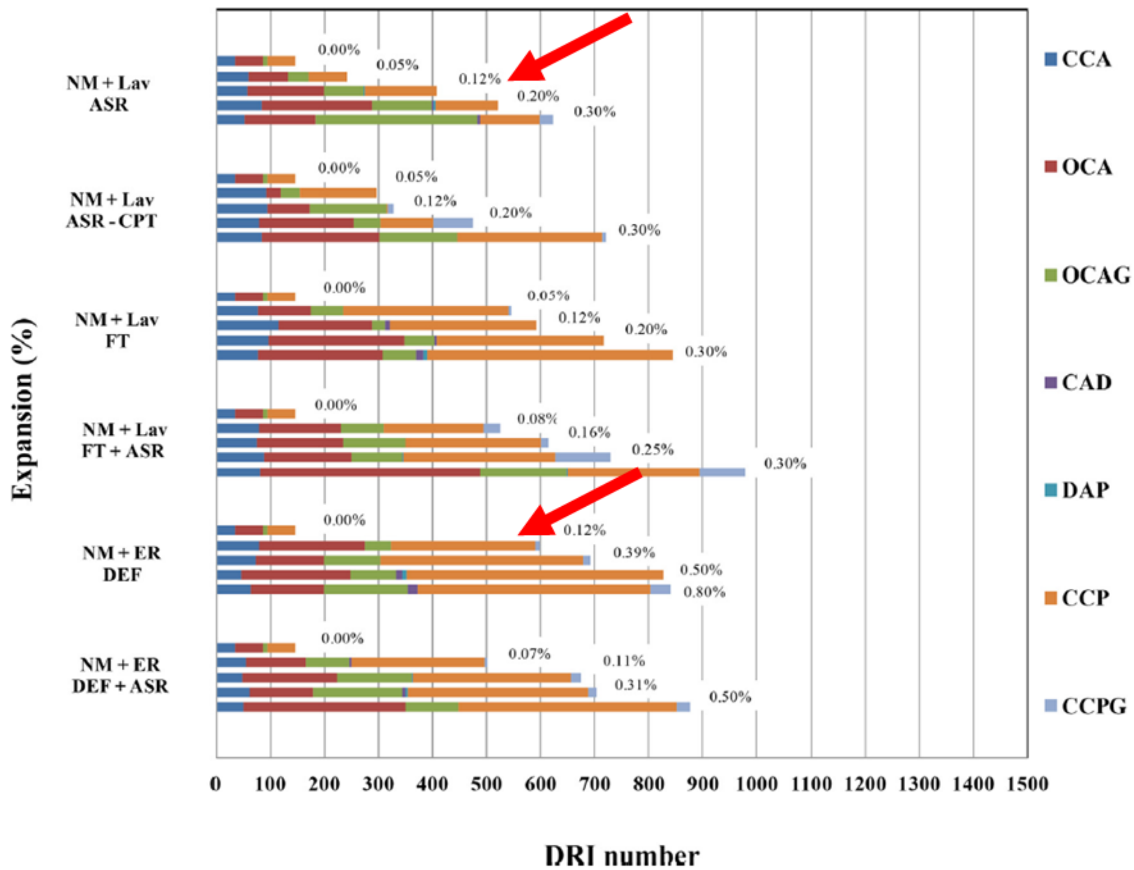

Figure 2.15. Comparison of various distress mechanisms as captured through DRI bar charts [45].

- *Considering the uncertainty*

The DRI is often regarded as a petrographic tool, which may not be the most suitable approach for correlating mechanical property losses and responses due to damage concerning the location and extent of the cracks. It is expected that an individual conducting the analysis and feature counts for DRI calculations possesses adequate knowledge and experience, thereby establishing the person as competent for the analysis. In ASTM C856/C856M – 20 "*Standard Practice for Petrographic Examination of Hardened Concrete*" [84], the qualifications of the operator (as a petrographer or technician under a petrographer's supervision) are outlined (Figure 2.16). Conversely, the DRI is a point-count method where cracks are counted, making it more similar to ASTM C457/C457M – 16 "*Standard Test Method for Microscopical Determination of Parameters* *of the Air-Void System in Hardened Concrete*" [79], which does not specify the qualifications of the operator.

4. Qualifications of Petrographers and Use of Technicians

4.1 All petrographic examinations of hardened concrete described in this practice shall be performed by or under the technical direction of a full time supervising petrographer with at least five years experience in petrographic examinations of concrete and concrete-making materials. The supervising concrete petrographer shall have college level courses that include petrography, mineralogy, and optical mineralogy, or five years of documented equivalent experience, and experience in their application to evaluations of concrete-making materials and concrete products in which they are used and in cementitious-based materials. A resume of the professional background and qualifications of all concrete petrographers shall be available.

4.2 A concrete petrographer shall be knowledgeable about the following: concrete-making materials; processes of batching, mixing, handling, placing, and finishing of concrete; the composition and microstructure of cementitious paste; the interaction of constituents of concrete; and the effects of exposure of such concrete to a wide variety of conditions of service.

4.3 Sample preparation shall be performed by concrete petrographers or trained technicians pursuant to instructions from and under the guidance of a qualified concrete petrographer. Aspects of the petrographic examination, such as the measurement of sample dimensions, photography of as-received samples, staining of sample surfaces, that do not require the education and skills outlined in 4.1, shall be performed by concrete petrographers or by trained technicians pursuant to instructions and under the guidance of a qualified concrete petrographer. The analysis and interpretation of the features that are relevant to the investigation and evaluation of the performance of the materials represented by the sample shall be made solely by concrete petrographers with qualifications consistent with those outlined in 4.1.

Figure 2.16. Excerpt taken from ASTMCC856/C856M – 20 describing the skill set and knowledge required to perform a petrographic evaluation of hardened concrete samples.

Indeed, a certain level of expertise and knowledge about concrete and geology is preferred to assist the operator in distinguishing cracks from rock features (i.e., grain boundaries, veins, weathering, etc.). Moreover, since these features may resemble closed cracks in the aggregate (CCA), the decision to conserve (or reduce their weighting factor from [64,74–76] to 0.25) was made to lessen their impact on the final calculation, as they are considered as not necessarily representative of damage. This reduction can also be seen as mitigating the effect of misclassification of these difficult-to-distinguish features.

In the literature, access to the procedure adopted for conducting the DRI is limited; therefore, a thorough protocol is necessary to promote the use of the DRI and reduce variability. Additionally, recent works have continued to employ the original weighting factors to calculate the DRI. This flexibility depends on the desired output from the DRI, where petrographic features and associated weighting factors can be considered if the operator or petrographer desires a more petrographic analysis. In contrast, an operator analyzing for engineering purposes focuses solely on the distress features (i.e., cracks) that indicate damage. Nonetheless, the operator may select the type of analysis conducted: i) petrographic features or ii) calculating the frequency of occurrences of features that best describe the observed damage using Equation 2.5 and the weighting factors that describe the damage as per the applicable guidelines. It should be noted that, up until now, the DRI calculation has always been descriptive rather than a mathematical equation.

$$DRI = \frac{\sum 0.25 \times CCA + 2 \times (OCA + OCA_{RP} + DAP) + 3 \times (CCP + CCP_{RP} + CAD)}{Number\ of\ analyzed\ 1\ cm^2\ squares} \times 100cm^2 \qquad \text{Eq. 2.5}$$

Where CCA is the total number of closed cracks in the aggregate;

$OCA\ and\ OCA_{RP}$ are the total numbers of open cracks in the aggregate without and with reaction product, respectively;

DAP is the total number of disaggregated/corroded particles;

$CCP\ and\ CCP_{RP}$ are the total numbers of cracks in the cement paste without and with reaction product, respectively, and

CAD is the total number of debonded aggregates.

Moreover, the approaches addressing the uncertainty of the DRI are seldom discussed [85], despite the fact that equipment and tools invariably exhibit a degree of uncertainty concerning the value produced. It is often asserted that a new "operator" should generate a DRI number within ±10%

of that of an experienced petrographer. Indeed, meeting this criterion may be challenging when a clear protocol and description are not readily available. This ±10% value can thus be interpreted as reflecting the uncertainty of an operator's result. However, this figure may not necessarily represent distinct levels of damage captured through the DRI or any other factors that can influence variability. For instance, if an operator analyzes two ASR-affected cores with a statistically significant area of analysis, such as 200 cm^2 (i.e., often mentioned without reference to a statistical verification, as discussed in the following), and the results differ by 15%, one might question whether "the level of damage can be considered different?" To delve into the answer to this inquiry, a review of results obtained from [44] was carried out to underscore the variability that can arise from various types of damage mechanisms.

Figure 2.17 illustrates the findings from the study, including the average value obtained for each damage level. The plots represent the ranges of DRI values at different deterioration levels for various mechanisms, as presented in Table 2.3. The shaded areas indicate ranges where the DRI values are similar while corresponding expansion values differ. Uncertainty bars are added to the minimum and maximum values from the operator (i.e., ±10%). It is noted that for ASR-affected concrete specimens with negligible damage or sound concrete, a ±20% range of values exists for all reactive aggregate types studied. At a low damage level, the DRI values range ±30%, while for all other damage levels, the range is ±20%, for DEF and ASR+DEF, a ±19% difference is observed at low damage levels, ±26% for moderate levels corresponding to 0.11% expansion, and ±10% at very high damage, reaching ±24% when exceeding 1% expansion. At low damage levels, cracks are thin and difficult to detect, thereby causing an operator to potentially produce greater variability in such cases (when an operator knows there is damage, bias may affect the result). When ASR is present, the highest variability is expected due to the variability of the reactive aggregate and the involvement of the cement paste. For mechanisms involving only the cement paste, cracks are more easily distinguished, provided they are sufficiently large to be observed at the magnification used for the DRI 15-16x).

a) ASR

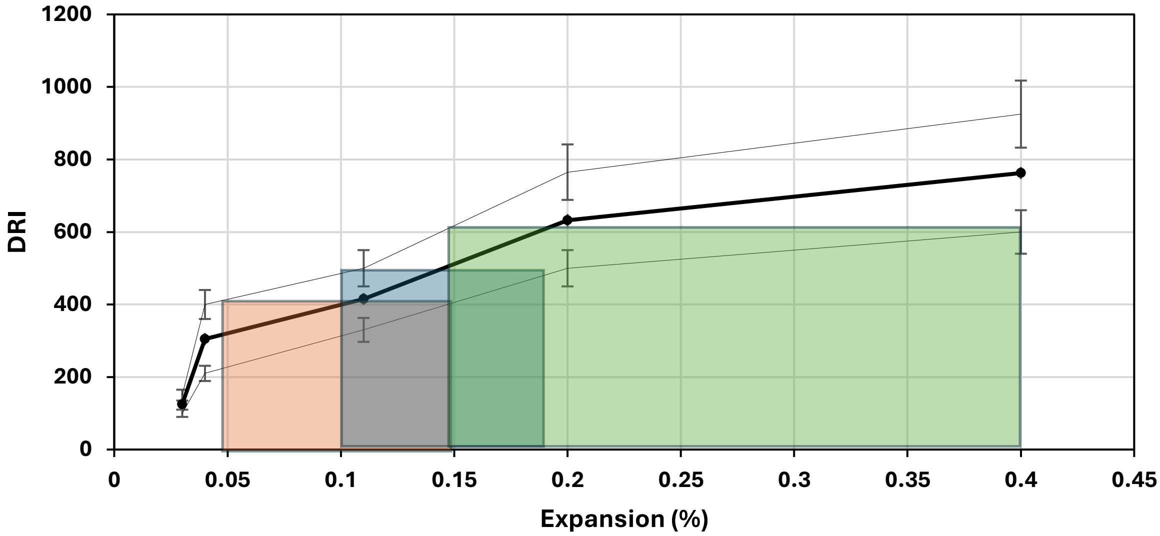

b) DEF and ASR+DEF

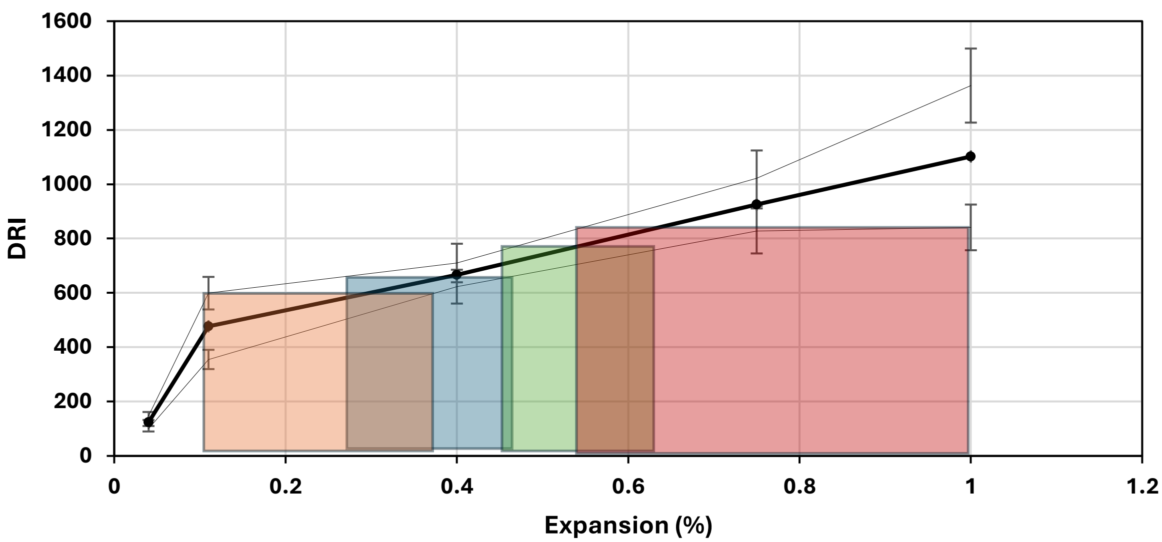

c) FT and ASR+FT

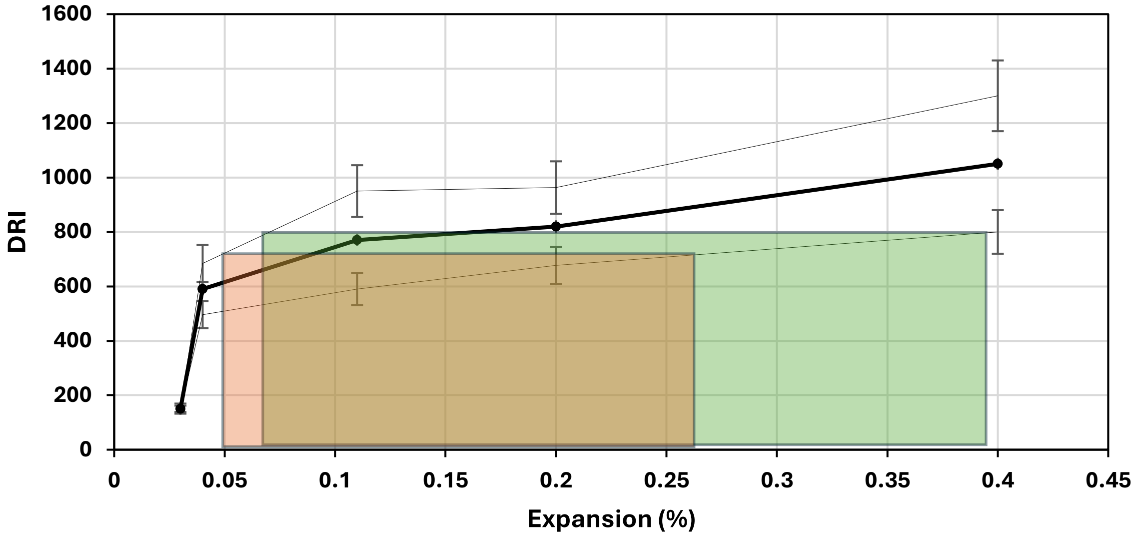

Figure 2.17. Visual interpretation of the damage classification as per the DRI with shaded areas representing ranges with similar DRI values for the corresponding different expansion levels[44].

Table 2.3. Summary of results obtained through multi-level assessment as per [44].

Distress mechanism	Classification of ASR damage degree (%)	Reference expansion level (%) a	Damage results				
			Stiffness loss (%)	Compressive strength loss (%)	Tensile strength loss (%)	SDI	DRI
ASR	Negligible	0.00–0.03	–	–	–	0.06–0.16	100–155
	Marginal	0.04 ± 0.01	5–37	(−)10–15	15–60	0.11–0.25	210–400
	Moderate	0.11 ± 0.01	20–50	0–20	40–65	0.15–0.31	330–500
	High	0.20 ± 0.01	35–60	13–25	45–80	0.19–0.32	500–765
	Very high	0.30 to 0.50 ± 0.01	40–67	20–35		0.22–0.36	600–925
	Ultra high	0.50 to 1.00 ± 0.01	–	–	–	–	–
		≥1.00 ± 0.01	–	–	–	–	–
FT and FT + ASR	Negligible	0.00–0.03	–	–	–	0.11	147–154
	Marginal	0.04 ± 0.01	0.23–0.35	0.12–0.32	0.44–0.67	0.16–0.23	496–684
	Moderate	0.11 ± 0.01	0.28–0.36	0.21–0.32	0.62–0.67	0.25–0.28	590–950
	High	0.20 ± 0.01	0.33–0.46	0.22–0.37	0.65–0.67	0.27–0.41	677–963
	Very high	0.30 to 0.50 ± 0.01	0.37–0.52	0.24–0.40	0.65–0.73	0.34–0.45	800–1300
	Ultra high	0.50 to 1.00 ± 0.01	–	–	–	–	–
		≥1.00 ± 0.01	–	–	–	–	–
DEF and DEF + ASR	Negligible	0.00–0.03	–	–	–	0.11	110–147
	Marginal	0.04 ± 0.01	–	–	–	–	–
	Moderate	0.11 ± 0.01	0.35–0.56	0.09–0.34	–	0.17–0.20	355–599
	High	0.20 ± 0.01	–	–	–	–	–
	Very high	0.30 to 0.50 ± 0.01	0.55–0.62	0.29–0.43	–	0.19–0.28	623–710
	Ultra high	0.50 to 1.00 ± 0.01	0.56–0.77	0.40–0.47	–	0.27–0.43	828–1022
		≥1.00 ± 0.01	0.60–0.86	0.40–0.50	–	0.30–0.54	841–1363

[a] These levels of expansion should not be considered as strict limits between the various classes of damage degree but rather indicators/reference levels of the three different mechanisms studied in this work.

This comprehensive evaluation of various distress mechanisms enabled the development of a table to begin applying engineering judgment to the observed and measured damage. However, the plots (Figure 2.17) reveal the subjectivity in the DRI results; for example, a DRI of 600 for ASR-affected concrete can represent expansions ranging from 0.15% to 0.40%, as illustrated by the large green area highlighted in Figure 2.17a. This underscores the necessity of combining tools through multi-level assessment to determine the cause and extent of the damage.

2.4.6. What defines a representative sample size?

There is a consensus that a surface area of at least 200 cm^2 should be analyzed when using the DRI to represent damage equivalent to a 10 cm by 20 cm specimen or core. Others have found that 110 cm^2 or less is insufficient as a sample size [76]. Meanwhile, 100 cm^2 has been deemed suitable for laboratory-made specimens [48], and even 50 cm^2 has been shown to provide a sensitive analysis when evaluating spatial damage in laboratory-made specimens subjected to leaching [85]. Therefore, the sample size in terms of 1 cm by 1 cm squares for any given location within the concrete (such as near the surface, depending on the type of element and exposure conditions, as well as the depth of the core) can be considered sufficient at 200 squares (i.e., summing multiple cores from one location when the width/depth of a single core cannot produce 200 cm^2). However, this sample size has not been verified. Sims et al. (1992) indicated that for their proposed analysis, a surface area exceeding 200 cm^2 becomes impractical, but it should be noted that their method is conducted at higher magnifications than that of the DRI (i.e., 50x vs 15-16x, respectively), thus requiring a longer analysis time [72]. Nevertheless, in ASTM C C457/C457M – 16 "*Standard Test Method for Microscopical Determination of Parameters of the Air-Void System in Hardened Concrete*" [86], the minimum area is defined per aggregate size (nominal if known, otherwise observed) and based on the desired output (Table 2.4).

Table 2.4: Minimum area of finished surface for microscopical measurement when determining the air-void content of hardened concrete (From ASTM C457/C457M – 16)

Nominal or Observed Maximum Size of Aggregate in the Concrete, mm [in.]	Total Area to be Traversed[C] for Determination of p,[D] A, α, or $\bar{L}$, min, cm^2 [in.^{2}] Based on Direct Measurement of:	
	Total Air-Void Content	Paste-Air Ratio, p/A
150 [6]	1613 [250]	645 [100]
75 [3]	419 [65]	194 [30]
37.5 [1½]	155 [24]	97 [15]
25.0 [1]	77 [12]	77 [12]
19.0 [¾]	71 [11]	71 [11]
12.5 [½]	65 [10]	65 [10]
9.5 [⅜]	58 [9]	58 [9]
4.75 (No. 4)	45 [7]	45 [7]

[A]The indicated values refer to reasonably homogeneous, well-compacted concrete. The microscopical measurement shall be made on proportionately larger area of sections if the concrete is markedly heterogeneous in distribution of aggregate or large air voids. If more than one finished surface is taken from a single portion of the concrete, the finished surfaces shall be separated by a distance greater than one half of the nominal or observed maximum size of aggregate.

The term "sample size” in the context of the DRI typically refers to the number of specimens or cores under evaluation; thus, the adoption of standard deviation and coefficient of variation is nonexistent [79]. Some suggest that the 10 by 20 cm sample size may be too small because it is considered a single specimen [56]. An attempt to incorporate a margin of error or confidence interval (C.I.) into the DRI of a specific sample size, in terms of the number of analyzed squares, was proposed by [85], where a single operator standard deviation was derived, as illustrated in Equation 2.6. This work aids in controlling operator variability. However, the results were based on laboratory-made specimens affected by ASR. Consequently, the differentiation of damage levels in relation to the type of damage was not addressed, indicating that the same specimen size may display varying distress mechanisms, where similar DRI values may not accurately reflect the same degradation in mechanical properties. Nonetheless, this approach describes the sample size in terms of squares (i.e., area in cm^2), rather than the number of full cores or specimens.

$$C.I. = \frac{\left(Z\sqrt{\frac{(0.4944 \times DRI + 105.53)^2}{N}}\right)}{DRI} \times 100\% \qquad \text{Eq. 2.6}$$

Where Z is the selected z-score, DRI is the obtained DRI, and N is the sample size in squares of 1 cm^2.

2.4.7. Visual character and adaptability to automation

Depending on the level of magnification used for the DRI procedure, the analysis takes place at the mesoscale, where petrographic and distress features are considered the most representative of measurable mechanical damage. Furthermore, the qualitative aspect of the DRI allows the operator to visualize the damage along with various characteristics of the cracks and the concrete itself, thus providing a comprehensive understanding of both the cause and extent of the damage. These visuals, as illustrated in Figure 2.18, can also be presented as damage or heat maps and patterns [30,71,83,85,87], from which a damage profile can be derived to aid in correlating damage at various locations on the analysis surface [67].

a)

	1	2	3	4	5	6	7	8	9	10	11	12	13	14	15	16	17
A	1	0	0	0	0	2	1	1	1	0	1	0	1	1	2	0	0
B	0	1	1	0	1	2	4	2	1	2	2	2	0	0	1	1	0
C	1	0	0	0	0	1	3	2	1	2	3	4	1	1	1	1	0
D	0	0	1	1	2	2	1	0	2	1	3	0	3	3	3	1	1
E	2	1	2	0	1	2	2	2	0	1	4	0	2	2	5	4	0
F	1	1	5	1	1	0	1	2	3	2	4	3	2	1	0	4	0
G	3	2	0	4	3	1	0	2	0	2	0	0	1	2	3	4	1
H	0	1	0	1	2	0	1	2	0	2	0	1	0	1	1	0	0

b)

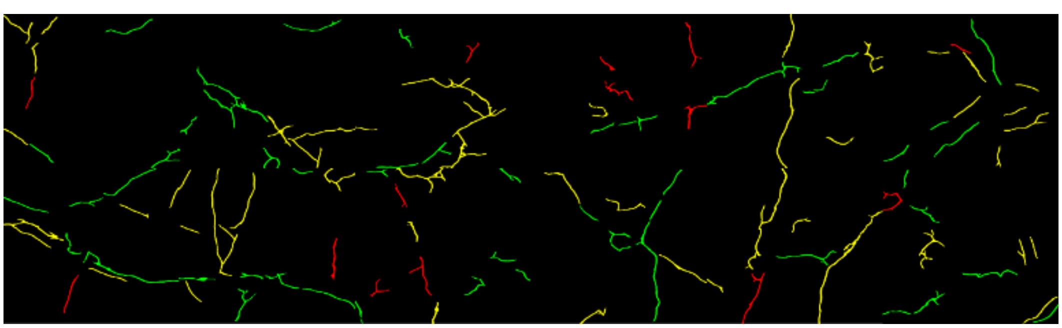

Figure 2.18. Damage mapping in the form of a) a heat map and b) traced cracks through artificial intelligence [87,88] to visually describe damage spread.

Moreover, the DRI is a flexible and versatile tool that goes beyond just counting. petrographic/distress features; it can also provide insight into the origin and extent of damage where crack extensions can be recorded [66,89,90]. Consequently, an abundance of a specific petrographic or distress feature may indicate an underlying cause not captured through mechanical testing. While image analysis is often associated with digital images, the DRI is fundamentally an image analysis method designed to address feature segmentation problems. With advancements in technology, high-resolution cameras, and the increasing application of machine learning algorithms for object segmentation in images, the outcomes of the methods used to derive the DRI number have been infrequently explored but demonstrate potential for automation. Digital images have facilitated computer vision and machine learning (ML) in detecting cracks in concrete, previously time-consuming tasks, especially when considering sample preparation time. As a result, automated surface cracking detection has significantly increased over the last decade [91–104]. Meanwhile, the applications of microscopy in concrete are limited and primarily focused on developing models rather than quantifying damage [105–109]. The feasibility of automating the DRI has been explored previously [88], yet the techniques employed to evaluate the machine's performance were limited to categorizing the various crack types. While DRI is well-suited for automation as an object segmentation task, research on automating the quantification of damage to concrete remains limited [87,88,110]. Moreover, artificial intelligence (AI) is rapidly becoming integrated into microscopy software as it generates vast datasets and provides analysis. Unlike manual pre-processing of images or using subroutines embedded within image analysis software, which still requires some intervention to specify and verify the output image—specifically to remove artifacts unrelated to cracks, such as voids and aggregates with a colour tone similar to that of the cement paste— [110,111]), object segmentation addresses such time-consuming tasks.

Object segmentation in an image involves identifying objects of interest, which are various types of cracks in the case of the DRI. Quantitative assessments of object segmentation in microscopy for concrete deterioration are limited. However, researchers are currently using SEM images [108,112–116] and tomography [114,117] to develop models for material characterization of cementitious and other alternative materials. The need for such tools and limited datasets has encouraged researchers to come together and create one large training pool for SEM-EDS [118]. This data-sharing concept extends to the macro-cracking of concrete surfaces and pavements [119–122]. Integrating AI into the DRI methodology will undoubtedly improve speed and variability (improving reproducibility and accuracy). Adopting and tailoring an already trained object segmentation model for a specific purpose is easing the burden of large image datasets [123]. This approach benefits applications such as the DRI as it can be trained on various ISR and beyond without the need to start over, only build upon itself. Nevertheless, the remaining impeding factor is the quantification of observed objects (cracks) in relation to an objective evaluation of ISR-induced deterioration in concrete.

2.5. Research gaps

The widespread occurrence of internal swelling reactions (ISR) in developed countries such as Canada raises concerns about the potential emergence of similar issues in developing nations. While some information is available regarding ISR and other durability-related problems, there is a notable lack of urgency and accountability regarding their long-term implications. Developing standardized protocols is crucial for promoting the knowledge of the damage rating index (DRI) as a cost-effective tool for assessing ISR. This work addresses key limitations that hinder the implementation of the DRI methodology in engineering practice. The primary challenges in evaluating damage using the DRI include the inaccessibility of the protocol, subjective interpretations of results for various ISRs, biases favouring alkali-silica reaction (ASR), the absence of an established training program to reduce operator variability, and the need to refine the understanding of the concepts behind the data collected for the DRI to apply statistical analysis for more objective result interpretation.

The DRI serves as a robust petrographic microscopy tool with the potential to be integrated into engineering practice and adaptable to different types of ISR and beyond. It can be utilized to develop a skill set and deepen the understanding of concrete deterioration.

2.6. References

[1] E. Elhacham, L. Ben-Uri, J. Grozovski, Y.M. Bar-On, R. Milo, Global human-made mass exceeds all living biomass, Nature 588 (2020) 442–444. https://doi.org/10.1038/s41586-020-3010-5.

[2] Innovation, Science and Economic Development Canada, Government of Canada and Cement Association of Canada launch Roadmap to Net-Zero Carbon Concrete by 2050, Government of Canada (2022). https://www.canada.ca/en/innovation-science-economic-development/news/2022/11/government-of-canada-and-cement-association-of-canada-launch-roadmap-to-net-zero-carbon-concrete-by-2050.html (accessed August 1, 2023).

[3] I Am the Magpie River, The Nature of Things (2024).

[4] Transport Canada, Government of Canada invests in Champlain Bridge, Government of Canada (2009). https://www.canada.ca/en/news/archive/2009/05/government-canada-invests-champlain-bridge.html (accessed August 1, 2023).

[5] The Jacques Cartier and Champlain Bridges Incorporated, Deconstruction of the original Champlain Bridge, Ponts Jacques Cartier - Champlain Bridges (2023).

https://jacquescartierchamplain.ca/en/major-projects/deconstruction-of-the-original-champlain-bridge/deconstruction-site/history/ (accessed August 1, 2023).

[6] New Brunswick Power, Mactaquac Life Achievement Project, (2021). http://www.nbpower.com/en/about-us/projects/mactaquac-project (accessed August 1, 2023).

[7] S.A. Miller, The role of cement service-life on the efficient use of resources, Environ. Res. Lett. 15 (2020) 024004. https://doi.org/10.1088/1748-9326/ab639d.

[8] A.T.M. Marsh, A.P.M. Velenturf, S.A. Bernal, Circular Economy strategies for concrete: implementation and integration, Journal of Cleaner Production 362 (2022) 132486. https://doi.org/10.1016/j.jclepro.2022.132486.

[9] Z. Peng, C. Shi, Z. Shi, B. Lu, S. Wan, Z. Zhang, J. Chang, T. Zhang, Alkali-aggregate reaction in recycled aggregate concrete, Journal of Cleaner Production 255 (2020) 120238. https://doi.org/10.1016/j.jclepro.2020.120238.

[10] C. Trottier, Evaluation of ASR-induced damage generation and prolongation in affected recycle concrete, Master’s Thesis., University of Ottawa, 2020.

[11] CSA A23.1:19, Aggregate made from recycled concrete for use in hydraulic cement concrete (Annex O - Informative), (2019).

[12] I. Sims, A. Poole, eds., Alkali-aggregate reaction in concrete: a world review, CRC Press, Taylor & Francis Group, a Balkema book, Boca Raton London New York Leiden, 2017.

[13] M. Beyene, A. Snyder, R.J. Lee, M. Blaszkiewicz, Alkali Silica Reaction (ASR) as a root cause of distress in a concrete made from Alkali Carbonate Reaction (ACR) potentially susceptible

aggregates, Cement and Concrete Research 51 (2013) 85–95. https://doi.org/10.1016/j.cemconres.2013.04.014.

[14] T. Katayama, The so-called alkali-carbonate reaction (ACR) - Its mineralogical and geochemical details, with special reference to ASR, Cement and Concrete Research 40 (2010) 643–675. https://doi.org/10.1016/j.cemconres.2009.09.020.

[15] P. Štukovnik, V.B. Bosiljkov, M. Marinšek, Detailed investigation of ACR in concrete with silica-free dolomite aggregate, Construction and Building Materials 216 (2019) 325–336. https://doi.org/10.1016/j.conbuildmat.2019.04.260.

[16] X. Chen, B. Yang, Z. Mao, M. Deng, The expansion cracks of dolomitic aggregates cured in TMAH solution caused by alkali-carbonate reaction, Materials 12 (2019) 1–11. https://doi.org/10.3390/ma12081228.

[17] P.E. Grattan-Bellew, L.D. Mitchell, J. Margeson, D. Min, Is alkali-carbonate reaction just a variant of alkali-silica reaction ACR = ASR?, Cement and Concrete Research 40 (2010) 556–562. https://doi.org/10.1016/j.cemconres.2009.09.002.

[18] Portland Cement Association, Ettringite formation and the performance of concrete, (2001).

[19] H.F.W. Taylor, C. Famy, K.L. Scrivener, Delayed ettringite formation, Cement and Concrete Research (2001).

[20] J. Skalny, J. Marchand, I. Odler, Sulfate attack on concrete, Spon Press, London ;, 2002. https://doi.org/10.4324/9780203301623.

[21] S. Diamond, Delayed ettringite formation — Processes and problems, Cement and Concrete Composites 18 (1996) 205–215. https://doi.org/10.1016/0958-9465(96)00017-0.

[22] V. Johansen, N. Thaulow, J. Skalny, Simultaneous presence of alkali — silica gel and ettringite in concrete, Advances in Cement Research 5 (1993) 23–29. https://doi.org/10.1680/adcr.1993.5.17.23.

[23] M. Thomas, K. Folliard, T. Drimalas, T. Ramlochan, Diagnosing delayed ettringite formation in concrete structures, Cement and Concrete Research 38 (2008) 841–847. https://doi.org/10.1016/j.cemconres.2008.01.003.

[24] R. Yang, C.D. Lawrence, C.J. Lynsdale, J.H. Sharp, Delayed ettringite formation in heat-cured Portland cement mortars, Cement and Concrete Research 29 (1999) 17–25. https://doi.org/10.1016/S0008-8846(98)00168-9.

[25] R. Yang, C.D. Lawrence, J.H. Sharp, Effect of type of aggregate on delayed ettringite formation, Advances in Cement Research 11 (1999) 119–132. https://doi.org/10.1680/adcr.1999.11.3.119.

[26] R.-P. Martin, Analyse sur structures modèles des effets mécaniques de la réaction sulfatique interne du béton, PhD Thesis, Université Paris-Est, 2010. https://pastel.archives-ouvertes.fr/tel-00558200v2.

[27] L.F.M. Sanchez, B. Fournier, D. Mitchell, J. Bastien, Condition assessment of an ASR-affected overpass after nearly 50 years in service, Construction and Building Materials 236 (2020) 117554. https://doi.org/10.1016/j.conbuildmat.2019.117554.

[28] S. Li, G. Chen, G. Ji, Y. Lu, Quantitative damage evaluation of concrete suffered freezing–thawing by DIP technique, Construction and Building Materials 69 (2014) 177–185. https://doi.org/10.1016/j.conbuildmat.2014.07.072.

[29] R. Xie, J. Yang, E. Xie, Investigation on mechanical properties deterioration of concrete subjected to freeze–thaw cycles, Sci Rep 12 (2022) 22612. https://doi.org/10.1038/s41598-022-27122-w.

[30] A. Zahedi, A. Komar, L.F.M. Sanchez, A.J. Boyd, Global assessment of concrete specimens subjected to freeze-thaw damage, Cement and Concrete Composites 133 (2022) 104716. https://doi.org/10.1016/j.cemconcomp.2022.104716.

[31] R.A.Jr. Deschenes, Mitigation and Evaluation of Alkali-Silica Reaction (ASR) and Freezing and Thawing in Concrete Transportation Structures, Doctorate, University of Arkansas, 2017. https://scholarworks.uark.edu/cgi/viewcontent.cgi?article=4007&context=etd.

[32] F. Gong, Y. Takahashi, I. Segawa, K. Maekawa, Mechanical properties of concrete with smeared cracking by alkali-silica reaction and freeze-thaw cycles, Cement and Concrete Composites 111 (2020) 103623. https://doi.org/10.1016/j.cemconcomp.2020.103623.

[33] R.H. Haddad, K.S. Numayr, Effect of alkali-silica reaction and freezing and thawing action on concrete–steel bond, Construction and Building Materials 21 (2007) 428–435. https://doi.org/10.1016/j.conbuildmat.2005.07.012.

[34] K. Kobayashi, Y. Kano, K. Rokugo, example of composite deterioration of R/C slab caused by ASR and frost attack in mountainous cold area and its verification test, J. JSCE, Ser. E2 70 (2014) 320–335. https://doi.org/10.2208/jscejmcs.70.320.

[35] British Cement Association (BCA), The diagnosis of alkali-silica reaction, British Cement Association (BCA), Wexham Springs, UK, 1992.

[36] T. Suzuki, T. Shiotani, M. Ohtsu, Evaluation of cracking damage in freeze-thawed concrete using acoustic emission and X-ray CT image, Construction & Building Materials 136 (2017) 619–626. https://doi.org/10.1016/j.conbuildmat.2016.09.013.

[37] H. Ahmed, A. Zahedi, L.F.M. Sanchez, P.-L. Fecteau, Condition assessment of ASR-affected reinforced concrete columns after nearly 20 years in service, Construction & Building Materials 347 (2022) 128570. https://doi.org/10.1016/j.conbuildmat.2022.128570.

[38] M.-A. Bérubé, N. Smaoui, B. Fournier, B. Bissonnette, B. Durand, Evaluation of the expansion attained to date by concrete affected by alkali–silica reaction. Part III: Application to existing structures, Can. J. Civ. Eng. 32 (2005) 463–479. https://doi.org/10.1139/l04-104.

[39] C.A. MacDonald, M. Piersanti, M. Shehata, J. Magnan, Use of the damage rating index (dri) to evaluate level of deterioration due to alkali-silica reaction in 34-year old concrete from the Sudbury area, in: 17th Euroseminar on Microscopy Applied to Building Materials, Toronto, Canada, 2019.

[40] F. Shrimer, Use of the Damage Rating Index as Input for Service Life Prediction in Alkali-Silica Reaction Affected Concrete, in: D. Cong, D. Broton (Eds.), Advances in Cement Analysis and Concrete Petrography, ASTM International, 100 Barr Harbor Drive, PO Box C700, West Conshohocken, PA 19428-2959, 2019: pp. 89–104. https://doi.org/10.1520/STP161320180246.

[41] K.J. Folliard, R. Barborak, T. Drimalas, L. Du, S. Garber, J.H. Ideker, T. Ley, S. Williams, M. Juenger, B. Fournier, M.D.A. Thomas, Preventing ASR/DEF in New Concrete: Final Report

(0-4085-5), Texas Department of Transportation and the Federal Highway Administration, Texas, USA, 2006.

[42] P.E. Grattan-Bellew, Petrographic methods for distinguishing between alkali- silica, alkali-carbonate reactions and other mechanisms of concrete deterioration, in: Proceedings of the 14th International Conference on Alkali-Aggregate Reaction in Concrete, Austin, Texas, USA, 2012.

[43] A. Leemann, Raman microscopy of alkali-silica reaction (ASR) products formed in concrete, Cement and Concrete Research 102 (2017) 41–47. https://doi.org/10.1016/j.cemconres.2017.08.014.

[44] L.F.M. Sanchez, T. Drimalas, B. Fournier, D. Mitchell, J. Bastien, Comprehensive damage assessment in concrete affected by different internal swelling reaction (ISR) mechanisms, Cement and Concrete Research 107 (2018) 284–303. https://doi.org/10.1016/j.cemconres.2018.02.017.

[45] L.F.M. Sanchez, T. Drimalas, B. Fournier, Assessing condition of concrete affected by internal swelling reactions (ISR) through the Damage Rating Index (DRI), Cement 1–2 (2020) 100001. https://doi.org/10.1016/j.cement.2020.100001.

[46] V. Villeneuve, Détermination de l’endommagement du béton par méthode pétrographique quantitative, Master’s Thesis., Université Laval, 2011.

[47] A. Leemann, T. Katayama, I. Fernandes, M.A.T.M. Broekmans, Types of alkali–aggregate reactions and the products formed, in: Proceedings of the Institution of Civil Engineers - Construction Materials, 2016: pp. 128–135. https://doi.org/10.1680/jcoma.15.00059.

[48] L.F.M. Sanchez, B. Fournier, M. Jolin, J. Duchesne, Reliable quantification of AAR damage through assessment of the Damage Rating Index (DRI), Cement and Concrete Research 67 (2015) 74–92. https://doi.org/10.1016/j.cemconres.2014.08.002.

[49] C.T. Rueden, J. Schindelin, M.C. Hiner, B.E. DeZonia, A.E. Walter, E.T. Arena, K.W. Eliceiri, ImageJ2: ImageJ for the next generation of scientific image data, BMC Bioinformatics 18 (2017) 529. https://doi.org/10.1186/s12859-017-1934-z.

[50] J. Schindelin, I. Arganda-Carreras, E. Frise, V. Kaynig, M. Longair, T. Pietzsch, S. Preibisch, C. Rueden, S. Saalfeld, B. Schmid, J.-Y. Tinevez, D.J. White, V. Hartenstein, K. Eliceiri, P. Tomancak, A. Cardona, Fiji: an open-source platform for biological-image analysis, Nat Methods 9 (2012) 676–682. https://doi.org/10.1038/nmeth.2019.

[51] P. Rivard, B. Fournier, G. Ballivy, Quantitative Petrographic Technique for Concrete Damage Due to ASR: Experimental and Application, Cement, Concrete and Aggregates 22 (2000) 63–72. https://doi.org/10.1520/CCA10465J.

[52] J. Lindgård, M. Haugen, N. Castro, M.D.A. Thomas, Advantages of using plane polished section analysis as part of microstructural analyses to describe internal cracking due to alkali-silica reactions, in: Austin, Texas, USA, 2012.

[53] J.B. Walsh, The effect of cracks on the uniaxial elastic compression of rocks, Journal of Geophysical Research 70 (1965) 399–411. https://doi.org/10.1029/JZ070i002p00399.

[54] T.M. Chrisp, P. Waldron, J.G.M. Wood, Development of a non-destructive test to quantify damage in deteriorated concrete, Magazine of Concrete Research 45 (1993) 247–256. https://doi.org/10.1680/macr.1993.45.165.247.

[55] A. Zahedi, C. Trottier, L. Sanchez, M. Noël, Evaluation of the induced mechanical deterioration of alkali-silica reaction affected concrete under distinct confinement conditions through the Stiffness Damage Test, Cement and Concrete Composites 126 (2022) 104343. https://doi.org/10.1016/j.cemconcomp.2021.104343.

[56] N. Smaoui, B. Fournier, M.-A. Bérubé, B. Bissonnette, B. Durand, Evaluation of the expansion attained to date by concrete affected by alkali-silica reaction. Part I. Experimental study, Canadian Journal of Civil Engineering (2004).

[57] N. Smaoui, B. Fournier, M.-A. Bérubé, B. Bissonnette, B. Durand, Evaluation of the expansion attained to date by concrete affected by alkali-silica reaction. Part II. Application to nonreinforced concrete specimens exposed outside, Canadian Journal of Civil Engineering (2004).

[58] E. Giannini, L.F.M. Sanchez, A. Tuinukuafe, K.J. Folliard, Characterization of concrete affected by delayed ettringite formation using the stiffness damage test, Construction and Building Materials 162 (2018) 253–264. https://doi.org/10.1016/j.conbuildmat.2017.12.012.

[59] R.-P. Martin, L. Sanchez, B. Fournier, F. Toutlemonde, Evaluation of different techniques for the diagnosis & prognosis of Internal Swelling Reaction (ISR) mechanisms in concrete, Construction and Building Materials 156 (2017) 956–964. https://doi.org/10.1016/j.conbuildmat.2017.09.047.

[60] R.H.R.Q. Melo, N.P. Hasparyk, F. Tiecher, Assessment of Concrete Impairments over Time Triggered by DEF, Journal of Materials in Civil Engineering 35 (2023). https://doi.org/10.1061/JMCEE7.MTENG-15041.

[61] J.S. Guo, P. Waldron, Development of the stiffness damage test (SDT) for characterisation of thermally loaded concrete, Mat. Struct. 33 (2000) 483–491. https://doi.org/10.1007/BF02480525.

[62] A.Y. Nassif, A new classification system for fire-damaged concrete based on the strain energy dissipated in a hysteresis loop, Magazine of Concrete Research 52 (2000) 287–295. https://doi.org/10.1680/macr.2000.52.4.287.

[63] A.Y. Nassif, E. Burley, S. Ridgen, A new quantitative method of assessing fire damage to concrete structures, Magazine of Concrete Research 47 (1995) 271–278. https://doi.org/10.1680/macr.1995.47.172.271.

[64] P.E. Grattan-Bellew, A. Danay, Comparison of laboratory and field evaluation of alkali-silica reaction in large dams, in: Collection / Collection : NRC Publications Archive / Archives des publications du CNRC, 1992: pp. 1–25.

[65] P.A. Dunbar, P.E. Grattan-Bellew, Results of damage rating evaluation of condition of concrete from a number of structures affected by AAR, in: CANMET/ACI International Workshop on Alkali-Aggregate Reactions in Concrete, 1995: pp. 257–265.

[66] P. Rivard, B. Fournier, G. Ballivy, The Damage Rating Index Method for ASR Affected Concrete—A Critical Review of Petrographic Features of Deterioration and Evaluation Criteria, Cement, Concrete, Aggr. 24 (2002) 11228. https://doi.org/10.1520/CCA10531J.

[67] P. Rivard, G. Ballivy, Assessment of the expansion related to alkali-silica reaction by the Damage Rating Index method, Construction and Building Materials 19 (2005) 83–90. https://doi.org/10.1016/j.conbuildmat.2004.06.001.

[68] L. Sanchez, B. Fournier, M. Jolin, M.A.B. Bedoya, J. Bastien, J. Duchesne, Use of Damage Rating Index to Quantify Alkali-Silica Reaction Damage in Concrete: Fine versus Coarse Aggregate, ACI Materials Journal 113 (2016). https://doi.org/10.14359/51688983.

[69] S. Tayfur, C. Yüksel, N. Alver, O. Akar, Ö. Andiç-Çakır, Evaluation of alkali–silica reaction damage in concrete by using acoustic emission signal features and damage rating index: damage monitoring on concrete prisms, Mater Struct 54 (2021) 146. https://doi.org/10.1617/s11527-021-01749-z.

[70] L.F.M. Sanchez, B. Fournier, M. Jolin, D. Mitchell, J. Bastien, Overall assessment of Alkali-Aggregate Reaction (AAR) in concretes presenting different strengths and incorporating a wide range of reactive aggregate types and natures, Cement and Concrete Research 93 (2017) 17–31. https://doi.org/10.1016/j.cemconres.2016.12.001.

[71] A. Zahedi, C. Trottier, L.F.M. Sanchez, M. Noël, Condition assessment of alkali-silica reaction affected concrete under various confinement conditions incorporating fine and coarse reactive aggregates, Cement and Concrete Research 153 (2022) 106694. https://doi.org/10.1016/j.cemconres.2021.106694.

[72] I.R. Sims, B. Hunt, B. Miglio, Quantifying Microscopical Examinations of Concrete for Alkali Aggregate Reactions (AAR) and Other Durability Aspects, in: Curability of Concrete, Toronto, Canada, 1992.

[73] P.E. Grattan-Bellew, D. Mitchell, Quantitative petrographic analysis of concrete : the damage rating index (DRI) method, a review, in: CANMET International Conference on Recent Advances in Concrete Technology, Natural Resources Canada, Ottawa, Canada, 2006.

[74] G.G. Clemena, S. Lane, T. Freeman, M. Lozev, Evaluation of nondestructive evaluation methods for application in early detection of deterioration in concrete pavements, VTRC 00-R13, Virginia Transortation Research Council, Charlottesville, USA, 2000. https://rosap.ntl.bts.gov/view/dot/14227.

[75] L. Powers, F.H. Shrimer, Quantification of ASR in concrete: an introduction to the Damage-Rating method, in: 29th International Conference on Cement Microscopy, Québec, Canada, 2007.

[76] N. Smaoui, M.-A. Bérubé, B. Fournier, B. Bissonnette, B. Durand, Evaluation of expansion attained by ASR-affected concrete, in: 12th International Conference on Alkali-Aggregate Reaction, Beijing, China, 2004: pp. 1005–1015.

[77] J. Lindgård, O. Skjølsvold, M. Haugen, P. Hagelia, B.J. Wigum, Experience from evaluation of degree of damage in fluorescent impregnated plan polished sections of half cores based on the cracking index method, in: Beijing, China, 2004.

[78] L.J. Monette, N.J. Gardner, P.E. Grattan-Bellew, Residual Strength of Reinforced Concrete Beams Damaged by Alkali-Silica Reaction—Examination of Damage Rating Index Method, MJ 99 (2002). https://doi.org/10.14359/11315.

[79] L.F.M. Sanchez, B. Fournier, M. Jolin, J. Bastien, Evaluation of the stiffness damage test (SDT) as a tool for assessing damage in concrete due to ASR Test loading and output responses for concretes incorporating fine or coarse reactive aggregates, Cement and Concrete Research 56 (2014) 213–229.

[80] H.N. Walker, D.S. Lane, Paul.E. Stutzman, Petrographic Methods of Examining Hardened Concrete: A Petrographic Manual, Federal Highway Administration (FHWA), 2006.

[81] M. Champagne, J. Lindgård, B. Fournier, B. Bissonnette, Profiling the internal damage within an ASR-affected dam component with the Damage Rating Index (DRI), in: 16th International Conference on Alkali-Aggregate Reaction, Lisboa, Portugal, 2022.

[82] M.-A. Bérubé, B. Fournier, T. Côté, Using the damage rating index for assessing the expansion of concrete affected by freeze-thaw, sulphate attack, or ASR, in: 14th International Conference on Alkali-Aggregate Reaction, Austin, Texas, USA, 2012.

[83] A. Zahedi, L. Saliba, L.F.M. Sanchez, A.J. Boyd, Reliability of the damage rating index to assess the condition of concrete affected by external sulfate attack, Magazine of Concrete Research 75 (2023) 135–148. https://doi.org/10.1680/jmacr.22.00061.

[84] ASTM Standard C865/C865M-20, Guide for Petrographic Examination of Aggregates for Concrete, (2020). https://doi.org/10.1520/C0295_C0295M-19.

[85] M. Champagne, Applying the damage rating index for the spatial damage assessment in concrete specimens affected by alkali-silica reaction (ASR), Master's Thesis., Université Laval, 2020.

[86] ASTM International, ASTM C457/457M:16 Test Method for Microscopical Determination of Parameters of the Air-Void System in Hardened Concrete, (2016). https://doi.org/10.1520/C0457_C0457M-16.

[87] A. Bezerra, C. Trottier, L.F.M. Sanchez, B. Fournier, The use of artificial intelligence for assessing an overpass affected by Alkali-Silica Reaction (ASR), in: Bridge Safety, Maintenance, Management, Life-Cycle, Resilience and Sustainability, CRC Press, London, 2022: pp. 354–361. https://doi.org/10.1201/9781003322641-40.

[88] A. Bezerra, The Use of Artificial Intelligence for Assessing Damage in Concrete Affected by Alkali-Silica Reaction (ASR), Master's Thesis., University of Ottawa, 2020.

[89] C. Trottier, R. Ziapour, A. Zahedi, L. Sanchez, F. Locati, Microscopic characterization of alkali-silica reaction (ASR) affected recycled concrete mixtures induced by reactive coarse and fine aggregates, Cement and Concrete Research 144 (2021) 106426. https://doi.org/10.1016/j.cemconres.2021.106426.

[90] Y. Zhu, A. Zahedi, L.F.M. Sanchez, B. Fournier, S. Beauchemin, Overall assessment of alkali-silica reaction affected recycled concrete aggregate mixtures derived from construction and demolition waste, Cement and Concrete Research 142 (2021) 106350. https://doi.org/10.1016/j.cemconres.2020.106350.

[91] İ. Akgül, Mobile-DenseNet: Detection of building concrete surface cracks using a new fusion technique based on deep learning, Heliyon 9 (2023) e21097. https://doi.org/10.1016/j.heliyon.2023.e21097.

[92] Y. Bai, H. Sezen, A. Yilmaz, End-to-end Deep Learning Methods for Automated Damage Detection in Extreme Events at Various Scales, in: 2020 25th International Conference on Pattern Recognition (ICPR), IEEE, Milan, Italy, 2021: pp. 6640–6647. https://doi.org/10.1109/ICPR48806.2021.9413041.

[93] U.H. Billah, A. Tavakkoli, H.M. La, Concrete Crack Pixel Classification Using an Encoder Decoder Based Deep Learning Architecture, in: G. Bebis, R. Boyle, B. Parvin, D. Koracin, D. Ushizima, S. Chai, S. Sueda, X. Lin, A. Lu, D. Thalmann, C. Wang, P. Xu (Eds.), Advances in Visual Computing, Springer International Publishing, Cham, 2019: pp. 593–604. https://doi.org/10.1007/978-3-030-33720-9_46.

[94] P.S. Chakurkar, D. Vora, S. Patil, S. Mishra, K. Kotecha, Data-driven approach for AI-based crack detection: techniques, challenges, and future scope, Front. Sustain. Cities 5 (2023) 1253627. https://doi.org/10.3389/frsc.2023.1253627.

[95] Y. Chen, Z. Zhu, Z. Lin, Y. Zhou, Building Surface Crack Detection Using Deep Learning Technology, Buildings 13 (2023) 1814. https://doi.org/10.3390/buildings13071814.

[96] V.P. Golding, Z. Gharineiat, H.S. Munawar, F. Ullah, Crack Detection in Concrete Structures Using Deep Learning, Sustainability 14 (2022) 8117. https://doi.org/10.3390/su14138117.

[97] Md.M. Islam, Md.B. Hossain, Md.N. Akhtar, M.A. Moni, K.F. Hasan, CNN Based on Transfer Learning Models Using Data Augmentation and Transformation for Detection of Concrete Crack, Algorithms 15 (2022) 287. https://doi.org/10.3390/a15080287.

[98] S. Katsigiannis, S. Seyedzadeh, A. Agapiou, N. Ramzan, Deep learning for crack detection on masonry façades using limited data and transfer learning, Journal of Building Engineering 76 (2023) 107105. https://doi.org/10.1016/j.jobe.2023.107105.

[99] J.-H. Kim, J. Lee, Efficient Dataset Collection for Concrete Crack Detection With Spatial-Adaptive Data Augmentation, IEEE Access 11 (2023) 121902–121913. https://doi.org/10.1109/ACCESS.2023.3328243.

[100] X. Meng, Concrete Crack Detection Algorithm Based on Deep Residual Neural Networks, Scientific Programming 2021 (2021) 1–7. https://doi.org/10.1155/2021/3137083.

[101] M. Padsumbiya, V. Brahmbhatt, S. Thakkar, Automatic Crack Detection Using Convolutional Neural Network, J. Soft Comput. Civ. Eng. 6 (2022). https://doi.org/10.22115/scce.2022.325596.1397.

[102] P. Palevičius, M. Pal, M. Landauskas, U. Orinaitė, I. Timofejeva, M. Ragulskis, Automatic Detection of Cracks on Concrete Surfaces in the Presence of Shadows, Sensors 22 (2022) 3662. https://doi.org/10.3390/s22103662.

[103] S. Shim, Self-training approach for crack detection using synthesized crack images based on conditional generative adversarial network, Computer Aided Civil Eng (2023) mice.13119. https://doi.org/10.1111/mice.13119.

[104] C. Tello, S. Jabari, L. Waugh, M. Masry, J. McGinn, Improving Crack Detection on Concrete Structures Using Real-World Data Augmentation for Deep Learning Convolutional Neural Networks, in: Springer International Publishing, Moncton, NB, 2023.

[105] P. Bajcsy, S. Feldman, M. Majurski, K. Snyder, M. Brady, Approaches to training multiclass semantic image segmentation of damage in concrete, Journal of Microscopy 279 (2020) 98–113. https://doi.org/10.1111/jmi.12906.

[106] A.P. Bajcsy, S. Feldman, M. Brady, K. Snyder, Semantic SEM Image Segmentation of Concrete with Contextual Labels, Microsc Microanal 25 (2019) 144–145. https://doi.org/10.1017/S1431927619001454.

[107] Y. Song, Z. Huang, C. Shen, H. Shi, D.A. Lange, Deep learning-based automated image segmentation for concrete petrographic analysis, Cement and Concrete Research 135 (2020) 106118. https://doi.org/10.1016/j.cemconres.2020.106118.

[108] S.S. Bangaru, C. Wang, M. Hassan, H.W. Jeon, T. Ayiluri, Estimation of the degree of hydration of concrete through automated machine learning based microstructure analysis – A study on effect of image magnification, Advanced Engineering Informatics 42 (2019) 100975. https://doi.org/10.1016/j.aei.2019.100975.

[109] A.N. Beskopylny, E.M. Shcherban', S.A. Stel'makh, L.R. Mailyan, B. Meskhi, I. Razveeva, A. Kozhakin, N. Beskopylny, D. El'shaeva, S. Artamonov, Method for Concrete Structure Analysis by Microscopy of Hardened Cement Paste and Crack Segmentation Using a Convolutional Neural Network, J. Compos. Sci. 7 (2023) 327. https://doi.org/10.3390/jcs7080327.

[110] A. Dehghan, P. Zhang, E. Ossetchkina, D. Sloan, K. Peterson, Digital Microscopy Applied to Damage Rating Index for Alkali-Silica Reaction in Concrete, in: D. Cong, D. Broton (Eds.), Advances in Cement Analysis and Concrete Petrography, ASTM International, 100 Barr Harbor Drive, PO Box C700, West Conshohocken, PA 19428-2959, 2016: pp. 105–125. https://doi.org/10.1520/STP161320180003.

[111] P. Rivard, Quantification de l'endommagement Du Béton Atteint de Réaction Alcalis-Silice Par Analyse d'images, Master's Thesis., Université de Sherbrooke, 1998.

[112] E. Qoku, K. Xu, J. Li, P.J.M. Monteiro, K.E. Kurtis, Advances in imaging, scattering, spectroscopy, and machine learning-aided approaches for multiscale characterization of cementitious systems, Cement and Concrete Research 174 (2023) 107335. https://doi.org/10.1016/j.cemconres.2023.107335.

[113] E. Ford, K. Maneparambil, N. Neithalath, Machine Learning on Microstructural Chemical Maps to Classify Component Phases in Cement Pastes, J. Soft Comput. Civ. Eng. 5 (2021). https://doi.org/10.22115/scce.2021.302400.1357.

[114] H. Sui, W. Wang, J. Lin, Z.Q. Tang, D.-S. Yang, W. Duan, Spatial correlation and pore morphology analysis of limestone calcined clay cement (LC3) via machine learning and image-based characterisation, Construction and Building Materials 401 (2023) 132721. https://doi.org/10.1016/j.conbuildmat.2023.132721.

[115] H. Qian, Y. Li, J. Yang, L. Xie, K.H. Tan, Segmentation and analysis of cement particles in cement paste with deep learning, Cement and Concrete Composites 136 (2023) 104819. https://doi.org/10.1016/j.cemconcomp.2022.104819.

[116] S.S. Bangaru, C. Wang, X. Zhou, M. Hassan, Scanning electron microscopy (SEM) image segmentation for microstructure analysis of concrete using U-net convolutional neural network, Automation in Construction 144 (2022) 104602. https://doi.org/10.1016/j.autcon.2022.104602.

[117] R. Lorenzoni, I. Curosu, S. Paciornik, V. Mechtcherine, M. Oppermann, F. Silva, Semantic segmentation of the micro-structure of strain-hardening cement-based composites (SHCC) by applying deep learning on micro-computed tomography scans, Cement and Concrete Composites 108 (2020) 103551. https://doi.org/10.1016/j.cemconcomp.2020.103551.

[118] F. Georget, W. Wilson, K.L. Scrivener, edxia: Microstructure characterisation from quantified SEM-EDS hypermaps, Cement and Concrete Research 141 (2021) 106327. https://doi.org/10.1016/j.cemconres.2020.106327.

[119] R. Sleem, DeepLearning-ConcreteDataset: Training dataset for Crack Detection, (2018). https://github.com/rakehsaleem/DeepLearning-ConcreteDataset?form=MG0AV3.

[120] S. Dorafshan, R.J. Thomas, M. Maguire, SDNET2018: An annotated image dataset for non-contact concrete crack detection using deep convolutional neural networks, Data in Brief 21 (2018) 1664–1668. https://doi.org/10.1016/j.dib.2018.11.015.

[121] Ç.F. Özgenel, Concrete Crack Images for Classification, (2019). https://doi.org/10.17632/5Y9WDSG2ZT.2.

[122] F. Yang, L. Zhang, S. Yu, D. Prokhorov, X. Mei, H. Ling, Feature Pyramid and Hierarchical Boosting Network for Pavement Crack Detection, (2019). https://doi.org/10.48550/arXiv.1901.06340.

[123] A. Kirillov, E. Mintun, N. Ravi, H. Mao, C. Rolland, L. Gustafson, T. Xiao, S. Whitehead, A.C. Berg, W.-Y. Lo, P. Dollár, R. Girshick, Segment Anything, (2023). https://doi.org/10.48550/ARXIV.2304.02643.

Chapter 3: Research methodology and experimental program

This research program addressed the limitations of using the DRI, specifically its applicability, variability, and subjectivity in engineering practice. The selected research methodology was based on a thorough literature review, practical experience as an operator and trainer of new operators, and interactions with subject matter experts. Currently, the DRI is not a standard test for evaluating internal swelling reactions (ISR); however, it was acknowledged among the tools referenced in the latest RILEM State-of-the-Art report [1]. Consequently, this study evaluated the adaptability of the DRI to capture deterioration induced by DEF, which involved modifications to the counting procedure, correlating distress features with deterioration as measured through expansion and mechanical responses. Using linear models, the impact of distress features is evaluated against expansion and mechanical responses for various ISRs (i.e., ASR, DEF, and FT, both singly and in combination) to comprehend the subjectivity surrounding the DRI. Additionally, a comprehensive autonomous training guide for operators was proposed to address variability through training, along with a methodology for assessing the outputs from an automated version of the DRI for practical applications. The preparation and analysis of the DRI samples were initially described, as these samples formed the basis for each topic discussed. The subsequent sections were organized by objectives, detailing the corresponding materials and methods employed.

3.1. The damage rating index (DRI)

3.1.2. Sample surface preparation

The DRI was conducted on the ISR-affected concrete specimens and cores that had been cut in half longitudinally with a masonry saw fitted with a diamond blade and water for cooling. The flat surfaces were ground and polished using successive grits of 30, 50-60, 100-140, 280-400 (80–100 μm), 600-800 (20–40 μm), 1200-1500 (10–20 μm), and 3000 (4–8 μm). The flat and reflective surface was then partitioned into 1 cm by 1 cm squares using a grid within the field of view of a stereomicroscope at 15-16x magnification.

3.1.3. Distress feature distinction and counting

The distinction of the distress features was made by following previous work proposed by Villeneuve (2011), Fournier et al. (2015), and Sanchez et al. (2016) [2–4], taking into account the operator's classifications of petrographic feature variability, various types of distress features, and degrees of deterioration in reactive coarse and fine aggregates. The distress features evaluated in this study relate to those indicative of ISR-induced concrete deterioration (Table 3.1). The distress features within each square were counted based on their type until the entire analysis surface had been assessed.

Table 3.1. Petrographic/distress features considered in this research program.

Petrographic/distress feature	Optimized weighting factor [2]	Type of feature
Crack in the aggregate	-	Distress
Closed crack in the aggregate (CCA)	0.25	Distress
Opened crack in the aggregate (OCA)	2	Distress
Opened crack in the aggregate with reaction product (OCA_{RP})*	2	Distress+ petrographic
Corroded/debonded aggregate	2	Distress
Crack in the cement paste (CCP)	3	Distress
Crack in the cement paste with reaction (CCP_{RP})	3	Distress+ petrographic
De-bonded aggregates (Debon)	3	Distress

3.1.4. DRI calculation and other outputs

The weighting factors from Table 3.1 were applied to the relevant distress features to balance their relative importance concerning the distress mechanism. The DRI calculation summed the weighted counts for each distress feature and normalized the result by dividing the total by the number of analyzed squares, then multiplied by 100 cm² (Equation 3.1). Bar charts were generated to delineate the features and visualize their relative significance. The extended version of the DRI represented the unweighted distress feature counts, as proposed by [5], where bar charts were created to compare expansion levels and distress mechanisms, presented as counts per 100 cm² and proportions (Equations 3.2 and 3.3, respectively). The crack density (CD) illustrated the total (OCA + OCA_{RP}) + (CCP + CCP_{RP}) counts per cm² (Equation 3.4).

$$DRI = \left[\frac{\sum(0.25(CCA) + 2(OCA + OCA_{RP} + DAP) + 3(CCP + CCP_{RP} + Debon))}{n}\right] \times 100\ cm^2 \qquad \text{Eq. 3.1}$$

$$Distress\ feature\ \left(\frac{counts}{100\ cm^2}\right) = \frac{Distress\ feature\ counts}{n} \times 100\ cm^2 \qquad \text{Eq. 3.2}$$

$$Distress\ feature\ (\%) = \frac{Distress\ feature\ counts}{CCA + (OCA + OCA_{RP}) + (CCP + CCP_{RP})} \times \frac{100\ cm^2}{n} \qquad \text{Eq. 3.3}$$

$$Crack\ density\ \left(\frac{counts}{cm^2}\right) = \frac{(OCA + OCA_{RP}) + (CCP + CCP_{RP})}{n} \qquad \text{Eq. 3.4}$$

Where CCA is the total number of closed cracks in the aggregate, $OCA\ and\ OCA_{RP}$ are the total numbers of open cracks in the aggregate without and with reaction product, respectively, DAP is the total number of disaggregated/corroded particles, $CCP\ and\ CCP_{RP}$ are the total numbers of cracks in the cement paste without and with reaction product, respectively, $Debon$ is the total number of debonded/dislodged aggregates, and n is the total number of 1 cm by 1 cm squares analyzed.

3.1.5. Mechanical testing

The compressive strength (f_c) of cylindrical cores was measured according to ASTM C39 [6] after 47 days of storage at 12°C to inhibit ASR development, followed by a 48-hour resaturation period [7,8]. The SDT, depicted in Figure 3.1, adhered to the procedure proposed by Sanchez et al. [7], where a test load of 40% of the design compressive strength (f'_c) served as the maximum test load and a loading rate of 0.10 MPa/s was applied [7,8]. The energy dissipated into the system relative to the total energy was calculated using the SDI from Equation 3.5, while the plastic deformation relative to the total deformation was computed using the PDI from Equation 3.6. The modulus of elasticity was subsequently calculated using the average slope of the second and third cycles (Equation 3.7).

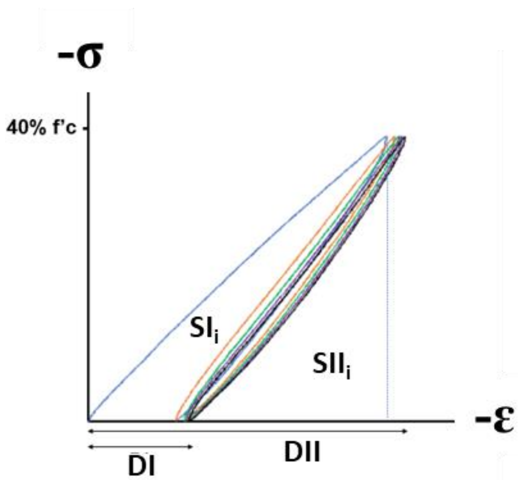

$$SDI = \frac{\sum_{i=1}^{5} SI_i}{\sum_{i=1}^{5}(SI_i + SII_i)} \quad \text{Eq. 3.5}$$

$$PDI = \frac{DI}{DII} \quad \text{Eq. 3.6}$$

$$E = ave.\, slope\ of\ cycles\ 2\ \&\ 3 \quad \text{Eq. 3.7}$$

Figure 3.1. Stress-strain curve with SDT outputs graphically represented.

3.2. Topic 1: Adapting the DRI tool to concrete affected by DEF

The first research topic adapted from the DRI tool centred on concrete that was impacted by distress mechanisms beyond ASR, such as DEF. Modifications to the counting procedure were suggested to underscore distress features indicative of DEF. Since DEF displayed a unique crack and distress pattern, the distress features were examined by introducing a counting method that accentuates DEF-related damage to concrete. This proposed counting method was elaborated on in Chapter 4 and was further employed alongside the mechanical responses outlined in Chapter 5. This topic was developed in collaboration with Dr. Renaud-Pierre Martin and Dr. François Toutlemonde, given their expertise in DEF damage at both material and structural levels. The current study aimed to define distress features readily accessible from the predetermined list in Table 3.1 without suggesting modifications beyond the counting method to illustrate cracks representative of DEF-induced deterioration.

3.2.2. Materials and methods for DEF development

The concrete cores used in this study were sourced from an unreinforced beam that was fabricated and monitored in a laboratory, which was affected by DEF. This beam used specifically chosen cement to enhance the likelihood of developing DEF, with higher C_3A, alkalis, and sulphate content than a companion cement, as described in [9]. Furthermore, the cement was alkali-boosted with KOH to achieve approximately 1% $Na_2O_{eq.}$ by cement mass, combined with non-reactive aggregates (Table 3.2). The targeted compressive strength of the concrete was 40 MPa, which was achieved using a water-to-cement ratio of 0.46 and a slump of 10 ±2 cm.

Table 3.2. Mixture proportions for DEF beam.

Cement	Total water	w/c	Coarse gravel (4-12 mm)	Sand (<2 mm)
410 kg/m^3	199 kg/m^3	0.46	929 kg/m^3	854 kg/m^3

To induce DEF, the beam was immersed in a water bath with increasing temperature for 2 hours after the batching commenced and maintained for 24 hours at a maximum rate of 10 °C/h until it reached a temperature of 81°C. This temperature was held constant for the following 72 hours. The cooling period was set at -1°C/h until the temperature reached 25°C, lasting 55 hours [10]. The beam was then stored under conditions conducive to DEF damage, with the bottom portion (70 mm) submerged in water while the top portion was allowed to dry at 30% relative humidity (RH). This arrangement created a hydraulic gradient across the height of the beam, leading to bending in the longitudinal direction and varying degrees of damage throughout. Aluminum adhesive layers were applied to the side faces to ensure a unidirectional gradient. Further details on the methodology for inducing DEF damage and effective thermal energy can be found in [9–11]. Cores measuring 110 mm in diameter and 250 mm in length were extracted from the unreinforced beam at various depths (Table 3.3) in the transverse direction, similar to the procedure outlined in [12].

Table 3.3. Expansions corresponding to core depths.

Beam	Reactivity	Hydraulic gradient (relative humidity)	Expansion per depth of beam (m)				
			0.08 (Top)	0.17	0.27	0.37	0.44 (Bottom)
P2	High	30% - Top 100% - Bottom	0.89%	1.27%	1.55%	1.69%	1.73%

3.2.3. Mechanical testing

The SDT was performed on cores measuring 110 mm in diameter and 250 mm in height, following the procedure outlined in Section 3.1.4. A test load of 30% of f'_c was applied as the maximum test load, with a loading rate of 0.10 MPa/s [7,8]. The SDI and modulus of elasticity (*E*) were calculated using Equations 3.5 and 3.7, respectively. Cores taken at depths of 0.37 and 0.44 m experienced failure in some specimens before completing the five cycles; therefore, only the first cycle was used to calculate the SDI [12].

3.3. Topic 2: Understanding the contribution of distress features towards concrete deterioration

The second topic examined the relationships between distress features and mechanical responses. Utilizing the DRI gathered from a previous research program conducted by [2,11], the distress feature counts were decomposed to understand how the extent of damage influenced the count distributions concerning the type of ISR. As interest grew in the application of the DRI in engineering practice, the tool's subjectivity was investigated by correlating the outputs from the DRI methodology, including the extended version of the DRI [13], as presented in Equations 3.1 to 3.4, with expansion and mechanical responses (i.e., tensile and compressive strengths, modulus of elasticity, SDI, PDI, and the corresponding hysteresis area). Furthermore, the data decomposition facilitated the creation of confidence intervals (CIs) for expected distress feature counts, boxplots, and statistical parameters. This topic was thoroughly examined and presented in Chapter 6.

3.3.2. Materials and ISR development

All mixtures individually used the reactive coarse aggregate from New Mexico (NM) and reactive sand from Texas (Tx). Table 3.4 outlines the characteristics of the coarse and fine aggregates utilized in the concrete mixtures. The reactive coarse aggregate was combined with non-reactive granite sand (i.e., Lav) across all groups. Similarly, the reactive sand was combined with non-reactive Canadian coarse limestone aggregate (i.e., HP) for the ASR mixtures (i.e., 35 MPa and CPT) and with non-reactive American coarse limestone aggregate (i.e., MM) for the DEF and DEF+ASR mixtures. A high alkali cement was employed (i.e., 0.90% Na_2O_{eq}. CSA Type GU, ASTM type I) in all of the mixtures, which were boosted to 1.25% Na_2O_{eq}. by cement mass, using reagent grade NaOH, according to ASTM C1293 [16].

Table 3.4. Characteristics of the coarse and fine aggregates.

Aggregate		**Reactivity**	**Location**	**Rock type**	**Specific gravity** [14]	**Absorption** [14]	**AMBT 14-day exp (%)** [14]
Coarse	NM	ASR reactive	New Mexico (USA)	Polymictic Gravel (Mixed Volcanic, quartzite, chert)	2.53	1.59	1.056
	MM	Non-reactive	North Carolina (USA)	Limestone	2.47	3.12	0.01
Fine	Tx	ASR reactive	Corpus Christi (USA)	Polymictic sand (granitic, mixed volcanic, quartzite, chert, quartz)	2.60	0.55	0.755
	Lav	Non-reactive	Quebec (CAN)	Natural derived from Granite	2.71	0.54	0.068

Concrete specimens (100 mm in diameter and 200 mm in length) were cast and moist-cured in a curing room for 48 hours after demoulding. Small holes, measuring 5 mm in diameter and 15 mm in length, were drilled into the ends. Stainless steel gauge studs were then affixed using a fast-setting cement paste slurry for longitudinal expansion measurements. Following 48 hours of moist curing, the initial readings were recorded.

The ASR specimens (i.e., 35 MPa and CPT proportioned) were stored above a few centimetres of water in 22-litre plastic pails lined with moisture-wicking fabric at 38℃ and 100% relative humidity. Length changes were monitored over time following standard procedure [16] until the targeted expansions were reached (i.e., 0.05%, 0.12%, 0.20%, and 0.30%).

The DEF-exposed specimens were cured for 12 hours at 95℃ (i.e., following a 4-hour period to reach the temperature) in an oven four hours after casting. The temperature then decreased to 23℃ for the subsequent 12 hours, after which the specimens were stored in water-filled pails at 23℃. Length changes were monitored over time until the specimens reached the selected expansion levels (i.e., 0.12%, 0.40%, 0.50%, 0.80%, 1.0%, and 2.0%). Specimens coupled with ASR were stored at 38℃ and 100% relative humidity (i.e., above water in a sealed bucket) to facilitate ASR and DEF. Length changes were monitored until the specimens reached the selected expansion levels (i.e., 0.08%, 0.12%, 0.30%, 0.50%, 0.6%, 0.90%, and 1.5%).

The FT-exposed specimens were stored in a freezing and thawing chamber (i.e., cycling from -20℃ to +5℃ for 3 hours per cycle, with 8 cycles per day) according to standard procedure (ASTM C666). Specimens were removed from the chamber once they reached the targeted expansion levels (i.e., 0.05%, 0.12%, 0.20%, and 0.30%). Specimens coupled with ASR were taken out at half of the targeted expansions and exposed to the previously described ASR-enabling conditions until they achieved full expansions (i.e., 0.05%, 0.12%, 0.20%, and 0.30%).

3.3.3. *Data analysis*

Regressions were developed using linear models with the distress features as the variables against expansion and mechanical responses. Variations of the linear models (Equation 3.8) were assessed using the Akaike information criterion (AIC) and the coefficient of determination (R^2).

$$Expansion\ or\ mechanical\ response = \beta_0 + \beta_1(x_1) + \beta_2(x_2) + \beta_3(x_3) + \cdots + \beta_n(x_n) \qquad \text{Eq. 3.8}$$

Part of the DRI data decomposition involved understanding the cumulative effects of those observations. This approach established a representative sample size based on the law of large numbers, as illustrated in Equation 3.9. Converging towards the mean (i.e., DRI) value occurred as the sample size n, representing the number of 1 cm^2 squares, increased.

$$DRI = \frac{X_1 + X_2 + X_3 + \cdots + X_n}{n} \qquad \text{Eq. 3.9}$$

The bootstrap method with replacement was employed to define confidence intervals (CIs) for all distress features across various distress mechanisms and expansion levels. The means were utilized as the parameters of interest, allowing for establishing the 2.5th and 97.5th percentiles of the bootstrap estimates to create the CI. The number of resampling iterations (R) was set at one thousand to ensure stability.

3.4. Topic 3: An operator’s guide for autonomous training

The third research topic focused on improving the DRI tool’s accessibility for engineering practitioners by establishing an autonomous operator training protocol and defining the ranges of expected values derived from experienced operators. This approach aimed to reduce variability among operators. The motivation for this topic arose from the high demand for DRI methodology training and ongoing concerns about minimizing operator variability when assessing the extent of deterioration. The cumulative counts presented a range of expected values for the six operators per reactive aggregate type, crack feature, and expansion level, which new operators could use to ensure their results aligned with these ranges. This enabled autonomous training, where new operators were expected to employ the same reactive aggregate and proportion the concrete according to the specifications (CSA A23.2-14A/ASTM C1293[15,16]) while preparing the specimens with their equipment and laboratory to meet the targeted expansion levels. This training protocol was detailed in Chapter 6.

3.4.2. Materials and specimen fabrication

Concrete specimen fabrication, ASR development, monitoring, and surface preparation followed the same procedures outlined in Topic 3. The DRI data from six operators was collected for two aggregate types: reactive coarse Springhill – Greywacke and reactive sand – Jobe Texas (Table 3.5), using the CPT mixture proportions (Table 3.6) at the following levels of expansion: 0.05%, 0.12%, 0.20%, and 0.30%. Data from at least three operators were selected for each expansion level.

Table 3.5. ASR reactive aggregate characterization for operator training.

Aggregate	Location	Rock type	Relative density	Absorption (%)	Reactivity
Fine	Ottawa, Ontario (Canada)	Derived from granite	2.60-2.65	0.82-1.18	Non-reactive
Fine	Bracebridge, Ontario (Canada)	Orthoclase, Quartz, Cristoballite, Albite, Bytowmite, Cordierite, Illite, Muscovite, Larnite	2.73	0.37	Non-reactive
Fine	Ottawa, Ontario (Canada)	Manufactured crushed limestone	2.74	0.65	Non-reactive
Fine	Corpus Christie, Texas (USA)	Polymictic sand (granitic, mixed volcanics, quartzite, chert, quartz)	2.60	0.55-0.89	Reactive
Coarse	Newfoundland (Canada)	High-purity limestone	2.68	0.44	Non-reactive
Coarse	Ottawa, Ontario (Canada)	Limestone	2.78	0.42	Non-reactive
Coarse	Springhill, New Brunswick (Canada)	Greywacke	2.68-2.72	0.602-0.89	Reactive

Table 3.6. Mix-design per operator.

Operator	Cement	Water	Water-to-cement ratio	Non-reactive sand	Reactive coarse aggregate Springhill
			kg per 1 m^3 of concrete		
1	420	189	0.45	823 (Ottawa sand)	934
2		189	0.45	860 (Bracebridge sand)	915
3		187	0.45	829 (Manufactured sand)	999
4		176	0.42	681 (Ottawa sand)	1044
5		189	0.45	836 (Ottawa sand)	938
Operator	**Cement**	**Water**		**Reactive sand Texas**	**Non-reactive coarse aggregate**
			kg per 1 m^3 of concrete		
1	420	189	0.45	760	1024 (limestone)
4		176	0.42	732	1072 (limestone)
5		189	0.45	765	1020 (limestone)
6		177	0.42	678	1093 (High-purity limestone)

3.4.3. Data preparation for ranges of acceptable values

The operator data was then used to establish data ranges (i.e., minimum and maximum), where the frequency in counts per 100 cm² was presented on the y-axis as a function of the crack feature count category referred to as “bins.” These count categories represented the squares displaying the number of cracks (i.e., the number of times 0, 1, 2,…,x cracks were counted in a square as integers) on the x-axis, allowing a histogram to be plotted from the DRI data per distress feature. The features selected for this topic relating to ASR damage were CCA, OCA+OCA_{RP}, and CCP+CCP_{RP}, which best described the distress features encountered for the aggregate types chosen for this topic (Springhill and Texas). This approach was chosen due to its similarity to a well-established standard procedure (CSA A23.1:19 clause 4.2.3.4.2.), ensuring familiarity for easier implementation into engineering practice.

3.5. Topic 4: A practical evaluation of the automated version of the DRI

The fourth and final part of this research involved re-assessing the outputs from the automated version of the DRI, applicable for comparing DRI results. This topic was a collaborative project between the Department of Civil Engineering and the Department of Mathematics at the University of Ottawa, alongside an industry partner, Englobe Corp. Following a feasibility study [17], limitations were identified regarding the automated DRI's applicability [18], particularly concerning the model's reliability in producing accurate DRI results. Consequently, the machine learning (ML) model faced inefficient use of the image dataset, requiring over 10,000 additional annotated images to achieve the targeted accuracy. This issue arose from the incompatibility between the distress feature counter and the distress feature detector. Nevertheless, the DRI effectively supported object segmentation problems, prompting another iteration of the model during this current PhD program. Chapter 8 presented the findings from the first trial using the same images employed in the feasibility study. Chapter 9 reevaluated the model's performance metrics based on the DRI's application to better understand the automated outputs and select additional training datasets more efficiently based on the results. This work highlighted an intriguing challenge encountered in multi-disciplinary projects, which was addressed using suitable model performance evaluation metrics.

3.5.2. Materials and image dataset

The images collected for this topic were gathered from a Springhill reactive coarse aggregate combined with non-reactive sand, using CPT mixture proportions, as noted by "Operator 1" in Tables 3.5 and 3.6. The concrete fabrication, ASR development, and monitoring followed the procedure outlined in Topic 3. The images were captured from previously prepared specimens with a 12-megapixel digital camera attached to a stereomicroscope and annotated with RGB colour codes. A total of 628 images were gathered at expansion levels of 0.05%, 0.12%, 0.20%, and 0.30%, with 141 taken from a 0.30% expansion specimen, annotating 121 distress features, and 50% of these were used for training.

3.5.3. Evaluating the performance of an automated version of the DRI

As part of the collaborative efforts, the ML model was developed by the Mathematics team, while the Civil Engineering team conducted data preparation and analysis. The first ML model adopted in this research program was divided into two parts: a detector of distress features and a classifier and a distress feature counter that utilized a U-Net architecture applied at the pixel level [19]. The second iteration of this project employed a Mask R-CNN (i.e., mask region-based convolutional neural network) to consider the distress features as objects (i.e., instance segmentation) while utilizing publicly available datasets [20–22]. However, the performance metrics used to develop identification and segmentation tasks with ML did not intuitively convey the machine's ability to perform these tasks for a specific application. In this context, the DRI, namely the types and counts of distinct distress features obtained by the operator as the ground truth, was compared to the results from the machine using the Chi-squared goodness of fit test, and the distribution of the counts was presented as histograms to interpret the automated DRI outputs.

$$\chi^2 = \sum_{i=0}^{k} \frac{(o_i - e_i)^2}{e_i} \qquad \text{Eq. 3.10}$$

Where o_i and e_i are the observed and expected counts for the ith count category, and k is the total number of count categories.

3.6. References

[1] V.E. Saouma, ed., Diagnosis & Prognosis of AAR Affected Structures: State-of-the-Art Report of the RILEM Technical Committee 259-ISR, Springer International Publishing, Cham, 2021. https://doi.org/10.1007/978-3-030-44014-5.

[2] V. Villeneuve, Détermination de l'endommagement du béton par méthode pétrographique quantitative, Master's Thesis., Université Laval, 2011.

[3] B. Fournier, P.-L. Fecteau, V. Villeneuve, S. Tremblay, L. Sanchez, Description of petrographic features of damage in concrete used in the determination of the, (2015).

[4] L. Sanchez, B. Fournier, M. Jolin, M.A.B. Bedoya, J. Bastien, J. Duchesne, Use of Damage Rating Index to Quantify Alkali-Silica Reaction Damage in Concrete: Fine versus Coarse Aggregate, ACI Materials Journal 113 (2016). https://doi.org/10.14359/51688983.

[5] L.F.M. Sanchez, B. Fournier, M. Jolin, D. Mitchell, J. Bastien, Overall assessment of Alkali-Aggregate Reaction (AAR) in concretes presenting different strengths and incorporating a wide range of reactive aggregate types and natures, Cement and Concrete Research 93 (2017) 17–31. https://doi.org/10.1016/j.cemconres.2016.12.001.

[6] ASTM C39, Test Method for Compressive Strength of Cylindrical Concrete Specimens, (2003). https://doi.org/10.1520/C0039.

[7] L.F.M. Sanchez, B. Fournier, M. Jolin, J. Bastien, D. Mitchell, Practical use of the Stiffness Damage Test (SDT) for assessing damage in concrete infrastructure affected by alkali-silica reaction, Construction and Building Materials 125 (2016) 1178–1188. https://doi.org/10.1016/j.conbuildmat.2016.08.101.

[8] L.F.M. Sanchez, B. Fournier, M. Jolin, J. Bastien, Evaluation of the Stiffness Damage Test (SDT) as a tool for assessing damage in concrete due to alkali-silica reaction (ASR): Input parameters and variability of the test responses, Construction and Building Materials 77 (2015) 20–32. https://doi.org/10.1016/j.conbuildmat.2014.11.071.

[9] R.-P. Martin, Analyse sur structures modèles des effets mécaniques de la réaction sulfatique interne du béton, PhD Thesis, Université Paris-Est, 2010. https://pastel.archives-ouvertes.fr/tel-00558200v2.

[10] R.-P. Martin, F. Toutlemonde, Theoretical and experimental validation of a simple method to reproduce representative DEF-prone conditions in laboratory, Mater Struct 46 (2013) 1245–1255. https://doi.org/10.1617/s11527-012-9967-2.

[11] B. Kchakech, R.-P. Martin, O. Omikrine-metlassi, J.-C. Renaud, L. Baron, Effect of temperature and curing duration of early heat treatments on the risk of expansion associated with delayed ettringite formation, in: 15th International Conference on Alkali-Aggregate Reaction (ICAAR), Sao Paulo, Brazil, 2016.

[12] R.-P. Martin, L. Sanchez, B. Fournier, F. Toutlemonde, Evaluation of different techniques for the diagnosis & prognosis of Internal Swelling Reaction (ISR) mechanisms in concrete, Construction and Building Materials 156 (2017) 956–964. https://doi.org/10.1016/j.conbuildmat.2017.09.047.

[13] L.F.M. Sanchez, B. Fournier, M. Jolin, J. Duchesne, Reliable quantification of AAR damage through assessment of the Damage Rating Index (DRI), Cement and Concrete Research 67 (2015) 74–92. https://doi.org/10.1016/j.cemconres.2014.08.002.

[14] L.F.M. Sanchez, B. Fournier, M. Jolin, D. Mitchell, J. Bastien, Overall assessment of Alkali-Aggregate Reaction (AAR) in concretes presenting different strengths and incorporating a wide range of reactive aggregate types and natures, Cement and Concrete Research 93 (2017) 17–31. https://doi.org/10.1016/j.cemconres.2016.12.001.

[15] CSA A23.2-14A Potential expansivity of aggregates (procedure for length change due to alkali-aggregate reaction in concrete prisms at 38 °C), (2019).

[16] ASTM C1293-18a, Test Method for Determination of Length Change of Concrete Due to Alkali-Silica Reaction, (2018). https://doi.org/10.1520/C1293-18A.

[17] A. Bezerra, The Use of Artificial Intelligence for Assessing Damage in Concrete Affected by Alkali-Silica Reaction (ASR), Master's Thesis., University of Ottawa, 2020.

[18] A. Bezerra, C. Trottier, L.F.M. Sanchez, B. Fournier, The use of artificial intelligence for assessing an overpass affected by Alkali-Silica Reaction (ASR), in: Bridge Safety, Maintenance, Management, Life-Cycle, Resilience and Sustainability, CRC Press, London, 2022: pp. 354–361. https://doi.org/10.1201/9781003322641-40.

[19] O. Ronneberger, P. Fischer, T. Brox, U-Net: Convolutional Networks for Biomedical Image Segmentation, (2015). https://doi.org/10.48550/ARXIV.1505.04597.

[20] A. Mohan, S. Poobal, Crack detection using image processing: A critical review and analysis, Alexandria Engineering Journal 57 (2018) 787–798. https://doi.org/10.1016/j.aej.2017.01.020.

[21] Y. Wu, A. Kirillov, F. Massa, W.-Y. Lo, R. Girshick, Detectron2, (2019). https://github.com/facebookresearch/detectron2.

[22] Y.-A. Hsieh, Y.J. Tsai, Machine Learning for Crack Detection: Review and Model Performance Comparison, J. Comput. Civ. Eng. 34 (2020) 04020038. https://doi.org/10.1061/(ASCE)CP.1943-5487.0000918.

Chapter 4: Capturing internal swelling reactions (ISR) damage in concrete through the damage rating index (DRI)

Cassandra Trottier[1], Leandro F.M. Sanchez[2], Renaud-Pierre Martin[3], and François Toutlemonde[4]

Abstract

Concrete, which forms the foundation of much of the infrastructure, is essential for ensuring a safe long-lasting, uninterrupted flow of goods and services to the public. However, deterioration in concrete can occur as service lives come to an end; in some cases, previously unknown factors at the time of construction may accelerate this process. These distress mechanisms include alkali-silica reaction (ASR), freezing and thawing (FT), and sulphate attack, with delayed ettringite formation (DEF) comprising the three major internal swelling reactions (ISR) identified to date. The advent of more efficient concrete materials has resulted in a lack of field performance, highlighting the need to identify damage at its initial onset. The damage rating index (DRI) is a microscopy tool currently employed in North America to semi-quantify damage in concrete. When combined with other tools, such as mechanical/durability property loss, the stiffness damage test (SDT), and characterization of the reaction products, the DRI can provide a comprehensive profile of the damage. This work, therefore, offers an overview of the DRI procedure and its adaptability to other distress mechanisms, such as DEF, at a representative scale while emphasizing its accessibility worldwide due to its low cost and energy requirements compared to other tools.

Keywords: *Concrete, Internal Swelling Reactions, Delayed Ettringite Formation, Damage Rating Index, Microscopy, Diagnosis, Durability.*

4.1. Introduction

Concrete has been the most prominent material used to build critical infrastructure, from bridges and transportation systems to hydroelectric dams while continuing to meet modern demands. Yet, past standards and practices and the lack of knowledge/awareness of some currently encountered durability-related issues compromise the serviceability of such concrete infrastructure. Moreover, it is well understood that cement production alone accounts for 8% of global CO_2 emissions [1] The industry's focus has been immediate efforts towards their reduction to meet the targeted imposed sustainability criteria. Meanwhile, the existing concrete infrastructure that continues to serve the public embodies energy, materials, and other resources for which CO_2 has already been emitted, perhaps even in a less efficient manner. Therefore, it is crucial to redirect sustainability goals toward the existing infrastructure's preservation and service life extension. However, internal swelling reactions (ISR) create an additional challenge when evaluating the condition of concrete infrastructure. The most common types of ISR known to date are alkali-silica reaction (ASR), delayed ettringite formation (DEF) and freezing and thawing (FT), all of which have distinct detrimental consequences on the mechanical properties of the concrete, stiffness of the structure (i.e., serviceability and/or structural stability), durability through accelerated ingress of harmful agents, and the overall physical appearance of the concrete causing concerns to the public. Generally, concrete damage caused by ASR originates from aggregate particles. It propagates into the bulk cement paste, whereas damage is generated in the cement paste for concrete affected by DEF (i.e., at the aggregate-paste interface) and FT (i.e., cracks parallel to the exposed concrete surface), as illustrated in Figure 4.1.

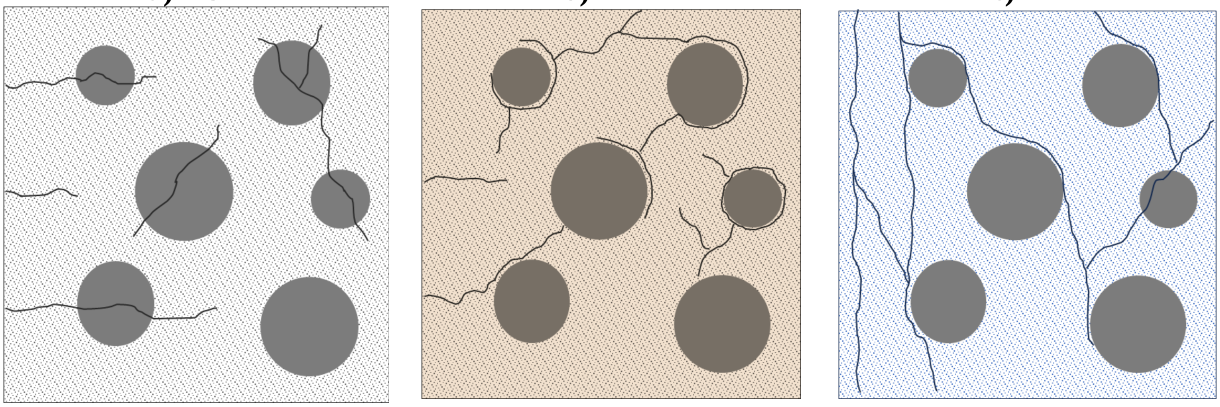

Figure 4.1. Typical damage/crack pattern for a) ASR, b) DEF, and c) FT-affected concrete. The exposed surface is on the left of the images. Adapted from [2].

Therefore, a reliable condition assessment of ISR-affected concrete infrastructure provides insight into the cause and extent of the damage to the owners and operators, hence supporting efficient upcoming decisions (i.e., monitoring, mitigation, rehabilitation, or demolition). Since the appearance of ISR in concrete infrastructure, many researchers and engineers worldwide have gained knowledge to understand their deteriorative process in concrete while developing tools to capture the damage and its further potential. Among those tools are the stiffness damage test (SDT) and the damage rating index (DRI) used in the multi-level approach to evaluate concrete damage caused by ISR at scales representative of the material under investigation. The SDT is a mechanical cyclical tool previously developed for rock cores [3] and further adapted to evaluate concrete affected by ASR [4–10]. The proposed testing procedure applies a maximum load of 40% of the compressive strength (i.e., within the concrete's elastic zone yet able to close cracks and obtain a response from the material itself) from an undamaged (or less damaged) core which produced a measurable degree of damage with the lowest variability thus, diagnostic character [5]. Indices were then attributed [7] to normalize the measured damage which evaluates the energy dissipation (measured by the stiffness damage index – SDI) within the damaged concrete and its plastic deformation (measured by the plastic deformation index – PDI) resulting in a mechanical response capturing the concrete's level of damage which may not be detected early enough using conventional tools or may be significantly compromised at early stages of the damage (i.e., compressive and tensile strengths, modulus of elasticity, etc.) [11–13]. Accordingly, the SDT is more easily adaptable to other types of distress mechanisms in concrete when compared to the DRI since the SDT is somewhat exempt from operator subjectivity. Results have thus shown that SDT outputs are more statistically significant when compared to compressive and tensile strength reductions for various types of ISR, single and combined, in laboratory-made specimens [12–14]. In contrast, the DRI is a microscopic technique used to identify the type(s) of ISR in the affected concrete, which is complemented by its ability to highlight the extent of damage (i.e., the extent of cracking into the aggregates and/or the cement paste). The combination of the DRI and SDT, therefore, allows for a more thorough investigation into the mechanical implications of the ISR-affected concrete by drawing conclusions based on the type, location, pattern, direction, and extent of the damage (i.e., cracks in the aggregate and/or cement paste) generated by distinct distress mechanisms for which the mechanical property losses differ. Nevertheless, the DRI was initially developed to assess concrete affected by alkali-aggregate reaction (AAR) [15] and further adapted to evaluate other types of ISR, such as FT and DEF, acting as a single mechanism or coupled with ASR.

The DRI procedure enables an operator to count distress features within a grid of 1 cm by 1 cm squares on a concrete section (i.e., cylinder, prism, or core sawn in half, ground flat, and polished to obtain a reflective surface) using a stereomicroscope at 15-16x magnification. The sum of the counts per distress feature is weighted using factors associated with the level of damage. Originally, these factors were selected to highlight signs of ASR and its damage; however, [16] have modified those factors to reduce the variability of the operators when distinguishing ASR features. A closed crack in the aggregate is associated with a low weighting factor (0.25) since this feature is not necessarily representative of damage. In contrast, an open crack in the aggregate without and with reaction product (OCA and OCA_{RP}, respectively) indicates the occurrence of damage. Hence, such cracks are given a weighting factor of 2. Although less frequent, disaggregated/corroded particles (DAP) are also weighted with a factor of 2. Cracks in the cement paste without and with reaction product (CCP and CCP_{RP}, respectively, factor of 3) represent more advanced stages of ASR or highlight a different type of deterioration mechanism while also capturing the severity of such cracks toward mechanical property and durability losses. Likewise, debonded aggregates correspond to cracks in the interfacial transition zone between the cement paste and aggregate hence, a weighting factor of 3 is applied to such cracks. Since that modification, it was shown that the DRI (i.e., the sum of all weighted features over 100 cm^2) using these modified factors increased in an almost linear fashion with expansion (a metric to represent a level of damage) and corresponded to mechanical damage, regardless of its source [12]. The DRI's qualitative nature provides the operator with bar charts underlining the types of cracks while allowing the operator to see the damage at the material scale where aggregates, cement paste, and crack extensions are observed as a whole. Yet, the DRI alone cannot identify the cause of all observed cracks without recording the pattern of such damage. Indeed, each ISR has their distinct crack pattern which the operator can record during the analysis. However, cracks in the cement paste may originate from various activities (i.e., mechanical sustained or cyclical loading, shrinkage, creep, etc.); thus, their implication towards the DRI result is more challenging as opposed to open cracks in the aggregate (with or without reaction product) [17–19]. As such, this work proposes a counting procedure for distress features caused by ISR other than ASR, such as DEF, to distinguish its damage through the DRI.

4.2.Materials and methods

The concrete cores used in this study were extracted from previously made unreinforced concrete beams exposed to varying hydraulic conditions, thus inducing various levels of deterioration throughout the depth of the beams. Five of the extracted cores were taken from DEF-affected concrete beams at various degrees of damage. In contrast, one core was taken from an ASR-affected concrete that had achieved its full damage potential to directly compare the cracking behaviour of DEF with that of ASR through the DRI. Further details about the materials, curing and expansion can be found in [20]). The level of DEF is represented by labels 1 through 5, in increasing magnitude of damage where 1 represents low damage (i.e., 0.08 m from the top of the beam) and 5 represents high damage (i.e., 0.44 m from the top of the beam) as per the hydraulic conditions [20]. The top of the beam was exposed to a relative humidity of 30% while the bottom was saturated, thus inducing a damage gradient across its depth.

The cores were cut in half longitudinally using a wet masonry saw with a diamond blade. One half of the core was then used for the analysis and ground/polished using a series of diamond-impregnated magnetic disks with grits of 30, 60, 140, 280 (80-100 microns), 600 (20-40 microns), 1200 (10-20 microns) and 3000 (4-8 microns) on a mechanically rotating polishing table to ensure a flat and reflective surface. A controlled and constant water supply was used to ensure optimal use of the diamond-impregnated disks while avoiding excess water that can remove reaction products from the cracks and voids. The surfaces were cleaned and dried with compressed air to remove any loose particles, yet care was taken for the DEF cores as aggregates easily dislodged from the surface. A grid of 1 cm by 1 cm was then placed on the surface, each square representing the field of view at 15-16x magnification (depending on the microscope model) through a stereomicroscope. Oblique gooseneck lights were used to illuminate the surface and reduce artifacts such as shadows while using the maximum brightness to ensure no variability of the light source between analyses. To conduct the DRI analysis, each square is observed, and the distinct types of cracks are recorded after which the corresponding weighting factors as per [16] are applied. The total counts are summed and normalized to 100 cm^2 as per Equation 4.1. Common practice to perform the DRI specifies that the operator's variability is to be calibrated within 10% of the DRI result of an experienced operator prior to performing the analysis.

$$DRI = \left[\frac{\sum(0.25(CCA) + 2(OCA + OCA_{RP} + DAP) + 3(CCP + CCP_{RP} + Debon))}{Number\ of\ analyzed\ 1\ cm\ by\ 1\ cm\ squares}\right] \times 100\ cm^2 \qquad \text{Eq. 4.1}$$

Where CCA is the total number of closed cracks in the aggregate, $OCA\ and\ OCA_{RP}$ are the total numbers of open cracks in the aggregate without and with reaction product, respectively, DAP is the total number of disaggregated/corroded particles, $CCP\ and\ CCP_{RP}$ are the total numbers of cracks in the cement paste without and with reaction product, respectively, and $Debon$ is the total number of debonded aggregates.

4.3. Results and discussion

The DRI is semi-quantitative yet is qualitative by nature therefore, the counting procedure can significantly affect the outcome of the result. As such, the crack counting procedure was divided into two methods: method 1 (M1) was conducted by considering the entire length of a crack in the cement paste (Figure 4.2a) and following the procedure proposed by [21] while method 2 (M2) distinguished/divided a crack in the cement paste adjacent to an aggregate particle thus, propagating from/through the interfacial transition zone (Figure 4.2b). This distinction however was only made when the crack in the interface surrounded a particle at 75% of its perimeter or more, regardless of its size (i.e., coarse and fine aggregate) and location within the 1 cm by 1 cm square. This modification was made to account for cracks propagating through the interface as opposed to a crack being obstructed by a particle while propagating which may be the case when considering only 50% of the aggregate perimeter as proposed by [21]. A fork in a crack represents a new branch through method 1 whereas through method 2, if 75% of the interface is accompanied by a crack, it is counted as a Debon type crack. Method 2 therefore requires consideration of adjacent squares to determine if a crack is of the Debon type when the particle is larger than the field of view of 1 cm by 1 cm.

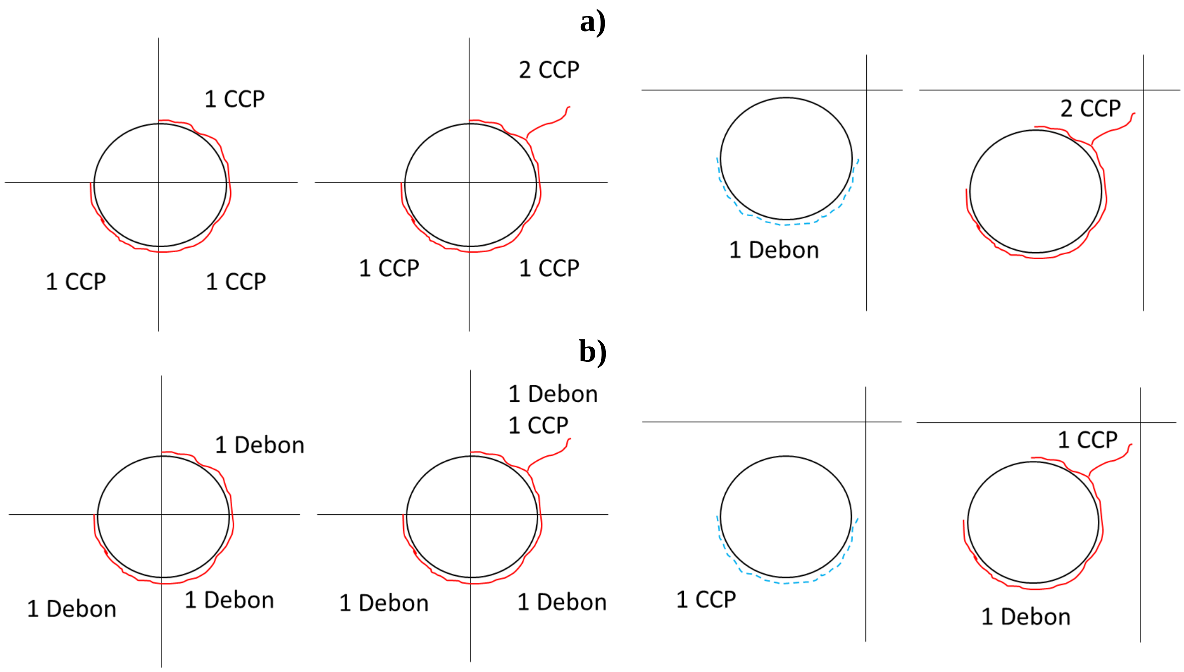

Figure 4.2. Crack counting details using a) method 1 and b) method 2. The solid red line represents a crack that surrounds an aggregate at 75% while the dashed blue line represents a crack that surrounds 50% of the particle.

Figure 4.3 thus presents the DRI bar charts for the ASR core that has achieved its full damage potential and all 5 DEF cores. It is to be noted that for the ASR core, method 1 counting procedure was followed since this type of damage mechanism rarely produces cracks that initiate and propagate through the interface although cracks may indeed propagate through the interface after extending from an aggregate particle. Therefore, the bar chart for the ASR core (at the bottom of Figure 4.3) shows a more abundant number of cracks within the aggregate without and with reaction product (OCA and OCA_{RP}, respectively) extending into the cement paste and a final DRI number of 874 which is in accordance with [11, 22]). On the other hand, all DEF cores exhibit negligible damage to the aggregate (i.e., closed cracks in the aggregate – CCA, open cracks in the aggregate without and with reaction product – OCA and OCA_{RP}, respectively) which is likely caused by aggregate weathering and processing. Yet, a slight increase in such cracks is observed at the most DEF damaged core which could be attributed to the internal pressure exerted onto the aggregate thus, further investigations are required. Noticeably, the open cracks in the aggregate (OCA) for DEF cores are empty whereas for the ASR affected concrete core, 30% of these cracks contain reaction product. Meanwhile, for the low damage DEF affected concrete core (i.e., DEF 1), both counting methods present similar results due to the extension of the cracks being within the interface at less than 75% of the perimeter thus, counted as cracks in the cement paste without and with reaction product (i.e., CCP and CCP_{RP}, respectively). The final DRI numbers for DEF damage level of 2 and 3 are similar, regardless of the counting method (824 and 801 for method 1 and 964 and 907 for method 2, respectively) both being within a 10% range. Likewise, the first counting method provided similar results (DRI of 853) for the DEF damage level 4 while for the second counting method, a significant difference is observed in the DRI number (1491). Hence, both the magnitude of the DRI number and the counting procedure through counting method 2 highlight the extensive damage caused by DEF. Nevertheless, when the extent of damage is less severe (and representative of damage in a real structure in service), counting method 2 can highlight damage caused by DEF through the counts of debonded aggregates (Debon), a common feature for DEF damaged concrete, which cannot be captured through the DRI number alone.

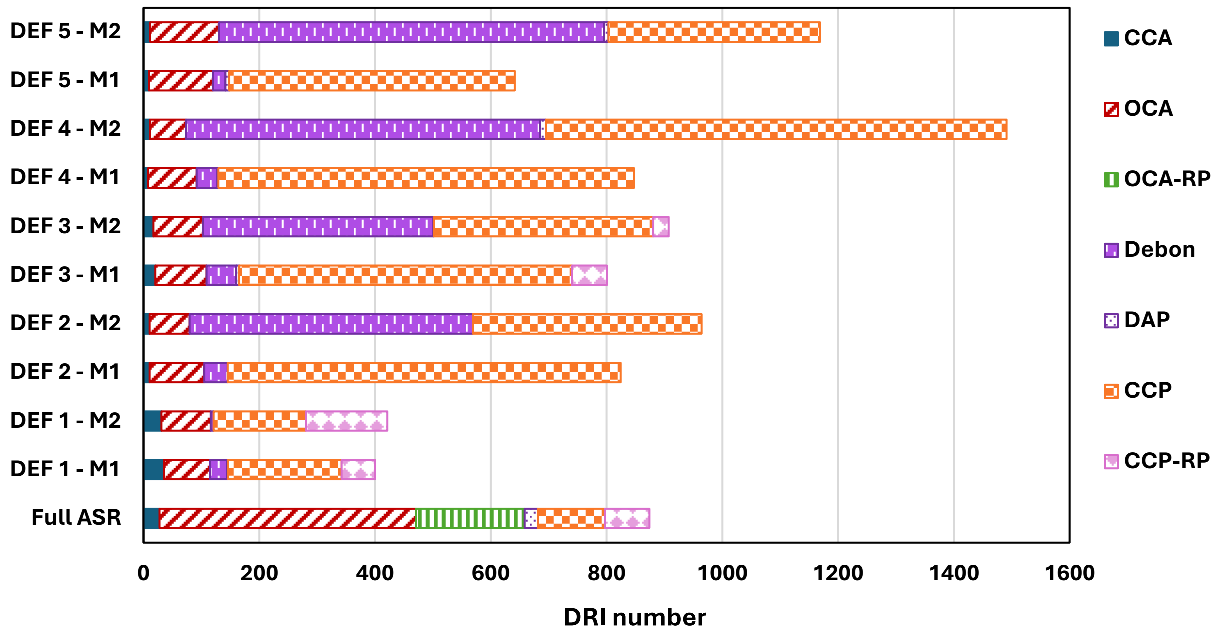

Figure 4.3. DRI numbers for a fully developed ASR affected concrete and various levels of damage to concrete due to DEF as captured through different counting methods.

As is the case for any other available tool, limitations of their use must be established to avoid high levels of uncertainty when interpreting results. In Figure 4.3, the most damaged concrete affected by DEF (i.e., DEF 5) does not represent the highest DRI number. This was due to the deterioration in the cement paste, which caused the absence of material in which cracks could be counted. However, this is a petrographic feature that can be obtained through the DRI procedure, and although the extent of the damage cannot be measured in such an extreme case, an insight into the cause of damage can still be recorded. Meanwhile, a DRI number and bar chart were still obtained using both methods, yet method 2 captured the debonded aggregates (Debon). It is to be noted that the proposed crack counting method may not necessarily affect the final DRI number. However, the significant distinction remains in the counted features most representative of DEF damage, such as the Debon-type cracks.

Figure 4.4 illustrates the unweighted distress features as counts per 100 cm^2 to show their distribution along with their proportions in percentages (i.e., extended version as per [22, 23]). A 10% error bar was applied to each feature, representing acceptable operator variability and helping to determine if a given result is significantly different from another while considering the operator's variability when conducting the test (i.e., the error bars must not overlap to consider results as possibly different). The lowest DEF damage shows no significant difference between the two counting methods; however, more Debon-type cracks were counted through method 1 (M1) due to the 50% criteria, which was increased to 75% for method 2 (M2). On the other hand, the difference is more apparent for all other levels of damage through the counts of cracks in the cement paste ($CCP+CCP_{RP}$) when compared to the lowest damaged concrete. Yet, it is still considered similar except for the most damaged DEF concrete. The difference between DEF 2 and DEF 3 using both counting methods is still insignificant. Nonetheless, method 2 shows the increase in damage through both cracks in the cement paste ($CCP+CCP_{RP}$) and debonded aggregates (Debon) for the DEF 4 core (i.e., higher level of damage). Interestingly, the difference between Debon is negligible between DEF 4 and DEF 5 through counting method 2 as no further Debon can be counted beyond the DEF 4 damage level, which indicates that the damage development due to DEF in the interface reaches its maximum.

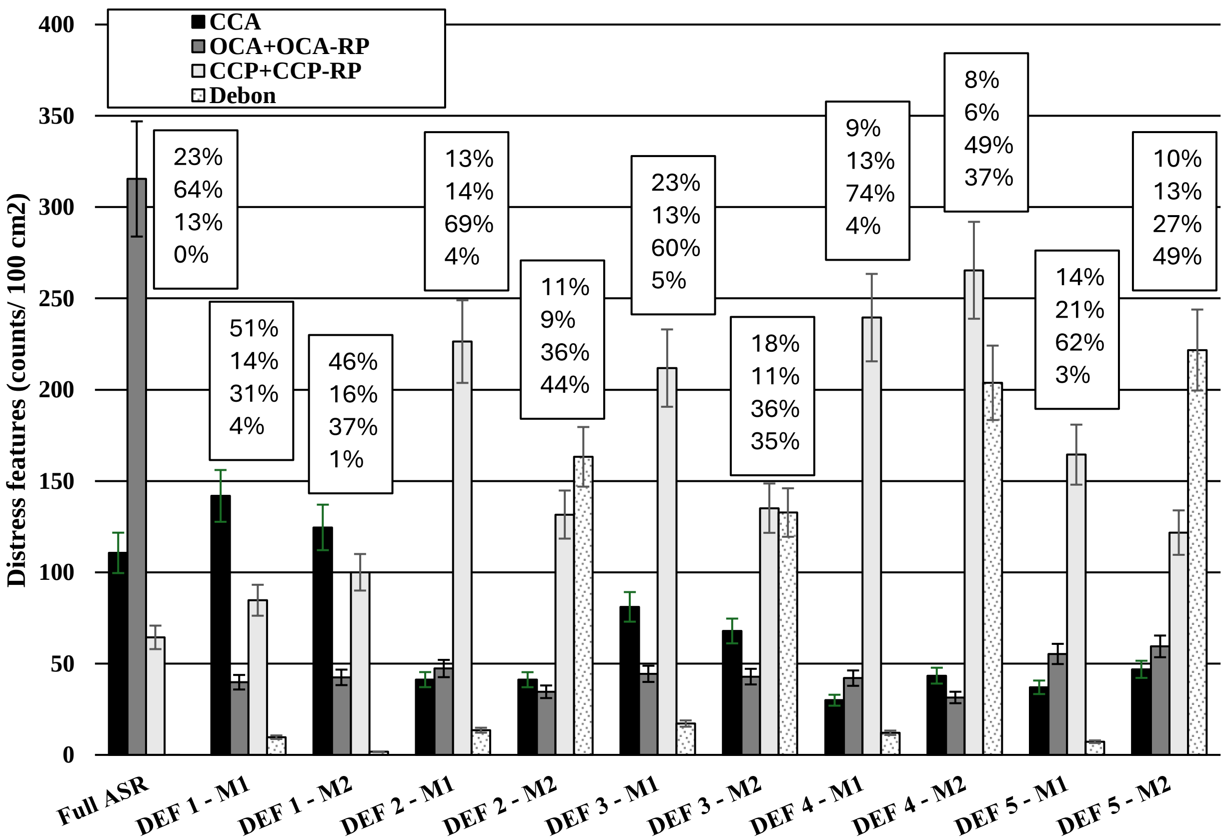

Figure 4.4. Unweighted counts of distress features per 100 cm^2 and their corresponding proportions (%).

According to the DRI procedure available at Université Laval in Québec (Canada) [21], ASR-generated cracks surrounding 50% of the aggregate particle can be considered a Debon crack type. However, the damage pattern for DEF-affected concrete generally produces cracks in the interfacial transition zone [18, 24], and therefore, this study adapted the Debon-type crack to represent a crack that surrounds 75% of any aggregate particle. This adaptation was made to ensure that a crack is not only propagating through the interface, which could be when half of the particle's interface is cracked but favouring its propagation into the interface instead of following a set path obstructed by an aggregate particle. Figure 4.5 demonstrates a portion of the DEF 2 core. All coarse aggregate particles are surrounded by a crack, resulting in debonding cracks (Debon), which are fairly evident in the figure. Some cracks in the cement paste (CCP) are indicated with purple arrows to show the extent of cracking and the pattern at a scale representative of the concrete material and its corresponding damage. Other cracks in the cement paste are more easily distinguished at 16x magnification. Moreover, the blurred spots outlined in red on the figure indicate dislodged particles, counted as debonded aggregates (Debon) as their contribution towards the final DRI number cannot be neglected. The distinction between a void and a dislodged aggregate is reasonably apparent. Debonded aggregates significantly impact the mechanical properties of the concrete such that the stress transfers from the paste to the aggregate become compromised, thus reducing the modulus of elasticity and significantly affecting the compressive strength of the concrete. Therefore, no modifications to the DRI weighting factor applied to Debon are required (i.e., 3) as they represent the severity of DEF damage in terms of mechanical property losses.

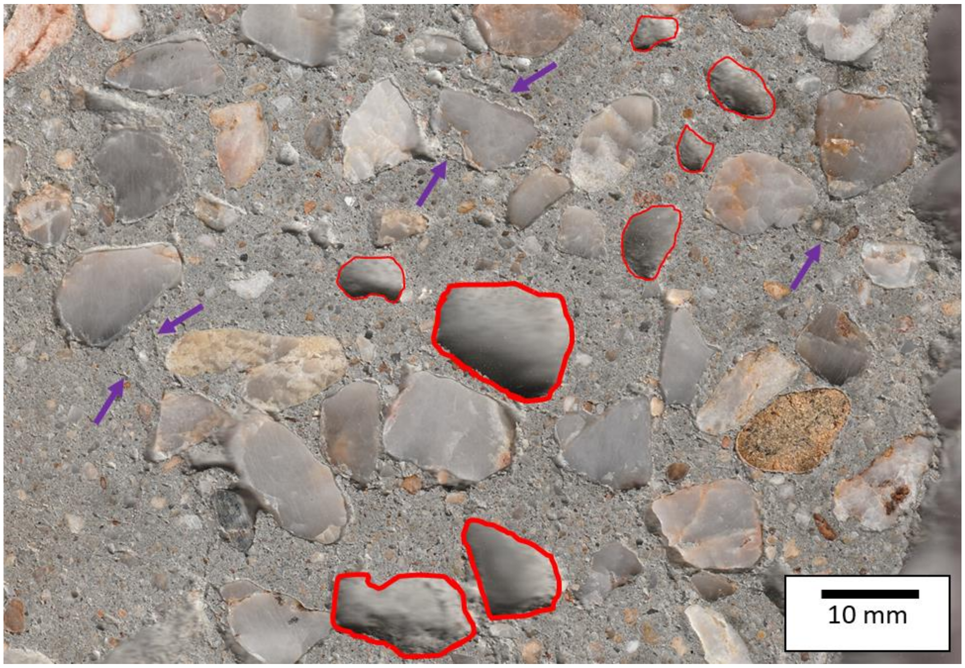

Figure 4.5. Micrograph of DEF affected concrete with all aggregates illustrating debonded aggregate type cracks, the connection between aggregates through the cement paste indicated by the purple arrows and dislodged aggregates outlines in red.

4.4. Conclusions

The DRI remains a tool with a diagnostic character due to its qualitative visual nature, yet further studies are in progress to determine the relationship between the proposed approach to distinguish DEF distress features and the corresponding losses in mechanical properties of the concrete. Some concluding remarks are presented hereafter:

- The proposed counting procedure (method 2) can distinguish cracks caused by DEF without modifying the weighting factors for debonded aggregate-type cracks. The distinction is evident through the bar chart obtained when performing the DRI, which provides necessary information about the cause of the damage. Further confirmation, however, is necessary through characterization of the reaction products within the damage features.
- The new counting procedure proposes to count a crack as a debonded aggregate when it affects 75% of its perimeter instead of 50% due to the DEF crack propagation being in the interface and bulk cement paste. This slight modification allows the operator to highlight DEF as a potential cause of damage instead of an aggregate obstructing the path of a propagating crack. Moreover, a crack is counted as Debon regardless of its position within the grid therefore, the operator is to take note of cracks and particles in the adjacent fields of view.
- In extreme cases where the extent of damage reaches material removal, such as when there are many cracks in the cement paste, which limit the counts of such cracks, the operator can note such petrographic/damage features. On the other hand, when aggregates are dislodged when cutting, grinding and polishing, they should be considered in the counts of Debon as the difference between a dislodged aggregate and a void is evident. Omitting

such feature could drastically reduce the DRI number and under-estimate the level of damage.

- The distinction between other mechanisms causing heterogeneous damage such as freezing and thawing damage can further be made using the DRI tool (not just the number!) through heatmaps in which the severity of cement paste cracks (most representative feature) would be more abundant at the surface of a concrete element (beginning of a core). This further highlights the DRI tool's characteristics as an engineering and petrographic tool.

Although a major drawback of the DRI remains its time-consuming character, such practical and accessible tool is capable of highlighting both potential cause and extent of damage. This tool can serve as a first step towards a more efficient use of resources towards complete diagnosis (i.e., multi-level assessment). Nevertheless, the energy/infrastructure needed to operate such tool is minimal which enhances its accessibility worldwide. This is especially imperative when using new sustainable concrete materials for which their long-term performance on the field remains unknown thus, reliable, verified and adaptable tools are necessary to capture early signs of damage and preserve existing and new concrete infrastructure.

4.5.References

[1] Lehne, Johanna, and Felix Preston. 2018. Making Concrete Change: Innovation in Low-carbon Cement and Concrete. London, UK: Chatham House.

[2] British Cement Association (BCA). 1992. The diagnosis of alkali-silica reaction. Report of a Working Party. Waxham Springs: British Cement Association.

[3] Walsh, J. B. 1965. The effect of cracks on the uniaxial elastic compression of rocks. Journal of Geophysical Research 70: 399–411. https://doi.org/10.1029/JZ070i002p00399.

[4] T.M. Chrisp, P. Waldron, J.G.M. Wood. 1993. Development of a non-destructive test to quantify damage in deteriorated concrete. Magazine of Concrete Research 45: 247–256. https://doi.org/10.1680/macr.1993.45.165.247.

[5] L.F.M. Sanchez, B. Fournier, M. Jolin, J. Bastien. 2014. Evaluation of the stiffness damage test (SDT) as a tool for assessing damage in concrete due to ASR Test loading and output responses for concretes incorporating fine or coarse reactive aggregates. Cement and Concrete Research 56: 213–229.

[6] L.F.M. Sanchez, B. Fournier, M. Jolin, J. Bastien. 2015. Evaluation of the Stiffness Damage Test (SDT) as a tool for assessing damage in concrete due to alkali-silica reaction (ASR): Input parameters and variability of the test responses. Construction and Building Materials 77: 20–32. https://doi.org/10.1016/j.conbuildmat.2014.11.071.

[7] L.F.M. Sanchez, B. Fournier, M. Jolin, J. Bastien, D. Mitchell. 2016. Practical use of the Stiffness Damage Test (SDT) for assessing damage in concrete infrastructure affected by alkali-silica reaction. Construction and Building Materials 125: 1178–1188. https://doi.org/10.1016/j.conbuildmat.2016.08.101.

[8] N. Smaoui, B. Bissonnette, M.-A Bérubé, B. Fournier, B. Durand. 2006. Mechanical Properties of ASR-Affected Concrete Containing Fine or Coarse Reactive Aggregates. Journal of ASTM International 3. https://doi.org/10.1520/JAI12010.

[9] N. Smaoui, B. Fournier, M.-A Bérubé, B. Bissonnette, B. Durand. 2004. Evaluation of the expansion attained to date by concrete affected by alkali-silica reaction. Part I. Experimental study. Canadian Journal of Civil Engineering. Canadian Business & Current Affaires Database.

[10] N. Smaoui, B. Fournier, M.-A Bérubé, B. Bissonnette, B. Durand. 2004. Evaluation of the expansion attained to date by concrete affected by alkali-silica reaction. Part II. Application to nonreinforced concrete specimens exposed outside. Canadian Journal of Civil Engineering. Canadian Business & Current Affaires Database.

[11] Sanchez, L.F.M., B. Fournier, M. Jolin, D. Mitchell, J. Bastien. 2017. Overall assessment of Alkali-Aggregate Reaction (AAR) in concretes presenting different strengths and incorporating a wide range of reactive aggregate types and natures. Cement and Concrete Research 93: 17–31. https://doi.org/10.1016/j.cemconres.2016.12.001.

[12] Sanchez, L.F.M., T. Drimalas, B. Fournier, D. Mitchell, J. Bastien. 2018. Comprehensive damage assessment in concrete affected by different internal swelling reaction (ISR) mechanisms. Cement and Concrete Research 107: 284–303. https://doi.org/10.1016/j.cemconres.2018.02.017.

[13] R.-P. Martin, L.F.M. Sanchez, B.t Fournier, F. Toutlemonde. 2017. Evaluation of different techniques for the diagnosis & prognosis of Internal Swelling Reaction (ISR) mechanisms in concrete. Construction and Building Materials 156: 956–964. https://doi.org/10.1016/j.conbuildmat.2017.09.047.

[14] E.R. Giannini, L.F.M. Sanchez, A. Tuinukuafe, K.J. Folliard. 2018. Characterization of concrete affected by delayed ettringite formation using the stiffness damage test. Construction and Building Materials 162: 253–264. https://doi.org/10.1016/j.conbuildmat.2017.12.012.

[15] Grattan-Bellew, P E. 1995. Laboratory Evaluation of Alkali-Silica Reaction in Concrete from Saunders Generating Station. ACI Materials Journal 92. https://doi.org/10.14359/9763.

[16] V. Villeneuve. 2011. Détermination de l'endommagement du béton par méthode pétrographique quantitative. M.Sc., Québec, QC: Université Laval.

[17] L.J. Monette, N.J. Gardner, P.E. Grattan-Bellew. 2002. Residual Strength of Reinforced Concrete Beams Damaged by Alkali-Silica Reaction—Examination of Damage Rating Index Method. ACI Materials Journal 99. https://doi.org/10.14359/11315.

[18] P.E. Grattan-Bellew. 2012. Petrographic methods foe distinguishing between alkali- silica, alkali-carbonate reactions and other mechanisms of concrete deterioration. In Proceedings of the 14th International Conference on Alkali-Aggregate Reaction in Concrete. Austin, Texas, USA.

[19] P.A. Dunbar, P.E. Grattan-Bellew. Results of damage rating evaluation of condition of concrete from a number of structures affected by AAR.

[20] R.P. Martin. 2010. Analyse sur structures modèles des effets mécaniques de la réaction sulfatique interne du béton. PhD Thesis, Paris, France: Université Paris-Est.

[21] B. Fournier, P.-L. Fecteau, V. Villeneuve, S. Tremblay, L.F.M. Sanchez. 2015. Description of petrographic features of damage in concrete used in the determination of the. Université Laval.

[22] L.F.M. Sanchez, B. Fournier, M. Jolin, and J. Duchesne. 2015. Reliable quantification of AAR damage through assessment of the Damage Rating Index (DRI). Cement and Concrete Research 67: 74–92. https://doi.org/10.1016/j.cemconres.2014.08.002.

[23] L.F.M. Sanchez, B. Fournier, M. Jolin, M.A.B. Bedoya, J. Bastien, J. Duchesne. 2016. Use of Damage Rating Index to Quantify Alkali-Silica Reaction Damage in Concrete: Fine versus Coarse Aggregate. ACI Materials Journal 113. https://doi.org/10.14359/51688983.

[24] M.D.A. Thomas, K. Folliard, T. Drimalas, T. Ramlochan. 2008. Diagnosing delayed ettringite formation in concrete structures. Cement and Concrete Research 38: 841–847. https://doi.org/10.1016/j.cemconres.2008.01.003.

Chapter 5: Evaluation of damage due to delayed ettringite formation (DEF) through the multi-level assessment

Cassandra Trottier[1], Leandro F.M. Sanchez[1], Renaud-Pierre Martin[2], François Toutlemonde[2]

Abstract

Delayed ettringite formation (DEF) is among the internal swelling reactions (ISR) that have a detrimental effect on concrete, thus compromising the material's strength, stiffness, and integrity. Previous research shows that the multi-level assessment applied to concrete affected by ISR is a reliable approach to evaluating the cause and extent of the damage. However, the stiffness damage test (SDT) has been more readily accepted for engineering applications, while further understanding of the application of the damage rating index (DRI) is necessary. This work, therefore, presents a condition assessment of a DEF-affected unreinforced concrete beam subjected to a moisture gradient to induce varying degrees of damage across the beam height by adapting the multi-level assessment. Correlations between the DEF damage features, as depicted through the DRI and outputs from the SDT, were found, highlighting the impact of the frequency of feature observation at a scale representative of the measured damage to the material.

Keywords: *delayed ettringite formation, multi-level assessment, stiffness damage test, damage rating index, point count, stereomicroscopy.*

5.1. Introduction

Delayed ettringite formation (DEF) damage has devastating effects on the functionality of concrete infrastructure due to large deformations and reductions in the concrete mechanical performance and durability due to excessive cracking. Diagnosis of damage to concrete due to DEF has been established through optical microscopy and SEM-EDS/EDX in which ettringite crystals are characterized in the aggregate-paste interface and cracks throughout the bulk of the cement paste [1] yet their presence may not necessarily indicate damage due to DEF. This damage can then be measured through mechanical testing, such as modulus of elasticity loss and reduction in compressive strength, which are mechanical properties used for structural design. However, the measurement of these properties may not directly quantify damage. As such, the multi-level assessment was developed due to its diagnostic character when measuring damage to a material [2–4]. Of the tools used in the multi-level assessment, the stiffness damage test (SDT), a mechanical tool, has been more readily adopted and accepted in the engineering context [5–7] whereas the damage rating index (DRI), a point-count microscopy tool initially developed to evaluate relative degrees of damage in a dam affected by alkali-aggregate reaction (AAR), has remained a tool in which the fundamental concept has not been established. Nevertheless, the use of the multi-level assessment to evaluate damage due to DEF is limited [2,4,6,8–10]. This work aims to evaluate the potential of the DRI to highlight damage cause (i.e. DEF) and extent as a point-count microscopy tool adapted for an engineering approach. Cores presenting various levels of damage were cored from an unreinforced laboratory-made concrete beam [11]. The beam was subjected to conditions enabling DEF damage. The multi-level assessment was conducted with particular attention to the damage features observed through stereomicroscopy.

5.2. Materials and methods

5.2.2. Concrete cores extracted from the unreinforced beam

The beam was made using a cement selected to increase the likelihood of developing DEF such that the content of C3A, alkalis, and sulphates were higher than a companion cement, as described in [11] and alkali boosted with KOH to achieve ~1% Na_2O_{eq}. by cement mass combined with non-reactive aggregates (Table 5.1). The targeted compressive strength of the concrete was 40 MPa, which was achieved by using a w/c of 0.46 and a slump of 10 ±2 cm.

Table 5.1. Mixture proportions.

Cement	Total water	w/c	Coarse gravel (4-12 mm)	Sand (<2 mm)
410 kg/m^3	199 kg/m^3	0.46	929 kg/m^3	854 kg/m^3

To induce DEF, the beams were exposed to an increasing temperature water bath 2 hours after the start of batching and for 24 hours, at a maximum rate of 10 °C/h, until a temperature of 81°C was reached, which remained constant for the following 72 hours. The cooling period was set at -1°C/h until a temperature of 25°C was reached, for a duration of 55 hours [12]. The beam was then stored in conditions to enable damage due to DEF where the bottom portion (70 mm) was submerged in water and the top portion left to dry at 30% Relative Humidity (RH), thus creating a hydraulic gradient across the height of the beam and causing bending in the longitudinal direction of the beam and various degrees of damage throughout. Aluminum adhesive layers were used on the side faces to ensure a unidirectional gradient. Cores were extracted from a laboratory-made unreinforced beam at various depths (i.e., 0.08, 0.17, 0.27, 0.37, and 0.44 m) in the transverse direction, similar to the procedure presented in [4]. Further details on the methodology to induce DEF damage and effective thermal energy can be found in [11–13].

5.2.3. *The stiffness damage test (SDT)*

The stiffness damage test (SDT) was performed on cores of 110 mm in diameter and about 250 mm in height, which were ground flat before testing. Using a universal testing machine, the cores were cyclically compressed, where 30% of f'_c was used as the maximum test load and a loading rate of 0.10 MPa/s [7,8]. The output parameters used in this study are presented in Eq. 5.1 through 5.3, where the variables are presented in Figure 5.1. It is to be noted that due to the extensive damage to cores taken at 0.37 and 0.44 m depths, failure of some specimens occurred before completing the 5 cycles therefore, only the first cycle was used to calculate the SDI, as expressed in Eq. 5.2 and explained in [4].

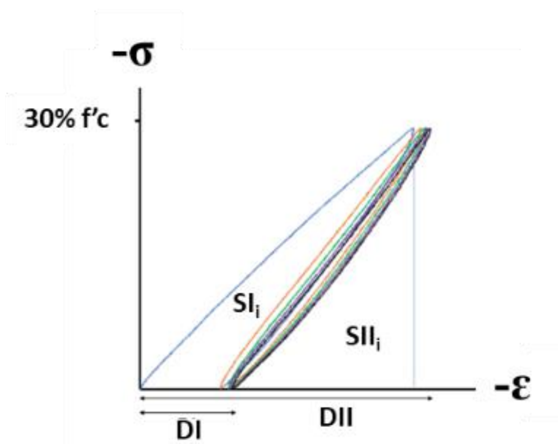

$$SDI = \frac{\sum_{i=1}^{5} SI_i}{\sum_{i=1}^{5}(SI_i + SII_i)} \quad \text{Eq. 5.1}$$

$$SDI = \frac{SI_1}{SI_1 + SII_1} \quad \text{Eq. 5.2}$$

$$E = ave.slope\ of\ cycles\ 2\ \&\ 3 \quad \text{Eq. 5.3}$$

Figure 5.1. Stress-strain curve with SDT outputs graphically represented.

5.2.4. *The damage rating index (DRI)*

The core samples used for the DRI analysis were cut in half longitudinally using a wet masonry saw and diamond blade. The flat surfaces were ground and polished using a mechanically rotating table with epoxy-impregnated diamond magnetic disks (grits of 30, 60, 140, 280 (80–100 μm), 600 (20–40 μm), 1200 (10–20 μm) and 3000 (4–8 μm)). A grid of 1 cm^2 squares was placed on the reflective surface for reference. The damage features (closed cracks in the aggregate – CCA, open cracks in the aggregate without and with reaction product – OCA and OCA_{RP} respectively, disaggregated particles – DAP, cracks in the cement paste without and with reaction product – CCP and CCP_{RP} respectively, and debonded/dislodged aggregates – Debon) were counted using a stereomicroscope at 16x magnification (Figure 5.2a) and tabulated in each 1 cm^2 (field of view) as described by [10]. The counts were weighted using the optimized weighing factors which best describe damage to concrete [8,10], and the DRI was calculated as defined in Eq. 5.4.

$$DRI = \left[\frac{\sum(0.25(CCA) + 2(OCA + OCA_{RP} + DAP) + 3(CCP + CCP_{RP} + Debond))}{n}\right] \times 100\ cm^2 \qquad \text{Eq. 5.4}$$

Moreover, a proposed counting method (M2) compared to the original (M1) adopted in this study was selected to highlight DEF damage. The proposed counting method [14] takes into account the Debon-type aggregate, regardless of where it is situated on the reference grid (Figure 5.2b).

a) **b)**

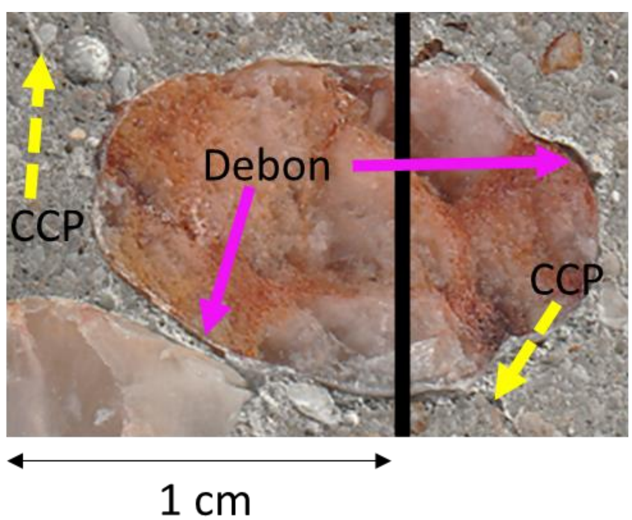

Figure 5.2. a) Stereomicroscope and specimen/core set-up and b) illustration of crack counting method on 1 cm^2 micrograph taken from a core under analysis in this current work. The black solid line represents a grid line to demonstrate the crack counting method considering adjacent squares for the particle's Debon-type crack.

5.3.Results

The outputs used from the multi-level assessment are the SDI, modulus of elasticity (E) and the DRI, along with the measured/known expansion level (the method to evaluate the expansion to date is presented in [4]). Figure 5.3a and Figure 5.3b illustrate the expansion as a function of SDI and E with a good linear correlation (R^2 of 0.938 and 0.983, respectively). The expansion as a function of the DRI (Figure 5.3c), as per both counting methods (original – M1 and proposed – M2 described in [14]) demonstrates a better correlation for the newly proposed counting method (R^2 of 0.783 for M2) in comparison to the original counting method (R^2 of 0.454 for M1). Likewise, the correlation of the DRI as a function of the mechanical response increases for the proposed counting method, where the modulus of elasticity presents an R^2 of 0.383 and 0.7021 (Figure 5.3d). At the same time, the SDI R^2 is 0.236 and 0.669 (Figure 5.3e) for counting methods M1 and M2, respectively.

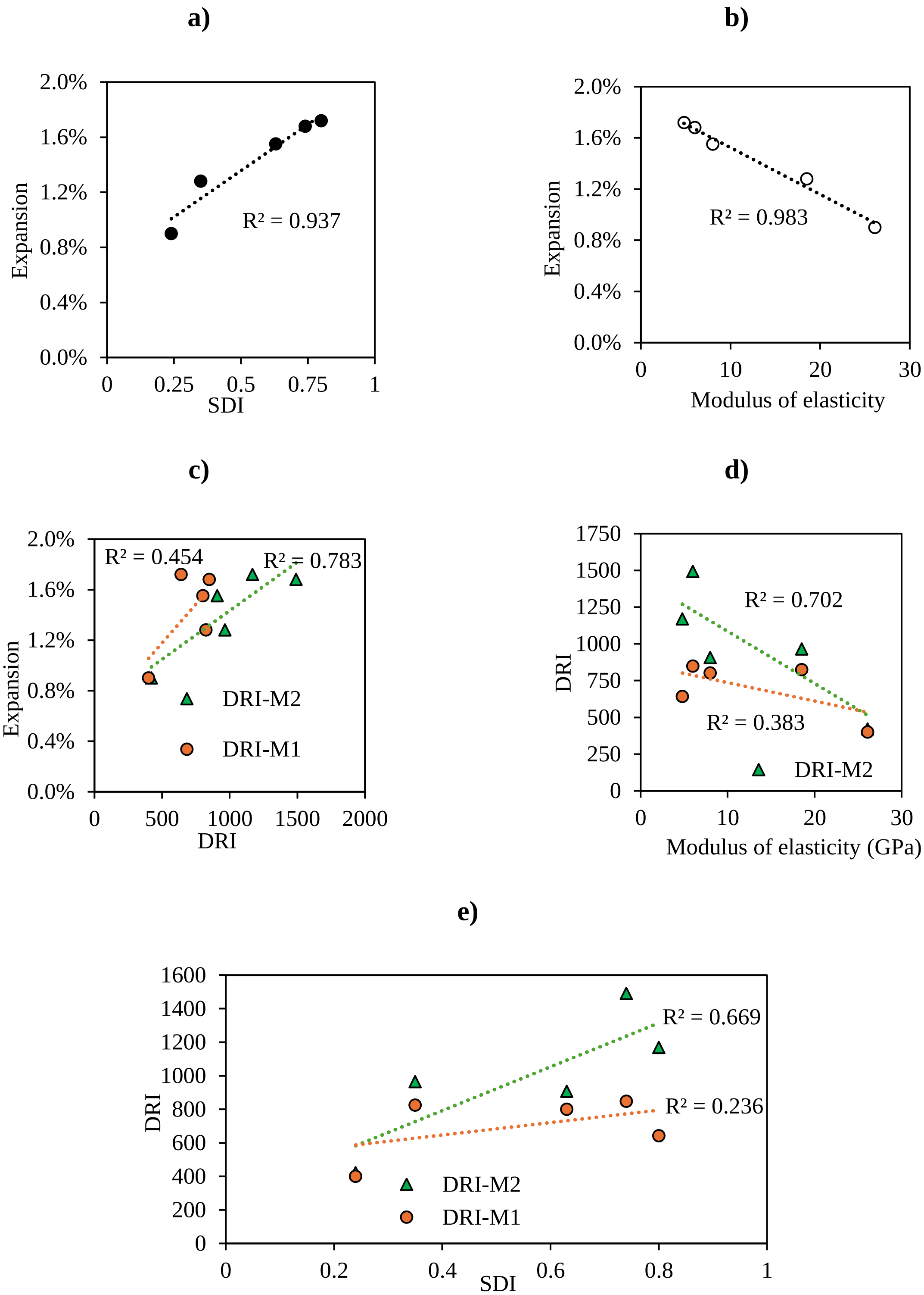

Figure 5.3. DEF expansion as a function of a) SDI, b) modulus of elasticity, c) the DRI as a function of (d) modulus of elasticity and e) SDI. The DRI plots also show both counting methods adopted in this study.

5.4. Discussion

5.4.1. Quantitative analysis through microscopy

The quantitative nature of the DRI and its data collection method have been evaluated as a tool used to diagnose damage since its development due to its qualitative and visual nature. However, cracks are distress features observed through stereomicroscopy, thus revealing their influence at the mesoscale, a scale representative of mechanical damage. This study aimed to perceive the DRI method as a tool to gather data on the occurrence (cause) and frequency (extent) of an observed damage. Features were segmented as counts per 100 cm^2 (extended version of the DRI) and described in Eq. 5.5 [10,15].

$$Absolute\ \left(\frac{Counts}{100cm^2}\right) \rightarrow C_i = \frac{counts_i}{number\ of\ squares\ analyzed} \times 100cm^2 \qquad \text{Eq. 5.5}$$

The contribution of each damage feature with respect to expansion due to DEF as captured by both the original (M1) and proposed (M2) counting methods is presented in Figures 5.4a and b, respectively. The most characteristic features of damage to concrete due to DEF are cracks in the aggregate-paste interface and cracks in the cement paste radiating from particles. To capture such damage, the Debon-type feature per the DRI was re-evaluated to consider its contribution while analyzing the counts. From Figure 5.4a representing the features as counted through the original method (M1), it can be observed that the Debon-type feature occurs but at a low frequency (below 28 counts/100 cm^2*)*, while the damage is best described by cracks in the cement paste (CCP). On the other hand, as observed in Figure 5.4b, the newly proposed methods (M2) show that the counts of Debon-type cracks increase with expansion, as do the cracks in the cement paste.

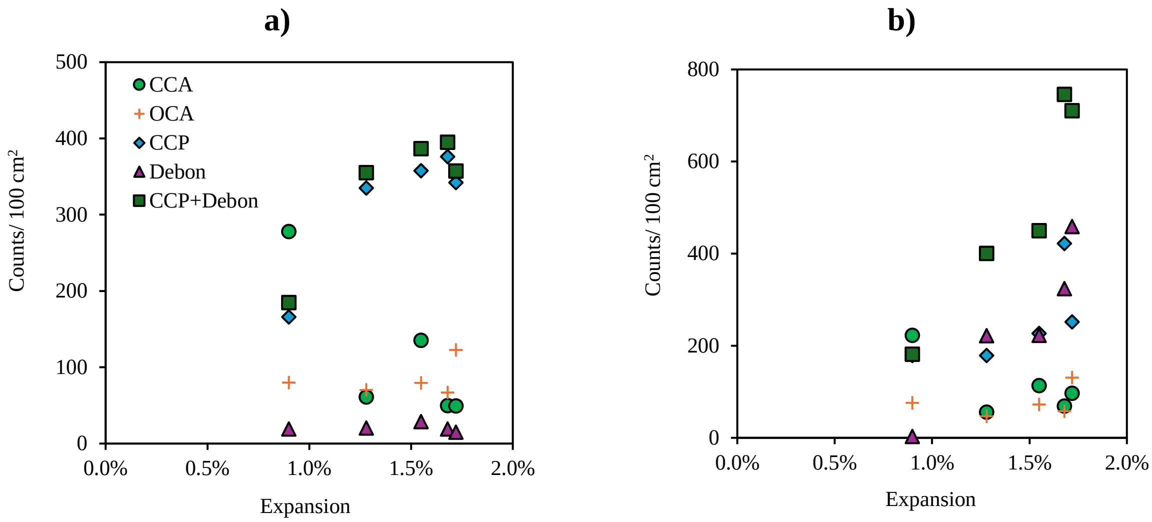

Figure 5.4. Damage feature counts per 100 cm² as a function of expansion for a) the original counting method (M1) and b) the proposed counting method (M2).

5.4.2. Correlation between frequency of damage features and mechanical response

Figure 5.5a and Figure 5.5b present the relation between damage features and the mechanical response (using only the newly proposed counting method – M2) for the SDI and modulus of elasticity, respectively. It can be observed that including crack types that influence the mechanical response improves the correlation with SDI and modulus of elasticity, such as the combination of cracks in the cement paste and Debon types (CCP+Debon) and the addition of open cracks in the aggregate (OCA+CCP+Debon). Overall, as the frequency (extent) of the cracks increases, the SDI increases, and the modulus of elasticity decreases. This highlights the quantitative aspect of point-count microscopy and its ability to capture damage features as measured through mechanical testing of the material.

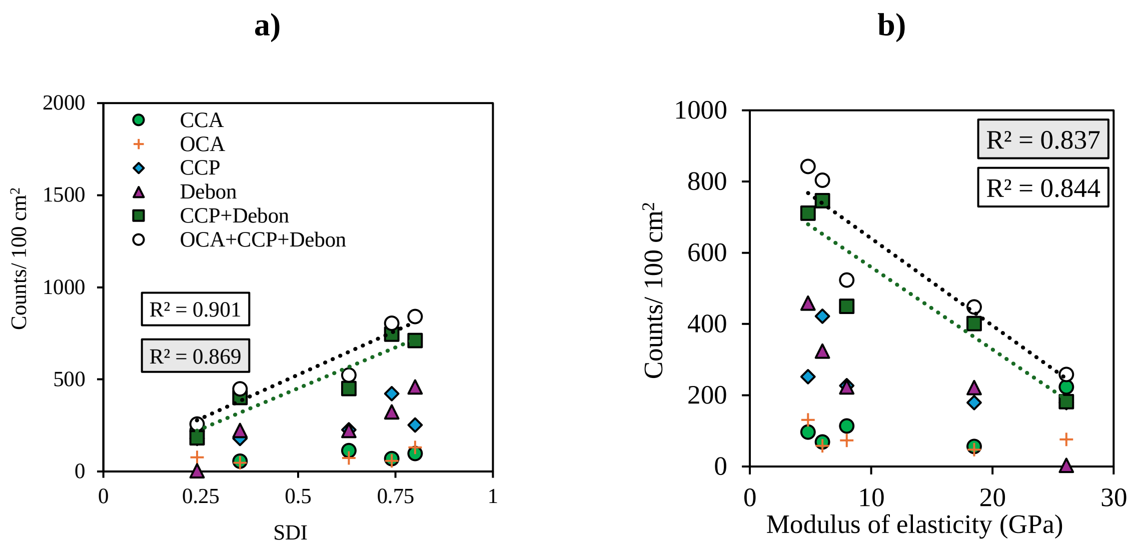

Figure 5.5. Damage feature counts per 100 cm^2 as a function of a) SDI and b) modulus of elasticity. Note that the SDI represents the outputs from the first cycle.

5.5.Conclusion

Damage due to DEF was evaluated through the multi-level assessment. Features most representative of DEF damage were highlighted by considering the Debon-type crack. It was shown that the proposed counting method to distinguish damage characteristics of DEF provided a better correlation with mechanical response. Therefore, the DRI presents an interesting engineering characteristic as a data collection tool for distress features/cracks representative of the damage to the material. Microscopy through the DRI may be the first necessary evaluation to define the mechanical testing protocol better. Nevertheless, the non-reinforced nature of the concrete beam produced a distributed crack propagation and pattern. The anisotropic behaviour of the crack propagation under various reinforcement configurations and coupled mechanisms may influence these results; thus, further research is necessary.

5.6.References

[1] M.D.A Thomas, K. Folliard, T. Drimalas, T. Ramlochan. Diagnosing delayed ettringite formation in concrete structures. Cement and Concrete Research. 2008;38:841–7.

[2] L.F.M. Sanchez, T. Drimalas, B. Fournier, D. Mitchell, J. Bastien. Comprehensive damage assessment in concrete affected by different internal swelling reaction (ISR) mechanisms. Cement and Concrete Research. 2018;107:284–303.

[3] M.-A. Bérubé, N. Smaoui, B.Fournier, B. Bissonnette, B. Durand. Evaluation of the expansion attained to date by concrete affected by alkali–silica reaction. Part III: Application to existing structures. Can J Civ Eng. 2005;32:463–79.

[4] R.-P. Martin, L.F.M. Sanchez, B. Fournier, F. Toutlemonde. Evaluation of different techniques for the diagnosis & prognosis of Internal Swelling Reaction (ISR) mechanisms in concrete. Construction and Building Materials. 2017;156:956–64.

[5] L.F.M. Sanchez, B. Fournier, M. Jolin, J. Bastien, D. Mitchell. Practical use of the Stiffness Damage Test (SDT) for assessing damage in concrete infrastructure affected by alkali-silica reaction. Construction and Building Materials. 2016;125:1178–88.

[6] R.H.R.Q. Melo, N.P. Hasparyk, F. Tiecher. Assessment of Concrete Impairments over Time Triggered by DEF. Journal of materials in civil engineering. 2023;35.

[7] E.R. Giannini, L.F.M. Sanchez, A. Tuinukuafe, K. Folliard. Characterization of concrete affected by delayed ettringite formation using the stiffness damage test. Construction and Building Materials. 2018;162:253–64.

[8] L.F.M. Sanchez, T. Drimalas, B. Fournier. Assessing condition of concrete affected by internal swelling reactions (ISR) through the Damage Rating Index (DRI). Cement. 2020;1–2:100001.

[9] M.-A. Bérubé, B. Fournier, T. Côté . Using the damage rating index for assessing the expansion of concrete affected by freeze-thaw, sulphate attack, or ASR. 14th International Conference on Alkali-Aggregate Reaction. Austin, Texas, USA; 2012.

[10] V. Villeneuve. Détermination de l'endommagement du béton par méthode pétrographique quantitative [Master's Thesis.]. [Québec, QC]: Université Laval; 2011.

[11] R.-P. Martin. Analyse sur structures modèles des effets mécaniques de la réaction sulfatique interne du béton [Internet] [PhD Thesis]. [Paris, France]: Université Paris-Est; 2010. Available from: https://pastel.archives-ouvertes.fr/tel-00558200v2

[12] R.-P. Martin, F. Toutlemonde. Theoretical and experimental validation of a simple method to reproduce representative DEF-prone conditions in laboratory. Mater Struct. 2013;46:1245–55.

[13] B. Kchakech, R.-P. Martin, O. Omikrine-Metlassi, J.-C. Renaud, L. Baron. Effect of temperature and curing duration of early heat treatments on the risk of expansion associated with delayed ettringite formation. 15th international conference on Alkali-Aggregate Reaction (ICAAR). Sao Paulo, Brazil; 2016.

[14] C. Trottier, L.F.M. Sanchez, R.-P. Martin, F. Toutlemonde. Capturing Internal Swelling Reactions (ISR) Damage in Concrete Through the Damage Rating Index (DRI). In: Banthia N, Soleimani-Dashtaki S, Mindess S, editors. Smart & Sustainable Infrastructure: Building a Greener Tomorrow [Internet]. Cham: Springer Nature Switzerland; 2024 [cited 2024 Feb 21]. p. 940–51. Available from: https://link.springer.com/10.1007/978-3-031-53389-1_84

[15] Sanchez LFM, Fournier B, Jolin M, Mitchell D, Bastien J. Overall assessment of Alkali-Aggregate Reaction (AAR) in concretes presenting different strengths and incorporating a wide range of reactive aggregate types and natures. Cement and Concrete Research. 2017;93:17–31.

Chapter 6: Evaluating concrete affected by internal swelling reactions (ISR) using the extended version of the damage rating index (DRI)

Cassandra Trottier[1] and Leandro F.M. Sanchez[2]

Abstract

Internal swelling reactions (ISRs) are distress mechanisms that compromise the service life of critical concrete infrastructure. The initiation, propagation, and cracking patterns associated with ISR can be analyzed via the damage rating index (DRI), a semi-quantitative microscopy procedure used to assess concrete deterioration. Although the DRI provides a systematic method for evaluating the causes and extent of deterioration, subjectivity and variability often hinder its application. This study depicts the distress features within the DRI analysis to understand their effects on expansion and mechanical responses. The findings indicate that each of the distress features, specifically the presence of closed and opened cracks within the aggregate, along with cracks in the cement paste and debonded aggregates, exerts distinct influences on the mechanical responses of the material. Furthermore, this research's key findings show that the average counts of distress features and the interquartile ranges of the count distributions for the various distress features and mechanisms resulted in predictions of expansion with R^2 values greater than 0.83. Variability in determining the extent of deterioration was then addressed using convergence plots, validating a sample size of 75 ±25 cm^2 for laboratory-made specimens as sufficient. Finally, the deconstruction of the distress feature counts enabled the creation of reference distress feature count ranges based on each expansion level and distress mechanism.

6.1. Introduction

Extending the service life of existing concrete infrastructure beyond its initially determined duration or ensuring it meets its intended lifespan when compromised—particularly due to internal swelling reactions (ISR)—continues to pose a significant global challenge [1]. The mitigation and rehabilitation strategies for such infrastructure depend on the causes of ISR, including alkali-aggregate reaction (AAR), delayed ettringite formation (DEF), and freeze-thaw cycles (FT), as well as the extent of damage encountered thus far. Nonetheless, the cause and extent of the damage to the concrete material impact the infrastructure's performance in terms of mechanical properties, serviceability, functionality, durability, physical integrity, and appearance. A current limitation in addressing ISR-affected concrete is the necessity for a reliable diagnosis of the existing damage and its anticipated prognosis. Deterioration from ISR is an ongoing process that evolves over time and can further accelerate under extreme environmental conditions. One promising approach involves using various tools (i.e., multi-level assessments [2]) based on observed mechanisms, incorporating mechanical and microscopy techniques. Among these tools, the damage rating index (DRI) is a microscopy technique employed to characterize damage caused by ISR at a scale representative of the concrete material. However, the interpretation of the results generated by the DRI remains subjective, leading to uncertainty regarding its use in diagnostic activities, particularly concerning the extent of the damage.

6.2. Background

6.2.1. The damage rating index (DRI)

The Damage Rating Index (DRI) is a microscopy tool that enables petrographers or operators to quantify deterioration by counting petrographic and distress features using a stereomicroscope at 15-16x magnification (1 cm^2 field of view) of a polished concrete section. The data collection process for the DRI employs a point-count method, distinguishing the features based on their location in the concrete (i.e., aggregate, cement paste, or their interface) and their nature (i.e., closed, open, and/or filled with a reaction product). These features are weighted according to their severity, summed, normalized to 100 cm^2 for comparative purposes, and further used to characterize the extent of specific types of damage. The selected weighting factors consider the influence and severity of a feature concerning a particular type of damage. Since the DRI's development, the weighting factors have transitioned from accounting for "petrographic features"—symptoms or signs that best represent the type of damage being assessed—to "distress features" that focus on those most indicative of damage (i.e., cracks visible at a magnification of 16x). Grattan-Bellew and Danay [3] developed the DRI to compare observable alkali-aggregate reaction (AAR) levels in concrete. Subsequently, researchers have sought to correlate the resulting DRI to AAR volumetric expansion, leading to modifications in grid sizes, weighting factors, and features considered in the DRI calculation, all aimed at minimizing operator variability [4–8]. Sanchez et al. (2017) further established ranges of expected DRI values as a function of the type and level of deterioration, thus serving as a practical tool for operators and engineering practitioners [2]. Additionally, the extended version of the DRI, which includes unweighted counts per 100 cm^2, proportions (%), maximum lengths and widths, as well as crack advancement (i.e., crack density – counts/cm^2) and extensions (i.e., proportional counts of cracks crossing an interface), as proposed by Sanchez et al. (2015,2016,2020), captures ISR-induced deterioration development to describe better the role of distress features concerning damage [9–11]. Nevertheless, the DRI remains a comprehensive assessment tool for distinguishing among various but not limited to, ISR distress mechanisms through occurrences of distress features and their corresponding abundance to ascertain the extent of the damage.

6.2.2. An overview of internal swelling reactions (ISR)

6.2.2.1. Alkali-aggregate reaction (AAR)

Alkali-aggregate reaction (AAR) in concrete is classified into two types: alkali-silica reaction (ASR) and alkali-carbonate reaction (ACR). Both are damaging mechanisms that involve reactive particles or minerals interacting with the hydroxides present in the pore solution of the cement paste. The mechanism responsible for ACR damage remains a topic of debate in the literature [12–15], with new evidence challenging the connection to ASR [16]. In contrast, the understanding of the mechanism behind ASR damage has been established over recent decades since its first occurrence and common presence worldwide [17]. Both mechanisms can be distinctly characterized; ACR shows dedolomitization and carbonate halo rims [14], whereas ASR damage is indicated by cracks in the aggregate particles filled with secondary products (i.e., so-called silica gel) that extend into the cement paste in more severe cases. Researchers have examined the propagation of ASR damage, evaluating the reliability of certain tools (i.e., mechanical and microscopical) to identify the cause and extent of the damage [18–21]. It was concluded that cracks originate within the reactive particle and extend into the cement paste as damage increases (i.e., concerning expansion levels). Furthermore, at each step of crack elongation, losses in mechanical properties were associated with the location of these cracks (i.e., aggregate vs. cement paste) [18], as illustrated in Figure 6.1.

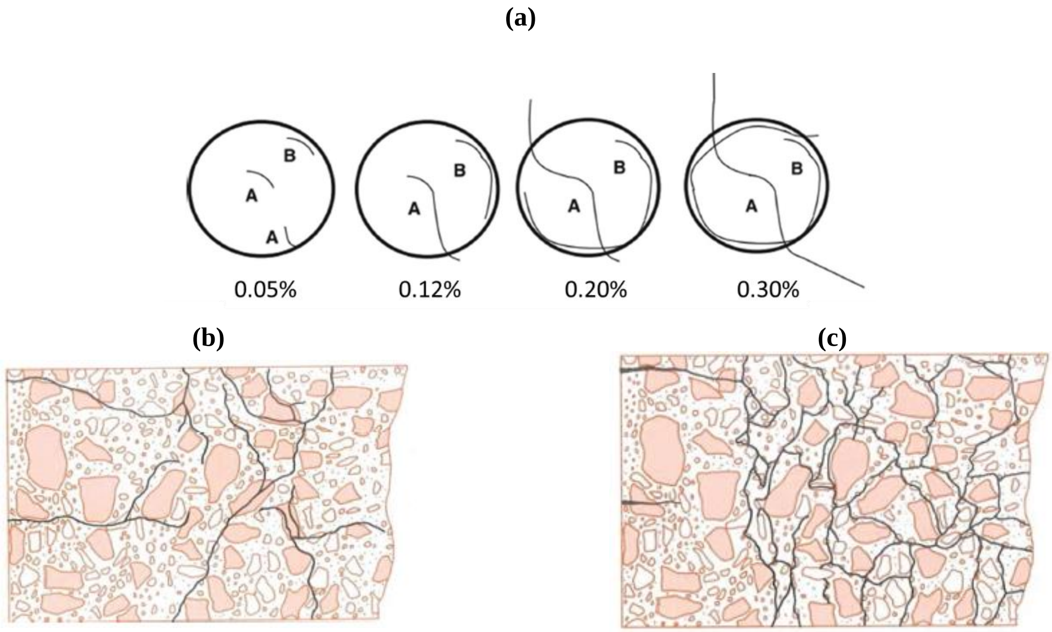

Figure 6.1. Descriptive ASR crack propagation model (a) as damage increases and at a high level of damage [9] where a reactive coarse aggregate triggers ASR, (b) reactive coarse aggregate and (c) reactive sand crack propagation patterns throughout the concrete [22].

For comparison, the ACR crack pattern observed through stereomicroscopy and the DRI differs significantly from that of ASR. The most prevalent distress features for ACR are cracks in the cement paste (Figure 6.2a), which are evident at low expansion levels and elevate the DRI number beyond the typical ranges established for ASR [23], as shown in Figure 6.2b. This current work does not include ACR in the analysis. However, distinguishing between ASR and ACR features remains crucial for a more accurate diagnosis of concrete damage [24].

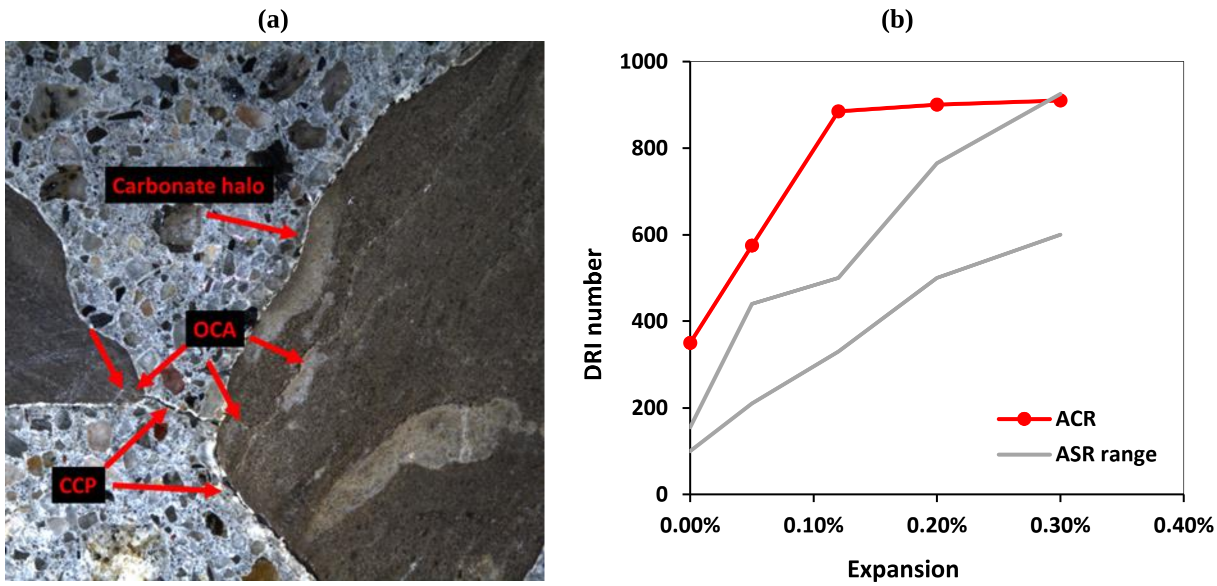

Figure 6.6.2. Typical ACR features with (a) cracks in the cement paste, both in the bulk and aggregate-paste interface [24], and (b) high DRI numbers generated by cracks in the cement paste [23].

6.2.2.2.Delayed ettringite formation (DEF)

Delayed ettringite formation (DEF) is an internal sulphate attack characterized by cracks in the concrete’s cement paste and the aggregate-paste interface, typically accompanied by ettringite crystals that fill these gaps without any external source of sulphates. However, the presence of ettringite in voids and cracks may not necessarily signify damage, as it can dissolve and recrystallize in these locations when exposed to prolonged moisture [25,26]. When internal temperatures rise above approximately 65°C during the early stages [26,27], conditions prevent ettringite formation. As the temperature decreases, ettringite develops in the hardened concrete. Elevated temperatures can occur in steam-cured concrete, mass concrete, and during casting in high-heat weather, after which ettringite crystals grow under humid conditions [27,28]. Some researchers argue that the excessive heat required for DEF to develop causes a homogeneous paste expansion that detaches it from the aggregate, creating gaps later filled by ettringite. In contrast, others contend that the formation of the crystals induces cracking [29–33]. Nonetheless, the damage characteristics in concrete due to DEF are manifested as cracks at the aggregate-paste interface and within the bulk cement paste, occasionally filled with a whitish substance (Figure 6.3).

(a) (b)

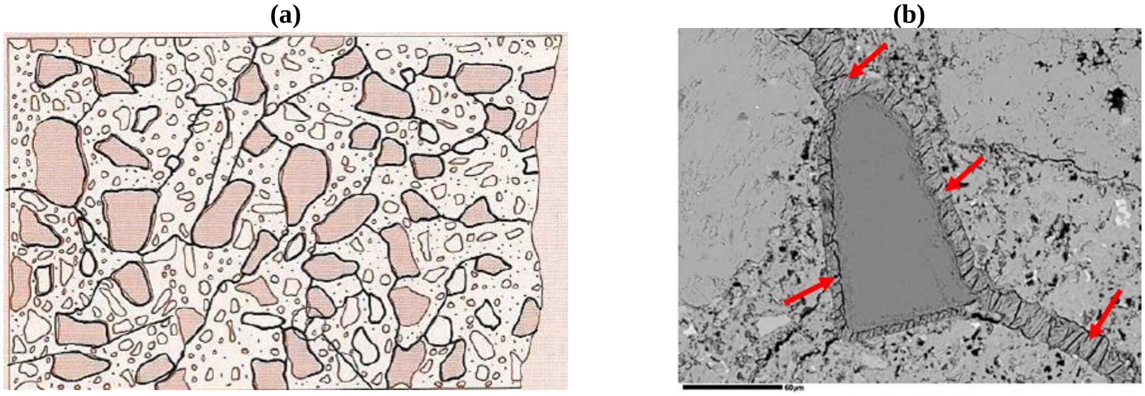

Figure 6.3. (a) DEF crack pattern [22] and (b) Damage to concrete due to DEF as observed through SEM in BSE mode where red arrows highlight ettringite-filled cracks surrounding the dark grey aggregate particle (black bar shows scale of 60 microns) [31].

Evidently, the crack pattern and its generation and propagation due to DEF differ from that of ASR (Figure 6.1), which can be highlighted through qualitative stereomicroscopy. Several researchers have utilized the DRI to quantify DEF damage to concrete [4,11,34–37]. However, when correlating expansion to DEF damage as measured through the DRI, it is apparent that modifications are still necessary [4,36]. Accordingly, to quantify the extent of damage corresponding to a specific type of ISR, some adjustments to the counting procedure were required to emphasize DEF as a leading cause of damage, such as considering the most observed damage feature of "debonded/dislodged" aggregates (i.e., the crack surrounding a particle or removed particle during surface preparation) [38]. The "Debon" distress feature is already part of the pre-determined list of features to consider towards the DRI [4]. Modifying the counting procedure when evaluating DEF (i.e., original – M1 and proposed – M2 counting methods) resulted in DRI bar charts demonstrating a higher number of "Debon" type cracks, which distinguishes DEF from ASR or other mechanisms where an abundance of cracks in the cement paste (CCP) would be observed (Figure 6.4). Additionally, the distinction of the "Debon" feature was found to correlate with mechanical responses [39].

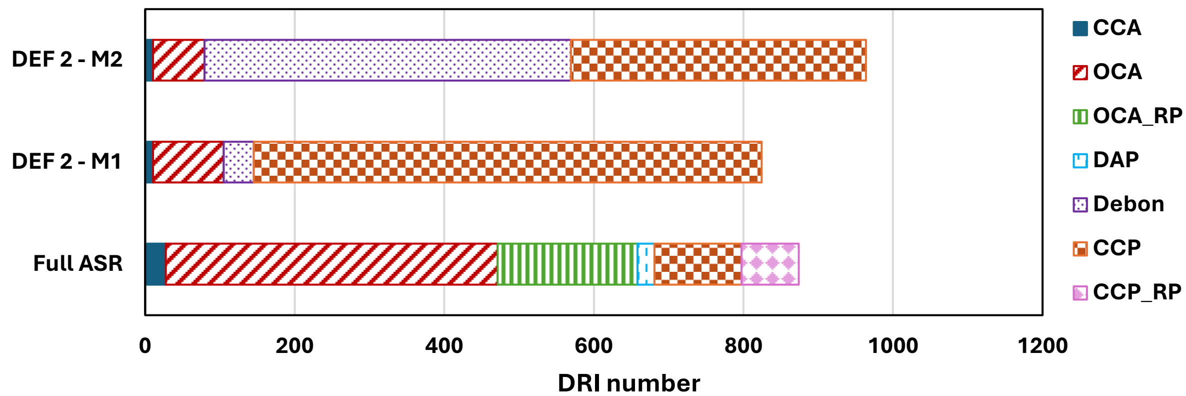

Figure 6.4. DRI bar charts distinguishing DEF from ASR under similar DRI numbers.

DEF is frequently found alongside ASR in the field, as a reduction in alkalis consumed by ASR promotes ettringite formation [31,40]. The difficulty in evaluating such combined mechanisms lies in identifying the contributions of the distinct mechanisms [31,37,41]. Moreover, the leaching of alkalis at a concrete surface could lead to heterogeneous damage in terms of level and cause, resulting in differing contributions from both mechanisms within the same concrete element.

6.2.2.3.Freezing and thawing (FT)

Freezing and thawing (FT) can occur in concrete exposed to harsh climates, such as those in Canada, which typically leads to deterioration through cracking in the cement paste (Figure 6.5a). This deterioration from FT may begin with moisture penetrating the surface and sequentially delaminating layers of concrete parallel to the surface (Figure 6.5b). Meanwhile, the inner portions of the concrete experience irregular pressures exerted within the void system of the cement paste, resulting in cracking around these voids. FT-induced cracks are generally located at the aggregate-paste interface and propagate into the cement paste [42,43]. FT deterioration further compromises the aggregate-paste interface, whereby micromechanical properties are most significantly affected in this region [44], aligning with the descriptive crack propagation model proposed by Zahedi et al. (2022) and illustrated in Figure 6.5c [45]. Research on the combined effects of FT and ASR is limited [42,46–49]. However, Gong et al. (2020) modelled the effects of FT and ASR when one distress mechanism was activated before the other. This modelling revealed that FT continues as ASR reaction products fill the entrained air voids, diminishing the effectiveness of air entrainment. [47].

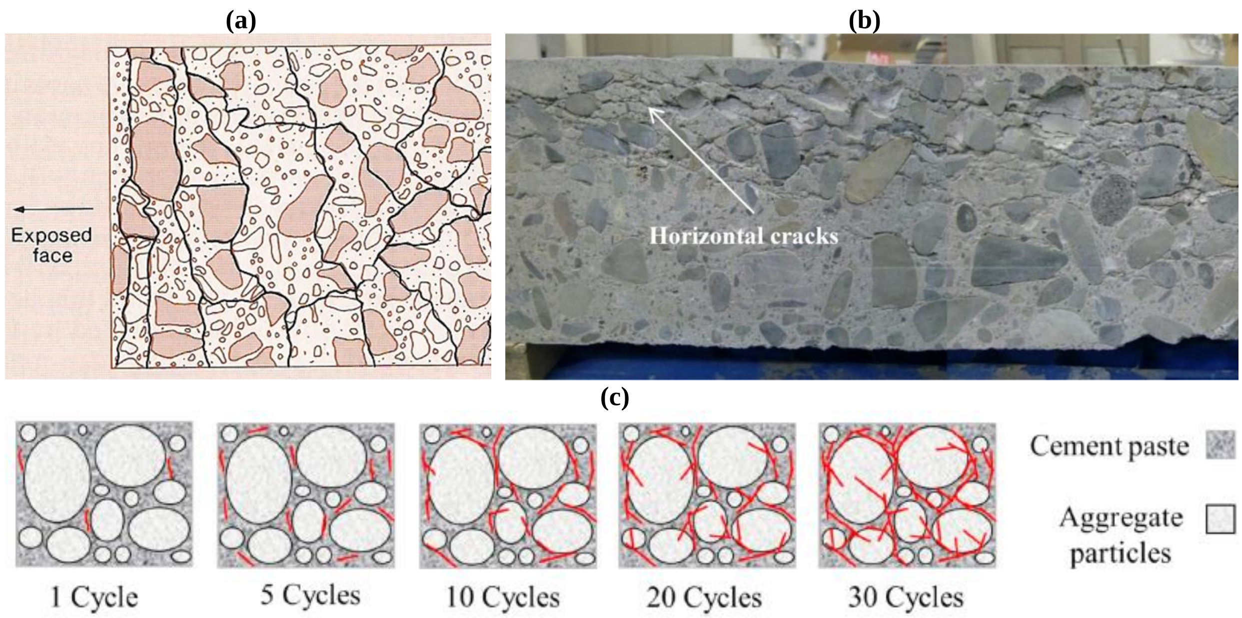

Figure 6.5. FT crack pattern: (a) as described by BCA (1992) [22], (b) from a cross-section of a 40-year canal wall exposed to water and soil (top and bottom of the image, respectively) [50], and (c) as a descriptive crack propagation model [45].

Nevertheless, understanding the damage caused by DEF and FT, as captured through stereomicroscopy, is essential before attempting to decouple the combined mechanisms. Instances where ASR was identified as the primary cause of ISR damage while employing the multi-level assessment have begun to increase [42,51–55]. However, due to the vast amount of literature focused on diagnosing ASR compared to DEF and FT, concerns persist regarding potential misdiagnosis, particularly with combined mechanisms. Therefore, a clearer understanding of how to differentiate DEF and FT from other mechanisms using tools that can visualize the spread and pattern of the damage to the concrete is essential, especially at early and intermediate stages.

6.3.Scope of the work

Given that distinct patterns are generated by ISR (i.e., ASR, FT, and DEF, both individually and in combination) distress mechanisms at varying degrees of deterioration, the ability to capture these patterns alongside the extent of ISR-induced deterioration through the DRI remains crucial for reducing subjectivity and enhancing acceptance in engineering practice. However, the distress features linked to these patterns have not been quantitatively correlated to expansion and mechanical responses, a vital step toward implementation in engineering practice. Therefore, DRI data, particularly the extended version of the DRI (i.e., unweighted counts) obtained from a previous comprehensive research program [2,11], were decomposed to analyze the distinct distress features associated with damage in concrete (i.e., expansion and mechanical responses). The concrete mixtures included reactive coarse aggregate (i.e., polymictic gravel from New Mexico) and reactive fine aggregate (i.e., polymictic sand from Texas), with expansion levels ranging from 0.05% to 0.30% evaluated for ASR and FT concrete specimens, and up to 1.87% expansion assessed for DEF concrete specimens. The weighting factors were first analyzed to determine their importance in the quantitative analysis of ISR-induced deterioration, followed by the extended version of the DRI to depict variations among the distress mechanisms. Linear regression models were then developed and used to understand the role of the distress features, considering all distress features as predictors and the responses as expansion and mechanical responses. Additionally, the sample size of 1 cm by 1 cm squares was evaluated using convergence, as outlined by the law of large numbers, to address variability within a specimen. This led to the deconstructed DRI data used to produce boxplots and descriptive statistics of the count distributions for a better representation of the extent of deterioration, along with ranges of distress feature counts for all distress mechanisms at the stated expansion levels, employing the bootstrap method with 1000 iterations for stability. This work addressed all current hesitations regarding using the DRI in engineering practice.

6.4.Materials and methods

The material and data used in this current research were gathered from a previous comprehensive research program by Sanchez et al. (2018,2020) [2,11].

6.4.1. Aggregates and mixture proportions

All mixtures utilized the reactive coarse aggregate (New Mexico – NM) and reactive sand (Texas – Tx) separately. Table 6.1 outlines the characteristics of the coarse and fine aggregates incorporated in the concrete mixtures. The reactive coarse aggregate was paired with the non-reactive granite sand (i.e., Lav) for all groups. In contrast, the reactive sand was paired with non-reactive Canadian coarse limestone aggregate (i.e., HP) for the ASR (i.e., 35 MPa and CPT) and FT mixtures and with non-reactive American coarse limestone aggregate (i.e., MM) for the DEF and DEF+ASR mixtures.

Table 6.1. Characteristics of the coarse and fine aggregates.

Aggregate		Reactivity	Location	Rock type	**Specific gravity** [56]	**Absorption** [56]	**AMBT 14-day exp (%)** [56]
Coarse	NM	ASR reactive	New Mexico (USA)	Polymictic Gravel (Mixed Volcanic, quartzite, chert)	2.53	1.59	1.056
	MM	Non-reactive	North Carolina (USA)	Limestone	2.47	3.12	0.01
	HP	NR	Newfoundland (CAN)	High-purity fine-grained limestone	2.68	0.44	0.001
Fine	Tx	ASR reactive	Corpus Christi (USA)	Polymictic sand (granitic, mixed volcanic, quartzite, chert, quartz)	2.60	0.55	0.755
	Lav	Non-reactive	Quebec (CAN)	Natural derived from Granite	2.71	0.54	0.068

Two main groups were utilized throughout the study: 1) FT and ASR proportioned as 35 MPa concrete and 2) DEF and ASR proportioned with concrete prism test (CPT) standard mixtures [57]. A high alkali cement was employed (i.e., 0.90% Na_2O_{eq}. CSA Type GU, ASTM type I) in all of the mixtures, which were boosted to 1.25% Na_2O_{eq}. by cement mass, using reagent grade NaOH, according to [57]. Admixtures were not employed in any of the mixtures.

6.4.2. Specimen fabrication and induced ISR

Concrete specimens (100 mm in diameter and 200 mm in length) were manufactured and moist-cured in a curing room for 48 hours after demoulding. This was followed by drilling small holes, 5 mm in diameter and 15 mm long, into the ends. Stainless steel gauge studs were then glued using a fast-setting cement paste slurry for longitudinal expansion measurements. After 48 hours of moist curing, the initial readings were taken and recorded.

The ASR specimens (i.e., 35 MPa and CPT proportioned) were stored over water in 22-l plastic pails lined with moisture-wicking fabric at 38°C and 100% relative humidity. Length changes were monitored over time following standard procedure [57] until the targeted expansions were reached (i.e., 0.05%, 0.12%, 0.20%, and 0.30%).

The DEF-exposed specimens were cured for 12 hours at 95°C (i.e., after a 4-hour period to reach the temperature) in an oven four hours after casting. The temperature decreased to 23°C for the subsequent 12 hours, after which the specimens were stored in water-filled pails at 23°C. Length changes were monitored over time until the specimens reached the selected expansion levels (i.e., 0.12%, 0.40%, 0.50%, 0.80%, ≈1.0%, and ≈2.0%). Specimens coupled with ASR were stored at 38°C and 100% relative humidity (i.e., over water in a sealed bucket) to facilitate ASR and DEF.

Length changes were monitored until the specimens reached the selected expansion levels (i.e., 0.08%, 0.12%, 0.30%, 0.50%, 0.6%, 0.90%, and 1.5%).

The FT-exposed specimens were stored in a freezing and thawing chamber (i.e., cycling from -20°C to +5°C for 3 hours per cycle, with 8 cycles per day) according to standard procedures [58]. Specimens were removed from the chamber once they reached the targeted expansion levels (i.e., 0.05%, 0.12%, 0.20%, and 0.30%). Specimens coupled with ASR were taken out at half of the desired expansions and exposed to the previously described ASR enabling conditions until they achieved full expansions (i.e., 0.05%, 0.12%, 0.20%, and 0.30%).

6.4.3. The damage rating index (DRI) and its extended version

The concrete cylinders were sliced in half lengthwise with a masonry saw, and one half was preserved for the DRI. A polishing sequence consisting of grits 50 (coarse), 100, 400, 800, 1500, and 3000 (4-8 microns) was employed to achieve a highly reflective surface using a portable hand-held polisher. A grid of 1 cm by 1 cm was drawn on the reflective surface with a fine-tipped permanent marker, creating the field of view for distress feature counts counted. The DRI calculation considers all counted and weighted distress features (weighting factors as per [4,5,56]), summing them up and "normalizing" the result by dividing the sum by the number of analyzed squares, then multiplying by 100 cm² (Equation 6.1). Bar charts are subsequently generated to delineate the features and visualize their relative significance. The extended version of the DRI represents the unweighted distress feature counts, as proposed by Sanchez et al. (2017) [56], where bar charts can be created to compare expansion levels and distress mechanisms, presented as counts/100 cm² and proportions (Equations 6.2 and 6.3, respectively). The crack density (CD) further illustrates the total ($OCA+OCA_{RP}$)+($CCP+CCP_{RP}$) counts/cm² (Equation 6.4).

$$DRI = \left[\frac{\sum(0.25(CCA) + 2(OCA + OCA_{RP} + DAP) + 3(CCP + CCP_{RP} + Debon))}{n}\right] \times 100\ cm^2 \quad \text{Eq. 6.1}$$

$$Distress\ feature\ \left(\frac{counts}{100\ cm^2}\right) = \frac{Distress\ feature\ counts}{n} \times 100\ cm^2 \quad \text{Eq. 6.2}$$

$$Distress\ feature\ (\%) = \frac{Distress\ feature\ counts}{CCA + (OCA + OCA_{RP}) + (CCP + CCP_{RP})} \times \frac{100\ cm^2}{n} \quad \text{Eq. 6.3}$$

$$Crack\ density\ \left(\frac{counts}{cm^2}\right) = \frac{(OCA + OCA_{RP}) + (CCP + CCP_{RP})}{n} \quad \text{Eq. 6.4}$$

Where CCA is the total number of closed cracks in the aggregate, $OCA\ and\ OCA_{RP}$ are the total numbers of open cracks in the aggregate without and with reaction product, respectively, DAP is the total number of disaggregated/corroded particles, $CCP\ and\ CCP_{RP}$ are the total numbers of cracks in the cement paste without and with reaction product, respectively, $Debon$ is the total number of debonded/dislodged aggregates, and *n* is the total number of 1 cm by 1 cm squares analyzed.

6.5. Results

6.5.1. Comparing the DRI proposed weighting factors

In the literature, the DRI number, along with any other damage indicator, has been compared to expansion, which serves as the measurable indicator for the level of deterioration in concrete. Thus, the weighting factors proposed by several authors [3,4,6,7,59] (Table 6.2) have been modified over time to establish a more accurate correlation with the expansion. Figure 6.6 illustrates the relationships between expansion and DRI numbers, calculated using the various weighting factors proposed for similar fields of view of 1 cm² [3,4,6,7]. The comparison focuses solely on the distress features to understand the role of the weighting factors associated with concrete damage, particularly cracks of 1 mm or longer, which correspond to coarse particles of reactive sand (i.e., Tx – Texas). Therefore, some petrographic features, such as product-filled voids and reaction rims, are not included in counts.

Table 6.2. Proposed weighting factors associated with the distress features.

Distress feature	Label	Weighting factors			
		Grattan-Bellew and Danay (1992) [3]	Smaoui et al. (2004), Grattan-Bellew and Mitchell (2006) [6,59]	Powers and Shrimer (2007) [7]	Villeneuve (2011) Villeneuve et al. (2012) [4,5]
Closed crack in the aggregate	CCA	0.25	0.75	0.5	0.25
Open crack in the aggregate	OCA	0.25	4	0.5	2
Open crack in the aggregate with reaction product	OCA_{RP}	2	2	2	2
Corroded/disaggregated particle	DAP	0	0	3	2
Crack in the cement paste	CCP	2	2	2	3
Crack in the cement paste with reaction product	CCP_{RP}	4	4	4	3
Debonded or dislodged aggregate	Debon	3	3	4	3

A positive relationship is observed for all distress mechanisms, regardless of the weighting factor utilized. Overall, higher DRI numbers are noted for the second proposed set of weighting factors (Smaoui et al. 2004, Grattan-Bellew and Mitchell, 2006 [6,59]), followed by those suggested by Villeneuve and Fournier (2011, 2012) [4,5] and Powers and Shrimer (2007) [7], with the lowest DRI numbers obtained by employing the original weighting factors from Grattan-Bellew and Danay (1992) [3]. The coefficients of determination (R^2) for each proposed set of weighting factors across all distress mechanisms range from 0.66 to 0.98 for Grattan-Bellew and Danay (1992), 0.59 to 0.99 for Smaoui et al. (2004) and Grattan-Bellew and Mitchell (2006), 0.67 to 0.98 for Powers and Shrimer (2007), and 0.80 to 1.00 for Villeneuve and Fournier (2011, 2012). Similarly, the R^2 for each distress mechanism ranges from 0.84 to 0.99 for ASR proportioned for the FT group (Figure 6.6a), 0.67 to 1.00 for ASR proportioned for the DEF group (Figure 6.6b), 0.77 to 0.99 for

ASR+FT (Figure 6.6c), 0.66 to 0.97 for ASR+DEF (Figure 6.6d), 0.82 to 1.00 for FT (Figure 6.6e), and 0.59 to 0.99 for DEF (Figure 6.6f).

In general, the DRI numbers per expansion for the reactive coarse (NM – New Mexico) and fine (Tx - Texas) aggregate do not align, except for the weighting factors proposed by Villeneuve and Fournier (2011, 2012) for the ASR proportioned for the FT group (Figure 6.6a) and those suggested by Grattan-Bellew and Danay (1992) for FT (Figure 6.6e). Meanwhile, no clear pattern indicates whether one type produces higher DRI numbers at a given expansion level. However, the difference between the DRI numbers from the concrete made with reactive coarse and fine aggregate for the ASR proportioned for the FT group is smaller at lower expansion levels, increasing with greater expansion. Additionally, the rise in DRI numbers for the ASR proportioned for the DEF group is steeper for reactive coarse aggregate than for reactive sand. For the combined mechanisms, all proposed weighting factors yield higher DRI numbers for reactive sand in the ASR+FT combined mechanisms (Figure 6.6c). In contrast, the opposite behaviour is noted, with the reactive coarse aggregate generating higher DRI numbers at the same expansion levels for the ASR+DEF combined mechanism (Figure 6.6d). Interestingly, the combined mechanisms show more parallel trendlines between both reactive aggregate types, represented by all proposed weighting factors. This parallelism between the trendlines of both reactive aggregates is further observed for the FT mechanisms (except for the results produced by Smaoui et al. (2004) and those from Grattan-Bellew and Mitchell, 2006) and the DEF mechanisms, where the NM coarse aggregate consistently produces higher DRI numbers. Nevertheless, the R^2 can be considered sufficient for all weighting factors in this context.

Validation for using the distress features proposed by Villeneuve and Fournier (2011, 2012) was conducted by applying the DRI to distress mechanisms beyond ASR [4,5]. The selection of distress features was based not only on operator variability but also on their indication of deterioration due to ISR. The occurrence of ASR in concrete shows features of a petrographic nature that are not associated with damage, such as the presence of gel as a reaction product within cracks in the aggregate, cement paste, and lining/filling voids. Additionally, reaction rims found at the inner boundary of the aggregates do not necessarily indicate concrete deterioration, thus emphasizing the distinction between petrographic and distress features. Conversely, DEF can exhibit petrographic features, such as reaction products within the aggregate-paste interface, which could migrate to any open gaps in the concrete (i.e., open cracks in the aggregate caused by excessive pressure from DEF expansion or voids). Furthermore, FT deterioration does not encompass any features of a petrographic nature other than its pattern (i.e., crack initiation and propagation). Therefore, it is the cumulative effect of each counted distress feature and their proportional distributions across the surface of a specimen that delineates the extent of the damage associated with a particular distress mechanism.

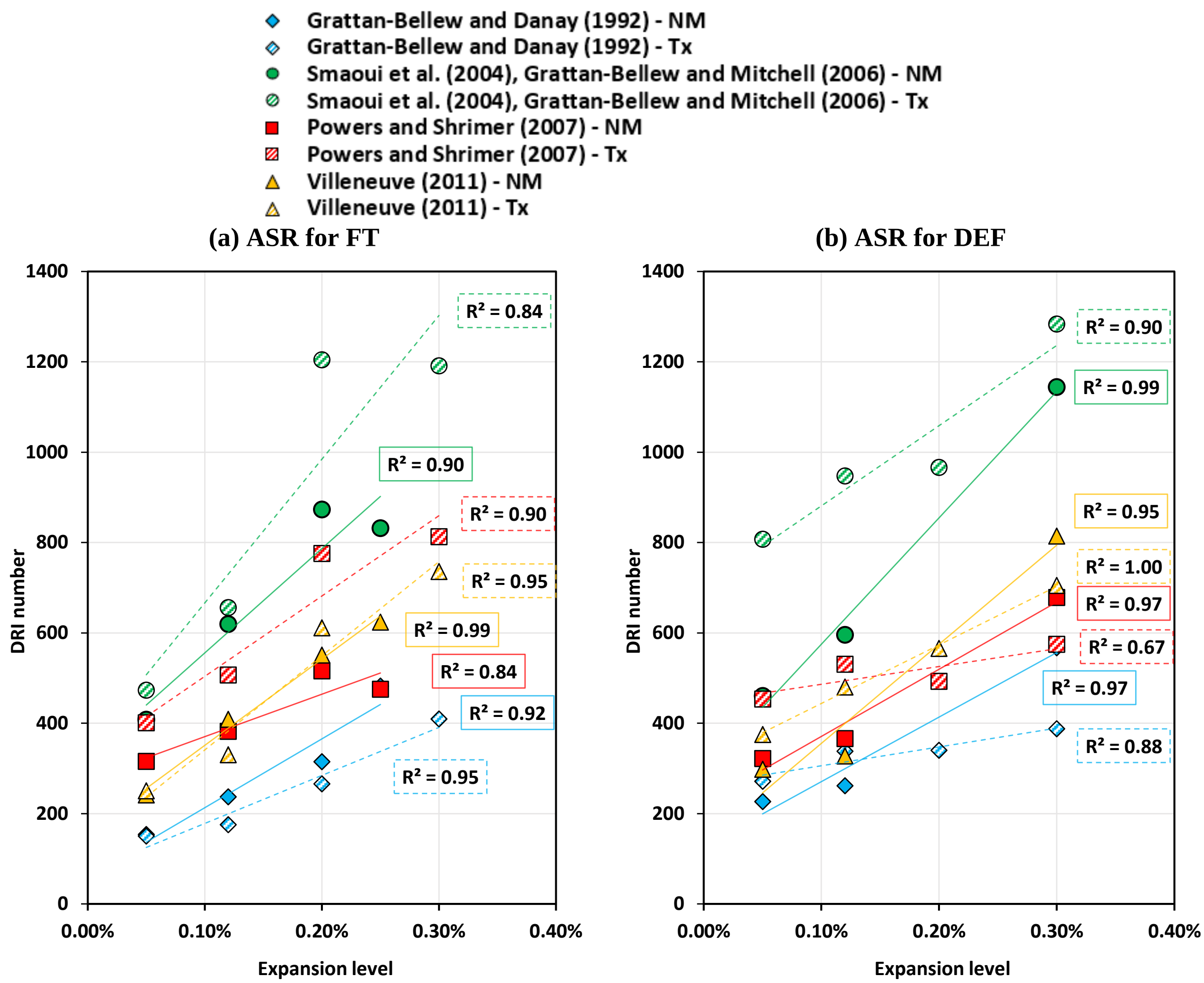
Grattan-Bellew and Danay (1992) - NM
Grattan-Bellew and Danay (1992) - Tx
Smaoui et al. (2004), Grattan-Bellew and Mitchell (2006) - NM
Smaoui et al. (2004), Grattan-Bellew and Mitchell (2006) - Tx
Powers and Shrimer (2007) - NM
Powers and Shrimer (2007) - Tx
Villeneuve (2011) - NM
Villeneuve (2011) - Tx
(a) ASR for FT
(b) ASR for DEF
DRI number
Expansion level
0
200
400
600
800
1000
1200
1400
0.00%
0.10%
0.20%
0.30%
0.40%
R² = 0.84
R² = 0.90
R² = 0.90
R² = 0.95
R² = 0.99
R² = 0.84
R² = 0.92
R² = 0.95
R² = 0.90
R² = 0.99
R² = 0.95
R² = 1.00
R² = 0.97
R² = 0.67
R² = 0.97
R² = 0.88

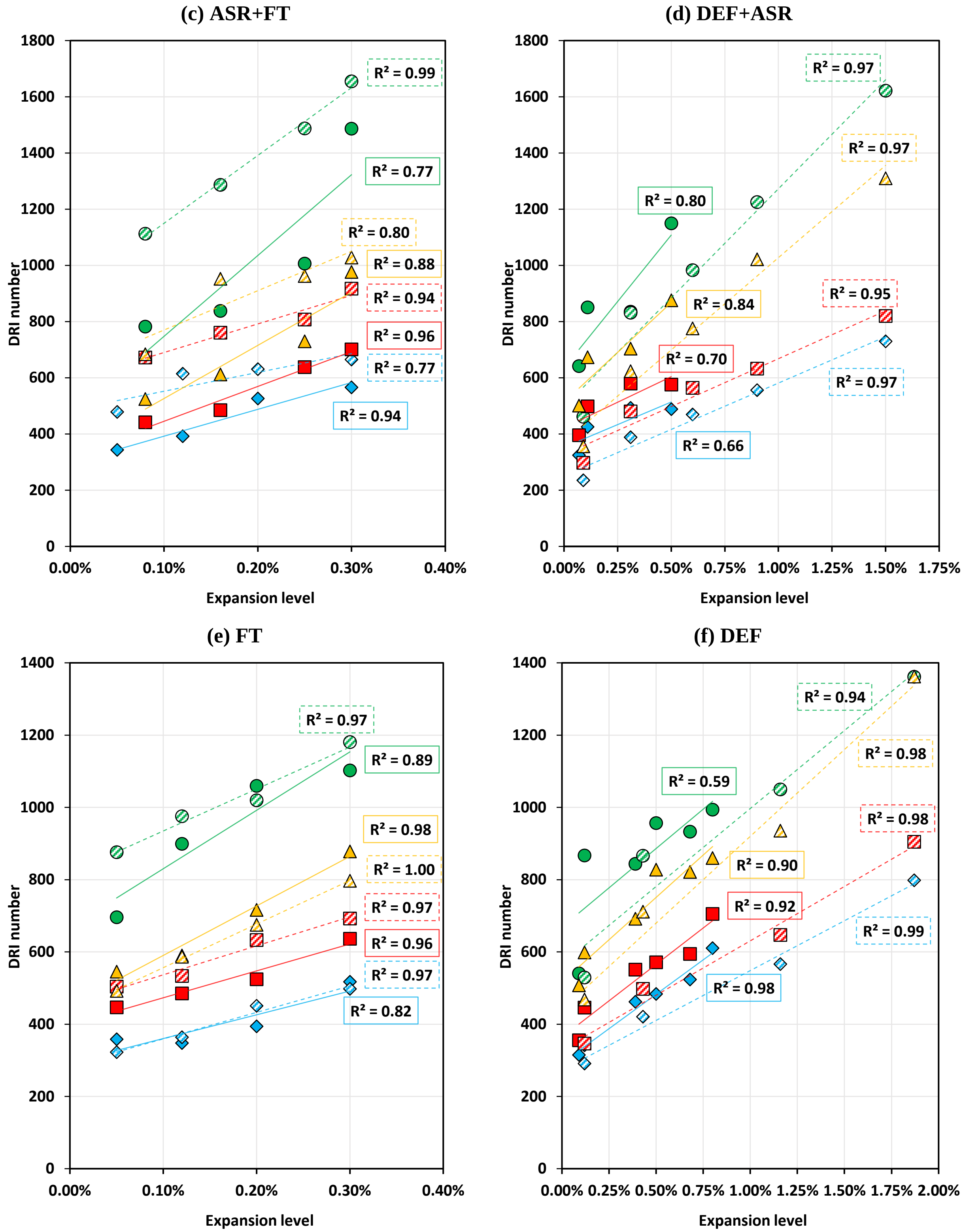

Figure 6.6. DRI as a function of expansion for various distress mechanisms using several weighting factors. The solid lines represent the trend line for the reactive coarse aggregate (NM – New Mexico) and the dashed lines represent the trend line for the reactive sand (Tx - Texas).

6.5.2. *Capturing ISR damage progress using the extended version of the DRI*

To improve the understanding and description of crack propagation, Sanchez et al. (2015, 2016) proposed an extended version of the DRI. This analysis employs unweighted counts of distress features, such as CCA, $OCA+OCA_{RP}$, and $CCA+CCP_{RP}$, expressed as counts per 100 cm² and proportions (%), alongside the summation of $OCA+OCA_{RP}$ and $CCA+CCP_{RP}$ per 1 cm², which represents the crack density [10,60], as demonstrated in Equations 6.2, 6.3, and 6.4, respectively. Figures 6.7 and 6.8 illustrate the distress features as counts per 100 cm² and proportions (%) for the ASR and FT and the ASR and DEF groups, respectively. The general trend from the first to the last level of expansion shows an increase in total distress feature counts, as observed in Figures 6.7a and 6.8a. However, this trend varies at the intermediate expansion levels, where higher counts may occur (such as for ASR 35 MPa and FT – NM). At the same time, other instances show a "dip," where an intermediate expansion level produces lower total distress feature counts than the lower expansion level. This is evident for ASR+FT and FT for the Tx specimens (Figure 6.7a), where the “dip” is mainly attributed to lower CCA counts at 0.16% and 0.12% expansion, respectively. Interestingly, the “dip" occurs at higher expansion levels for DEF – NM, DEF+ASR, and DEF – Tx, at expansion levels of 0.50%, 0.90%, and 1.16%, again attributed to lower CCA counts. The reactive sand concrete generates more CCA than the reactive coarse aggregate for ASR (35 MPa and CPT mixtures), FT, and ASR+FT. In contrast, the opposite behaviour is noted for DEF and DEF+ASR mixtures—nevertheless, both $OCA+OCA_{RP}$ and $CCP+CCP_{RP}$ increase with expansion. The proportions of CCA are above 45% for the ASR and FT groups, while a minimum of 9% of CCA is noted for the ASR and DEF groups. Generally, the proportions of $OCA+OCA_{RP}$ are larger than those of $CCP+CCP_{RP}$ for ASR and the combined mechanisms, while the proportions of CCP+CCP_{RP} tend to exceed those of OCA+OCA_{RP} for the distress mechanisms originating from cement paste (i.e., FT and DEF).

(a)

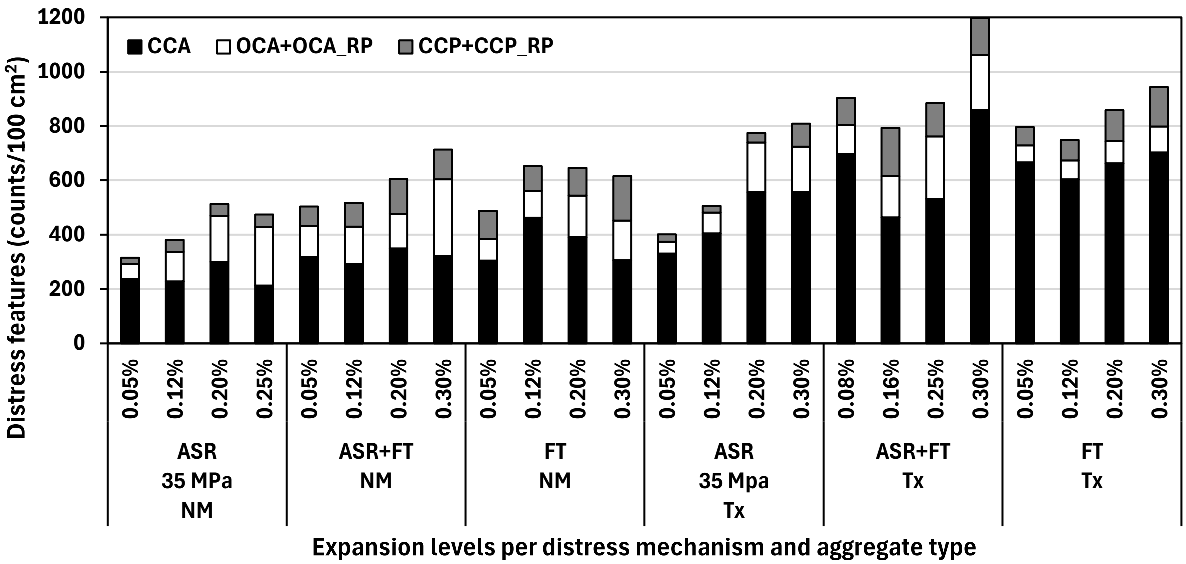

(b)

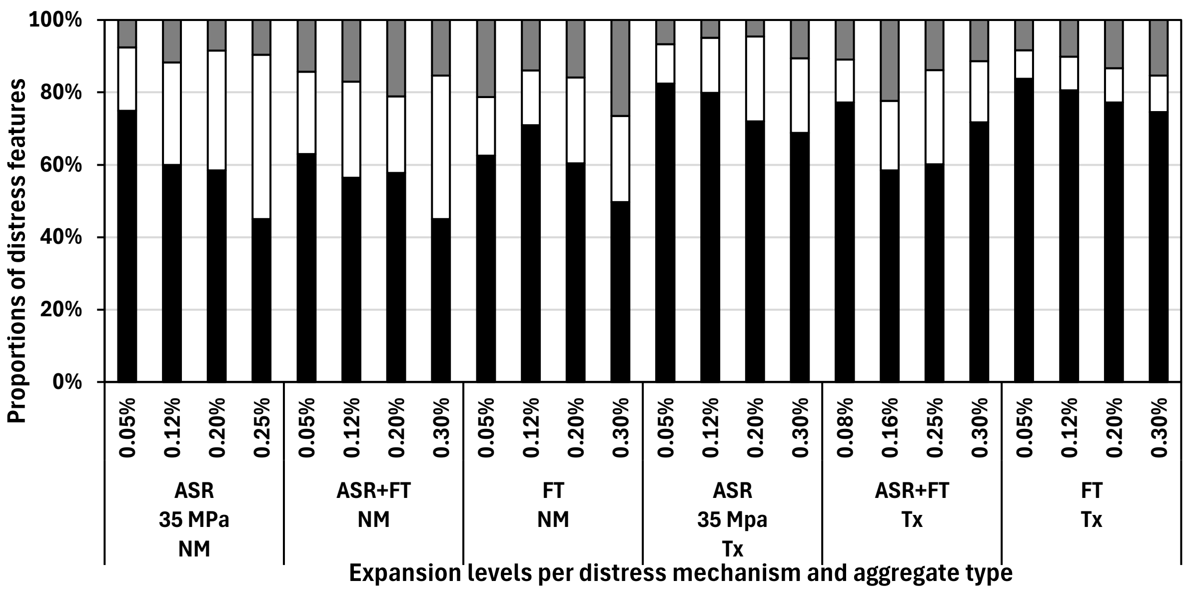

Figure 6.7. Extended version of the DRI as (a) distress feature counts/100 cm^2 and (b) proportions (%) for the ASR and FT groups.

(a)

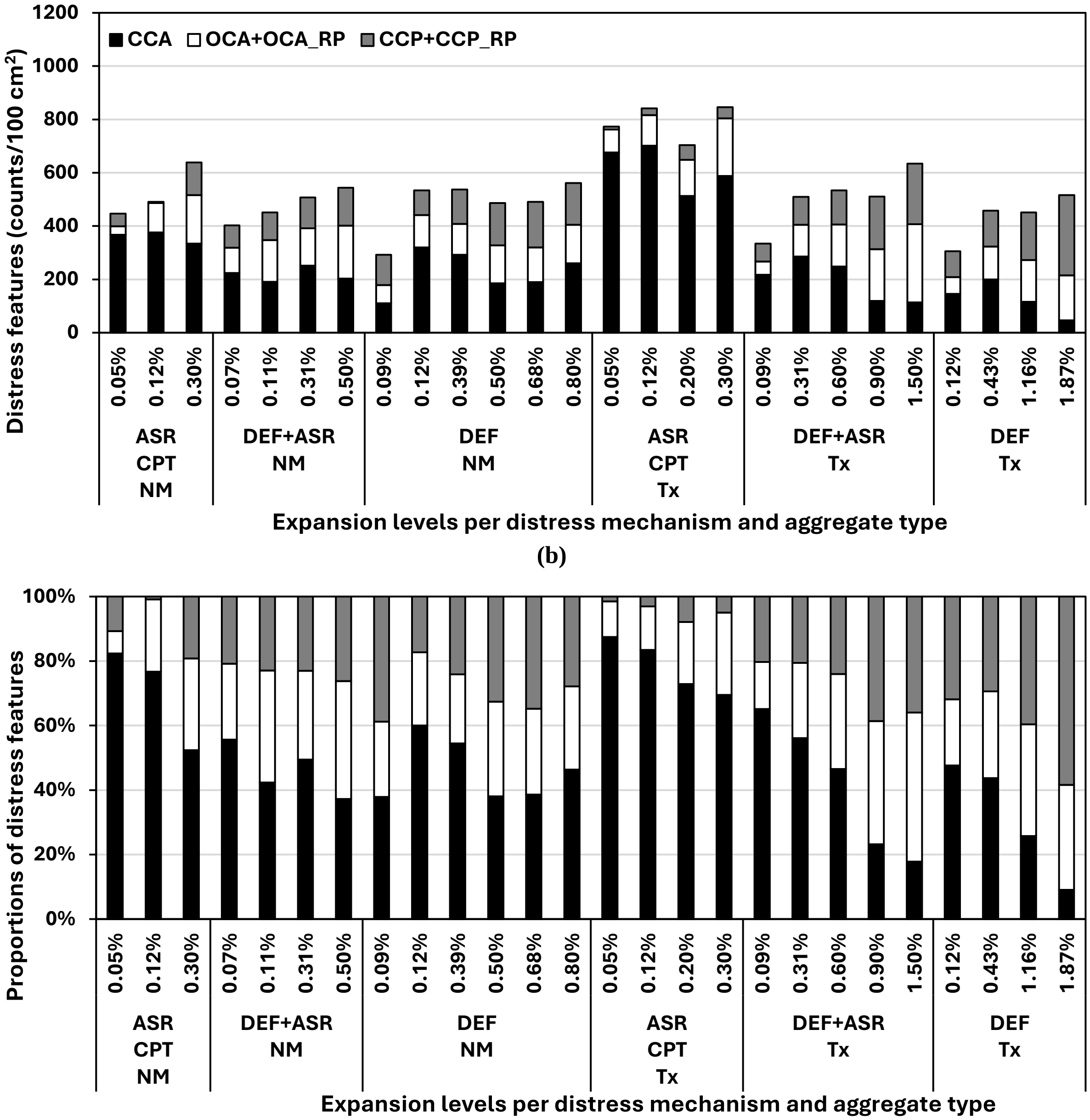

Figure 6.8. Extended version of the DRI as (a) distress feature counts/100 cm^2 and (b) proportions (%) for the ASR and DEF groups.

The crack density, represented as the summation of OCA+OCA_{RP} and CCP+CCP_{RP} per 1 cm^2, further illustrates the propagation of the distress features in combination within one square, as shown in Figure 6.9. The crack density is plotted as a function of expansion, revealing an increase in crack density as expansion increases for all distress mechanisms. Generally, crack density rises with expansion at varying rates, indicated by the different slopes of the trendlines and the starting points where ASR proportioned for the FT groups (i.e., 35 MPa) presents the lowest initial values at 0.79 and 0.70 counts/cm² for the reactive coarse – NM and fine – Tx aggregates, respectively, while 0.79 and 0.97 counts/cm² for the reactive coarse – NM and fine – Tx aggregates, respectively, are obtained from the ASR CPT mixtures (proportioned for the DEF groups). Therefore, an average of less than one open crack in the aggregate or crack in the cement paste is observed per square unit. Conversely, all other distress mechanisms exhibit crack density values greater than 1 count/cm², with the highest value at low expansion levels achieved by ASR+FT at 1.87 counts/cm² and, comparably, FT at 1.80 counts/cm², both made with the reactive coarse aggregate (i.e., NM). Interestingly, the spread of the crack density results at each expansion level is consistent throughout the ASR and FT groups (Figure 6.9a), where the range of values observed at low expansion levels varies by 1.17 counts/cm² and slightly widens to 1.52 counts/cm² at 0.30% expansion, creating an envelope of results (ranging from 2.40 to 3.92 counts/cm²) with a fairly linear relationship, except for ASR + FT made with the reactive sand (Tx). Consequently, the lower coefficient of determination (R^2) of 0.71 can be increased to 0.99 using a parabolic relationship. Moreover, the crack density increases at similar rates for each aggregate type for ASR and FT, while the combined ASR+FT mechanism shows a variable increase for both reactive aggregates. In contrast, the crack densities for the DEF+ASR and DEF groups exhibit a more concave behaviour as expansion increases (Figure 6.9b), where the relationship between crack density and expansion for the DEF specimens made with the reactive coarse aggregate is better represented by a logarithmic model (increasing R^2 to 0.92). Similar to the ASR and FT groups, parallelism is observed between the aggregate types, except for the ASR proportioned with the CPT. The initial and final value ranges are less evident due to the dissimilarity in the studied expansion levels; however, a clear envelope is present.

(a)

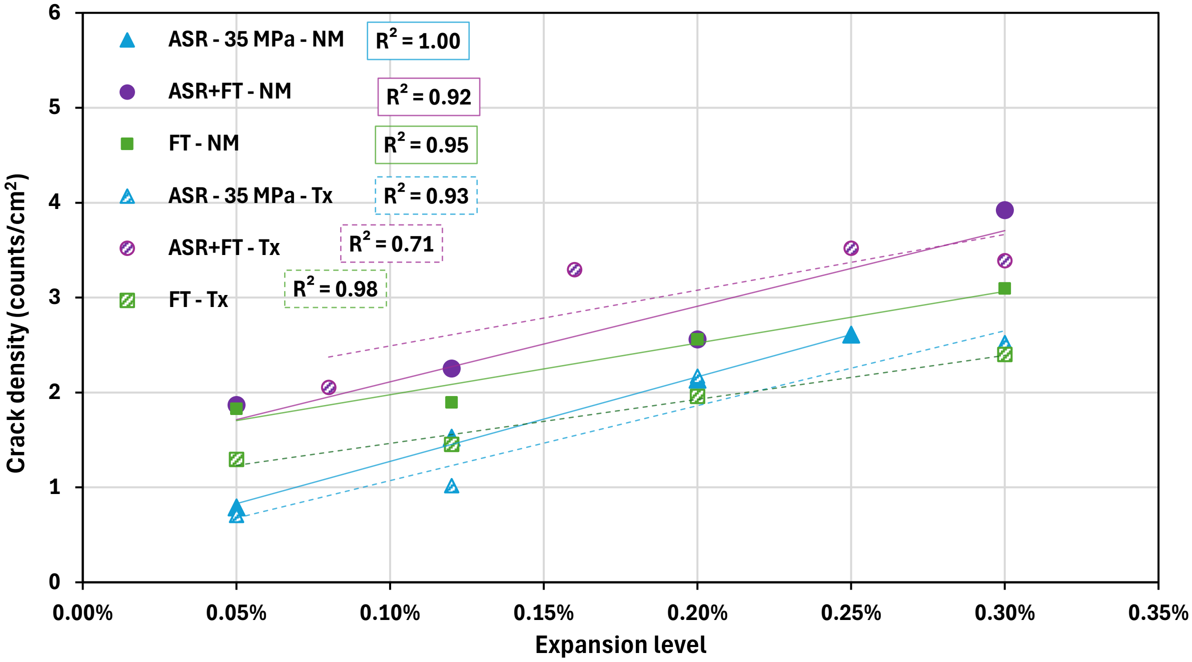

(b)

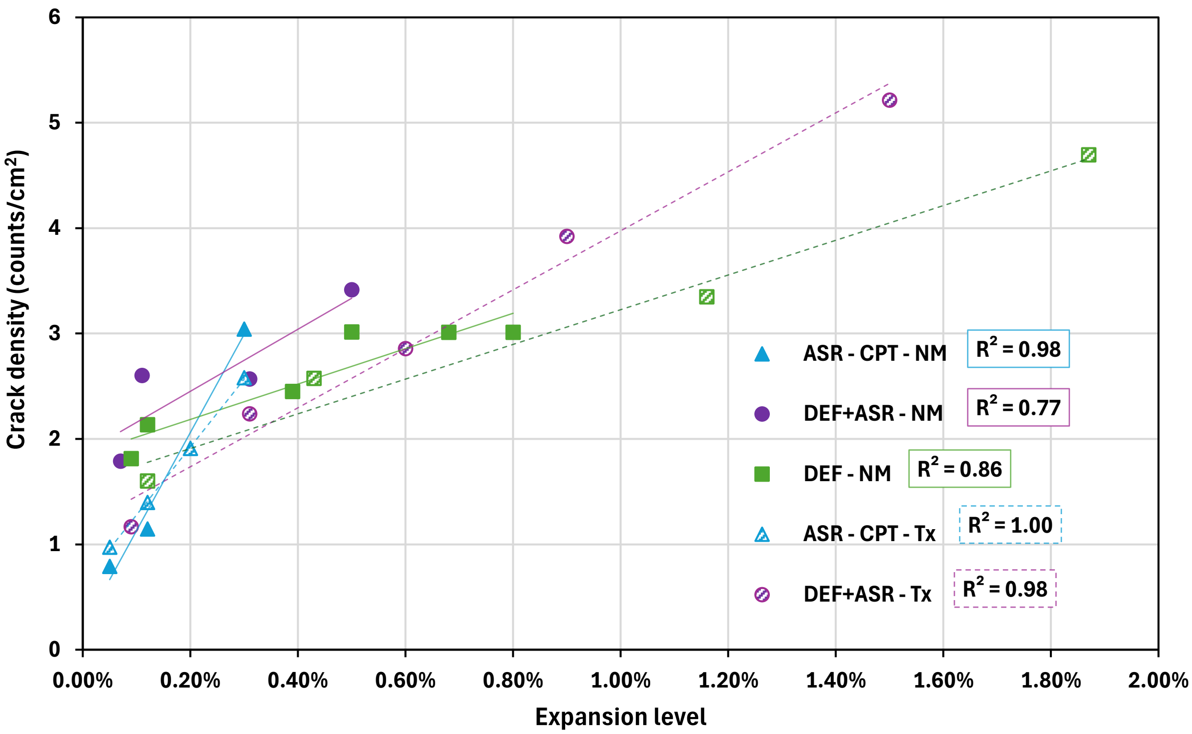

Figure 6.9. Crack density as a function of expansion for (a) ASR and FT groups and (b) ASR and DEF groups.

6.5.3. *Representing damage as a function of the distress features*

The types and numbers of distress features vary with the type of ISR and its extent. Figure 6.10 demonstrates the expansion as a function of the distress features according to the extended version of the DRI (i.e., CCA, $OCA+OCA_{RP}$, and $CCP+CCP_{RP}$) for all distress mechanisms. The increase in colour intensity (from grey to red) indicates the rise in expansion level within each distress mechanism category. Expansion does not respond to the counts of CCA due to the nature of such cracks being unrelated to volumetric increase (Figure 6.10a). On the other hand, $OCA+OCA_{RP}$ and $CCP+CCP_{RP}$ play a more significant role in the resulting expansion levels (Figures 6.10b and c, respectively), where an overall increase in expansion is observed with rising counts. Some clustering is seen for $OCA+OCA_{RP}$, where mechanisms including ASR present the highest counts. Meanwhile, the clustering of the distress mechanisms is more pronounced for $CCP+CCP_{RP}$, thus indicating the influence of the distress mechanism. Consequently, Equation 6.5 describes the increase in expansion (%) as a function of the distinct distress features (counts/100 cm^2), excluding the CCA (i.e., due to the model's decrease in performance when CCA was included to predict expansion) while relating expansion related to $OCA+OCA_{RP}$ and $CCP+CCP_{RP}$. The relationship was further verified using various model combinations and selecting the model with the lowest Akaike Information Criterion (AIC) and Adjusted R^2 (0.88). AIC measures the best fit between models by generalizing the data without overfitting, and the model with the lowest AIC was selected. The Adjusted R^2 considers unnecessary predictors to prevent overfitting, and the highest value was selected. Interactions between the two features are included (Figure 6.11a), and a term to define the mechanism's effect. ASR is presented as the base model, such that other mechanisms are added using the corresponding terms (i.e., 0 – do not include and 1 – include). The error is implicitly accounted for when fitting the linear model.

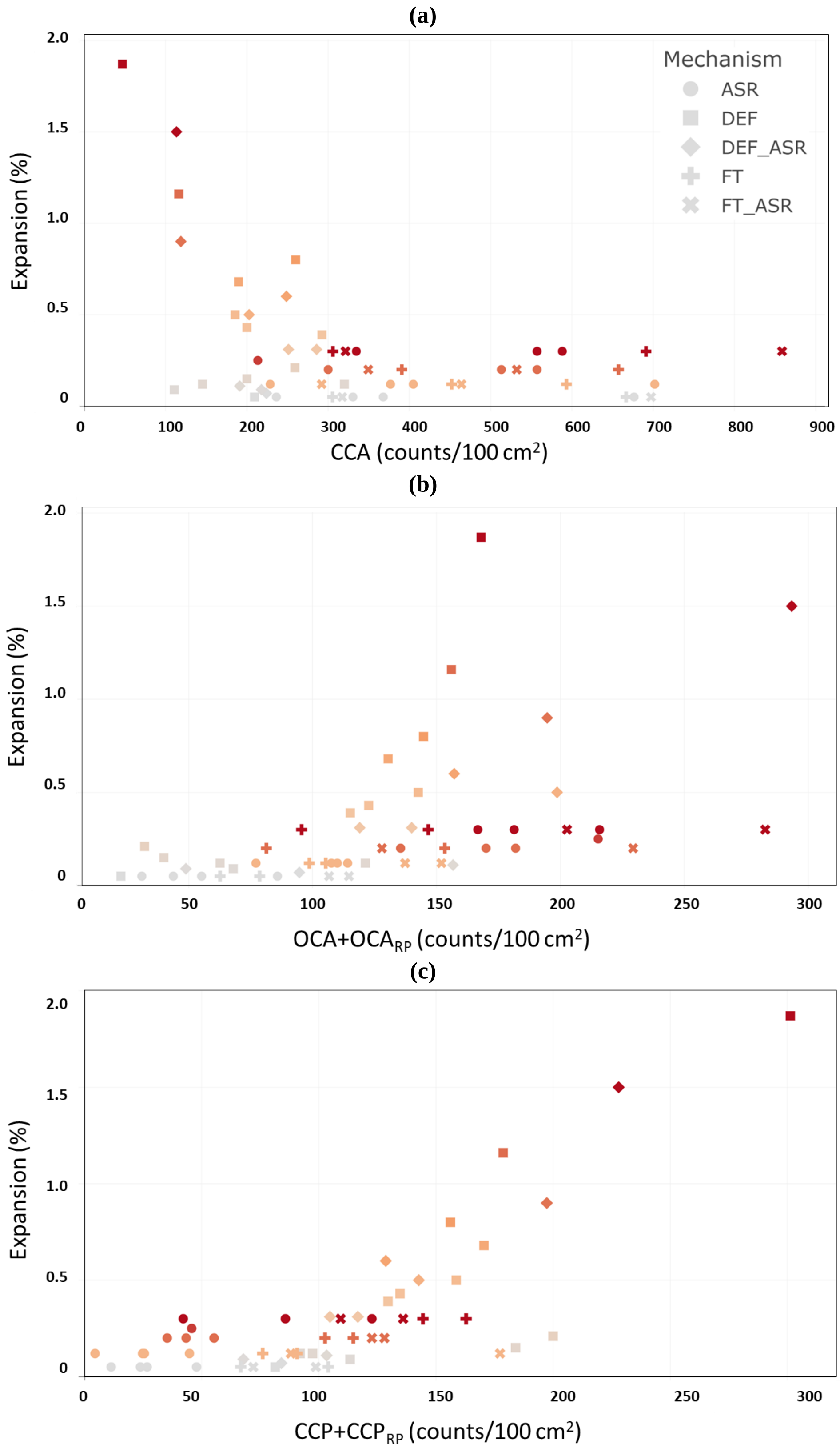

Figure 6.10. Expansion as a function of: (a) CCA, (b) OCA+OCA$_{RP}$, and (c) CCP+CCP$_{RP}$ distress feature counts for all distress mechanisms.

$$\varepsilon(\%) = (-2.226\times10^{-2}) + (9.718\times10^{-4})(OCA_{TOTAL}) + (2.699\times10^{-6})(CCP_{TOTAL})^2 + (8.333\times10^{-8})(OCA_{TOTAL})(CCP_{TOTAL})^2 + (7.608\times10^{-2})(DEF) - (4.025\times10^{-2})(DEF\&ASR) - (7.981\times10^{-2})(FT) - (2.437\times10^{-1})(FT\&ASR) \quad \text{Eq. 6.5}$$

Where OCA_{TOTAL} and CCP_{TOTAL} are the distress feature counts/100 cm^2, and $DEF, DEF\&ASR, FT$ and $FT\&ASR$ are the distress mechanism factors.

(a)

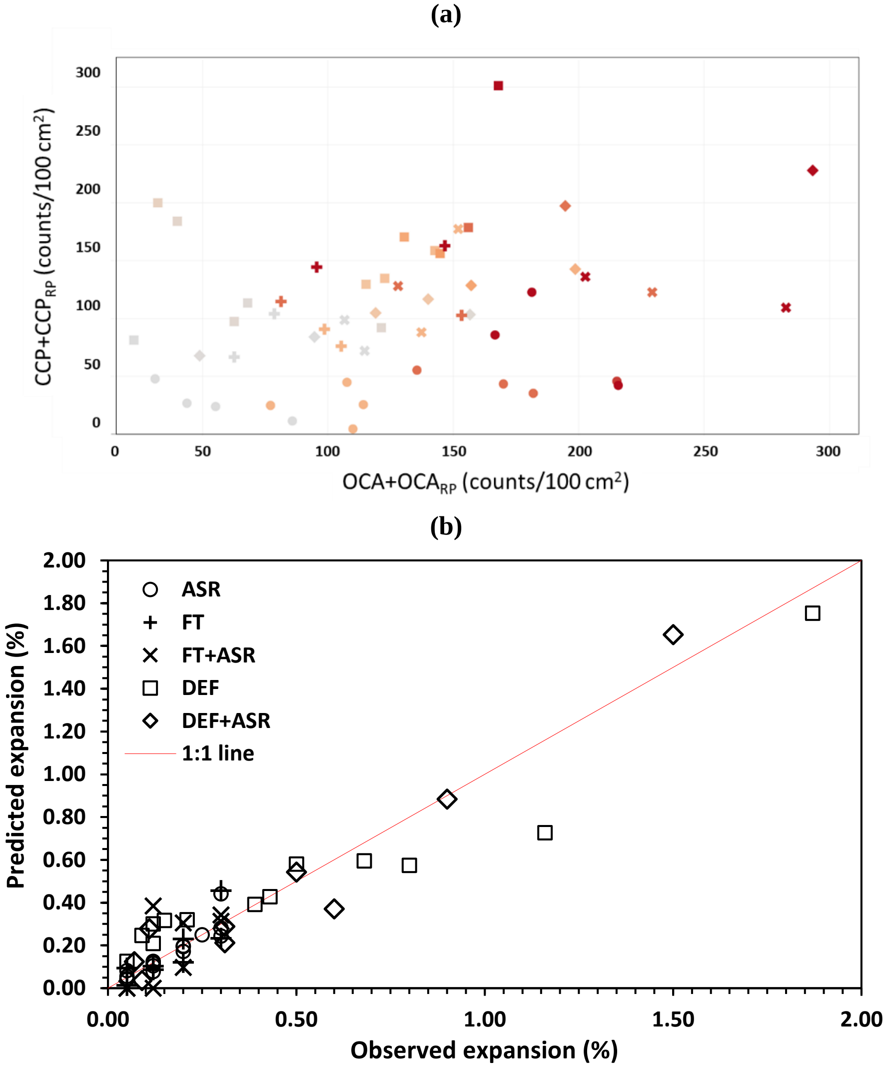

Figure 6.11. (a) CCP+CCP$_{RP}$ vs OCA+OCA$_{RP}$ and (b) predicted vs observed expansion.

While the chosen model and obtained coefficients offer the best fit, important discrepancies remain where an observed expansion of 0.05% is predicted at 0 to 0.09%, and an observed expansion of 0.12% is predicted at 0 to 0.39%. At the observed expansions of 0.20% and 0.30%, the predicted values vary from 0.10 to 0.31% and 0.23 to 0.46% of expansion, respectively. However, for greater levels of expansion, the predicted values stay closer to the 1:1 line, except for DEF at 1.16% of observed expansion, predicted at 0.73%. Nonetheless, both are deemed ultra-high degrees of damage, falling within the same damage extent category as per [2].

6.5.4. Using the distress features to describe mechanical responses

Expansion signifies volumetric changes in concrete influenced by ISR; however, the mechanical responses to a specific expansion differ based on the type of ISR encountered. Consequently, the mechanical responses related to the distress features, represented by the extended version of the DRI (i.e., CCA, $OCA+OCA_{RP}$, $CCP+CCP_{RP}$, and Debon), were utilized for linear regression. This method enhanced the understanding of each distress feature's role in ISR-induced deterioration. The predicted mechanical responses (i.e., remaining mechanical properties and SDT output parameters) are determined using Equation 6.6 and Tables 6.3 and 6.4 coefficients, respectively. ASR is the base model, incorporating additional mechanisms using the corresponding terms (i.e., 0 – do not include and 1 – include). The relationships between the predicted and observed remaining mechanical properties (i.e., tensile – f_t and compressive - f_c strengths and elastic modulus - E) for all distress mechanisms are illustrated in Figures 6.12a, b, and c, respectively, while the SDT output parameters (i.e., hysteresis area – HA, stiffness damage index – SDI, and plastic deformation index – PDI) are shown in Figures 6.12d, e, and f, respectively. Appendix D details the remaining mechanical properties in relation to each distress feature. The Adjusted R^2 values are reported as 0.43, 0.83, and 0.85 for the tensile and compressive strengths and the elastic modulus, respectively. The remaining tensile strength solely encompasses the ASR and FT groups, while the remaining compressive strength and modulus of elasticity consider all distress mechanisms.

Some clustering is observed for the remaining tensile strength despite a ±20% difference between the predicted and observed values (Figure 6.12a). Overestimations of 20% for the FT+ASR compressive strengths are shown, while a maximum difference of 7% is recorded for all other distress mechanisms (Figure 6.12b). Regarding the modulus of elasticity, significantly smaller variations are noted at ±6% (Figure 6.12c). There is a certain degree of clustering evident for both compressive strength and modulus of elasticity; however, this is attributed to various levels of deterioration.

$$Remaining\ mechanical\ property\ or\ mechanical\ response = \beta_0 + \beta_1(x_1) + \beta_2(x_2) + \beta_3(x_3) + \cdots + \beta_{19}(x_{19}) \quad \text{Eq. 6.6}$$

Table 6.3. Regression coefficient estimates for the remaining mechanical property as a function of distress features and mechanism.

	Mechanical property (%)	f_t	f_c	E
Coefficient	Raised variable, x_i	-	CCP^4	$CCA^{0.25}$, OCA^3, CCP^6
β_0	Intercept	5.450E+01	1.490E+02	7.743E+01
β_1	CCA	-7.546E-03	-7.087E-02	-1.229E+00
β_2	OCA+OCA_{RP}	-4.381E-02	-6.254E-01	-7.345E-07
β_3	CCP+CCP_{RP}	-1.357E-08	-4.630E-01	1.368E-11
β_4	Debon	0	1.997E+01	1.140E+02
β_5	CCA*(OCA+OCA_{RP})	0	8.597E-04	-4.810E-07
β_6	CCA*(CCP+CCP_{RP})	0	6.004E-04	-3.992E-12
β_7	(OCA+OCA_{RP})*(CCP+CCP_{RP})	0	4.308E-03	-1.515E-18
β_8	CCA*Debon	0	-1.115E-01	-3.072E+01
β_9	(OCA+OCA_{RP})*Debon	0	-2.085E-01	-1.818E-05
β_{10}	(CCP+CCP_{RP})*Debon	0	-2.613E-03	-4.856E-11
β_{11}	CCA*(OCA+OCA_{RP})*(CCP+CCP_{RP})	0	-6.574E-06	4.804E-19
β_{12}	CCA*(OCA+OCA_{RP})*Debon	0	1.066E-03	5.152E-06
β_{13}	CCA*(CCP+CCP_{RP})*Debon	0	4.576E-04	1.307E-11
β_{14}	(OCA+OCA_{RP})*(CCP+CCP_{RP})*Debon	0	2.355E-04	1.509E-17
β_{15}	CCA*(OCA+OCA_{RP})*(CCP+CCP_{RP})*Debon	0	-4.482E-06	-4.048E-18
β_{16}	DEF	-	-1.841E+01	-3.605E+01
β_{17}	DEF&ASR	-	-1.461E+01	-2.077E+01
β_{18}	FT	-1.045E+01	-2.530E+00	2.491E+00
β_{19}	FT&ASR	-2.643E-01	-1.017E-01	1.128E+01
	Adjusted R^2	0.43	0.83	0.85

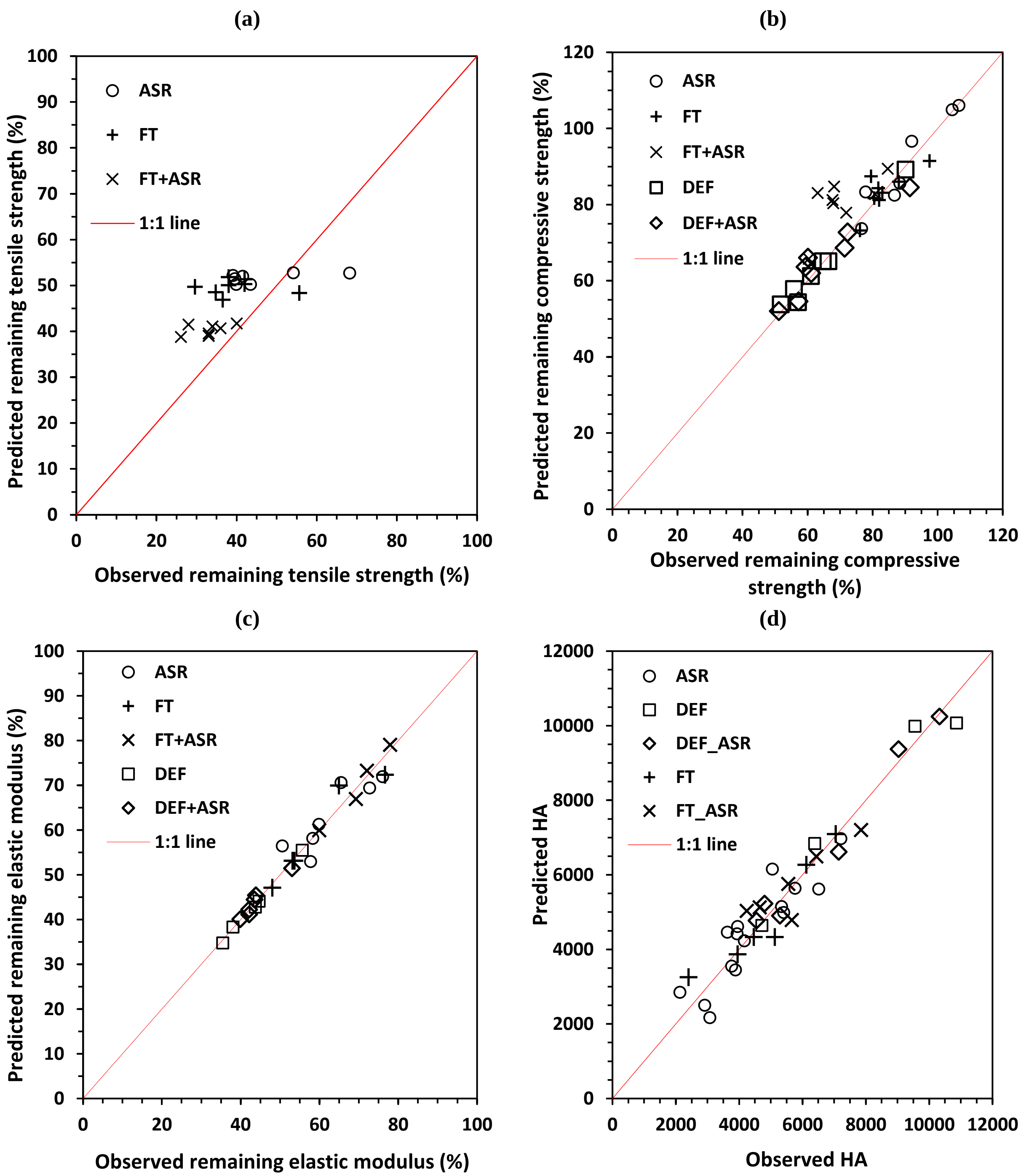
(a)
Predicted remaining tensile strength (%)
Observed remaining tensile strength (%)
ASR
FT
FT+ASR
1:1 line
(b)
Predicted remaining compressive strength (%)
Observed remaining compressive strength (%)
ASR
FT
FT+ASR
DEF
DEF+ASR
1:1 line
(c)
Predicted remaining elastic modulus (%)
Observed remaining elastic modulus (%)
ASR
FT
FT+ASR
DEF
DEF+ASR
1:1 line
(d)
Predicted HA
Observed HA
ASR
DEF
DEF_ASR
FT
FT_ASR
1:1 line

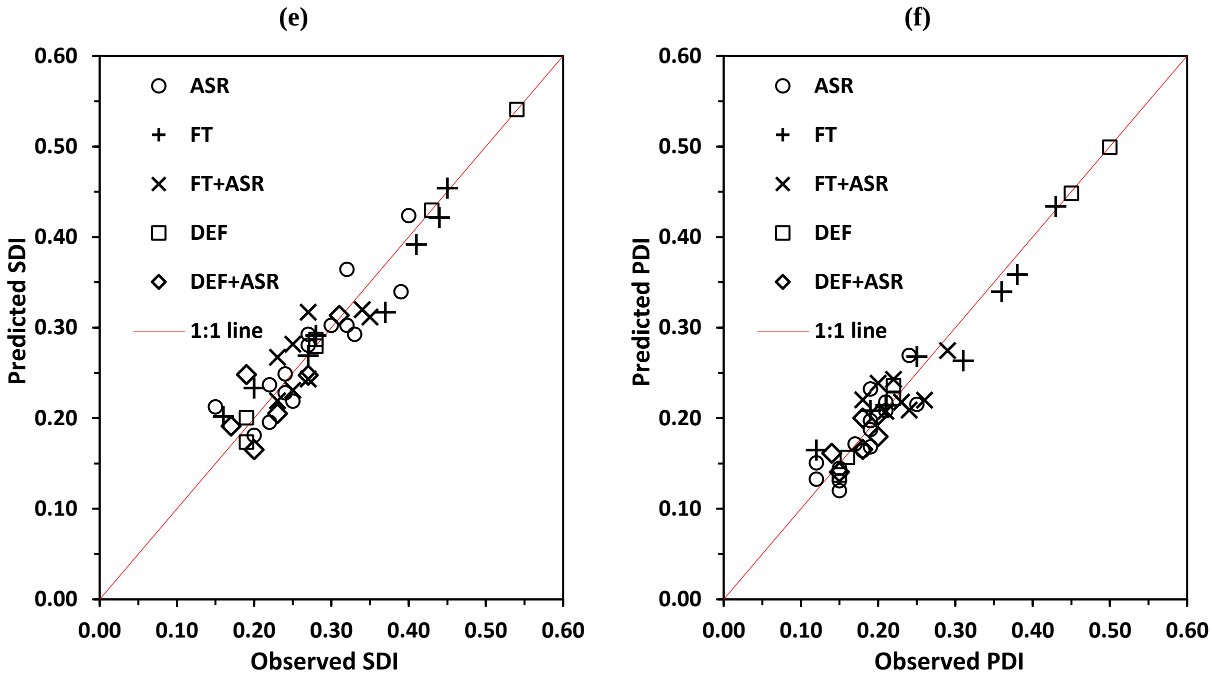

Figure 6.12. Predicted vs observed remaining mechanical properties (a) tensile strength, (b) compressive strength, (c) elastic modulus, and SDT output parameters, (d) the hysteresis area – HA, (e) stiffness damage index- SDI, and f) the plastic deformation index -PDI.

The SDT output parameters are compared using the same number of coefficients as the remaining mechanical properties. Table 6.4 presents the estimates of each coefficient for the hysteresis area (HA), the stiffness damage index (SDI), and the plastic deformation index (PDI), along with the R^2 values of 0.85, 0.80, and 0.88, respectively. Figures 6.12e and f illustrate a more scattered fit along the 1:1 line for the SDI compared to the PDI. The most considerable difference in predicted versus observed SDI and PDI is ±0.05 and ±0.04, respectively.

Table 6.4. Regression coefficient estimates for the SDT output parameters as a function of distress features and mechanism.

	SDT output parameter	HA	SDI	PDI
Coefficient	Raised variable, x_i	CCP^4	CCP^4	CCP^4
β_0	Intercept	9.956E+02	2.456E-01	1.826E-01
β_1	CCA	6.095E-01	-2.515E-04	-2.259E-04
β_2	OCA+OCA_{RP}	3.413E+01	-2.237E-04	-3.285E-05
β_3	CCP+CCP_{RP}	5.873E-06	-5.794E-10	-5.573E-10
β_4	Debon	3.311E+03	-2.576E-03	-1.971E-02
β_5	CCA*(OCA+OCA_{RP})	-1.363E-02	2.956E-06	1.792E-06
β_6	CCA*(CCP+CCP_{RP})	1.649E-08	2.357E-12	2.204E-12
β_7	(OCA+OCA_{RP})*(CCP+CCP_{RP})	-1.171E-07	3.802E-12	3.177E-12
β_8	CCA*Debon	-2.275E+01	-8.521E-05	5.187E-05
β_9	(OCA+OCA_{RP})*Debon	-4.750E+01	6.031E-05	1.227E-04
β_{10}	(CCP+CCP_{RP})*Debon	-3.289E-05	-5.303E-11	2.730E-11
β_{11}	CCA*(OCA+OCA_{RP})*(CCP+CCP_{RP})	2.053E-11	-1.537E-14	-1.338E-14
β_{12}	CCA*(OCA+OCA_{RP})*Debon	2.080E-01	6.976E-07	-1.928E-07
β_{13}	CCA*(CCP+CCP_{RP})*Debon	3.123E-07	1.579E-12	7.732E-13
β_{14}	(OCA+OCA_{RP})*(CCP+CCP_{RP})*Debon	2.886E-07	3.298E-13	-1.744E-13
β_{15}	CCA*(OCA+OCA_{RP})*(CCP+CCP_{RP})*Debon	-2.270E-09	-9.855E-15	-4.098E-15
β_{16}	DEF	2.196E+03	-5.517E-02	-2.025E-02
β_{17}	DEF&ASR	2.166E+03	-4.541E-02	-8.919E-03
β_{18}	FT	7.547E+01	2.760E-03	4.891E-02
β_{19}	FT&ASR	4.706E+02	-2.990E-02	3.472E-02
	Adjusted R^2	0.85	0.80	0.88

6.6. Discussion

6.6.1. Representative sample to capture damage pattern

The DRI and its extended version generalize the deterioration pattern across the analyzed surface, where the counts may vary from square to square. Establishing a significant sample size can depend on many variables, such as the operator's experience and familiarity with the type and level of deterioration, crack pattern, and damage homogeneity. While a sample in laboratory testing is often referred to as a collection of three or more specimens for conducting further statistical analyses, microscopy samples, in general, are limited by constraints imposed by the equipment and the time required to prepare and analyze the specimens. For the DRI, the prepared surface is divided into 1 cm by 1 cm squares, and these incremental squares represent the space frame in which the analysis is conducted. Fluctuations in the cumulative DRI number can be observed, and convergence towards a stable DRI number is generally achieved after observing a certain number of squares. This convergence effect can be explained by the law of large numbers, where, as the sample size increases, convergence towards the mean (i.e., final DRI number) is reached, as expressed in Equation 6.7.

$$DRI = \bar{X}_n = \frac{\sum_{i=1}^{n} X_i}{i} = \frac{X_1 + X_2 + X_3 + \cdots + X_n}{n} \qquad \text{Eq. 6.7}$$

Where X_i represents the DRI number until square i and n is the total number of analyzed squares or sample size.

The convergence plots, therefore, can validate the significance of the sample size (Figure 6.13). It is advisable to use the convergence plots to verify the homogeneity of the sample rather than to define a minimum sample size. Convergence is generally achieved at smaller n for lower levels of expansion, which corresponds to the less connected spread of the distress features at low levels of expansion. In contrast, a larger sample size is necessary to achieve this convergence at higher expansion levels, likely due to extensive crack propagation. Nevertheless, this visual representation of the converging cumulative DRI can indicate damage homogeneity and determine whether the value reaches convergence based on the number of 1 cm by 1 cm squares. Sanchez et al. (2016) initially indicated that a minimum of 100 cm^2 is sufficient to analyze laboratory-made specimens [10], validated through the convergence plots. It is, therefore, suggested to use 75±25 cm^2 for laboratory-made specimens, while 200 cm^2 continues to be recommended for field concrete. However, due to damage distribution across the depth of a core from field concrete, a fixed sample size may not always be representative. Conditions such as configurations for testing aggregate reactivity, mixture reactivity, and residual expansion; reinforcement ratios, bar distances, cover thickness, humidity and weather conditions; cyclical wetting and drying, among others, may influence the damage pattern and, consequently, the homogeneity of the distribution of distress features. Therefore, heat maps illustrating deterioration regions can assist in defining a damage profile and segmenting homogeneous regions [61,62].

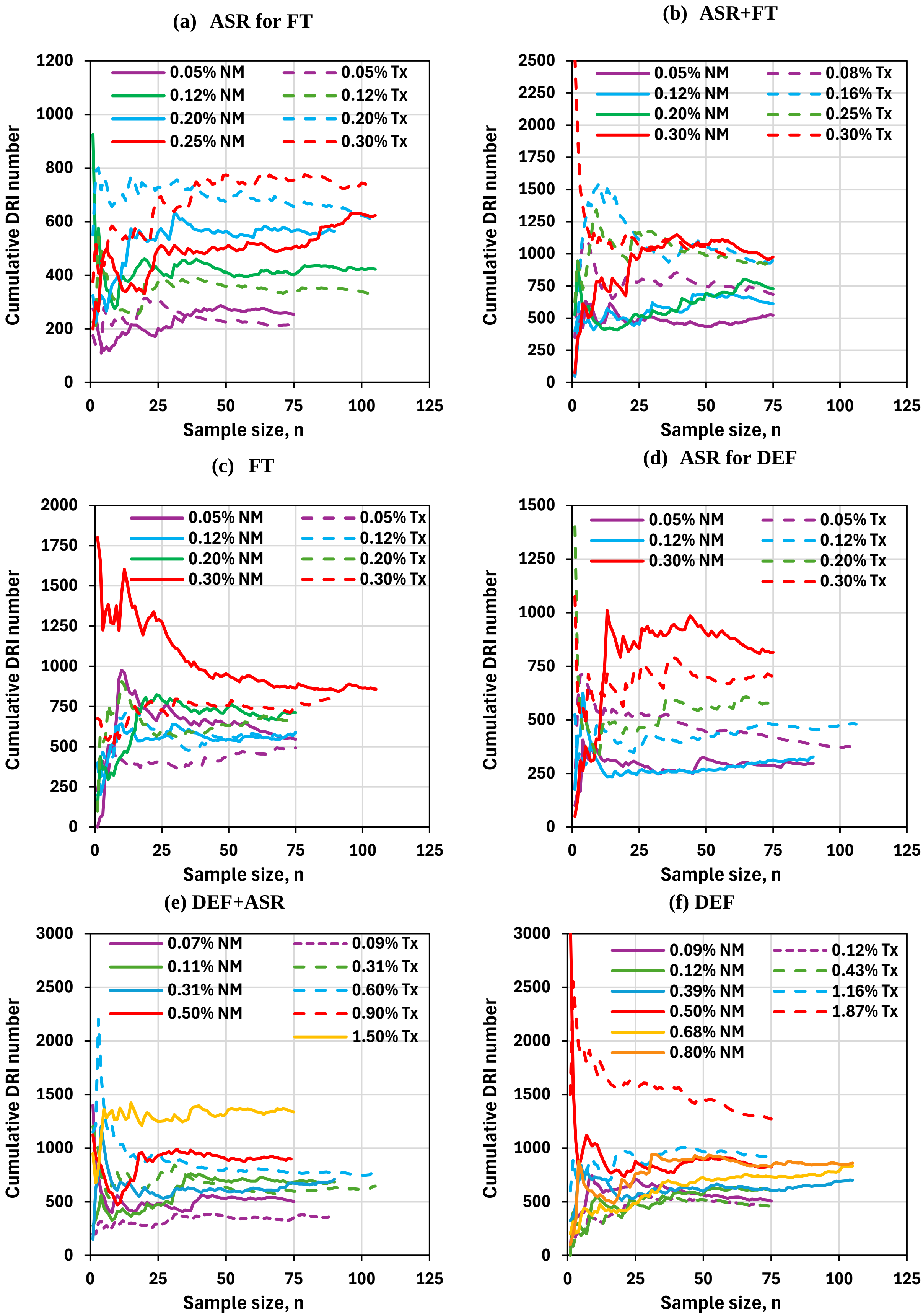
(a) ASR for FT
Cumulative DRI number
Sample size, n
0.05% NM
0.12% NM
0.20% NM
0.25% NM
0.05% Tx
0.12% Tx
0.20% Tx
0.30% Tx
(b) ASR+FT
Cumulative DRI number
Sample size, n
0.05% NM
0.12% NM
0.20% NM
0.30% NM
0.08% Tx
0.16% Tx
0.25% Tx
0.30% Tx
(c) FT
Cumulative DRI number
Sample size, n
0.05% NM
0.12% NM
0.20% NM
0.30% NM
0.05% Tx
0.12% Tx
0.20% Tx
0.30% Tx
(d) ASR for DEF
Cumulative DRI number
Sample size, n
0.05% NM
0.12% NM
0.30% NM
0.05% Tx
0.12% Tx
0.20% Tx
0.30% Tx
(e) DEF+ASR
Cumulative DRI number
Sample size, n
0.07% NM
0.11% NM
0.31% NM
0.50% NM
0.09% Tx
0.31% Tx
0.60% Tx
0.90% Tx
1.50% Tx
(f) DEF
Cumulative DRI number
Sample size, n
0.09% NM
0.12% NM
0.39% NM
0.50% NM
0.68% NM
0.80% NM
0.12% Tx
0.43% Tx
1.16% Tx
1.87% Tx

Figure 6.13. DRI sample size convergence plots.

6.6.2. Indicators of the cause of ISR deterioration

Homogenizing the DRI weighting factors [4,5] associated with distress features, both without and with reaction products, aimed to reduce operator variability. This was further supported by Sanchez et al. (2015,2020), where an increase in expansion was not linked to an increase in distress features with reaction products, illustrating the contribution of such distress and petrographic characteristics [11,60]. Additionally, Sanchez et al. (2020) explored the correlation between the DRI and the distress features that best describe concrete deterioration. They observed strong correlations between the modulus of elasticity and SDI as a function of the DRI, with the different slopes in the SDI versus DRI plot demonstrating the impact of the type of aggregate and distress mechanism. Distress features that have a less evident effect on mechanical properties include closed cracks in the aggregates (CCA), therefore, some researchers have pointed out the limited role of CCA concerning expansion [61]. However, their impact on crack propagation remains significant, as illustrated by Figures 6.7 and 6.8 through the extended version of the DRI. When incorporating CCA into the regression to predict the remaining mechanical properties, the Adjusted R^2 for the remaining compressive strength and modulus of elasticity increased. Overall, the deviations for compressive strength and modulus of elasticity from the observed values are less impactful from a practical standpoint, except for the FT+ASR mechanism. As such, differences in compressive strength losses of 20-40% result in marginal to very high damage degree classification, as noted in [2]. Nonetheless, the influence of the distress features on the mechanical properties is reflected in these relationships, showcasing the contribution of CCA to mechanical responses. The significance of these features is underscored when comparing the magnitudes of the linear model coefficient estimates for each distress feature and mechanism relating to all mechanical responses.

All estimates for the remaining tensile strength of the ASR and FT groups are negative, with $CCP+CCP_{RP}$ showing the smallest effect and $OCA+OCA_{RP}$ demonstrating the largest effect. Generally, in sound concrete, tensile strength is influenced by "defects" such as the aggregate-paste interface and pre-existing cracks in the cement paste [63]. However, in ASR-affected concrete, pre-existing defects include cracks in the aggregates, particularly open ones. Furthermore, the stop-arrest mechanism described in [64] may be diminished for ASR-affected concrete due to the open cracks in the aggregate serving as a pathway for the leading crack. Both mechanisms (i.e. FT and FT+ASR) exhibit more significant tensile strength reductions than the ASR baseline. Nonetheless, it is established that the tensile strength of ISR-affected concrete depends on the length of the leading crack reaching a critical value (i.e., faster crack propagation), resulting in a brittle failure [64]. Therefore, in this context, higher crack counts only affect the rate at which this critical length is reached rather than being directly related to tensile strength. Consequently, the remaining tensile strength is not adequately described by the counts of distress features.

The $OCA+OCA_{RP}$, regarding the remaining compressive strength, on the other hand, has a more significant negative effect, followed by the CCA. The Debon-type crack demonstrates the largest positive effect, indicating that the remaining mechanical property also increases as Debon increases. This may stem from the limited number of such cracks due to the adopted counting method, which applies only to DEF and DEF+ASR. The interaction among all the distress features does not reveal a clear pattern, as some interactions cause an increase in the remaining compressive strength. Compressive strength, compared to tensile strength, is less governed by fracture mechanics since the mechanism of concrete failure in compression is relatively more "ductile" than in tension and is not fully governed by a singular crack reaching a critical length. Cracks generated by compressive loading form in the weaker zones, such as the aggregate-paste interface, and propagate into the cement paste until they interlink to cause failure under compression [63]. ISR creates cracks that spread throughout the concrete; consequently, the distances required for distress features to connect are reduced. Thus, as more cracks are identified, resistance to compressive failure diminishes. Cracks contained within the aggregates (i.e., without extending into the cement paste) do not directly affect compressive strength; however, when they reach the cement paste (i.e., due to ASR advancement), a decrease is observed [64]. While the proportion of $OCA+OCA_{RP}$ is more significant than $CCP+CCP_{RP}$ for ASR, cracks in the cement paste result from cracks widening in the aggregate. Meanwhile, for ISR mechanisms that develop in the cement paste (i.e., FT and DEF), a reduction in compressive strength is seen earlier than with ASR, further underscored by the negative estimates from Table 6.3 from these mechanisms.

As expected, the modulus of elasticity appears to be most influenced by CCA, $OCA+OCA_{RP}$ and Debon-type cracks. From a petrographic standpoint, CCA may not affect expansion but demonstrates a mechanical impact. In some instances, CCA may represent a shear crack characterized by slippage rather than opening, thereby producing virtually no expansion. The modulus of elasticity of concrete is determined by aggregate stiffness, cement paste porosity, and the aggregate-paste interface [63]. Cracks in the aggregates inherently weaken the aggregate as a defect, reducing its stiffness. Moreover, debonded/disaggregated (i.e., Debon) type cracks impact the remaining mechanical properties rather than the expansion predicted by Equation 6.5; this underscores the need to include such features in the counts to describe damage deterioration at the aggregate-paste interface more accurately. As such, a gap in the aggregate-paste interface diminishes the capacity to transfer stresses from the cement paste to the aggregate, thereby reducing the modulus of elasticity [63]. This type of distress is most commonly found in DEF-affected concrete, contributing to the petrographic nature of the distress feature. However, additional work is needed to integrate the counting procedure proposed by Trottier et al. (2024) [39]. All ISR, in comparison to the ASR baseline, show greater declines in mechanical properties, except for the modulus of elasticity of FT and FT+ASR. A greater decline in the modulus of elasticity for the DEF and DEF+ASR-affected concrete is likely due to the presence of Debon-type cracks.

When analyzing the coefficient estimates of the SDT output parameters, the influence of the hysteresis area (HA), as proposed by Sanchez et al. (2014) [65] and considering the energy required to close open cracks, was captured in Table 6.4. The HA estimates were primarily affected by OCA+OCA_{RP} and Debon-type cracks, while most were impacted by DEF, DEF+ASR, FT+ASR, and FT, followed by ASR. The SDI and PDI generally presented similar estimates (very small), yet OCA+OCA_{RP} has a greater influence on the SDI due to the closure of such cracks. Debon-type cracks exert a greater influence on the PDI, likely due to the volumetric expansion of the cement paste, which is akin to the effect of high temperatures [63,66,67]. The CCA demonstrated a similar influence on both output parameters, again underscoring its role in mechanical response. Likewise, the effect on SDI and PDI of DEF and DEF+ASR is less severe than that of ASR alone, while FT+ASR decreases the SDI and increases the PDI, and FT alone increases both the SDI and PDI compared to ASR. In summary, the extent of ISR deterioration does not produce the same deterioration pattern for a given expansion. The distress features vary concerning the observed ISR, resulting in distinct deterioration patterns for each distress mechanism expansion.

Lindgård et al. (2012) further emphasized the necessity for the DRI to encompass a parameter for crack extensions from the aggregate to the cement paste [68]. In response, Sanchez et al. (2020) examined the proportions of cracks originating from or extending to aggregate-paste, interface-paste, and isolated pore/paste cracks [11]. Plotting mechanical responses against crack extensions (Figure 6.14) does not reveal a clear relationship; however, distinct clustering based on distress mechanisms is observed. This suggests that the distress mechanism influences crack extension proportions. Although the total count of crack extensions may not accurately depict the extent of damage as indicated by mechanical responses, it effectively represents the type of deterioration. These crack extensions might exhibit a more petrographic nature, helping to identify the causes of ISR deterioration, significantly affecting damage.

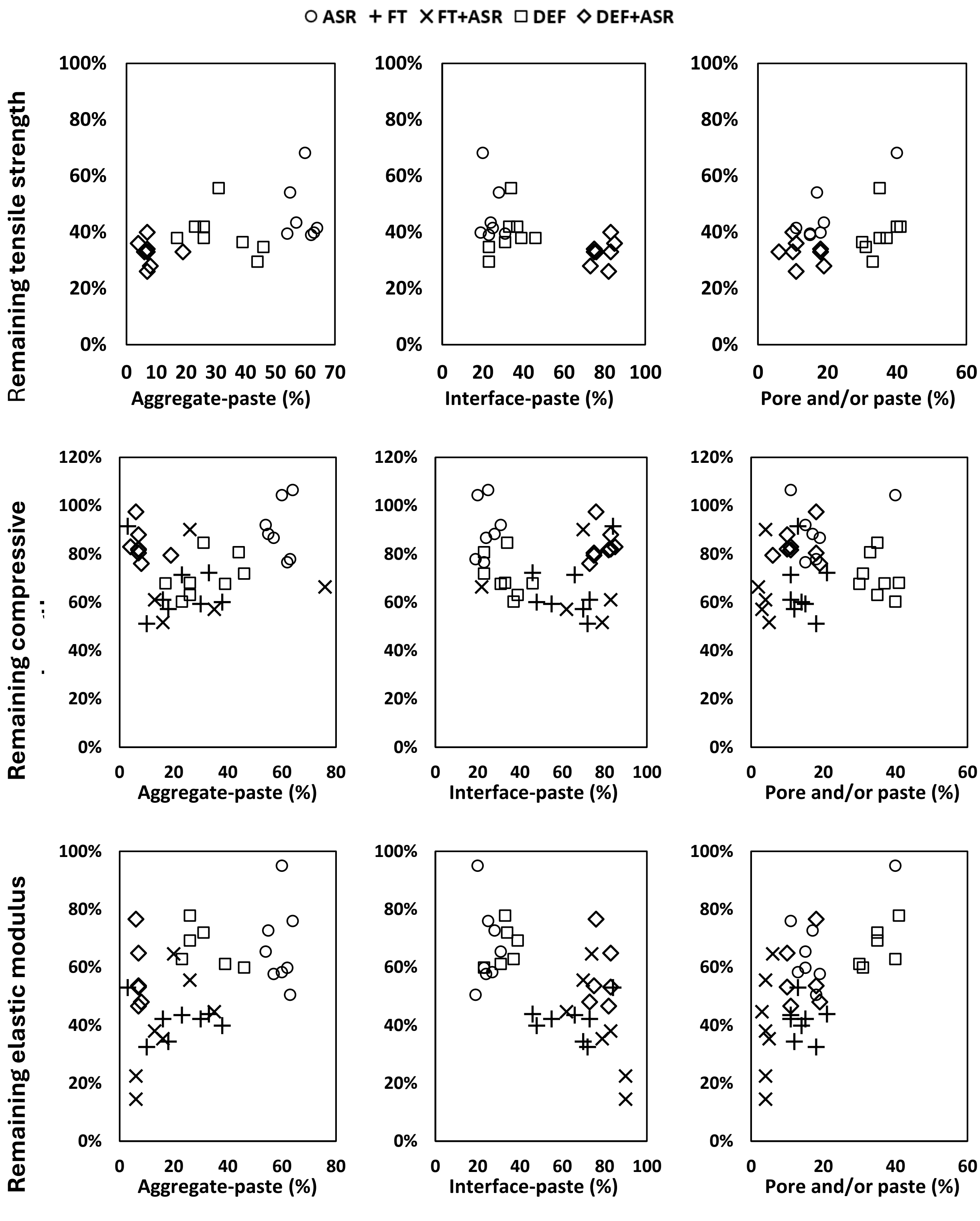

ASR
FT
FT+ASR
DEF
DEF+ASR
Remaining tensile strength
Remaining compressive
Remaining elastic modulus
Aggregate-paste (%)
Interface-paste (%)
Pore and/or paste (%)

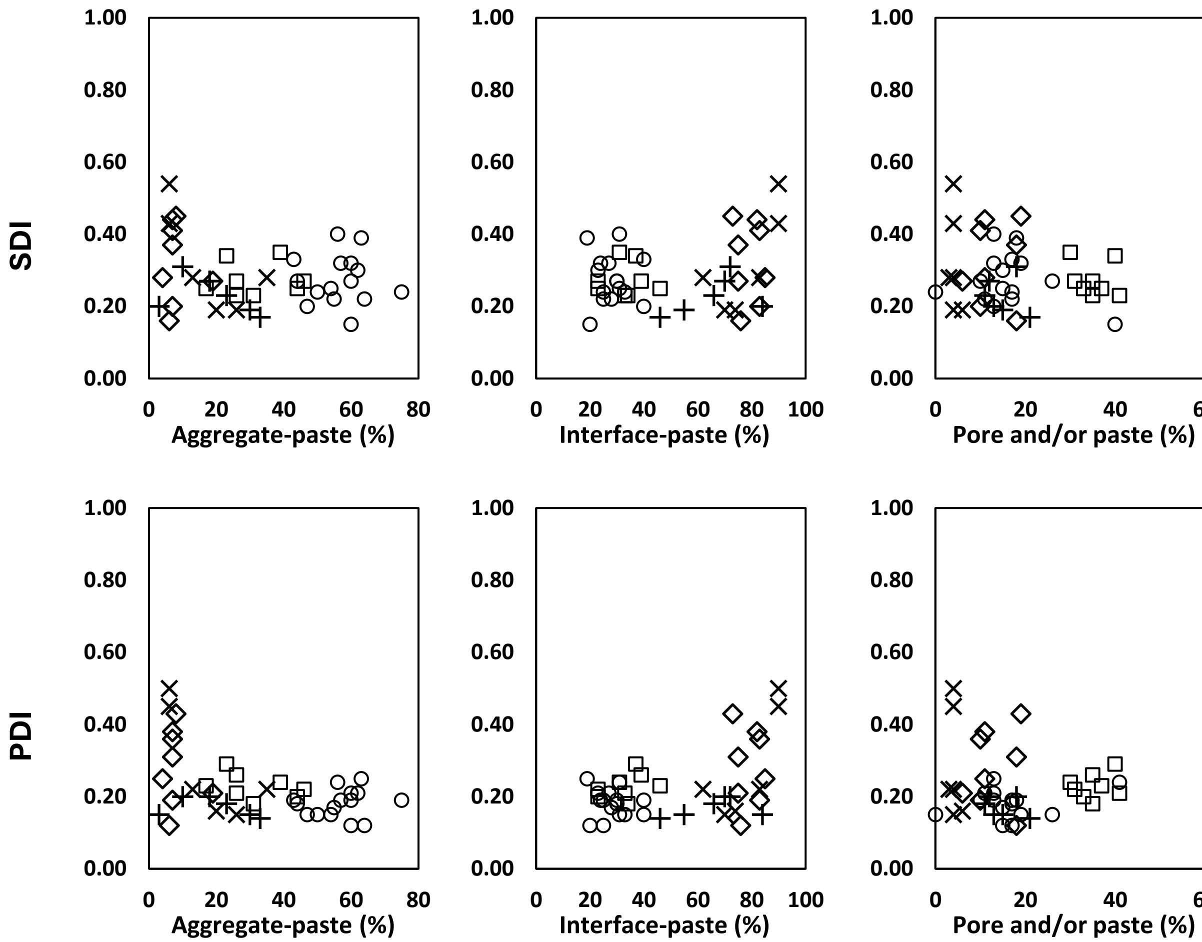

Figure 6.14. Mechanical responses as a function of the distress feature extensions.

The distress mechanism is a categorical variable defined by petrographic and distress features, crack extensions, and overall deterioration patterns. The extent of its damage can be viewed as a categorical variable since the magnitude of expansion does not lead to the same deterioration for each ISR. Nevertheless, this work presents a comprehensive framework of the various methods to characterize the causes of ISR deterioration through the extended version of the DRI.

6.6.3. Predicted extent of the deterioration

An increasing level of ISR-induced deterioration generally results in more distress features produced per 1 cm by 1 cm square, and/or previously formed distress features may become connected, which varies depending on the distress mechanism observed. However, this increase can be localized and may not occur in every 1 cm by 1 cm square. Moreover, the varying trends observed in Figure 6.9 regarding crack density, which demonstrates different slopes and linearities, and the clustering per ISR in Figures 6.12 and 6.14 indicate the specific influence of ISR on expansion and mechanical responses, respectively. However, in Equations 6.5 and 6.6, the type of ISR is included as a variable that only proportionally affects the expansion and mechanical response, respectively. Nonetheless, expansion remains the key metric for describing ISR-induced deterioration; therefore, encompassing these aspects for classifying ISR deterioration based on expansion is necessary. In addition to the total counts of distress features, boxplots (i.e., summarizing the data distribution) of the count frequencies illustrate the frequency of distinct distress features recorded in the 1 cm by 1 cm squares, thereby capturing these localized effects (e.g., as deterioration increases, the number of distress features per square also rises, thereby shifting the descriptive statistics of the distress feature boxplot counts upwards). The boxplots display the mean, median, upper and lower whiskers, interquartile ranges, and outliers (as shown in Appendix B). Furthermore, analyzing the data from the deconstructed extended version of the DRI enabled the acquisition of descriptive statistics such as the mean, variance, standard deviation (SD), minimum and maximum values, and the number of analyzed squares (n), which are tabulated in Appendix C for further reference.

The average count value (i.e., total counts divided by n, which can be multiplied by 100 to obtain counts/100 cm^2) and the interquartile range (IQR) from the boxplots were used as variables to describe the extent of damage concerning the distress mechanism, as presented in Figure 6.15, Equation 6.8, and Table 6.5. The IQR was selected as a parameter measuring the spread of counts per distress feature due to the non-normal distribution of the count data. The R^2 values were found to be 0.96, 1, 0.83, 0.95, and 1.00 for the ASR, FT, ASR+FT, DEF, and DEF+ASR distress mechanisms, respectively. For ASR, the largest difference in predicted expansion is at 0.12% of observed expansion for the reactive sand (i.e., Texas – Tx) proportioned for the FT group (i.e., 35 MPa), where a predicted expansion was found to be 0.08%, underestimating the expansion by 0.04%. However, 0.08% of ASR expansion was categorized between a low and moderate level of ASR deterioration, whereas 0.12% of ASR expansion was categorized as moderate ASR deterioration [2,56]. The FT distress mechanism presented a perfect fit due to the limited data points. The FT+ASR predicted expansions were influenced by the aggregate type (i.e., ASR originating from a reactive coarse or fine aggregate), resulting in overestimated values of 0.17% and 0.27% for the reactive sand mixture at 0.12% and 0.20% of observed FT+ASR expansion, categorizing the level of FT+ASR deterioration as moderately high and high/very high, respectively. On the other hand, larger differences are observed for DEF, where up to 0.13% of DEF expansion is underestimated at 0.80% of observed expansion yet remains categorized as ultra-high DEF damage (i.e., between 0.50% and 1.00% of expansion). The observed moderately low DEF deterioration (i.e., 0.09% of expansion) was underestimated as low DEF deterioration (i.e., 0.05% of expansion). In contrast, the moderate DEF deterioration (i.e., 0.12% of expansion) was overestimated as high DEF deterioration (i.e., 0.19% of expansion). The DEF+ASR predicted expansions were within a maximum of 0.02% of the observed. While further refinement may improve the predictions, complementing the extended version of the DRI with mechanical responses from the multi-level assessment will ultimately lead to a more efficient determination of the extent of the deterioration given the distress mechanism(s).

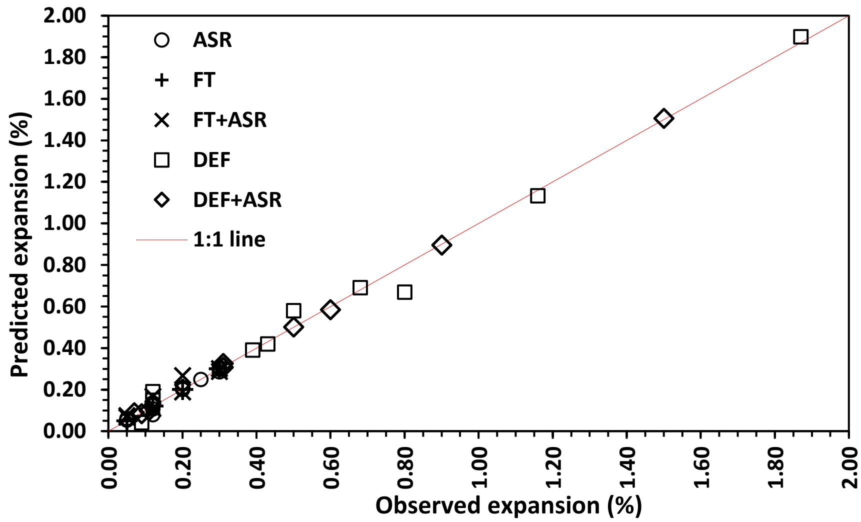

Figure 6.15. Predicted vs observed expansion per distress mechanism based on average counts and IQR.

$$Expansion\ (\%) = \beta_0 + \beta_1(x_1) + \beta_2(x_2) + \beta_3(x_3) + \cdots + \beta_7(x_7)$$ Eq. 6.8

Table 6.5. Regression coefficients for the expansion as a function of counts and IQR of the distress features for each distress mechanism.

Coefficient	Distress mechanism	ASR	FT	FT&ASR	DEF	DEF&ASR
β_0	Intercept	-7.735E-02	9.337E-01	-1.958E-01	-7.522E-01	-2.904
β_1	CCA	-1.128E-02	5.274E-01	-8.005E-03	-1.265E-01	7.251E-01
β_2	$OCA+OCA_{RP}$	1.139E-01	6.144E-01	-9.088E-02	2.806E-01	-6.036E-01
β_3	$CCP+CCP_{RP}$	1.723E-01	2.085	3.254E-01	4.222E-01	4.155
β_4	Debon	-1.377E-01	1.194E+01	-	2.895	-7.181
β_5	CCA IQR	1.213E-02	-1.052	1.030E-02	1.226E-01	6.032E-02
β_6	$OCA+OCA_{RP}$ IQR	2.394E-02	1.620E-01	1.210E-01	4.907E-02	-3.280E-01
β_7	$CCP+CCP_{RP}$ IQR	-5.668E-02	-1.076	-1.074E-01	-3.441E-02	-1.010
Adjusted R^2		0.96	1*	0.83	0.95	1.00

* R^2 used due to insufficient data.

6.6.4. *Acceptable variability in distress feature counts*

Concrete affected by ISR shows variability due to factors such as the type of aggregate, the porosity of the cement paste, and the nature and extent of the distress mechanisms. Regarding the DRI, Rivard et al. (2002) previously noted that weighting factors should be adjusted by aggregate type, which may help reduce subjectivity, particularly at intermediate expansion levels (i.e., between low and very high) [69]. Although further adjustments to the weighting factors may slightly enhance correlations (as thoroughly observed), it is advisable to consider the aggregate type in the analysis of concrete affected by ISR whenever possible. The aggregate type does not only influence mechanisms related to ASR but also affects other mechanisms [16]. Considering the aggregate type for each distress mechanism and the aforementioned interpretation of a sample, the bootstrap method with replacement was employed to define confidence intervals (CIs) for all distress features across all distress mechanisms and expansion levels. The means were utilized as the parameters of interest, which were used to establish the 2.5th and 97.5th percentiles of the bootstrap estimates to create the CI. The number of resampling iterations (R) was set at one thousand since differences between one thousand and fifteen thousand iterations with increments of 1000 do not significantly affect the final DRI number (i.e., CCA, OCA+OCA_{RP}, and CCP+CCP_{RP} yield counts of less than 13, 9, and 4 counts/100 cm^2, respectively, resulting in 3.25, 18, and 12 DRI units, respectively). Therefore, the CIs were determined for the 1000 iterations, and the results are outlined in Tables 6.6 and 6.7, including the mean DRI numbers. The CIs derived from the bootstrap method do not necessarily indicate a perfectly symmetrical distribution around the mean; while overlap is observed between expansion levels and distress mechanism groups, they may serve as a reference for highlighting distress features at various extents of ISR damage.

Table 6.6. Confidence intervals of distress features for the FT and ASR groups.

	exp.	CCA		OCA		CCP		DRI
		Lower	Upper	Lower	Upper	Lower	Upper	Mean
ASR - NM	0.05%	190	291	36	74	13	35	241
	0.12%	178	287	82	136	33	56	409
	0.20%	248	367	136	213	30	58	551
	0.25%	160	281	176	261	30	66	624
FT+ASR - NM	0.05%	269	371	77	151	45	100	525
	0.12%	241	355	103	177	52	131	612
	0.20%	304	400	93	168	83	176	730
	0.30%	261	389	208	363	75	145	976
FT -NM	0.05%	251	367	51	113	72	141	546
	0.12%	392	535	67	133	63	120	590
	0.20%	317	465	107	207	75	132	716
	0.30%	256	357	107	190	127	201	878
ASR - Tx	0.05%	281	394	30	61	13	42	250
	0.12%	351	465	55	106	15	35	330
	0.20%	486	649	148	224	24	48	611
	0.30%	455	694	129	211	66	108	735
FT+ASR - Tx	0.08%	599	803	76	137	71	127	684
	0.16%	383	560	111	201	139	216	952
	0.25%	459	616	168	288	89	152	962
	0.30%	751	1119	157	249	111	161	1028
FT - Tx	0.05%	581	757	33	100	43	93	492
	0.12%	505	696	72	148	49	105	587
	0.20%	571	759	52	116	88	143	675
	0.30%	603	806	63	130	118	172	797

Table 6.7. Confidence intervals of distress features for the DEF and ASR groups.

	exp.	CCA		OCA		CCP		DRI
		Lower	Upper	Lower	Upper	Lower	Upper	Mean
ASR - NM	0.05%	302	450	19	46	27	71	298
	0.12%	312	450	83	142	1*	9*	328
	0.30%	268	408	132	233	75	172	814
DEF+ASR - NM	0.07%	159	296	67	133	55	116	501
	0.11%	143	249	117	238	70	129	673
	0.31%	200	303	114	189	84	153	704
	0.50%	148	261	151	263	105	183	876
DEF -NM	0.09%	75	152	40	108	89	141	508
	0.12%	229	412	76	184	67	119	599
	0.39%	226	367	84	150	104	159	692
	0.50%	121	253	109	195	125	199	828
	0.68%	143	244	99	185	144	199	839
	0.80%	187	334	113	214	127	194	840
ASR - Tx	0.05%	596	754	64	109	5	20	375
	0.12%	625	778	86	143	14	39	480
	0.20%	439	596	97	176	28	89	565
	0.30%	503	674	149	291	22	63	705
DEF+ASR - Tx	0.09%	174	262	30	71	47	92	356
	0.31%	239	334	94	159	81	137	624
	0.60%	205	290	125	202	108	154	775
	0.90%	87	153	157	265	153	256	1022
	1.50%	61	172	239	368	191	287	1310
DEF - Tx	0.12%	113	181	43	91	69	131	468
	0.43%	149	256	92	172	99	176	711
	1.16%	81	153	123	215	147	220	936
	1.87%	23	77	135	228	260	345	1362

*Abnormally low CCP in this specimen caused a small interval.

6.7.Conclusion

The findings of this study establish a comprehensive framework for assessing concrete affected by internal swelling reaction (ISR). This research introduces an innovative perspective that complements the traditional representation of damage rating index (DRI) data by breaking it down to improve the understanding of how each distress feature contributes to deterioration induced by ISR. The key conclusions of this investigation are outlined below.

- Adjustments to the weighting factors were considered unnecessary, as the correlation coefficients were found to be acceptable across all proposed weighting factors for the same field of view. However, a distinction can be made between a DRI analysis aimed at describing ISR damage to concrete for engineering practices by utilizing the distress features and weighting factors proposed by Villeneuve and Fournier [4,5], the extended version of the DRI [10,56], including the currently proposed deconstructed version.
- The spread of the distress features varied due to the extent of damage resulting from the cracking. The homogeneity of this spread was captured through DRI convergence plots, indicating that 75±25 cm^2 for laboratory-made specimens is a sufficient sample size in terms of the number of 1 cm^2 units. Therefore, the convergence plots can serve as significant indicators for sample size. Further work is, however, necessary to implement convergence in cores extracted from field structures exposed to various internal/external conditions.
- The contribution of the distress features to the DRI and expansion was found to be non-linear and inconsistent throughout. However, the DRI often correlates with expansion, which increases linearly in most instances. The contribution of closed cracks in the aggregate to the DRI and its extended version, while not corresponding to volumetric

expansion, is significant compared to other distress features and varies with expansion level. Through linear regressions, the role of closed cracks in the aggregates and Debon-type cracks revealed that while they did not contribute to the predicted expansion, they influenced the mechanical responses when considering only their average counts. Various distress mechanisms produce different combinations and magnitudes of distress features, which can, in turn, yield similar DRI values and/or expansions. Therefore, deconstructing the DRI distress features through boxplots allowed for expressing distinct ISR expansion as a function of all distress features, including their count distribution, resulting in R^2 values of 0.96, 1.00, 0.83, 0.95, and 1.00 for the ASR, FT, ASR+FT, DEF, and DEF+ASR distress mechanisms, respectively.

- Confidence intervals were created for each of the distress features, mechanisms, and levels of expansion using the bootstrap method at 1000 iterations with replacement. Some overlap remains among the levels of expansion; however, the confidence intervals help define the limits of the counts for each distress feature. These can be further used in conjunction with the extent of cracking, its pattern, and propagation, while assisting new operators in understanding the distribution of crack counts for each distress mechanism and level of expansion level.

The DRI is a powerful and versatile tool that can be tailored to various forms of concrete deterioration and types of investigation (e.g., petrographic and engineering). While subjectivity may persist during complex diagnostic evaluations, it can be minimized by considering the degree of deterioration in relation to a distress mechanism, which involves examining the cracking pattern and propagation, along with the corresponding mechanical response for distinct types of distress mechanisms.

6.8. References

[1] New Brunswick Power, Mactaquac Life Achievement Project, (2021). http://www.nbpower.com/en/about-us/projects/mactaquac-project (accessed August 1, 2023).

[2] L.F.M. Sanchez, T. Drimalas, B. Fournier, D. Mitchell, J. Bastien, Comprehensive damage assessment in concrete affected by different internal swelling reaction (ISR) mechanisms, Cement and Concrete Research 107 (2018) 284–303. https://doi.org/10.1016/j.cemconres.2018.02.017.

[3] P.E. Grattan-Bellew, A. Danay, Comparison of laboratory and field evaluation of alkali-silica reaction in large dams, in: Collection / Collection : NRC Publications Archive / Archives des publications du CNRC, 1992: pp. 1–25.

[4] V. Villeneuve, Détermination de l’endommagement du béton par méthode pétrographique quantitative, Master’s Thesis., Université Laval, 2011.

[5] V. Villeneuve, B. Fournier, J. Duchesne, Determination of the damage in concrete affected by ASR – the damage rating index (DRI), in: 14th International Conference on Alkali-Aggregate Reaction, Texas, USA, 2012.

[6] P.E. Grattan-Bellew, D. Mitchell, Quantitative petrographic analysis of concrete : the damage rating index (DRI) method, a review, in: CANMET International Conference on Recent Advances in Concrete Technology, Natural Resources Canada, Ottawa, Canada, 2006.

[7] L. Powers, F.H. Shrimer, Quantification of ASR in concrete: an introduction to the Damage-Rating method, in: 29th International Conference on Cement Microscopy, Québec, Canada, 2007.

[8] P. Rivard, G. Ballivy, Assessment of the expansion related to alkali-silica reaction by the Damage Rating Index method, Construction and Building Materials 19 (2005) 83–90. https://doi.org/10.1016/j.conbuildmat.2004.06.001.

[9] L.F.M. Sanchez, B. Fournier, M. Jolin, J. Duchesne, Reliable quantification of AAR damage through assessment of the Damage Rating Index (DRI), Cement and Concrete Research 67 (2015) 74–92. https://doi.org/10.1016/j.cemconres.2014.08.002.

[10] L.F.M. Sanchez, B. Fournier, M. Jolin, M.A.B. Bedoya, J. Bastien, J. Duchesne, Use of Damage Rating Index to Quantify Alkali-Silica Reaction Damage in Concrete: Fine versus Coarse Aggregate, ACI Materials Journal 113 (2016). https://doi.org/10.14359/51688983.

[11] L.F.M. Sanchez, T. Drimalas, B. Fournier, Assessing condition of concrete affected by internal swelling reactions (ISR) through the Damage Rating Index (DRI), Cement 1–2 (2020) 100001. https://doi.org/10.1016/j.cement.2020.100001.

[12] T. Katayama, The so-called alkali-carbonate reaction (ACR) — Its mineralogical and geochemical details, with special reference to ASR, Cement and Concrete Research 40 (2010) 643–675. https://doi.org/10.1016/j.cemconres.2009.09.020.

[13] M. Beyene, A. Snyder, R.J. Lee, M. Blaszkiewicz, Alkali Silica Reaction (ASR) as a root cause of distress in a concrete made from Alkali Carbonate Reaction (ACR) potentially susceptible aggregates, Cement and Concrete Research 51 (2013) 85–95. https://doi.org/10.1016/j.cemconres.2013.04.014.

[14] P.-L. Fecteau, B. Fournier, Alkali-Carbonate Reaction Concrete Prism Test Samples Macroscopic Petrography and Damage Evaluation through the Damage Rating Index Method, in: 16th International Conference on Alkali-Aggregate Reaction, Lisboa, Portugal, 2022.

[15] F. Locati, D. Falcone, S. Marfil, Dedolomitization and alkali-silica reactions in low-expansive marbles from the province of Córdoba, Argentina. A microstructural and chemical study, Construction and Building Materials 58 (2014) 171–181. https://doi.org/10.1016/j.conbuildmat.2014.02.019.

[16] A. Leemann, B. Münch, C. Trottier, L. Sanchez, Microstructural Consequences of Alkali-Carbonate Reaction, in: L.F.M. Sanchez, C. Trottier (Eds.), Proceedings of the 17th International Conference on Alkali-Aggregate Reaction in Concrete, Springer Nature Switzerland, Cham, 2024: pp. 87–94. https://doi.org/10.1007/978-3-031-59419-9_11.

[17] I. Sims, A. Poole, eds., Alkali-aggregate reaction in concrete: a world review, CRC Press, Taylor & Francis Group, a Balkema book, Boca Raton London New York Leiden, 2017.

[18] L.F.M. Sanchez, B. Fournier, M. Jolin, D. Mitchell, J. Bastien, Overall assessment of Alkali-Aggregate Reaction (AAR) in concretes presenting different strengths and incorporating a wide range of reactive aggregate types and natures, Cement and Concrete Research 93 (2017) 17–31. https://doi.org/10.1016/j.cemconres.2016.12.001.

[19] P. Rivard, B. Fournier, G. Ballivy, Quantitative Petrographic Technique for Concrete Damage Due to ASR: Experimental and Application, Cement, Concrete and Aggregates 22 (2000) 63–72. https://doi.org/10.1520/CCA10465J.

[20] N. Smaoui, B. Bissonnette, M.-A. Bérubé, B. Fournier, B. Durand, Mechanical Properties of ASR-Affected Concrete Containing Fine or Coarse Reactive Aggregates, J. ASTM Int. 3 (2006). https://doi.org/10.1520/JAI12010.

[21] M. Shakoorioskooie, M. Griffa, A. Leemann, R. Zboray, P. Lura, Alkali-silica reaction products and cracks: X-ray micro-tomography-based analysis of their spatial-temporal evolution

at a mesoscale, Cement and Concrete Research 150 (2021) 106593. https://doi.org/10.1016/j.cemconres.2021.106593.

[22] British Cement Association (BCA), The diagnosis of alkali-silica reaction, British Cement Association (BCA), Wexham Springs, UK, 1992.

[23] L.F.M. Sanchez, B. Fournier, M. Jolin, D. Mitchell, J. Bastien, Overall assessment of Alkali-Aggregate Reaction (AAR) in concretes presenting different strengths and incorporating a wide range of reactive aggregate types and natures, Cement and Concrete Research 93 (2017) 17–31. https://doi.org/10.1016/j.cemconres.2016.12.001.

[24] C. Trottier, L.F.M. Sanchez, Damage Generated and Propagated by the AAR Reactive Aggregate from Kingston, Ontario, Canada, Materials 17 (2023) 166. https://doi.org/10.3390/ma17010166.

[25] Portland Cement Association, Ettringite formation and the performance of concrete, (2001).

[26] H.F.W. Taylor, C. Famy, K.L. Scrivener, Delayed ettringite formation, Cement and Concrete Research (2001).

[27] Jan. Skalny, J. (Jacques) Marchand, I. Odler, Sulfate attack on concrete, Spon Press, London ;, 2002. https://doi.org/10.4324/9780203301623.

[28] A. Pavoine, X. Brunetaud, L. Divet, The impact of cement parameters on Delayed Ettringite Formation, Cement and Concrete Composites 34 (2012) 521–528. https://doi.org/10.1016/j.cemconcomp.2011.11.012.

[29] S. Diamond, Delayed ettringite formation — Processes and problems, Cement and Concrete Composites 18 (1996) 205–215. https://doi.org/10.1016/0958-9465(96)00017-0.

[30] V. Johansen, N. Thaulow, J. Skalny, Simultaneous presence of alkali — silica gel and ettringite in concrete, Advances in Cement Research 5 (1993) 23–29. https://doi.org/10.1680/adcr.1993.5.17.23.

[31] M. Thomas, K. Folliard, T. Drimalas, T. Ramlochan, Diagnosing delayed ettringite formation in concrete structures, Cement and Concrete Research 38 (2008) 841–847. https://doi.org/10.1016/j.cemconres.2008.01.003.

[32] R. Yang, C.D. Lawrence, C.J. Lynsdale, J.H. Sharp, Delayed ettringite formation in heat-cured Portland cement mortars, Cement and Concrete Research 29 (1999) 17–25. https://doi.org/10.1016/S0008-8846(98)00168-9.

[33] R. Yang, C.D. Lawrence, J.H. Sharp, Effect of type of aggregate on delayed ettringite formation, Advances in Cement Research 11 (1999) 119–132. https://doi.org/10.1680/adcr.1999.11.3.119.

[34] R.H.R.Q. Melo, N.P. Hasparyk, F. Tiecher, Assessment of Concrete Impairments over Time Triggered by DEF, Journal of Materials in Civil Engineering 35 (2023). https://doi.org/10.1061/JMCEE7.MTENG-15041.

[35] P.E. Grattan-Bellew, Petrographic methods for distinguishing between alkali- silica, alkali-carbonate reactions and other mechanisms of concrete deterioration, in: Proceedings of the 14th International Conference on Alkali-Aggregate Reaction in Concrete, Austin, Texas, USA, 2012.

[36] M.-A. Bérubé, B. Fournier, T. Côté, Using the damage rating index for assessing the expansion of concrete affected by freeze-thaw, sulphate attack, or ASR, in: 14th International Conference on Alkali-Aggregate Reaction, Austin, Texas, USA, 2012.

[37] R.-P. Martin, L. Sanchez, B. Fournier, F. Toutlemonde, Evaluation of different techniques for the diagnosis & prognosis of Internal Swelling Reaction (ISR) mechanisms in concrete, Construction and Building Materials 156 (2017) 956–964. https://doi.org/10.1016/j.conbuildmat.2017.09.047.

[38] C. Trottier, L.F.M. Sanchez, R.-P. Martin, F. Toutlemonde, Capturing internal swelling reactions (ISR) damage in concrete through the damage rating index (DRI), in: Springer, Vancouver, BC, 2023.

[39] C. Trottier, L.F.M. Sanchez, R.-P. Martin, F. Toutlemonde, Evaluation of Damage Due to DEF Through the Multi-level Assessment, in: L.F.M. Sanchez, C. Trottier (Eds.), Proceedings of the 17th International Conference on Alkali-Aggregate Reaction in Concrete, Springer Nature Switzerland, Cham, 2024: pp. 209–216. https://doi.org/10.1007/978-3-031-59419-9_25.

[40] R.-P. Martin, Analyse sur structures modèles des effets mécaniques de la réaction sulfatique interne du béton, PhD Thesis, Université Paris-Est, 2010. https://pastel.archives-ouvertes.fr/tel-00558200v2.

[41] N.P. Hasparyk, S.C. Kuperman, J.R. Torres, Combined attack from AAR and DEF in the foundation blocks of a building, in: 15th International Conference on Alkali-Aggregate Reaction, Sao Paulo, Brazil, 2016.

[42] L.F.M. Sanchez, B. Fournier, D. Mitchell, J. Bastien, Condition assessment of an ASR-affected overpass after nearly 50 years in service, Construction and Building Materials 236 (2020) 117554. https://doi.org/10.1016/j.conbuildmat.2019.117554.

[43] S. Li, G. Chen, G. Ji, Y. Lu, Quantitative damage evaluation of concrete suffered freezing–thawing by DIP technique, Construction and Building Materials 69 (2014) 177–185. https://doi.org/10.1016/j.conbuildmat.2014.07.072.

[44] R. Xie, J. Yang, E. Xie, Investigation on mechanical properties deterioration of concrete subjected to freeze–thaw cycles, Sci Rep 12 (2022) 22612. https://doi.org/10.1038/s41598-022-27122-w.

[45] A. Zahedi, A. Komar, L.F.M. Sanchez, A.J. Boyd, Global assessment of concrete specimens subjected to freeze-thaw damage, Cement and Concrete Composites 133 (2022) 104716. https://doi.org/10.1016/j.cemconcomp.2022.104716.

[46] R.A.Jr. Deschenes, Mitigation and Evaluation of Alkali-Silica Reaction (ASR) and Freezing and Thawing in Concrete Transportation Structures, Doctorate, University of Arkansas, 2017. https://scholarworks.uark.edu/cgi/viewcontent.cgi?article=4007&context=etd.

[47] F. Gong, Y. Takahashi, I. Segawa, K. Maekawa, Mechanical properties of concrete with smeared cracking by alkali-silica reaction and freeze-thaw cycles, Cement and Concrete Composites 111 (2020) 103623. https://doi.org/10.1016/j.cemconcomp.2020.103623.

[48] R.H. Haddad, K.S. Numayr, Effect of alkali-silica reaction and freezing and thawing action on concrete–steel bond, Construction and Building Materials 21 (2007) 428–435. https://doi.org/10.1016/j.conbuildmat.2005.07.012.

[49] K. Kobayashi, Y. Kano, K. Rokugo, Example of composite deterioration of R/C slab caused by ASR and frost attack in mountainous cold area and its verification test, J. JSCE, Ser. E2 70 (2014) 320–335. https://doi.org/10.2208/jscejmcs.70.320.

[50] T. Suzuki, T. Shiotani, M. Ohtsu, Evaluation of cracking damage in freeze-thawed concrete using acoustic emission and X-ray CT image, Construction & Building Materials 136 (2017) 619–626. https://doi.org/10.1016/j.conbuildmat.2016.09.013.

[51] H. Ahmed, A. Zahedi, L.F.M. Sanchez, P.-L. Fecteau, Condition assessment of ASR-affected reinforced concrete columns after nearly 20 years in service, Construction & Building Materials 347 (2022) 128570. https://doi.org/10.1016/j.conbuildmat.2022.128570.

[52] M.-A. Bérubé, N. Smaoui, B. Fournier, B. Bissonnette, B. Durand, Evaluation of the expansion attained to date by concrete affected by alkali–silica reaction. Part III: Application to existing structures, Can. J. Civ. Eng. 32 (2005) 463–479. https://doi.org/10.1139/l04-104.

[53] C.A. MacDonald, M. Piersanti, M. Shehata, J. Magnan, Use of the damage rating index (dri) to evaluate level of deterioration due to alkali-silica reaction in 34-year old concrete from the Sudbury area, in: 17th Euroseminar on Microscopy Applied to Building Materials, Toronto, Canada, 2019.

[54] F. Shrimer, Use of the Damage Rating Index as Input for Service Life Prediction in Alkali-Silica Reaction Affected Concrete, in: D. Cong, D. Broton (Eds.), Advances in Cement Analysis and Concrete Petrography, ASTM International, 100 Barr Harbor Drive, PO Box C700, West Conshohocken, PA 19428-2959, 2019: pp. 89–104. https://doi.org/10.1520/STP161320180246.

[55] K.J. Folliard, R. Barborak, T. Drimalas, L. Du, S. Garber, J.H. Ideker, T. Ley, S. Williams, M. Juenger, B. Fournier, M.D.A. Thomas, Preventing ASR/DEF in New Concrete: Final Report

(0-4085-5), Texas Department of Transportation and the Federal Highway Administration, Texas, USA, 2006.

[56] L.F.M. Sanchez, B. Fournier, M. Jolin, D. Mitchell, J. Bastien, Overall assessment of Alkali-Aggregate Reaction (AAR) in concretes presenting different strengths and incorporating a wide range of reactive aggregate types and natures, Cement and Concrete Research 93 (2017) 17–31. https://doi.org/10.1016/j.cemconres.2016.12.001.

[57] ASTM C1293-18a, Test Method for Determination of Length Change of Concrete Due to Alkali-Silica Reaction, (2018). https://doi.org/10.1520/C1293-18A.

[58] ASTM International, ASTM C666: Standard Test Method for Resistance of Concrete to Rapid Freezing and Thawing (Withdrawn 2024), (2015). https://doi.org/10.1520/C1356-07R20.

[59] N. Smaoui, B. Fournier, M.-A. Bérubé, B. Bissonnette, B. Durand, Evaluation of the expansion attained to date by concrete affected by alkali-silica reaction. Part I. Experimental study, Canadian Journal of Civil Engineering (2004).

[60] L.F.M. Sanchez, B. Fournier, M. Jolin, J. Duchesne, Reliable quantification of AAR damage through assessment of the Damage Rating Index (DRI), Cement and Concrete Research 67 (2015) 74–92. https://doi.org/10.1016/j.cemconres.2014.08.002.

[61] M. Champagne, Applying the damage rating index for the spatial damage assessment in concrete specimens affected by alkali-silica reaction (ASR), Master's Thesis., Université Laval, 2020.

[62] A. Zahedi, L. Saliba, L.F.M. Sanchez, A.J. Boyd, Reliability of the damage rating index to assess the condition of concrete affected by external sulfate attack, Magazine of Concrete Research 75 (2023) 135–148. https://doi.org/10.1680/jmacr.22.00061.

[63] P.K. Mehta, P.J.M. Monteiro, Concrete : microstructure, properties, and materials, 4th ed., New York : McGraw-Hill Education, 2014.

[64] L.F.M. Sanchez, Internal Swelling Reactions in Concrete: Mechanisms and Condition Assessment, 1st ed., CRC Press, Boca Raton, 2024. https://doi.org/10.1201/9781003188155.

[65] L.F.M. Sanchez, B. Fournier, M. Jolin, J. Bastien, Evaluation of the stiffness damage test (SDT) as a tool for assessing damage in concrete due to ASR Test loading and output responses for concretes incorporating fine or coarse reactive aggregates, Cement and Concrete Research 56 (2014) 213–229.

[66] A.Y. Nassif, A new classification system for fire-damaged concrete based on the strain energy dissipated in a hysteresis loop, Magazine of Concrete Research 52 (2000) 287–295. https://doi.org/10.1680/macr.2000.52.4.287.

[67] J.S. Guo, P. Waldron, Development of the stiffness damage test (SDT) for characterisation of thermally loaded concrete, Mat. Struct. 33 (2000) 483–491. https://doi.org/10.1007/BF02480525.

[68] J. Lindgård, M. Haugen, N. Castro, M.D.A. Thomas, Advantages of using plane polished section analysis as part of microstructural analyses to describe internal cracking due to alkali-silica reactions, in: Austin, Texas, USA, 2012.

[69] P. Rivard, B. Fournier, G. Ballivy, The Damage Rating Index Method for ASR Affected Concrete—A Critical Review of Petrographic Features of Deterioration and Evaluation Criteria, Cement, Concrete, Aggr. 24 (2002) 11228. https://doi.org/10.1520/CCA10531J.

6.9. Appendices

Appendix A: Debon and DAP average counts

Table 6.8. Average counts/100 cm^2 of debonded (Debon) and disaggregated/corroded (DAP) aggregate particles.

Distress mechanism	Expansion	Debon	DAP
ASR 35 MPa NM	0.05%	0	0
	0.12%	0	2
	0.20%	3	2
	0.25%	3	0
ASR+FT NM	0.05%	0	0
	0.12%	0	0
	0.20%	0	3
	0.30%	0	3
FT NM	0.05%	0	0
	0.12%	8	0
	0.20%	4	0
	0.30%	14	6
ASR 35 MPa Tx	0.05%	0	0
	0.12%	0	0
	0.20%	0	2
	0.30%	0	6
ASR+FT Tx	0.08%	0	0
	0.16%	0	0
	0.25%	0	3
	0.30%	0	0
FT Tx	0.05%	0	0
	0.12%	0	0
	0.20%	4	0
	0.30%	0	0

Distress mechanism	Expansion	Debon	DAP
ASR CPT NM	0.05%	0	0
	0.12%	0	0
	0.30%	0	0
DEF+ASR NM	0.07%	4	0
	0.11%	0	2
	0.31%	7	4
	0.50%	0	0
DEF NM	0.09%	4	0
	0.12%	0	0
	0.39%	0	0
	0.50%	12	8
	0.68%	17	2
	0.80%	17	0
ASR CPT Tx	0.05%	0	0
	0.12%	0	0
	0.20%	0	0
	0.30%	0	0
DEF+ASR Tx	0.09%	0	0
	0.31%	0	0
	0.60%	11	2
	0.90%	8	3
	1.50%	8	3
DEF Tx	0.12%	12	3
	0.43%	12	0
	1.16%	56	3
	1.87%	92	19
DEF NR	0.05%	0	0
	0.15%	0	0
	0.21%	0	0

Appendix B: Boxplots of the distress feature counts

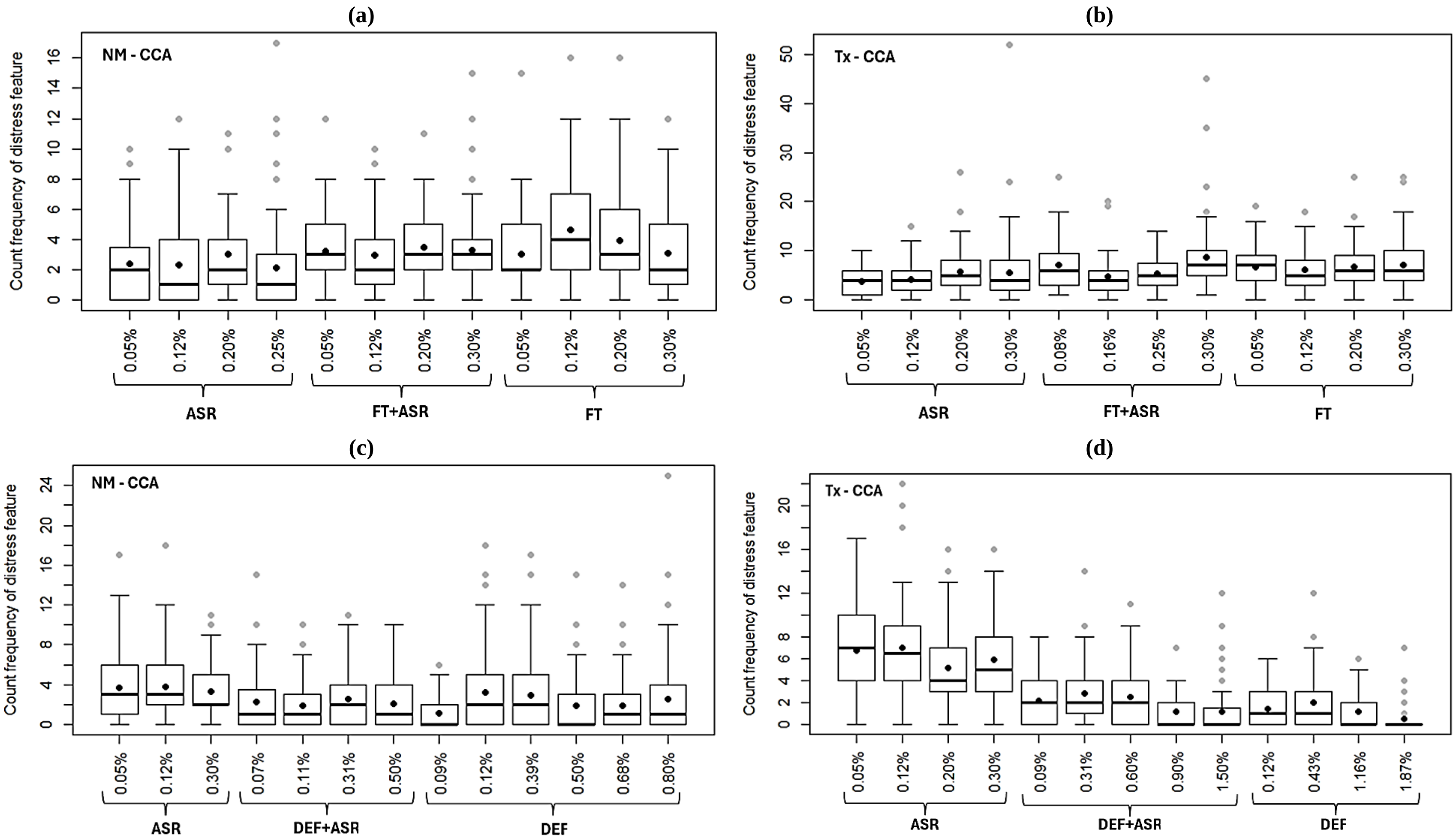

Figure 6.16. Boxplots of the CCA counts per square unit.

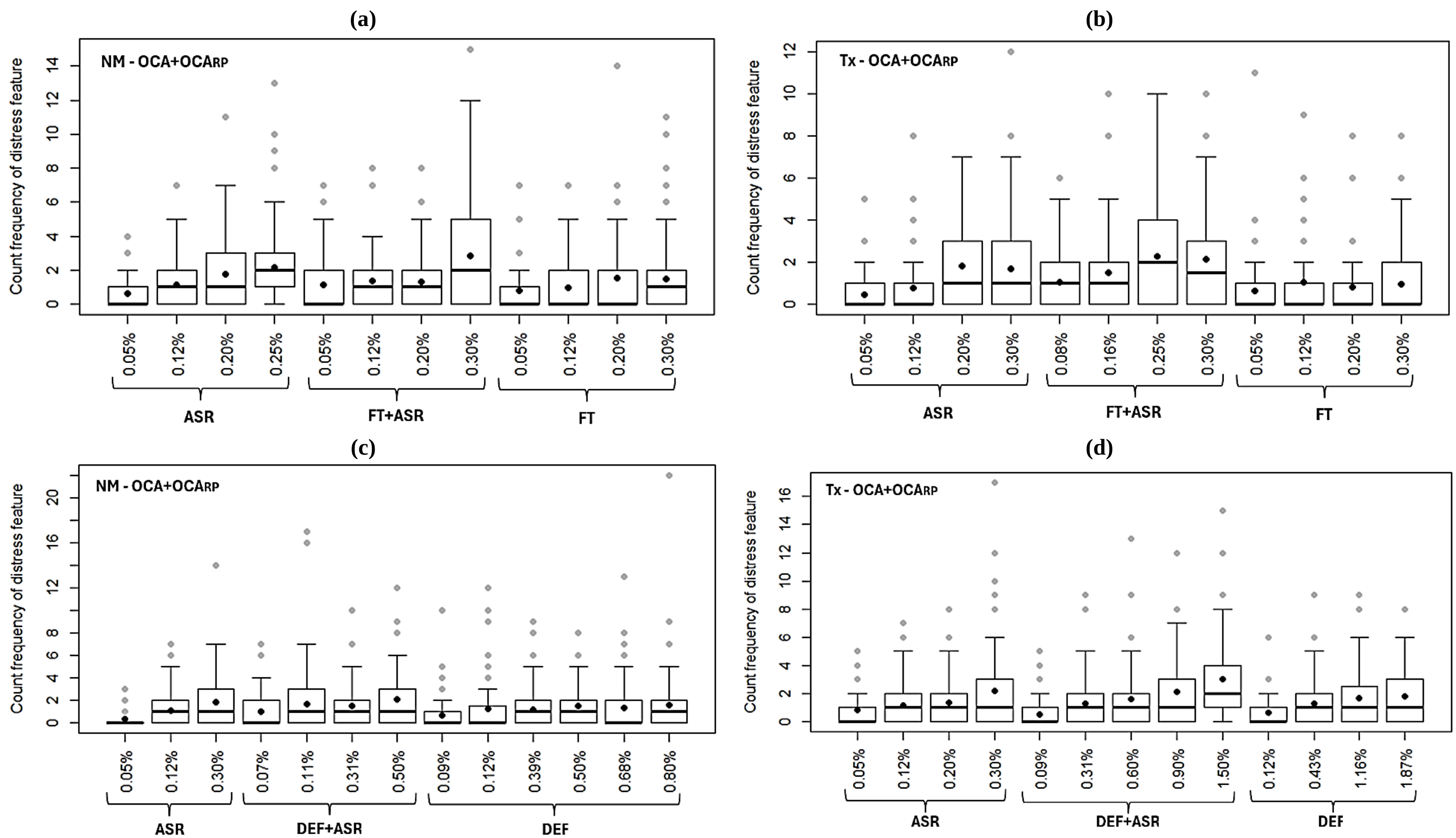

Figure 6.17. Boxplots of the OCA+OCA$_{RP}$ counts per square unit.

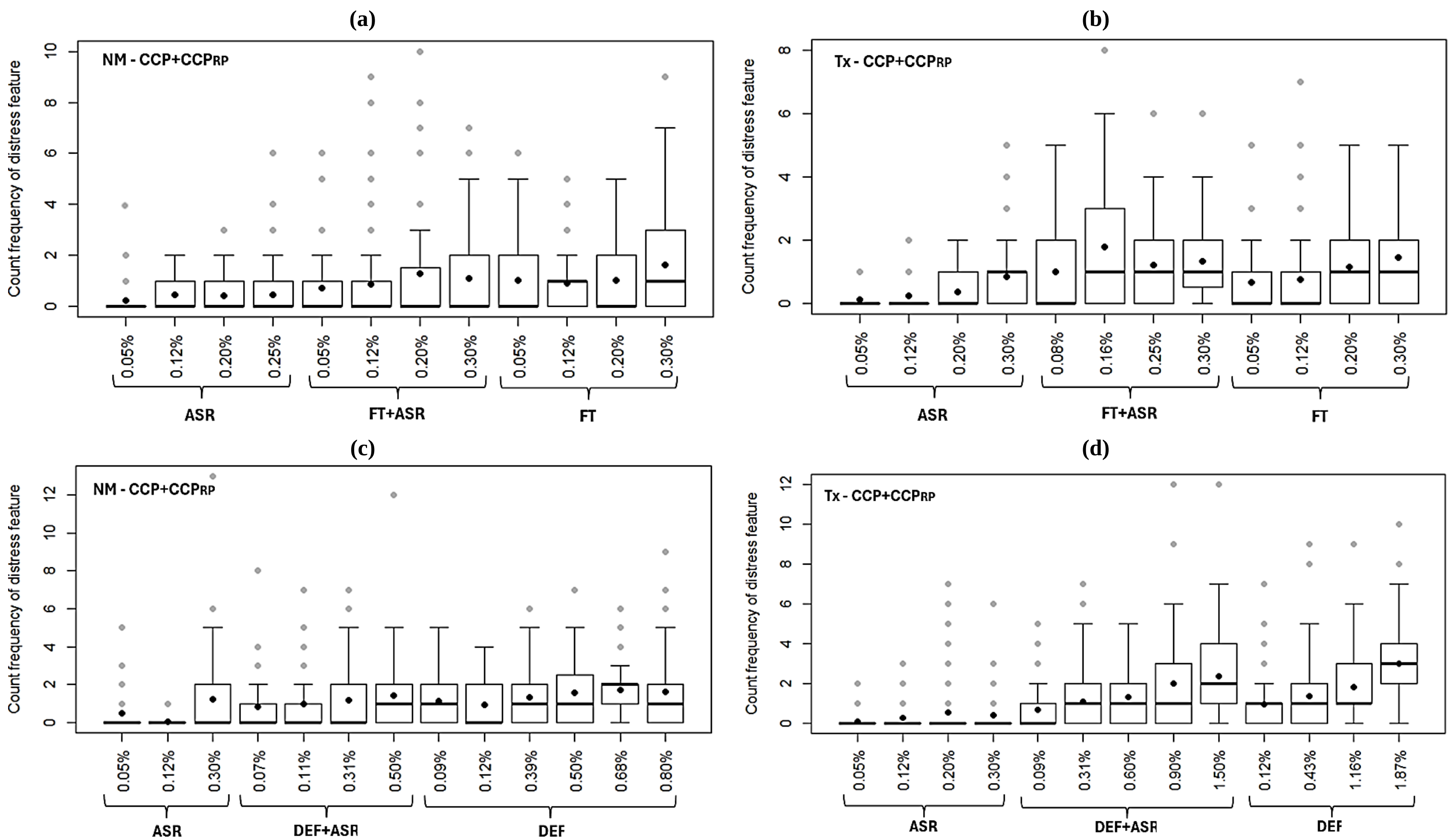

Figure 6.18. Boxplots of the CCP+CCP$_{RP}$ counts per square unit.

Appendix C: Descriptive statistics

Appendix C1 – FT ± ASR

Table 6.9. Summary of CCA counts descriptive statistics for the FT ± ASR groups.

Aggregate	Distress mechanism	Expansion level	Mean	Variance	SD	Minimum	Maximum	n
NM	ASR	0.05%	2.390	6.683	2.585	0	10	105
		0.12%	2.295	8.806	2.968	0	12	105
		0.20%	3.056	7.514	2.741	0	11	90
		0.25%	2.133	9.309	3.051	0	17	105
	ASR+FT	0.05%	3.200	5.162	2.272	0	12	75
		0.12%	2.973	6.540	2.557	0	10	75
		0.20%	3.507	4.551	2.133	0	11	75
		0.30%	3.253	8.462	2.909	0	15	75
	FT	0.05%	3.053	6.375	2.525	0	15	75
		0.12%	4.627	10.561	3.250	0	16	75
		0.20%	3.907	10.815	3.289	0	16	75
		0.30%	3.057	6.958	2.638	0	12	105
Tx	ASR	0.05%	3.662	8.090	2.844	0	10	74
		0.12%	4.057	8.727	2.954	0	15	105
		0.20%	5.629	17.409	4.172	0	26	105
		0.30%	5.600	38.665	6.218	0	52	105
	ASR+FT	0.05%	7.000	20.486	4.526	1	25	75
		0.12%	4.667	13.631	3.692	0	20	75
		0.20%	5.333	10.847	3.293	0	14	75
		0.30%	9.187	72.397	8.509	1	45	75
	FT	0.05%	6.667	14.495	3.807	0	19	75
		0.12%	6.040	17.850	4.225	0	18	75
		0.20%	6.627	17.940	4.236	0	25	75
		0.30%	7.033	24.235	4.923	0	25	90

Table 6.10. Summary of OCA+OCA_{RP} counts descriptive statistics for the FT ± ASR groups.

Aggregate	Distress mechanism	Expansion level	Mean	Variance	SD	Minimum	Maximum	n
NM	ASR	0.05%	0.552	1.000	1.000	0	4	105
		0.12%	1.076	1.994	1.412	0	7	105
		0.20%	1.700	3.763	1.940	0	11	90
		0.25%	2.152	5.227	2.286	0	13	105
	ASR+FT	0.05%	1.133	2.523	1.588	0	7	75
		0.12%	1.373	2.670	1.634	0	8	75
		0.20%	1.280	2.853	1.689	0	8	75
		0.30%	2.827	10.740	3.277	0	15	75
	FT	0.05%	0.787	2.170	1.473	0	7	75
		0.12%	0.987	2.175	1.475	0	7	75
		0.20%	1.533	5.631	2.373	0	14	75
		0.30%	1.467	4.886	2.210	0	11	105
Tx	ASR	0.05%	0.446	0.689	0.830	0	5	74
		0.12%	0.771	1.563	1.250	0	8	105
		0.20%	1.838	3.599	1.897	0	7	105
		0.30%	1.686	5.025	2.242	0	12	105
	ASR+FT	0.05%	1.067	2.009	1.417	0	6	75
		0.12%	1.520	3.983	1.996	0	10	75
		0.20%	2.267	6.793	2.606	0	10	75
		0.30%	2.027	4.459	2.112	0	10	75
	FT	0.05%	0.627	2.345	1.531	0	11	75
		0.12%	1.053	2.943	1.716	0	9	75
		0.20%	0.813	2.046	1.430	0	8	75
		0.30%	0.956	2.492	1.579	0	8	90

Table 6.11. Summary of CCP+CCP$_{RP}$ counts descriptive statistics for the FT ± ASR groups.

Aggregate	Distress mechanism	Expansion level	Mean	Variance	SD	Minimum	Maximum	n
NM	ASR	0.05%	0.238	0.356	0.597	0	4	105
		0.12%	0.448	0.365	0.604	0	2	105
		0.20%	0.433	0.496	0.704	0	3	90
		0.25%	0.467	0.905	0.951	0	6	105
	ASR+FT	0.05%	0.720	1.421	1.192	0	6	75
		0.12%	0.880	3.026	1.740	0	9	75
		0.20%	1.280	4.556	2.134	0	10	75
		0.30%	1.093	2.383	1.544	0	7	75
	FT	0.05%	1.040	2.579	1.606	0	6	75
		0.12%	0.907	1.356	1.164	0	5	75
		0.20%	1.027	1.594	1.262	0	5	75
		0.30%	1.629	3.755	1.938	0	9	105
Tx	ASR	0.05%	0.108	0.098	0.313	0	1	74
		0.12%	0.248	0.265	0.515	0	2	105
		0.20%	0.352	0.403	0.635	0	2	105
		0.30%	0.857	1.258	1.122	0	5	105
	ASR+FT	0.05%	0.987	1.581	1.257	0	5	75
		0.12%	1.773	3.259	1.805	0	8	75
		0.20%	1.200	1.973	1.405	0	6	75
		0.30%	1.360	1.315	1.147	0	6	75
	FT	0.05%	0.667	1.387	1.178	0	5	75
		0.12%	0.760	1.752	1.324	0	7	75
		0.20%	1.147	1.451	1.205	0	5	75
		0.30%	1.444	1.823	1.350	0	5	90

Appendix C2 – DEF ± ASR

Table 6.12. Summary of CCA counts descriptive statistics for the DEF ± ASR groups.

Aggregate	Distress mechanism	Expansion level	Mean	Variance	SD	Minimum	Maximum	n
NM	ASR	0.05%	3.678	11.547	3.398	0	17	90
		0.12%	3.767	9.979	3.159	0	18	90
		0.30%	3.347	8.473	2.911	0	11	75
	ASR+DEF	0.07%	2.240	9.293	3.048	0	15	75
		0.11%	1.911	6.801	2.608	0	10	90
		0.31%	2.511	6.747	2.598	0	11	90
		0.50%	2.027	6.513	2.552	0	10	75
	DEF	0.09%	1.107	2.988	1.729	0	6	75
		0.12%	3.200	15.865	3.983	0	18	75
		0.39%	2.924	13.283	3.645	0	17	105
		0.50%	1.853	8.424	2.902	0	15	75
		0.68%	1.895	6.595	2.568	0	14	105
		0.80%	2.600	15.646	3.956	0	25	105
Tx	ASR	0.05%	6.764	16.811	4.100	0	17	106
		0.12%	7.019	16.133	4.017	0	22	106
		0.20%	5.132	12.142	3.485	0	16	76
		0.30%	5.882	14.319	3.784	0	16	76
	ASR+DEF	0.09%	2.178	4.283	2.069	0	8	90
		0.31%	2.857	6.335	2.517	0	14	105
		0.60%	2.486	5.137	2.266	0	11	105
		0.90%	1.187	2.181	1.477	0	7	75
		1.50%	1.133	5.306	2.304	0	12	75
	DEF	0.12%	1.453	2.575	1.605	0	6	75
		0.43%	2.000	5.378	2.319	0	12	75
		1.16%	1.160	2.515	1.586	0	6	75
		1.87%	0.467	1.495	1.223	0	7	75

Table 6.13. Summary of OCA+OCA$_{RP}$ counts descriptive statistics for the DEF ± ASR groups.

Aggregate	Distress mechanism	Expansion level	Mean	Variance	SD	Minimum	Maximum	n
NM	ASR	0.05%	0.311	0.486	0.697	0	3	90
		0.12%	1.100	2.046	1.430	0	7	90
		0.30%	1.813	5.019	2.240	0	14	75
	ASR+DEF	0.07%	0.973	2.188	1.479	0	7	75
		0.11%	1.700	8.033	2.834	0	17	90
		0.31%	1.478	3.219	1.794	0	10	90
		0.50%	2.040	6.120	2.473863	0	12	75
	DEF	0.09%	0.693	2.270	1.507	0	10	75
		0.12%	1.240	5.698	2.387	0	12	75
		0.39%	1.162	2.925	1.710	0	9	105
		0.50%	1.507	4.253	2.062	0	8	75
		0.68%	1.371	4.870	2.207	0	13	105
		0.80%	1.571	7.151	2.674	0	22	105
Tx	ASR	0.05%	0.858	1.418	1.191	0	5	106
		0.12%	1.142	2.065	1.437	0	7	106
		0.20%	1.355	2.925	1.710	0	8	76
		0.30%	2.158	9.815	3.133	0	17	76
	ASR+DEF	0.09%	0.500	0.994	0.997	0	5	90
		0.31%	1.257	2.789	1.670	0	9	105
		0.60%	1.610	4.125	2.031	0	13	105
		0.90%	2.093	5.626	2.372	0	12	75
		1.50%	3.000	8.216	2.866	0	15	75
	DEF	0.12%	0.653	1.230	1.109	0	6	75
		0.43%	1.307	2.972	1.724	0	9	75
		1.16%	1.680	4.166	2.041	0	9	75
		1.87%	1.787	4.251	2.062	0	8	75

Table 6.14. Summary of CCP+CCP_{RP} counts descriptive statistics for the DEF ± ASR groups.

Aggregate	Distress mechanism	Expansion level	Mean	Variance	SD	Minimum	Maximum	n
NM	ASR	0.05%	0.478	1.196	1.094	0	5	90
		0.12%	0.044	0.043	0.207	0	1	90
		0.30%	1.227	4.718	2.172	0	13	75
	ASR+DEF	0.07%	0.840	1.893	1.376	0	8	75
		0.11%	0.989	2.034	1.426	0	7	90
		0.31%	1.167	2.792	1.671	0	7	90
		0.50%	1.427	3.059	1.749	0	12	75
	DEF	0.09%	1.133	1.387	1.178	0	5	75
		0.12%	0.920	1.291	1.136	0	4	75
		0.39%	1.314	2.025	1.423	0	6	105
		0.50%	1.587	2.651	1.628	0	7	75
		0.68%	1.705	1.999	1.414	0	6	105
		0.80%	1.600	3.012	1.735	0	9	105
Tx	ASR	0.05%	0.113	0.158	0.398	0	2	106
		0.12%	0.255	0.382	0.618	0	3	106
		0.20%	0.553	1.824	1.351	0	7	76
		0.30%	0.421	0.914	0.956	0	6	76
	ASR+DEF	0.09%	0.678	1.300	1.140	0	5	90
		0.31%	1.076	2.110	1.452	0	7	105
		0.60%	1.295	1.595	1.263	0	5	105
		0.90%	2.013	5.365	2.316	0	12	75
		1.50%	2.360	4.585	2.141	0	12	75
	DEF	0.12%	0.973	1.756	1.325	0	7	75
		0.43%	1.347	3.203	1.790	0	9	75
		1.16%	1.800	2.730	1.652	0	9	75
		1.87%	3.013	3.554	1.885	0	10	75

Appendix D: Remaining mechanical property as a function of distress features

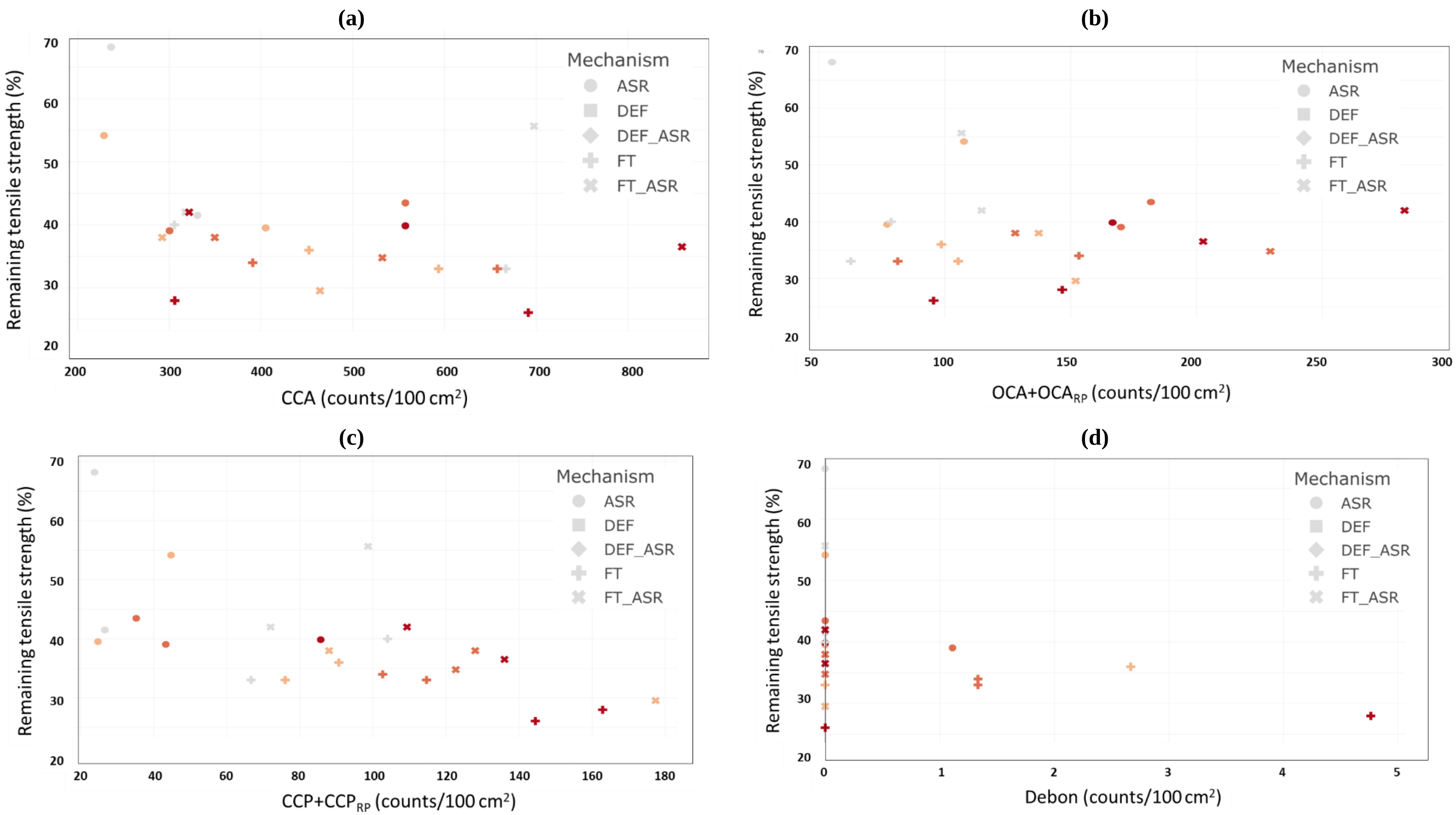

Figure 6.19. Remaining tensile strength as a function of distress feature counts.

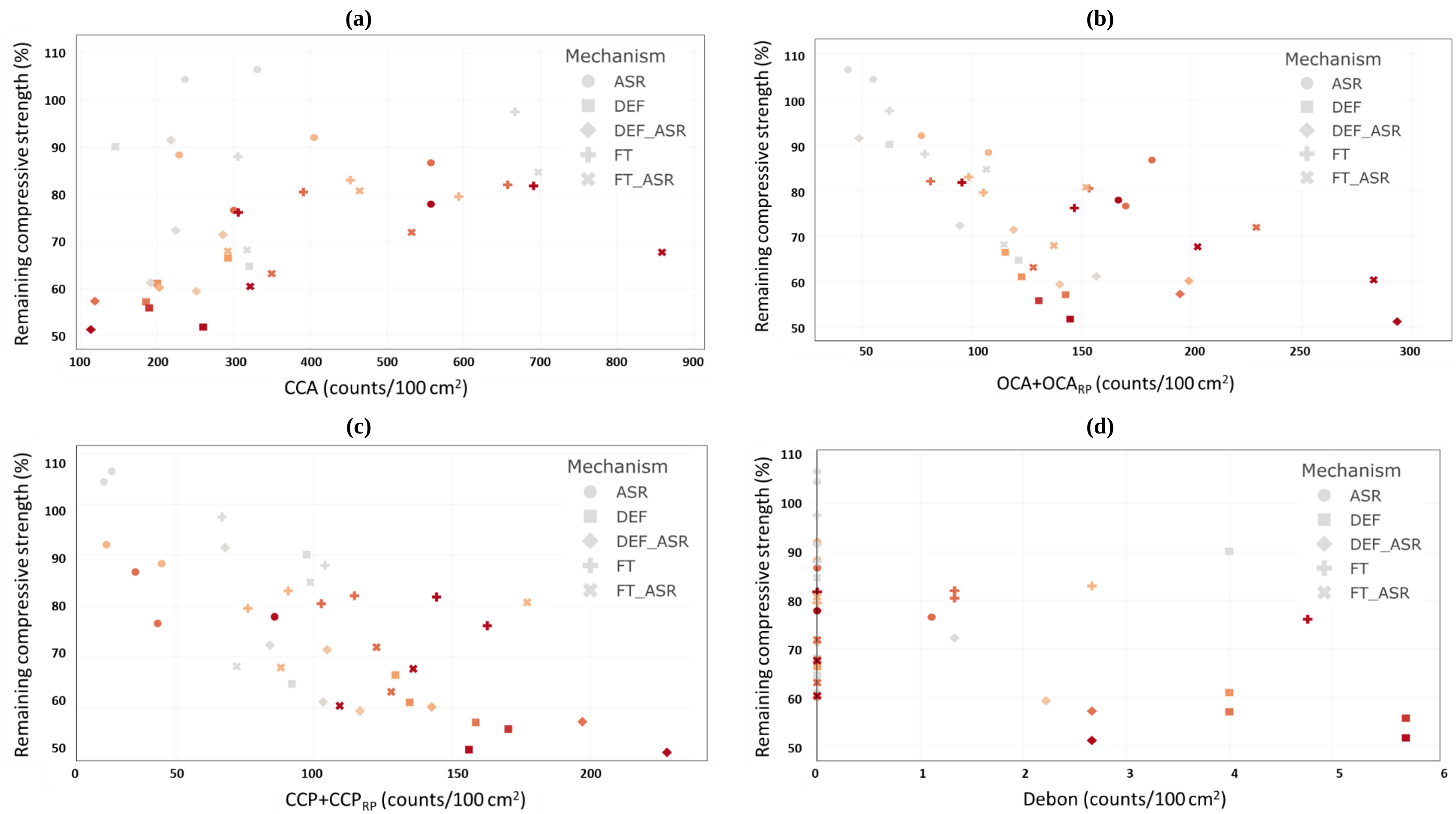

Figure 6.20. Remaining compressive strength as a function of distress feature counts.

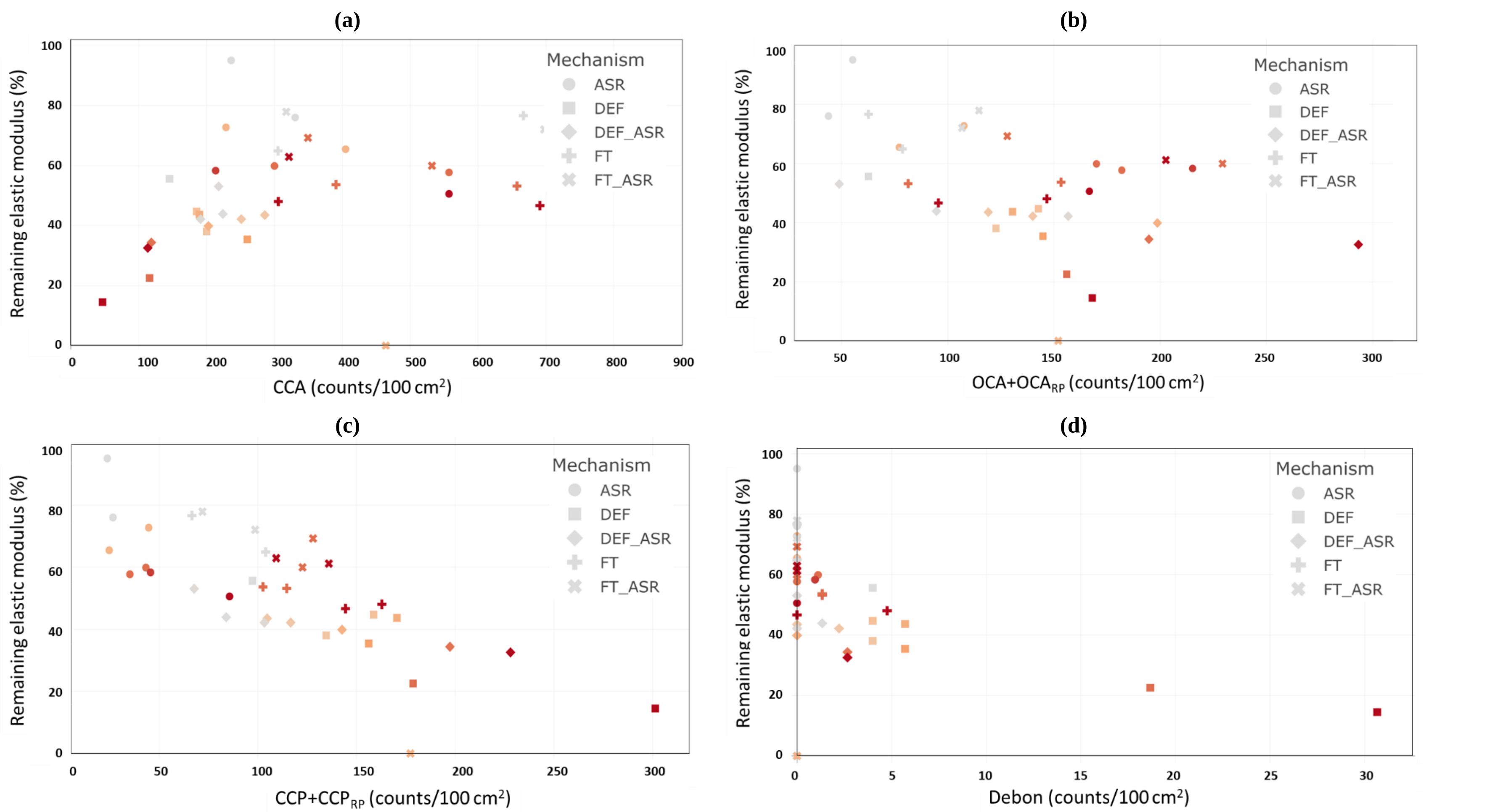

Figure 6.21. Remaining elastic modulus as a function of distress feature counts.

Chapter 7: The damage rating index (DRI): a practical guideline for autonomous operator training

Cassandra Trottier and Leandro F.M. Sanchez

Abstract

The damage rating index (DRI) is a microscopy tool that captures the extent of internal swelling reaction-induced deterioration (ISR). Although engineering practitioners more widely use mechanical tests, it is necessary to attest to the presence and degree of ISR through microscopy. A more detailed evaluation can be achieved by combining mechanical and microscopy techniques, including the DRI, which has proven reliable in diagnosing the extent of ISR-induced deterioration. However, there is currently a lack of practical guidelines and standards in the literature explaining how to perform the DRI, raising concerns about the tool's use, particularly regarding operator variability and subjectivity. This work aims to create practical guidelines for conducting the DRI analysis methodology on concrete affected by alkali-silica reaction (ASR) originating from either reactive coarse or fine aggregates at various degrees of damage (i.e., 0.05%, 0.12%, 0.20%, and 0.30% expansion). Ranges of expected values were established to serve as autonomous training for new operators using the same reactive aggregates and mixtures.

Keywords: *Alkali-silica reaction; damage rating index; operator training; point-count microscopy; damage characterization.*

7.1. Introduction

7.1.1. Internal selling reactions (ISR) in concrete: current practices for diagnosis

Internal swelling reactions (ISR) arise from a lack of awareness and understanding of material incompatibility and the processes contributing to concrete deterioration. Industry needs drive education and training practices in the concrete sector; therefore, engineering practitioners are well-trained in designing concrete mixtures and structures. However, due to the age of the existing concrete infrastructure in Canada, resources (i.e., tools, literature, training, etc.) are crucial for addressing durability-related issues. Several documents are available [1–5] that outline theoretical concepts for using diagnostic tools; however, they do not directly guide practitioners on using and implementing these evaluation tools or interpreting the data for characterizing ISR-induced deterioration. ISR (e.g., alkali-aggregate reaction – AAR, delayed ettringite formation – DEF, freezing and thawing – F/T, etc.) are distress mechanisms that compromise the mechanical properties of concrete and its durability, leading to structural instability, deformations or deflections, and an overall reduction in the service life of concrete infrastructure. While non-destructive and mechanical testing are often preferred for estimating properties of concern (i.e., compressive and tensile strengths and the modulus of elasticity), concrete petrography in this context remains the technique used to confirm the presence of ISR. Globally, microscopy allows an operator to inspect microscopic distress features in concrete and their associated characteristics to draw conclusions based on observations. Similarly, the damage rating index (DRI) methodology and analysis can effectively capture the extent of damage at a scale that accurately represents ISR-affected concrete when conducted by a trained operator, and it can also identify the cause of deterioration when performed by an experienced professional petrographer.

7.1.2. A review of the damage rating index (DRI)

The DRI is a microscopy tool used to assess concrete deterioration. Grattan-Bellew and Danay [6] first proposed the DRI to assess concrete cores extracted from dams exhibiting distinct deterioration levels related to alkali-silica reaction (ASR). It was established to quantify the progression of ASR relatively; however, the considered petrographic features and weighting factors were selected to emphasize signs of ASR. Since then, researchers have suggested modifications to these features and factors from a petrographic standpoint [6–9]; nonetheless, variability among operators has remained a concern regarding systematic evaluations. Villeneuve et al. (2011, 2012) subsequently tackled the issue of variability among operators, aiming to distinguish the petrographic aspect of distress features (i.e., a crack without or with reaction products) by proposing a uniform weighting factor for these features, regardless of the presence of reaction products [10,11]. Therefore, these weighting factors most accurately represent the damage to concrete rather than merely indicating ASR, and they have been correlated with expansion [10,11]. Sanchez et al. [12,13] further examined the relationship between the DRI and mechanical responses, thereby validating the selection of the proposed weighting factors [10,11] for damage to concrete caused by ASR stemming from reactive coarse and fine aggregates down to 1 mm in size, thus confirming the applicability of the DRI methodology and analysis to reactive fine aggregates [14]. Other ISR mechanisms have been assessed using the DRI [10,15–20], attesting to its adaptability to a broader range of deterioration mechanisms.

The data collection procedure for calculating the DRI is performed on a sawn, flat, polished inner concrete surface from a core or specimen using a stereomicroscope at 15-16x magnification, where squares measuring 1 cm^2 are within the field of view. Distress features are counted and recorded in each square. Weighting factors related to the severity of each distress feature encountered

(Table 7.1) are applied, and the sum of those features is calculated over 100 cm² to normalize the value, as illustrated in Equation 7.1.

$$DRI = \frac{\sum[0.25(CCA) + 2(OCA + OCA_{RP} + DAP) + 3(CCP + CCP_{RP} + Debon)]}{n} \times 100\ cm^2 \qquad \textbf{Equation 7.1}$$

Where CCA is the total number of closed cracks in the aggregate, $OCA\ and\ OCA_{RP}$ are the total numbers of open cracks in the aggregate without and with reaction products, respectively, DAP is the total number of disaggregated/corroded particles, $CCP\ and\ CCP_{RP}$ are the total numbers of cracks in the cement paste without and with reaction products, respectively, $Debon$ is the total number of debonded/dislodged aggregates, and *n* is the number of analyzed 1 cm^2 squares.

Table 7.1. Pre-determined list of distress/petrographic features and associated weighting factors.

Distress/petrographic feature	Original weighting factor [6]	Updated weighting factor [10]	Type of feature
Crack in the aggregate	0.25	-	Distress
Closed crack in the aggregate (CCA)	-	0.25	Distress
Opened crack in the aggregate (OCA)	-	2	Distress
Opened crack in the aggregate with reaction products (OCA_{RP})	2	2	Distress/petrographic
Corroded/disaggregated aggregate (DAP)	-	2	Distress/petrographic
Reaction rim in aggregate	0.5	-	Petrographic
Crack in the cement paste (CCP)	2	3	Distress
Crack in the cement paste with reaction products (CCP_{RP})	4	3	Distress/petrographic
Air void lined/filled with RP	0.5	-	Petrographic
Debonded aggregate particles (Debon)	3	3	Distress

The observed data can be visualized as a plot of the DRI number as a function of expansion when the cause and level of damage are known. In contrast, bar charts (weighted or unweighted – extended version of the DRI [12,14]) separate distinct distress features, enabling a more diagnostic character by visualizing the proportions of features. Although complexities are associated with identifying certain crack types, especially in coarse-grained aggregates for untrained operators, the DRI remains a point-count method similar to standard procedures (e.g., ASTM C295/295M: Guide for petrographic examination of aggregates for concrete, ASTM C1356: Test Method for Quantitative Determination of Phases in Portland Cement Clinker by Microscopical Point-Count Procedure, and ASTM C457/457M: Test Method for Microscopical Determination of Parameters of the Air-Void System in Hardened Concrete) [21–23]. Nevertheless, concerns regarding operator variability persist, which can be mitigated through adherence to a training procedure. Consequently, providing a methodology for new operators to perform such analyses autonomously is fundamental to integrating this tool into engineering practice.

7.2.Motivation and objective

The nuances surrounding the DRI have led to the establishment of a practical guideline for autonomous operator training on DRI methodology and analysis, further assisting engineering practitioners in evaluating damage to concrete using microscopy. This guideline presents ASR as the distress mechanism utilized for the training. The concrete mixtures were fabricated using two types of ASR-susceptible aggregates selected for their distinct deterioration patterns and variety of associated features: a reactive coarse aggregate (i.e., Springhill – Greywacke) was combined with non-reactive sand to produce ASR damage originating from the coarse aggregate, while a reactive sand (i.e., Texas – Polymictic sand) was combined with a non-reactive coarse aggregate to generate ASR damage originating from the fine aggregate. To guide the operator through various extents of damage, four levels of expansion were selected (i.e., 0.05%, 0.12%, 0.20%, and 0.30%), helping to capture the propagation of damage and its associated features. The proposed approach aims to reduce operator variability as training will be conducted on concrete under similar conditions (i.e., reactive aggregates, proportioned using standard mixtures, ASR development, and equipment for surface preparation and conducting the analysis).

7.3. Materials and methods

7.3.1. Materials and specimen fabrication

Laboratory-made cylindrical concrete specimens (i.e., 10 cm by 20 cm) are created using standard mixture proportions according to ASTM C1293-18a: Test Method for Determination of Length Change of Concrete Due to Alkali-Silica Reaction and CSA A23.2-14A: Potential expansivity of aggregates (procedure for length change due to alkali-aggregate reaction in concrete prisms at 38°C) [24,25] with a cement content of 420 kg/m^3. The characterization of aggregates and details of the mixtures are presented in Table 7.2 and Table 7.3, respectively. A reactive coarse aggregate (i.e., Springhill – Greywacke) is combined with non-reactive sand to produce ASR damage stemming from the coarse aggregate, while a reactive sand (i.e., Texas – Polymictic sand) is combined with a non-reactive coarse aggregate to generate ASR damage originating from the fine aggregate. The total alkali content of all concrete mixtures is increased to 5.25 kg/m^3 (equivalent to 1.25% Na_2O_{eq}. by cement mass) using reagent-grade NaOH to accelerate the reaction, as specified in ASTM C1293-18a and CSA A23.2-14A. The concrete specimens are then demoulded after moist curing for 24 hours (i.e., 100% RH and 20°C). Holes measuring 8 mm in diameter and 25 mm in length are drilled into both ends of the cylinders. Stainless steel screws, 19 mm in length, are used as reference points and installed in the holes with a quick-setting cement paste slurry. The concrete specimens cure for an additional 24 hours under the same conditions. Specimens are then stored after the initial length readings in environments conducive to ASR development (i.e., 100% RH and 38°C), and length change measurements are taken periodically to monitor the expansion time.

Table 7.2. Aggregate characterization.

Aggregate	Location	Rock type	Relative density	Absorption (%)	Reactivity
Fine	Ottawa, Ontario (Canada)	Derived from granite	2.60-2.65	0.82-1.18	Non-reactive
Fine	Bracebridge, Ontario (Canada)	Orthoclase, Quartz, Cristoballite, Albite, Bytowmite, Cordierite, Illite, Muscovite, Larnite	2.73	0.37	Non-reactive
Fine	Ottawa, Ontario (Canada)	Manufactured crushed limestone	2.74	0.65	Non-reactive
Fine	Corpus Christie, Texas (USA)	Polymictic sand (granitic, mixed volcanics, quartzite, chert, quartz)	2.60	0.55-0.89	Reactive
Coarse	Newfoundland (Canada)	High-purity limestone	2.68	0.44	Non-reactive
Coarse	Ottawa, Ontario (Canada)	Limestone	2.78	0.42	Non-reactive
Coarse	Springhill, New Brunswick (Canada)	Greywacke	2.68-2.72	0.602-0.89	Reactive

Table 7.3. Mix-design per operator.

Operator	Cement	Water	Water-to-cement ratio	Non-reactive sand	Reactive coarse aggregate Springhill
				kg per 1 m^3 of concrete	
1	420	189	0.45	823 (Ottawa sand)	934
2		189	0.45	860 (Bracebridge sand)	915
3		187	0.45	829 (Manufactured sand)	999
4		176	0.42	681 (Ottawa sand)	1044
5		189	0.45	836 (Ottawa sand)	938
Operator	**Cement**	**Water**		**Reactive sand Texas**	**Non-reactive coarse aggregate**
				kg per 1 m^3 of concrete	
1	420	189	0.45	760	1024 (limestone)
4		176	0.42	732	1072 (limestone)
5		189	0.45	765	1020 (limestone)
6		177	0.42	678	1093 (High-purity limestone)

7.3.2. Sample preparation

The specimens are cut in half longitudinally with a wet masonry saw. To achieve a highly reflective surface, the suggested grinding and polishing grit sequence includes 30, 60, 140, 280 (80–100 μm), 600 (20–40 μm), 1200 (10–20 μm), and 3000 (4–8 μm). A visual guide on sample preparation for such analysis is available in [26].

7.3.3. The damage rating index (DRI) calculation

The DRI calculation considers all counted and weighted distress features (Table 7.1) by summing them, normalizing the result by dividing it by the number of analyzed squares and multiplying by 100 cm^2 (Equation 7.1). While the DRI can be applied to various ISRs, the currently proposed protocol emphasizes damage due to ASR, using the weighting factors from Villeneuve [10] in Equation 7.1. The distress features in the aggregates include coarse and fine aggregates [12]. Bar charts are created to separate the features and visualize their relative importance towards the overall assessment deterioration.

7.3.4. Referencing system and microscope set-up

A grid was utilized as a referencing system with stepping intervals of 1 cm in both the X and Y directions, which can be drawn using a fine-tip permanent marker or a 3D-printed grid. Letters and numbers are used to identify the rows and columns, respectively. Figure 7.1 illustrates the referencing system on a polished concrete specimen, facilitating the tabulation of observations. It is recommended to set up the spreadsheet so that the rows represent the squares under analysis and the columns reflect the categories of features while analyzing the squares from left to right. Gooseneck oblique lights illuminated the surface and highlighted the features (Figure 7.1).

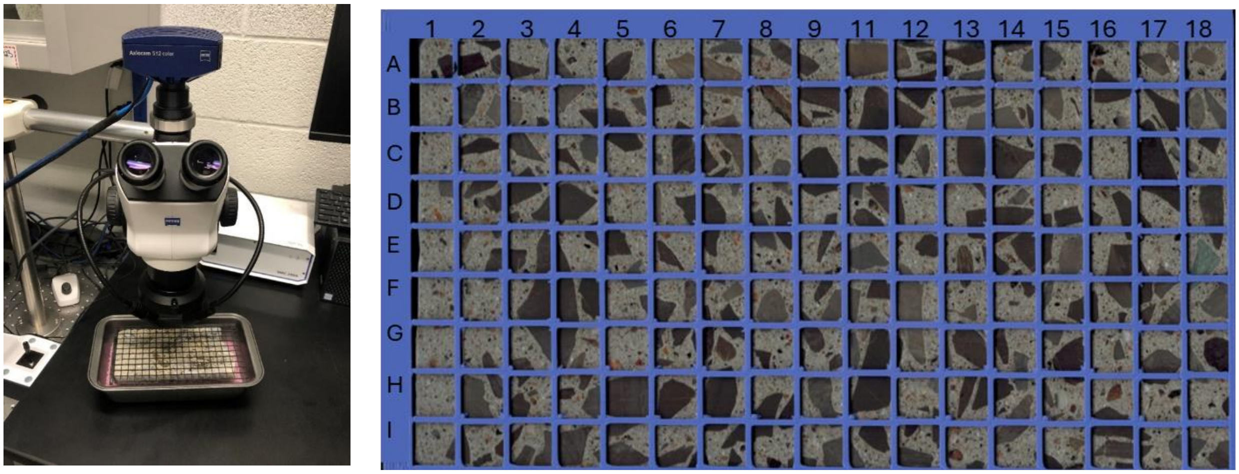

Figure 7.1. Stereomicroscope and specimen surface configuration.

7.3.5. Data collection

In this proposed training guide, the distress features associated with ASR damage (i.e., cracks) are listed in Table 7.1, and only the common features produced by the reactive Springhill and Texas aggregates will be discussed. ASR is recognizable by its cracks in the aggregate, particularly when it contains a gel-like reaction product. CCA does not exhibit an opening or gap between the edges of the crack (Figures 7.2a to d). OCA and OCA_{RP} present an opening between the crack edges and can be either empty or filled with reaction products, respectively (Figures 7.2e and f). A partially filled OCA is regarded as an OCA_{RP}, while a combination of CCA and OCA may be observed on a single crack segment (Figures 7.2g and h, respectively). CCP and CCP_{RP} refer to those within the bulk cement paste (Figure 7.2i). An OCA or OCA_{RP} that extends from the aggregate to the cement paste is counted as two distinct crack types (Figures 2j to l).

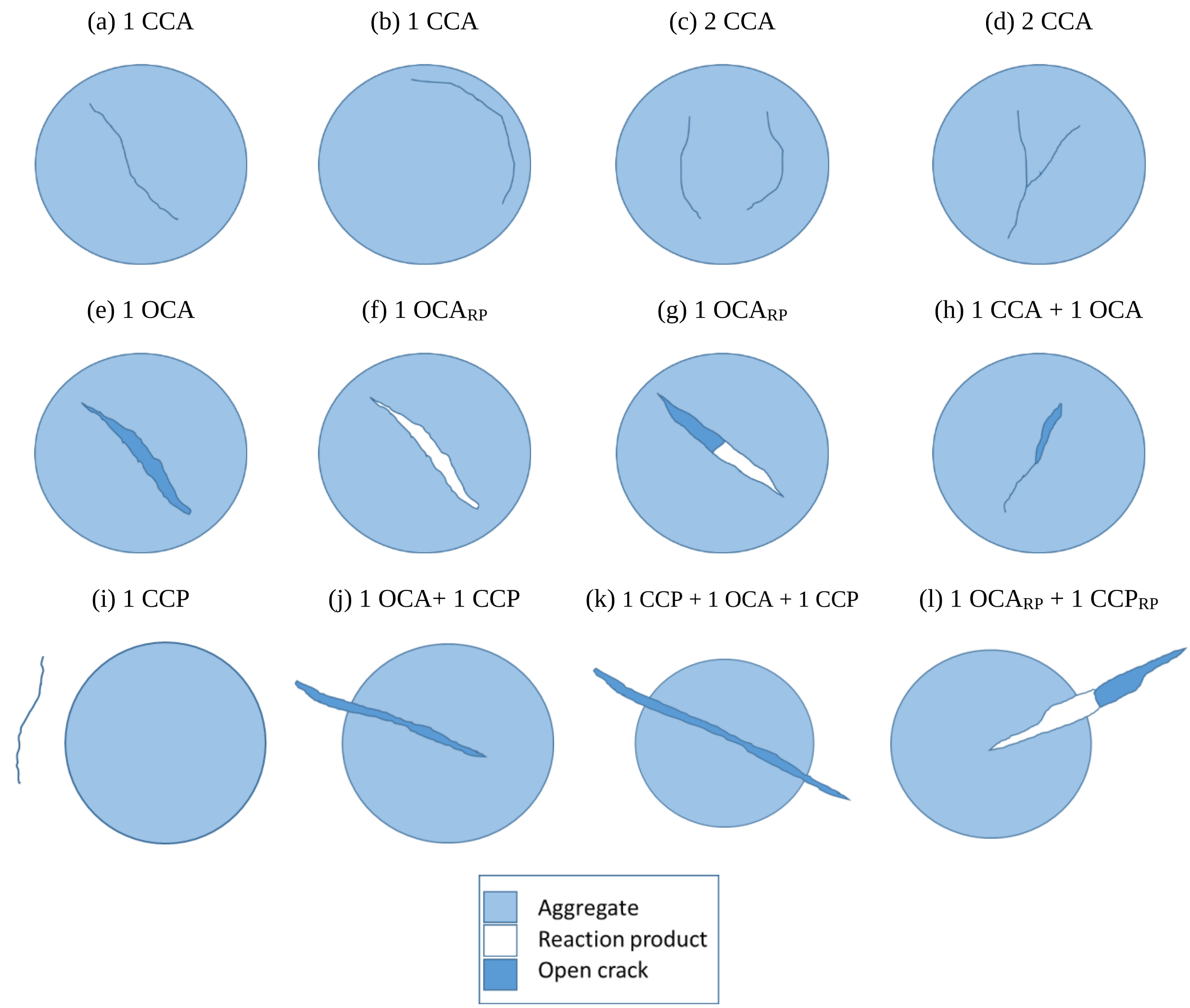

Figure 7.2. Crack type and counts schematics.

Multiple connected cracks can be observed; therefore, the point-counting technique applied to cracks in networks is illustrated in Figure 7.3. In practice, cracks are counted starting from one segment tip (starting point) and following the crack until all ends have been considered (endpoints indicated by numbers).

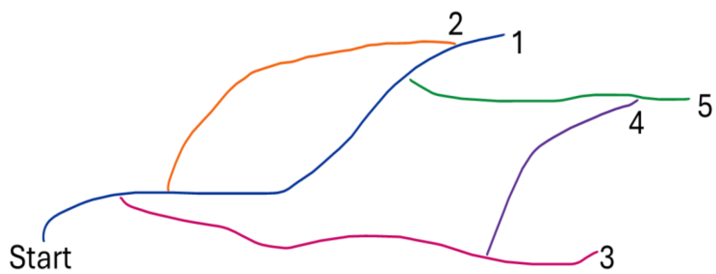

Figure 7.3. Counts in a crack network.

For instance, in Figure 7.4a, the OCA and OCA_{RP} are linked by a CCP. Figure 7.4b presents a longer CCP present in the bulk cement paste, in the aggregate-paste interface, and a crack connecting several reactive sand particles through the cement paste. Figure 7.4c illustrates a CCA and natural veins in the aggregate. Furthermore, in the images, natural veins and cracks can easily be confused; however, their appearance under the microscope with proper lighting conditions reveals their distinctive characteristics, where depth is noticeable in an OCA. The reactive sand used in this work is shown in Figure 7.4d, where the OCA and CCP can be observed. More examples of micrographs can be found in the literature [10,12,27].

a) field of view is 10 mm **b) field of view is 10 mm**

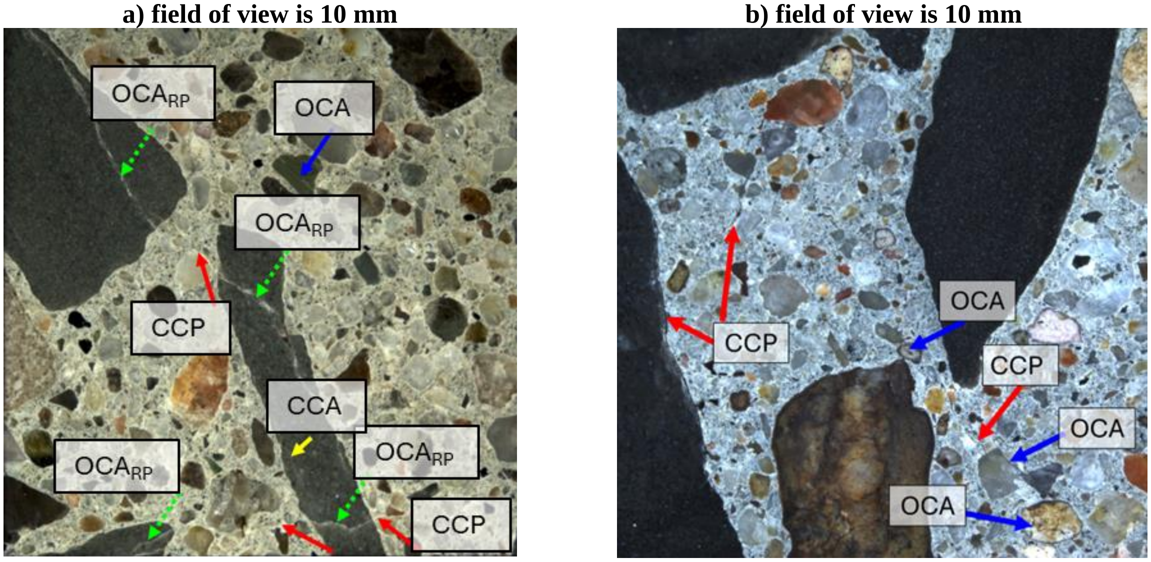

c) field of view is 10 mm d) field of view is 5 mm

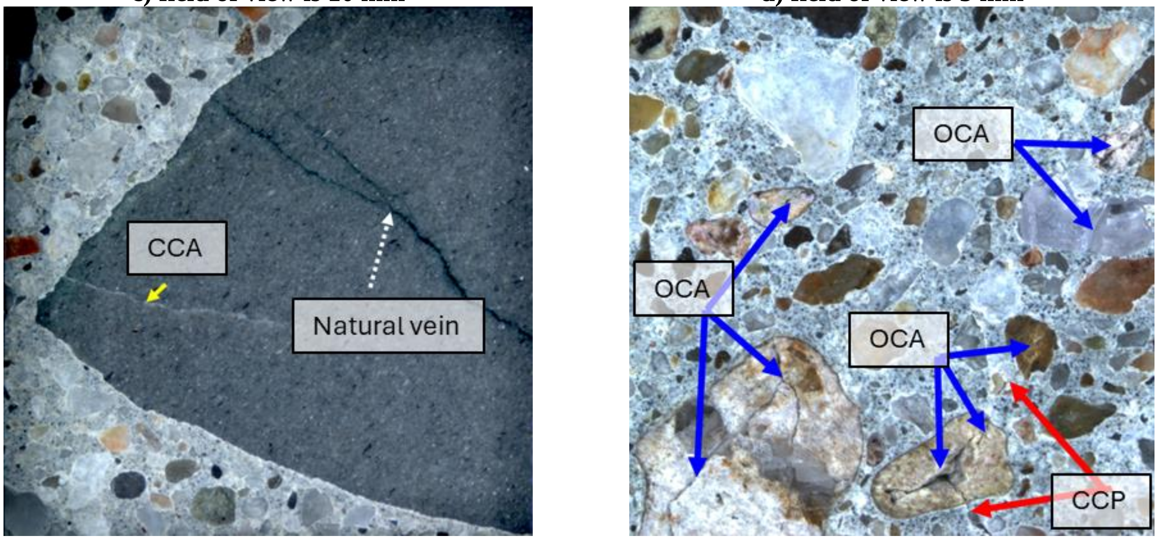

Figure 7.4. Examples of crack types.

7.4.Proposed approach

7.4.1. A new perspective on the analysis of DRI results

The DRI is typically represented as a number or through bar charts to differentiate the various distress features. Sanchez et al. [12,14] proposed an extended version of the DRI, which includes unweighted counts per 100 cm² and proportions to aid in damage propagation analyses. Figure 7.5 illustrates the operators' combined unweighted counts and proportions as lower and upper limits (i.e., the minimum and maximum values obtained) and the DRI number displayed above the corresponding bar. The DRI numbers increase with expansion; however, overlap is observed between adjacent expansion levels' lower and upper limits. Overall, the differences in DRI numbers between the lower and upper limits grow with expansion, from 136 and 201 for the Springhill reactive coarse aggregate and Texas reactive sand, respectively, at 0.05% expansion to 419 and 614 at 0.30% expansion. These differences are significant when assessing the extent of damage due to ASR; therefore, it is necessary to break down the distress features into unweighted bar charts to better understand their propagation and distribution. The CCA typically accounts for over 45% of the distress features, followed by the $OCA+OCA_{RP}$, which ranges from 23% to 46%

and 6% to 37% for Springhill and Texas, respectively. The CCP+CCP_{RP} is less prevalent because the distress mechanisms are more common in the aggregates, at 3% to 14%. Similarly, the OCA+OCA_{RP} and CCP+CCP_{RP} increase with expansion, yet the results overlap.

a)

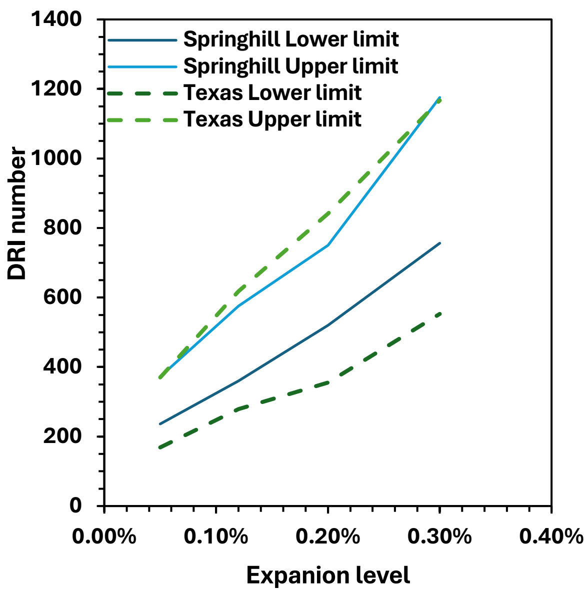

b)

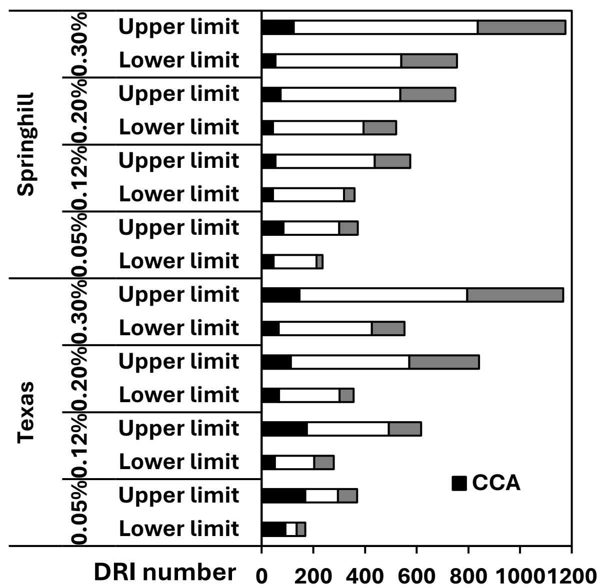

c)

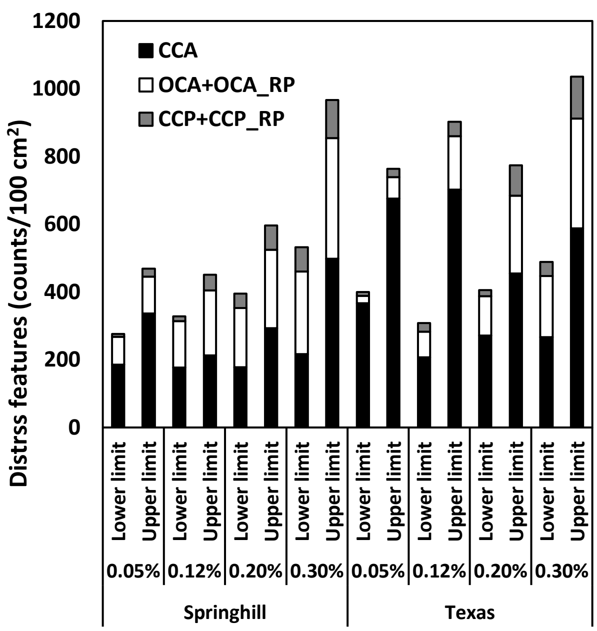

d)

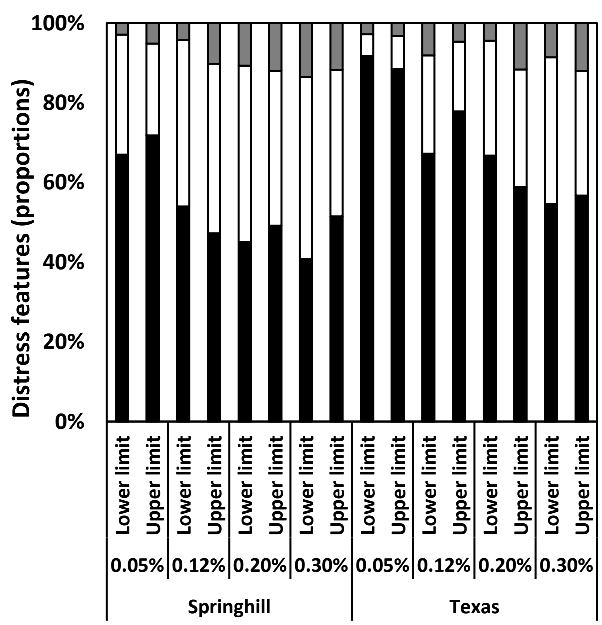

Figure 7.5. The DRI as a function of expansion is presented as a) the DRI number obtained for all operators, b) weighted bar charts, c) an extended version of the DRI as c) counts/100 cm^2 and d) proportions.

The observed count data was converted into histograms for each distress feature (i.e., CCA, $OCA+OCA_{RP}$, and $CCP+CCP_{RP}$) and reactive aggregate type (Figure 7.6), where the frequencies of counts (y-axis) are displayed as a function of count categories (x-axis), with the categories representing the number of instances of "*i*" counts. The histograms showcase the pooled results, illustrating their sensitivity to various expansion levels. The maximum count category increases with expansion, as evidenced by the longer and thicker tail. The shapes of the histograms differ for the CCA when comparing the aggregate type, with means ranging from 1.95 to 3.56 and 4.02 to 4.95 for the Springhill and Texas reactive aggregates, respectively. The means for $OCA+OCA_{RP}$ also increase with expansion, ranging from 0.98 to 2.9 and 0.54 to 2.31 for the Springhill and Texas reactive aggregates, respectively. The $OCA+OCA_{RP}$ for the Springhill aggregate exhibits a decreasing frequency from zero counts at 0.05% expansion, an increase from 0 to 1 count at 0.12% expansion, a consistent slope from 0 to 2 counts at 0.20% expansion, and a peak at 3 counts for the 0.30% expansion. Conversely, $OCA+OCA_{RP}$ for the Texas sand at 0.05%, 0.12%, and 0.20% expansion shows a decrease in frequency from zero count and peaks at 1 count for the 0.30% expansion. The $CCP+CCP_{RP}$ decreases frequencies from zero counts for the Springhill and Texas aggregates, with means ranging from 0.14 to 1.01 for the Springhill aggregate and 0.16 to 0.86 for the Texas sand. Furthermore, the magnitude of frequencies varies by reactive aggregate type, thereby highlighting the histogram's capacity to capture these differences.

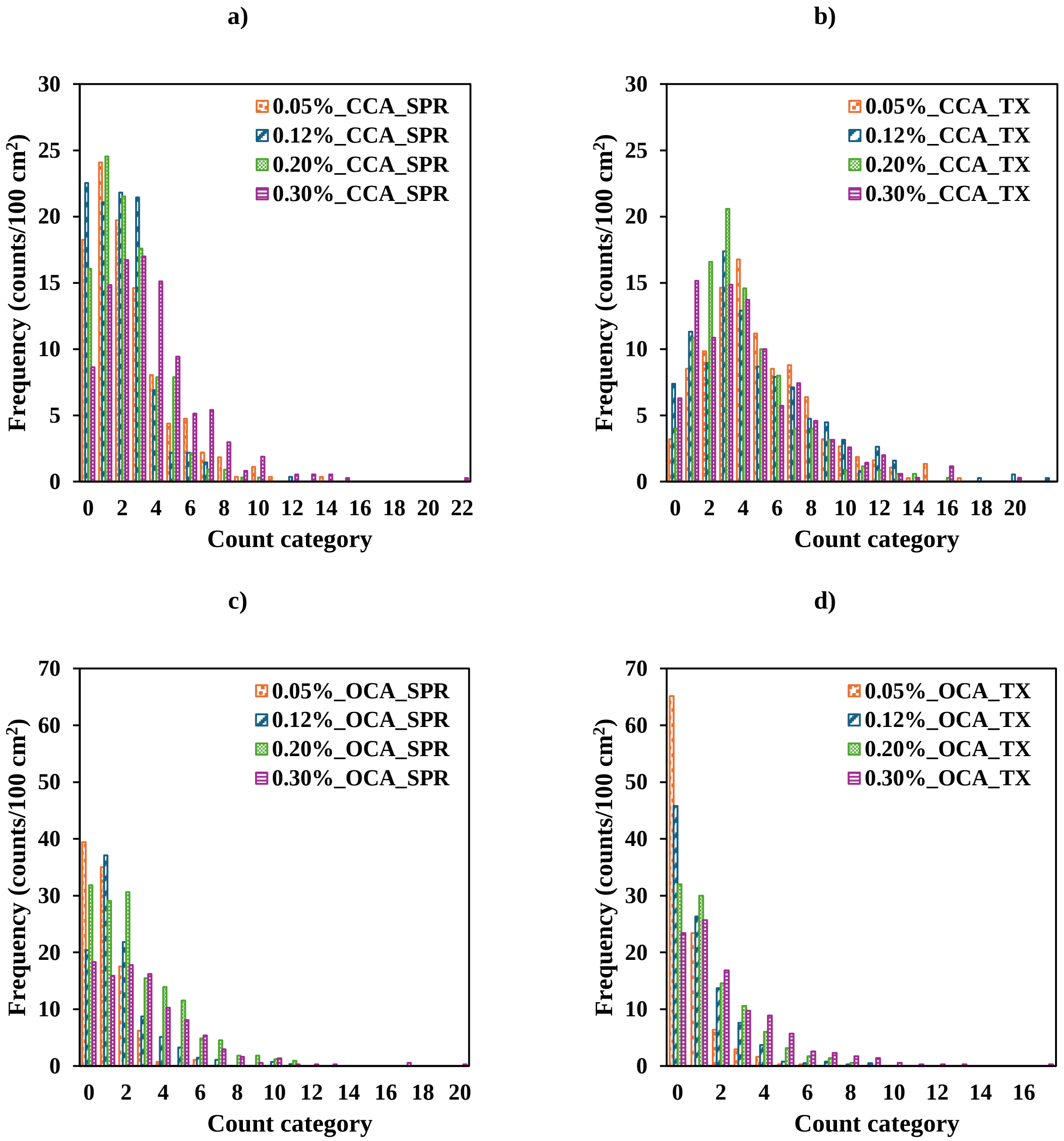
a)
b)
c)
d)
Frequency (counts/100 cm²)
Count category
0.05%_CCA_SPR
0.12%_CCA_SPR
0.20%_CCA_SPR
0.30%_CCA_SPR
0.05%_CCA_TX
0.12%_CCA_TX
0.20%_CCA_TX
0.30%_CCA_TX
0.05%_OCA_SPR
0.12%_OCA_SPR
0.20%_OCA_SPR
0.30%_OCA_SPR
0.05%_OCA_TX
0.12%_OCA_TX
0.20%_OCA_TX
0.30%_OCA_TX

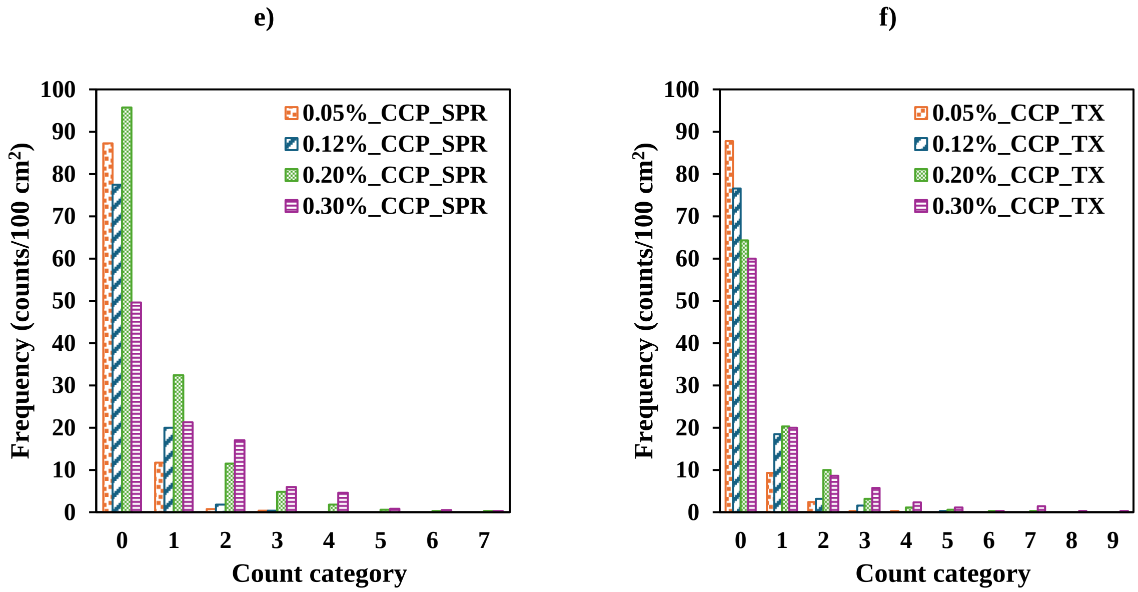

Figure 7.6. Histograms of distress feature counts per reactive aggregate type.

7.4.2. Autonomous operator training

Operator-dependent testing can lead to patterns requiring acceptable value ranges for each distress feature category. Moreover, during training, histograms can help eliminate encountered biases and ensure that operator counts align with the distribution of expected counts rather than over or under-compensating to achieve a desired result. Consequently, the data collected from operators was used to create cumulative curves with lower and upper-value limits to establish the acceptable ranges a new operator should achieve when assessing ASR damage to concrete derived from Springhill and Texas reactive aggregates (Tables 7.4 and 7.5, respectively). These tables outline the lower and upper limits for the total counts, as the operator is expected to remain within these total counts and within the cumulative frequency ranges.

Table 7.4. Cumulative count frequencies for Springhill coarse aggregate.

Expansion level	0.05%						0.12%					
Distress feature	CCA		$OCA+OCA_{RP}$		$CCP+CCP_{RP}$		CCA		$OCA+OCA_{RP}$		$CCP+CCP_{RP}$	
Counts/100 cm^2	185	337	83	108	8	24	177	213	137	192	14	46
Count category												
0	5.7	26.0	38.1	40.2	78.1	92.9	7.6	31.8	3.8	30.6	57.1	90.0
1	20.0	56.2	70.4	81.0	98.8	99.0	29.5	52.4	51.8	66.7	97.1	97.6
2	42.9	74.0	88.2	98.1	99.0	100.0	60.0	68.8	71.2	92.4	98.8	100.0
3	61.0	86.4	97.0	100.0	100.0		84.1	91.4	80.6	100.0	99.4	
4	73.3	91.7	98.2				91.2	98.1	88.8		100.0	
5	82.9	92.9	98.2				93.5	100.0	94.1			
6	89.5	96.5					97.1		96.5			
7	93.3	97.6					99.4		98.2			
8	97.1	98.2					99.4		98.2			
9	98.1	98.2					99.4		98.2			
10	99.1	99.4					99.4		99.4			
11	100.0	99.4					99.4		100.0			
12		99.4					100.0					
13-14		99.4-100										

Expansion level	0.20%						0.30%					
Counts/100 cm^2	178	293	175	232	42	71	217	498	243	356	72	113
Count category												
0	2.9	22.7	19.1	34.5	50.5	68.9	2.7	21.0	10.2	30.3	44.9	53.3
1	26.7	47.2	44.3	51.3	81.5	92.5	11.6	46.2	23.8	50.4	66.4	80.0
2	46.7	74.0	58.5	78.1	89.9	98.1	24.5	62.2	40.1	67.2	84.0	95.2
3	71.4	85.7	71.7	90.5	95.0	100.0	39.5	75.6	57.8	76.5	89.9	99.0
4	79.1	95.8	83.0	93.3	97.5		54.4	88.2	71.4	85.7	97.5	100.0
5	91.4	99.2	91.5	98.1	98.3		63.3	94.1	81.0	95.2	98.3	
6	94.3	99.2	95.3	100.0	99.7		71.4	97.1	88.4	97.1	99.2	
7	96.2	100.0	98.1		100.0		81.0	100.0	91.8	100.0	100.0	
8	99.1		99.1				87.8		95.0			
9	99.1		99.1				89.8		95.2			
10	100.0		99.1				94.6		97.3			
11			100.0				94.6		98.0			
12							95.9		98.3			
13							97.3		98.6			
14							98.6		98.6			
15							99.3		98.6			
16							99.3		98.6			
						17-22	99.3-100	17-20	99.2-100			

Table 7.5. Cumulative count frequencies for Texas fine aggregate.

	Expansion level	0.05%						0.12%					
	Distress feature	CCA		OCA+OCA$_{RP}$		CCP+CCP$_{RP}$		CCA		OCA+OCA$_{RP}$		CCP+CCP$_{RP}$	
	Counts/100 cm^2	367	676	22	63	11	25	207	702	76	158	25	42
Count category	0	2.8	3.8	47.6	83.6	79.0	91.5	1.9	18.3	30.8	58.8	60.6	82.9
	1	9.4	15.2	77.4	97.6	96.2	97.6	1.9	50.0	56.7	81.2	94.1	97.1
	2	16.0	26.7	86.8	98.1	98.8	100.0	8.5	60.6	76.9	90.6	97.1	100.0
	3	23.6	47.6	100.0	100.0	99.4		16.0	84.6	89.4	95.3	99.4	
	4	34.9	68.6			100.0		31.1	91.3	94.3	98.8	99.4	
	5	43.4	82.9					37.7	97.1	96.2	99.4	100.0	
	6	49.1	93.3					50.0	97.1	97.1	100.0		
	7	62.3	96.2					63.2	98.1	98.1			
	8	68.9	99.0					71.7	98.1	99.0			
	9	74.5	100.0					77.4	99.0	100.0			
	10	79.2						85.8	99.0				
	11	84.0						86.8	100.0				
	12	89.6						92.5					
	13	93.4						96.2					
	14	94.3						96.2					
	15-17	99.1-100					15-22	96.2					
	Expansion level	0.20%						0.30%					
	Counts/100 cm^2	271	455	117	229	18	90	267	588	180	324	42	124
Count category	0	3.8	4.1	17.1	39.5	47.3	82.9	3.9	8.6	7.6	34.2	50.9	76.3
	1	9.2	26.7	41.0	72.8	74.0	99.0	9.2	41.0	28.6	58.0	72.2	88.2
	2	23.7	48.6	61.0	84.0	91.7	100.0	17.1	57.1	44.8	75.7	80.5	97.4
	3	36.8	75.2	75.2	93.5	94.7		31.6	69.5	59.0	83.4	88.8	100.0
	4	55.3	85.7	88.6	97.6	96.1		46.1	83.8	74.3	89.9	93.5	
	5	61.8	94.3	94.3	98.2	97.4		52.6	86.7	82.9	95.3	95.9	
	6	69.7	96.2	95.2	99.4	98.7		57.9	92.4	87.6	97.0	95.9	
	7	78.9	99.0	98.7	100.0	100.0		71.1	96.2	90.8	97.6	98.8	
	8	85.5	99.0	100.0				77.6	99.0	93.4	98.1	99.4	
	9	89.5	100.0					82.9	99.0	96.1	99.0	100.0	
	10	90.8						86.8	100.0	97.4	100.0		
	11	93.4						90.8		97.4			
	12	94.7						93.4		98.7			
	13	96.1						96.1		98.7			
	14-16	98.7-100					14-20	97.4-100	14-17	98.7-100			

7.4.3. *Representative sample size*

The number of analyzed 1 cm² squares was also considered to ensure that the DRI values were derived from a representative sample. Convergence (approaching a slope of ± 20 DRI units) was noted through the law of large numbers (Equation 7.2) from cumulative DRI values as a function of the number of analyzed squares (Figure 7.7).

$$DRI = \frac{\sum_{i=1}^{n} X_i}{i} = \frac{X_1 + X_2 + X_3 + \cdots + X_n}{n} \quad \text{Eq. 7.2}$$

Where X_i represents the DRI number until square i and n is the total number of analyzed squares.

This cumulative concept confirmed representative samples based on 1 cm² squares rather than multiple concrete specimens. This ensures that the operator's DRI number converges toward a mean value, provided the damage is homogeneous across the analyzed surface. Convergence was achieved at a smaller *n* for lower expansion levels. Larger sample sizes are necessary for higher expansion levels, where the average surface area needed to reach convergence for the Springhill coarse aggregate was 21, 35, 46, and 65 cm², at expansion levels of 0.05%, 0.12%, 0.20%, and 0.30%, respectively. In contrast, 21, 52, 51, and 64 cm² were required for the Texas fine aggregate at expansion levels of 0.05%, 0.12%, 0.20%, and 0.30%, respectively. This indicates that the sample size partially depends on the observed level of damage and the source of ASR damage. A sample size of 100 cm² for laboratory-made specimens is therefore sufficient to capture all extents of ASR-induced deterioration [14]. However, concrete extracted from field structures requires further studies to better understand the varying patterns caused by external and internal factors. Consequently, 200 cm² remains the suggested sample size for extracted cores from the field concrete.

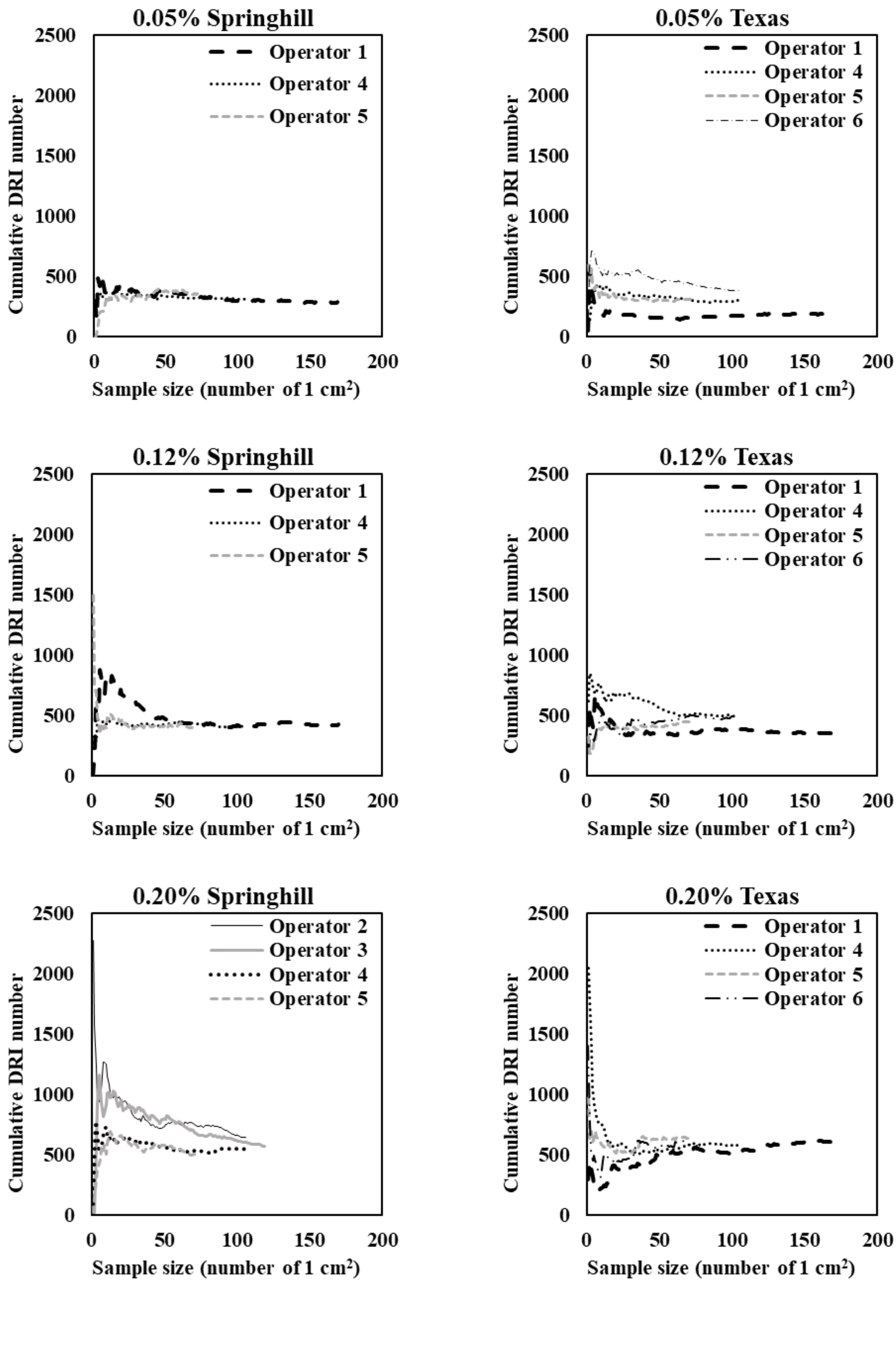
0.05% Springhill
Operator 1
Operator 4
Operator 5
Cumulative DRI number
Sample size (number of 1 cm²)
0.05% Texas
Operator 1
Operator 4
Operator 5
Operator 6
Cumulative DRI number
Sample size (number of 1 cm²)
0.12% Springhill
Operator 1
Operator 4
Operator 5
Cumulative DRI number
Sample size (number of 1 cm²)
0.12% Texas
Operator 1
Operator 4
Operator 5
Operator 6
Cumulative DRI number
Sample size (number of 1 cm²)
0.20% Springhill
Operator 2
Operator 3
Operator 4
Operator 5
Cumulative DRI number
Sample size (number of 1 cm²)
0.20% Texas
Operator 1
Operator 4
Operator 5
Operator 6
Cumulative DRI number
Sample size (number of 1 cm²)

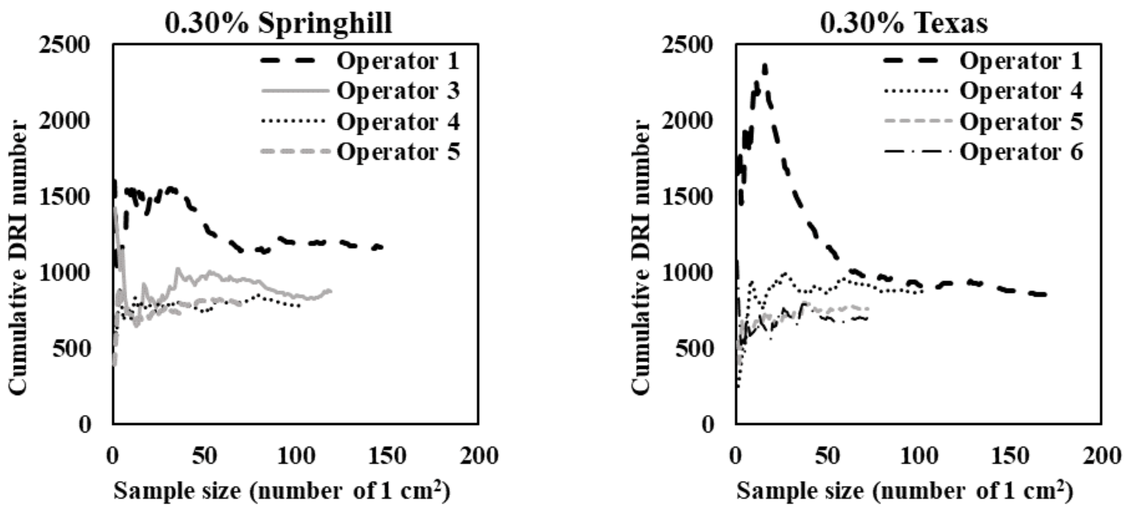

Figure 7.7. Convergence plots.

7.5. Concluding remarks and future perspectives

When viewed as a tool rather than purely a numerical output, the DRI can provide valuable information into the cause(s) and extent of damage in affected concrete. This guide aims to facilitate the adoption of the DRI technique with reduced variability and subjectivity introduced by the operator. The proposed method builds upon an extended version of the DRI, utilizing unweighted counts, histograms illustrating the frequency of plotted count categories, and calculated means. These histograms have demonstrated an influence on changes in damage levels. They can establish acceptable value ranges for operators when autonomously training and assessing ASR damage to concrete across various degrees of damage. Further research is required to incorporate additional aggregate types into the training portfolio and other forms of ISR for a more comprehensive approach to characterizing the extent of ISR-induced deterioration with respect to its cause using the DRI. This tool offers an opportunity to include microscopy for informed engineering decision-making.

7.6.References

[1] V.E. Saouma, ed., Diagnosis & Prognosis of AAR Affected Structures: State-of-the-Art Report of the RILEM Technical Committee 259-ISR, Springer International Publishing, Cham, 2021. https://doi.org/10.1007/978-3-030-44014-5.

[2] B. Godart, M. De Rooij, J.G.M. Wood, eds., Guide to Diagnosis and Appraisal of AAR Damage to Concrete in Structures: Part 1 Diagnosis (AAR 6.1), Springer Netherlands, Dordrecht, 2013. https://doi.org/10.1007/978-94-007-6567-2.

[3] M.-A. Bérubé, N. Smaoui, B. Bissonnette, B. Fournier, Outil d'évaluation et de gestion des ouvrages d'art affectés de réactions alcalis-silice (RAS), Ministère des transports du Québec, Québec, 2005.

[4] Laboratoire central des ponts et chaussées, ed., Aide à la gestion des ouvrages atteints de réactions de gonflement interne: guide méthodologique, Laboratoire central des ponts et chaussées, Paris, 2003.

[5] CSA A864-00 (R2005), Guide to the Evaluation and Management of Concrete Structures Affected by Alkali-Aggregate Reaction, (2005). https://www.csagroup.org/store/product/A864-00/.

[6] P.E. Grattan-Bellew, A. Danay, Comparison of laboratory and field evaluation of alkali-silica reaction in large dams, in: Collection / Collection : NRC Publications Archive / Archives des publications du CNRC, 1992: pp. 1–25.

[7] G.G. Clemena, S. Lane, T. Freeman, M. Lozev, Evaluation of nondestructive evaluation methods for application in early detection of deterioration in concrete pavements, VTRC 00-R13,

Virginia Transortation Research Council, Charlottesville, USA, 2000. https://rosap.ntl.bts.gov/view/dot/14227.

[8] L. Powers, F.H. Shrimer, Quantification of ASR in concrete: an introduction to the Damage-Rating method, in: 29th International Conference on Cement Microscopy, Québec, Canada, 2007.

[9] N. Smaoui, M.-A. Bérubé, B. Fournier, B. Bissonnette, B. Durand, Evaluation of expansion attained by ASR-affected concrete, in: 12th International Conference on Alkali-Aggregate Reaction, Beijing, China, 2004: pp. 1005–1015.

[10] V. Villeneuve, Détermination de l'endommagement du béton par méthode pétrographique quantitative, Master's Thesis., Université Laval, 2011.

[11] V. Villeneuve, B. Fournier, J. Duchesne, Determination of the damage in concrete affected by ASR – the damage rating index (DRI), in: 14th International Conference on Alkali-Aggregate Reaction, Texas, USA, 2012.

[12] L.F.M. Sanchez, B. Fournier, M. Jolin, J. Duchesne, Reliable quantification of AAR damage through assessment of the Damage Rating Index (DRI), Cement and Concrete Research 67 (2015) 74–92. https://doi.org/10.1016/j.cemconres.2014.08.002.

[13] L.F.M. Sanchez, B. Fournier, M. Jolin, D. Mitchell, J. Bastien, Overall assessment of Alkali-Aggregate Reaction (AAR) in concretes presenting different strengths and incorporating a wide range of reactive aggregate types and natures, Cement and Concrete Research 93 (2017) 17–31. https://doi.org/10.1016/j.cemconres.2016.12.001.

[14] L. Sanchez, B. Fournier, M. Jolin, M.A.B. Bedoya, J. Bastien, J. Duchesne, Use of Damage Rating Index to Quantify Alkali-Silica Reaction Damage in Concrete: Fine versus Coarse Aggregate, ACI Materials Journal 113 (2016). https://doi.org/10.14359/51688983.

[15] M.-A. Bérubé, B. Fournier, T. Côté, Using the damage rating index for assessing the expansion of concrete affected by freeze-thaw, sulphate attack, or ASR, in: 14th International Conference on Alkali-Aggregate Reaction, Austin, Texas, USA, 2012.

[16] L.F.M. Sanchez, T. Drimalas, B. Fournier, D. Mitchell, J. Bastien, Comprehensive damage assessment in concrete affected by different internal swelling reaction (ISR) mechanisms, Cement and Concrete Research 107 (2018) 284–303. https://doi.org/10.1016/j.cemconres.2018.02.017.

[17] L.F.M. Sanchez, T. Drimalas, B. Fournier, Assessing condition of concrete affected by internal swelling reactions (ISR) through the Damage Rating Index (DRI), Cement 1–2 (2020) 100001. https://doi.org/10.1016/j.cement.2020.100001.

[18] P.E. Grattan-Bellew, Petrographic methods for distinguishing between alkali- silica, alkali-carbonate reactions and other mechanisms of concrete deterioration, in: Proceedings of the 14th International Conference on Alkali-Aggregate Reaction in Concrete, Austin, Texas, USA, 2012.

[19] R.-P. Martin, L. Sanchez, B. Fournier, F. Toutlemonde, Evaluation of different techniques for the diagnosis & prognosis of Internal Swelling Reaction (ISR) mechanisms in concrete, Construction and Building Materials 156 (2017) 956–964. https://doi.org/10.1016/j.conbuildmat.2017.09.047.

[20] A. Zahedi, A. Komar, L.F.M. Sanchez, A.J. Boyd, Global assessment of concrete specimens subjected to freeze-thaw damage, Cement and Concrete Composites 133 (2022) 104716. https://doi.org/10.1016/j.cemconcomp.2022.104716.

[21] ASTM International, ASTM C295/295M:19 Guide for Petrographic Examination of Aggregates for Concrete, ASTM International, West Conshohocken, PA, USA, 2019. https://doi.org/10.1520/C0295_C0295M-19.

[22] ASTM International, ASTM C457/457M:16 Test Method for Microscopical Determination of Parameters of the Air-Void System in Hardened Concrete, (2016). https://doi.org/10.1520/C0457_C0457M-16.

[23] ASTM International, ASTM C1356-07: Test Method for Quantitative Determination of Phases in Portland Cement Clinker by Microscopical Point-Count Procedure, (2020). https://doi.org/10.1520/C1356-07R20.

[24] ASTM C1293-18a, Test Method for Determination of Length Change of Concrete Due to Alkali-Silica Reaction, (2018). https://doi.org/10.1520/C1293-18A.

[25] CSA A23.2-14A Potential expansivity of aggregates (procedure for length change due to alkali-aggregate reaction in concrete prisms at 38 °C), (2019).

[26] L.F.M. Sanchez, Internal Swelling Reactions in Concrete: Mechanisms and Condition Assessment, 1st ed., CRC Press, Boca Raton, 2024. https://doi.org/10.1201/9781003188155.

[27] M. Champagne, Applying the damage rating index for the spatial damage assessment in concrete specimens affected by alkali-silica reaction (ASR), Master's Thesis., Université Laval, 2020.

Chapter 8: Reviewing the damage rating index (DRI) concept towards its automation

Cassandra Trottier, Haixu Zhang, Laurent Emile Ramos Cheret, Maia Fraser, Leandro F.M. Sanchez, Anthony Allard

Abstract

Automating the detection and segmentation of objects in images has been fundamental to many self-driving protocols. Point-count stereomicroscopy, such as the data collection procedure used to calculate the damage rating index (DRI), follows this protocol in which objects (features) are detected, segmented, and counted. This work, therefore, presents the foundation of a novel automated DRI while assessing the variability and subjectivity of the method. The Mask R-CNN model, trained on 110 annotated images of a severely damaged concrete specimen from a laboratory affected by alkali-silica reaction (ASR), achieved a model loss of 0.8, targeting 0.1 in this study. Further evaluation to graphically represent variability has demonstrated that a cumulative DRI number converges towards the expected value as the sample size, in terms of the number of analyzed squares, increases. Moreover, the observed occurrences and frequencies of the counted features were plotted as distributions, which helps reduce subjectivity in interpreting the result.

Keywords: alkali-silica reaction, damage rating index, point count, stereomicroscopy, machine learning.

8.1. Introduction

The Damage Rating Index (DRI) is a microscopy tool used to analyze concrete deterioration. Initially developed to differentiate between areas displaying varying damage levels in a dam affected by alkali-silica reaction (ASR) [1], the DRI is not limited to ASR [1,2]. The original pre-determined list of petrographic features for observation was selected to emphasize the presence of ASR [1,3]. Weighting factors were chosen and applied based on the importance of each feature in indicating ASR. Meanwhile, many researchers have attempted to correlate the DRI with expansion; however, the method is often considered too variable owing to the operator's experience, leading to a subjective interpretation of the results, which accounts for its "semi-quantitative" nature. To address this variability, [4] proposed a new pre-determined list of petrographic features and adjusted weighting factors to reduce inconsistencies. Despite these advancements, the DRI has not gained as much acceptance in the engineering community as the mechanical stiffness damage test (SDT) [5]. The remaining concerns include the decoupling of combined mechanisms and adaptation to other mechanisms, such as delayed ettringite formation (DEF) [2,6–8] and freeze-thaw cycles [9]. Therefore, the fundamental concept of the DRI, particularly its data collection methodology, must be re-evaluated as a point-count technique using stereomicroscopy, which collects data on the occurrence of observed features (causes of damage) and their frequency (extent of damage).

8.2. Materials and methods

8.2.1. Concrete specimens and sample preparation

Cylindrical concrete specimens made with a reactive coarse aggregate (i.e., Springhill – Greywacke) and exhibiting various levels of damage (i.e., 0, 0.05, 0.12, 0.20, 0.30, and 0.50%

expansion) were utilized in this study. Details regarding the concrete mixture, fabrication process, and storage conditions that promote ASR, along with sample preparations, are described in [10].

8.2.2. Data collection for damage rating index (DRI) calculation

The damage features (closed cracks in the aggregate – CCA, open cracks in the aggregate without and with reaction product – OCA and OCA_{RP}, disaggregated particles – DAP, cracks in the cement paste without and with reaction product – CCP and CCP_{RP}, and debonded/dislodged aggregates – Debon) were counted using a stereomicroscope at 16x magnification and tabulated in each 1 cm2 as described by [4,11]. The counts were weighted using the optimized weighting factors [4], and the sum of the weighted counts was divided by the number of analyzed squares (n) and multiplied by 100 cm2 to normalize the final result as the DRI number, as defined in Eq. 8.1.

$$\left[\frac{\sum(0.25(CCA) + 2(OCA + OCA_{RP} + DAP) + 3(CCP + CCP_{RP} + Debon))}{n}\right] \times 100\ cm^2 = DRI \qquad \text{Eq. 8.1}$$

8.2.3. Image acquisition and machine learning

Following the works of [12,13], a new model utilizing the novel Mask R-CNN [14–16] was developed due to its requirement for a smaller dataset to train further and produce more reliable outcomes. This model employs publicly available datasets [15] and leverages the concept of transfer learning to enhance its ability to detect cracks rather than being trained on a large dataset for a specific task. The dataset used in this study comprises 110 images of 1 cm by 1 cm squares captured with a 12-megapixel digital camera linked to a stereomicroscope, providing a field of view of 1 cm by 1 cm. The images were sourced from one specimen (i.e., 0.30% expansion) that contained a wealth of features and objects per image. Image acquisition was conducted automatically using a programmable moving stage. The annotated images consist of crack types outlined by [4,11], manually traced with distinct colours as detailed in [12] to assist in training the algorithm to detect and segment the cracks).

8.3.Results and discussion

8.3.1. Outcomes from automatic detection

The model's loss was found to be 0.8, while a target model loss of 0.1 was established for this research. Furthermore, the model is trained exclusively on one type of concrete that presents ASR, leading to cracks in the aggregate. Additional algorithm training using a larger and more diverse dataset will incorporate images from mechanisms that generate cracks in the cement paste, such as freeze-thaw cycles and delayed ettringite formation. Figures 8.2a and b depict the visual results of the automated crack detection. Figure 8.2c further illustrates the segmentation of crack types (closed crack in the aggregate – CCA and open crack in the aggregate – OCA). The number in the bounding box indicates the probability of belonging to that group.

a)

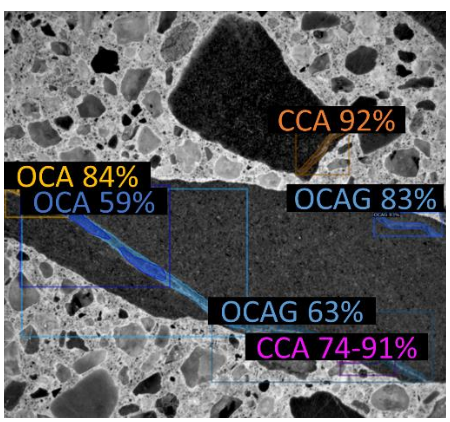

b)

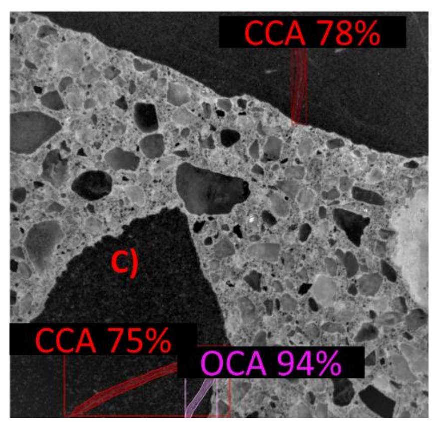

c)

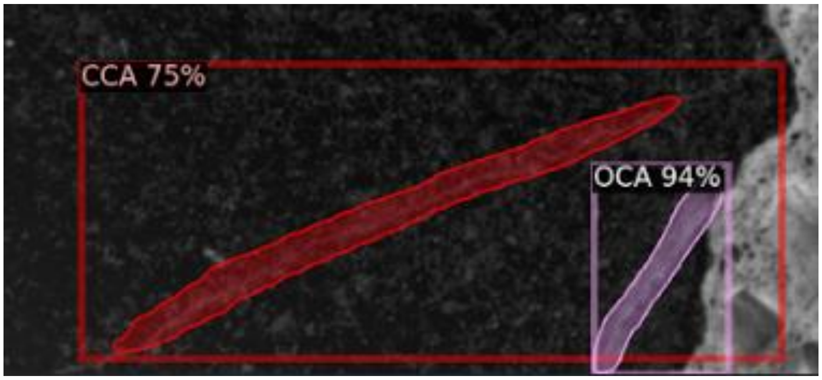

Figure 8.1. Micrographs of 1 cm by 1 cm illustrating the results from automated a) crack detection, b) detecting and segmenting the crack types, and (c) a zoomed-in portion to illustrate the segmentation

8.3.2. The damage rating index (DRI)

The damage rating index (DRI) is typically represented using bar charts (Figure 8.2) to illustrate the severity of the features and inform the suggested type of damage. In the case of ASR, larger counts of open cracks in the aggregate, both without and with the reaction product, can be observed (OCA and OCA_{RP}, respectively). As these specimens solely exhibited ASR damage, the extent of the damage is further indicated by the propagation of cracking into the cement paste (cracks in the cement paste, both without and with reaction products, CCP and CCP_{RP}), respectively).

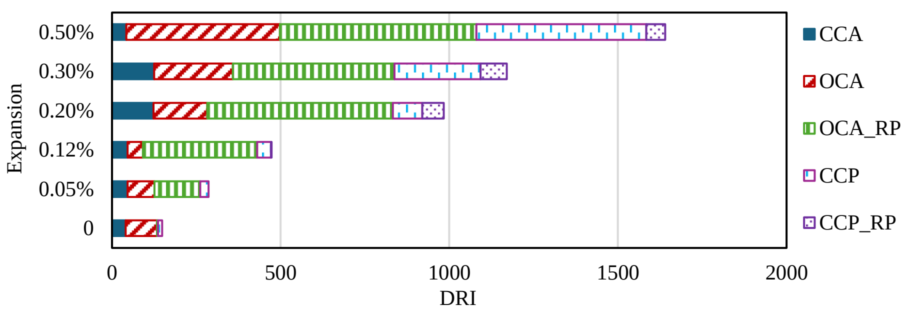

Figure 8.2. DRI bar charts for concrete made with reactive coarse aggregate at various expansion levels.

8.3.3. Observing the collected data through probability distribution

The collected data can be represented in various ways beyond the conventional bar charts, including extended versions of the DRI as proposed by [11]. However, the sample size is often referred to as 200 cm², for which statistical significance has not been verified. Although the data collection methodology to calculate the DRI can be conducted automatically or by an operator, the method remains a point-to-point technique and lacks transparency regarding sample size and the variability of the operator. Figures 8.3a and b present the cumulative DRI of a specimen at 0.05% and 0.50% of expansion, respectively, where convergence towards the expected DRI is observed (250 for 0.05% and 1623 for 0.50%). Meanwhile, Figures 8.3c and d show the corresponding histograms, where peak values tend to differ slightly from those selected as the final DRI numbers (i.e., 300 for 0.05% and 1700 for 0.50%). However, these values can be considered similar, as per [11], for those expansion levels.

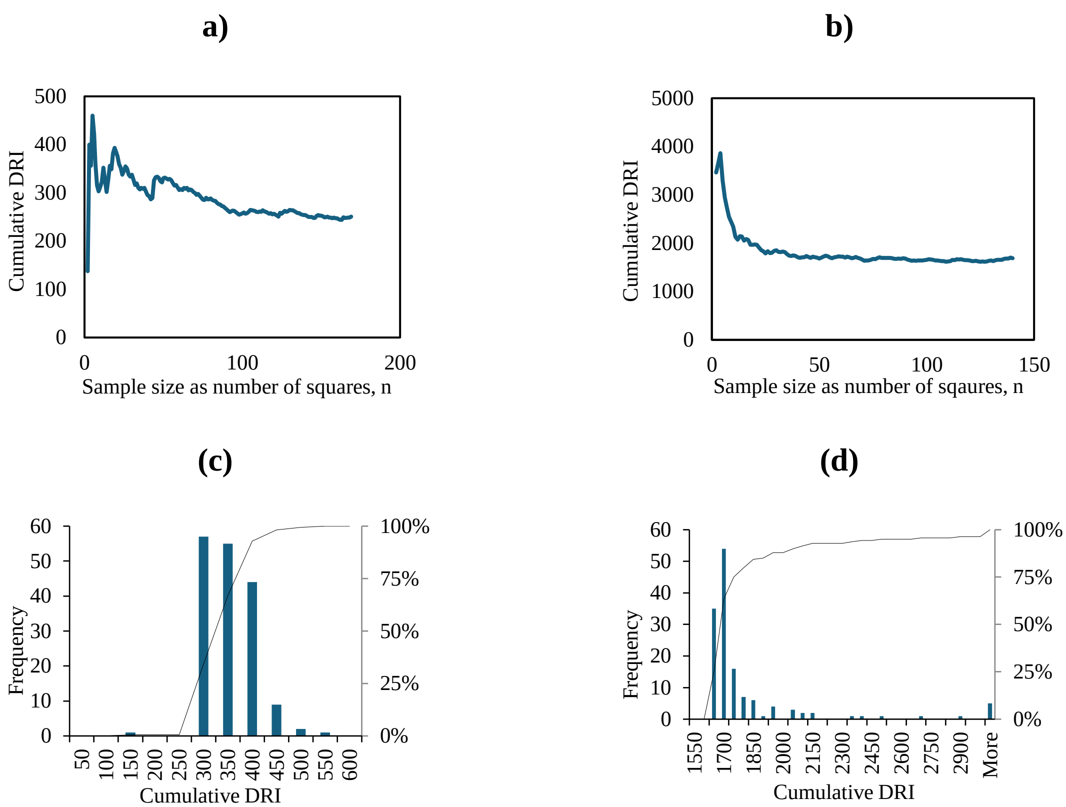

Figure 8.3. Cumulative DRI as a function of sample size (number of squares analyzed) for a) 0.05% expansion and b) 0.50% expansion. Histogram of the cumulative DRI for c) 0.05% expansion and d) 0.50% expansion.

In addition, the occurrences of encountered features were evaluated as discrete frequencies per 1 cm by 1 cm analyzed square (Figure 8.4). The peak value of open cracks in the aggregate (OCA) remains at zero until 0.20% expansion, after which the peak shifts to 2 occurrences per square. However, the tail to the right of the peak extends to a maximum of 11 counts per square at 0.20% expansion. A similar pattern is observed for the cracks in the cement paste (CCP), where at 0.20% expansion, a longer tail begins to appear while the peak value remains at 0 counts across all expansion levels. Interestingly, the distributions resemble each other more closely after 0.20% expansion, as seen through the frequencies and the cumulative distribution curves.

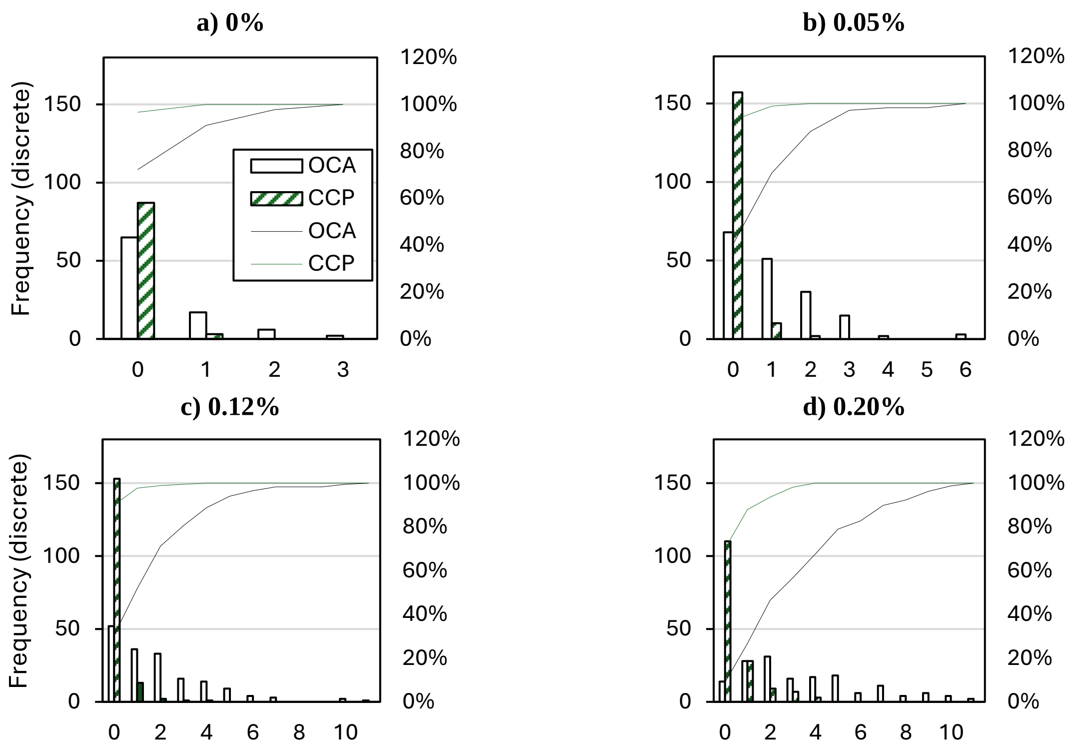

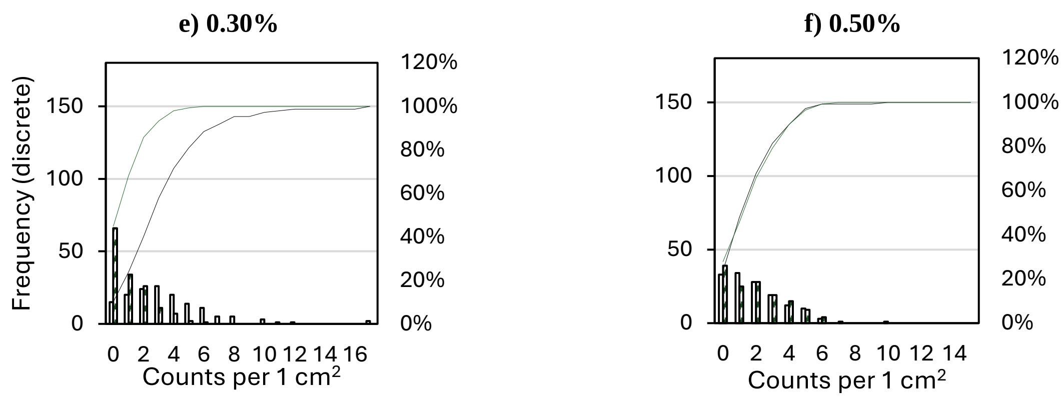

Figure 8.4. Counts of common ASR features in each 1 cm by 1 cm square per expansion level are shown by discrete and cumulative frequencies.

8.4.Conclusion

The works presented in this study are part of a research project aimed at automating the DRI and cracking index and improving the accessibility of the DRI as a practical engineering tool for quantifying damage through probability distributions obtained by point counts. However, further machine training is necessary to achieve a reliable level from the automated version, which remains a work in progress. While the automation of the DRI is expected to reduce operator variability, the point-count stereomicroscopy method can still be performed manually, provided that operators are trained and able to compare their outputs to a standard or a publicly available dataset within a specific tolerance interval yet to be established. Due to the limited datasets of both DRI-annotated images and transparent DRI data, the method remains ambiguous and subjective, highlighting the need to create larger datasets that incorporate various aggregate types and levels of damage, among other factors. A graphical representation of the cumulative results provides transparency regarding variability while presenting the sample size in terms of the number of squares analyzed. Furthermore, by considering the sample size as the number of squares, the frequency of observing a certain number of features per square can assist in determining the cause and extent of damage through probability distributions. Additional data is thus required to validate this assumption and predict the cause and extent of damage through occurrences and frequencies of observed features, thereby clarifying the interpretation of the damage through point counts of segmented features.

8.5.References

[1] P.E. Grattan-Bellew, A. Danay, Comparison of laboratory and field evaluation of alkali-silica reaction in large dams, in: Collection / Collection : NRC Publications Archive / Archives des publications du CNRC, 1992: pp. 1–25.

[2] P.E. Grattan-Bellew, Petrographic methods for distinguishing between alkali- silica, alkali-carbonate reactions and other mechanisms of concrete deterioration, in: Proceedings of the 14th International Conference on Alkali-Aggregate Reaction in Concrete, Austin, Texas, USA, 2012.

[3] I.R. Sims, B. Hunt, B. Miglio, Quantifying Microscopical Examinations of Concrete for Alkali Aggregate Reactions (AAR) and Other Durability Aspects, in: Curability of Concrete, Toronto, Canada, 1992.

[4] V. Villeneuve, Détermination de l'endommagement du béton par méthode pétrographique quantitative, Master's Thesis., Université Laval, 2011.

[5] L.F.M. Sanchez, T. Drimalas, B. Fournier, D. Mitchell, J. Bastien, Comprehensive damage assessment in concrete affected by different internal swelling reaction (ISR) mechanisms, Cement and Concrete Research 107 (2018) 284–303. https://doi.org/10.1016/j.cemconres.2018.02.017.

[6] C. Trottier, L.F.M. Sanchez, R.-P. Martin, F. Toutlemonde, Capturing internal swelling reactions (ISR) damage in concrete through the damage rating index (DRI), in: Springer, Vancouver, BC, 2023.

[7] R.H.R.Q. Melo, N.P. Hasparyk, F. Tiecher, Assessment of Concrete Impairments over Time Triggered by DEF, Journal of Materials in Civil Engineering 35 (2023). https://doi.org/10.1061/JMCEE7.MTENG-15041.

[8] R.-P. Martin, L. Sanchez, B. Fournier, F. Toutlemonde, Evaluation of different techniques for the diagnosis & prognosis of Internal Swelling Reaction (ISR) mechanisms in concrete, Construction and Building Materials 156 (2017) 956–964. https://doi.org/10.1016/j.conbuildmat.2017.09.047.

[9] A. Zahedi, A. Komar, L.F.M. Sanchez, A.J. Boyd, Global assessment of concrete specimens subjected to freeze-thaw damage, Cement and Concrete Composites 133 (2022) 104716. https://doi.org/10.1016/j.cemconcomp.2022.104716.

[10] C. Trottier, R. Ziapour, A. Zahedi, Leandro.F.M. Sanchez, F. Locati, Microscopic characterization of alkali-silica reaction (ASR) affected recycled concrete mixtures induced by reactive coarse and fine aggregates, Cement and Concrete Research 144 (2021) 106426. https://doi.org/10.1016/j.cemconres.2021.106426.

[11] L.F.M. Sanchez, B. Fournier, M. Jolin, D. Mitchell, J. Bastien, Overall assessment of Alkali-Aggregate Reaction (AAR) in concretes presenting different strengths and incorporating a wide range of reactive aggregate types and natures, Cement and Concrete Research 93 (2017) 17–31. https://doi.org/10.1016/j.cemconres.2016.12.001.

[12] A. Bezerra, The Use of Artificial Intelligence for Assessing Damage in Concrete Affected by Alkali-Silica Reaction (ASR), Master's Thesis., University of Ottawa, 2020.

[13] A. Bezerra, C. Trottier, L.F.M. Sanchez, B. Fournier, The use of artificial intelligence for assessing an overpass affected by Alkali-Silica Reaction (ASR), in: Bridge Safety, Maintenance,

Management, Life-Cycle, Resilience and Sustainability, CRC Press, London, 2022: pp. 354–361. https://doi.org/10.1201/9781003322641-40.

[14] Y.-A. Hsieh, Y.J. Tsai, Machine Learning for Crack Detection: Review and Model Performance Comparison, J. Comput. Civ. Eng. 34 (2020) 04020038. https://doi.org/10.1061/(ASCE)CP.1943-5487.0000918.

[15] Y. Wu, A. Kirillov, F. Massa, W.-Y. Lo, R. Girshick, Detectron2, (2019). https://github.com/facebookresearch/detectron2.

[16] A. Mohan, S. Poobal, Crack detection using image processing: A critical review and analysis, Alexandria Engineering Journal 57 (2018) 787–798. https://doi.org/10.1016/j.aej.2017.01.020.

Chapter 9: Enhancing efficiency in evaluating alkali-silica reaction (ASR) damage: an automated approach to point-count microscopy

Cassandra Trottier, Laurent Ramos Cheret, Haoye Lu, Anthony Allard,

Maia Fraser, Leandro F.M. Sanchez

Abstract

The damage rating index (DRI) is a valuable microscopy tool for collecting and counting data on various types of concrete cracks, such as those linked to alkali-silica reaction (ASR) induced deterioration. However, the procedure presents drawbacks, including time consumption and variability associated with operator experience, sparking debates about the subjectivity of its outcomes. Embracing the latest technological advancements, this study investigates the feasibility of automating the DRI's data collection through artificial intelligence (AI) and machine learning. Like many image processing and analysis applications utilizing AI, the DRI involves an object classification and segmentation task. This study represents a significant step forward in leveraging automation to improve the objectivity and efficiency of ASR damage characterization in concrete through point-count microscopy. It also proposes a set of tools to assess the results from the application's perspective, facilitating more efficient training data selection. Results indicate that while acceptable performance is achieved individually—with the detector-classifier showing an accuracy of 0.744 and the crack counter demonstrating an accuracy of 0.988—the current version of the proposed machine still exhibits high variability in detecting, classifying, and counting different crack types. Overall, the machine tends to overestimate ASR-induced damage, as

confirmed by the Chi-square goodness of fit test, suggesting that further training and enhancement of the proposed machine are necessary.

Keywords: Image analysis, point count, damage rating index, stereomicroscopy, alkali-aggregate reaction, automation.

9.1. Introduction

The alkali-silica reaction (ASR) is the most prevalent type of internal swelling reaction (ISR) mechanism in concrete globally [1]. Since its discovery in 1940, numerous condition assessment tools have been developed to evaluate the extent of damage ASR causes to concrete infrastructure. Grattan-Bellew proposed the damage rating index (DRI) [2] to differentiate levels of ASR-induced deterioration in concrete. The DRI was subsequently modified to minimize operator variability and incorporate other ISRs. Furthermore, correlations have been identified between the DRI's outputs (i.e., DRI number and extended version [3,4]) and mechanical responses for various ISRs [5,6], demonstrating its effectiveness in capturing the degree of deterioration based on its cause. However, the DRI's procedure is still time-consuming and varies among operators. Emerging technologies such as digitization, automation, and artificial intelligence (AI) are being rapidly adopted in the concrete industry, as they hold the potential to expedite testing procedures. While most of these advancements focus on visual inspections, some researchers employ AI to carry out standard testing procedures [7,8]. This work, therefore, seeks to promote a microscopy tool (i.e., the DRI) by emphasizing its data collection method, which is defined as a task frequently encountered in object segmentation problems used in machine learning, assessing the feasibility of its automation, and developing a practical approach to evaluating the machine's outcomes.

9.2. Background

9.2.1. Alkali-aggregate reaction (AAR)

Alkali-aggregate reaction (AAR) is one of the primary causes of early deterioration of concrete infrastructure worldwide [1]. There are two types of AAR in concrete: a) alkali-silica reaction (ASR), which involves aggregate-bearing siliceous mineral phases, and b) alkali-carbonate reaction (ACR), which involves carbonate aggregates. The latter is less understood and less common in the field. Conversely, ASR consists of a chemical reaction between unstable siliceous mineral phases from the aggregates and the alkalis (Na^+, K^+, OH^-) present in the concrete pore solution, resulting in a secondary reaction product that swells upon water uptake. This secondary reaction product, commonly known as "ASR gel," exerts pressure that often exceeds the tensile strength of the concrete, leading to the formation of cracks (Figure 9.1) and resulting in a loss of performance (i.e., mechanical properties, stiffness, serviceability, durability, and physical integrity) of the affected concrete. While diagnosing the cause of damage in ASR-affected concrete is well established [9], capturing the extent of damage caused by ASR, along with its implications for concrete performance and future damage potential, remains a challenge. Thus, developing quantitative and reliable tools to depict and measure the cause and extent of damage is crucial to preserving existing infrastructure.

a) **b)**

Figure 9.1 Likely ASR-affected concrete from a) a retaining wall next to an on-ramp in Québec City, Canada and b) a micrograph from a core of a nearby decommissioned overpass (Du Vallon-Charest, Québec) with a field of view of 1 cm by 1 cm where the white lines are cracks in the aggregates filled with reaction product.

9.2.2. Damage rating index (DRI)

The damage rating index (DRI) is a quantitative microscopy tool for assessing damage in concrete caused by internal swelling reactions. The methodology used to collect data for DRI calculation (Eq. 9.1) requires the operator to count (i.e., quantify) petrographic/distress features on a polished concrete section with a stereomicroscope at 15-16x magnification. The fundamental concept of the DRI is a point-count method in which the "objects/features" are distinguished based on their location in the concrete (i.e., aggregate, cement paste, or their interface) along with their nature (closed, open, and/or filled with a reaction product), as illustrated in Figure 9.2. To account for the influence of a feature on a specific type of damage, weighting factors reflecting the severity of the features towards the damage are applied. Since the development of the DRI, the weighting factors have evolved from accounting for the "petrographic features," representing the symptoms/signs that most depict the type of damage being evaluated, to the "distress features," which represent the most indicative cracks associated with mechanical properties and physical integrity losses of affected concrete. Researchers have since attempted to correlate the resulting DRI to AAR volumetric expansion, the most commonly used metric for determining the degree of damage caused by internal swelling reactions. These studies have resulted in changes to the grid sizes, weighting factors, and the features used to calculate the DRI [10–14]. Villeneuve [10,11] addressed variability issues in quantifying the damage by modifying the weighting factors. Following this work, Sanchez et al. [5] established ranges of expected DRI values as a function of type and level of damage, providing a valuable tool for operators and practitioners. Despite these efforts, the DRI continues to present subjective interpretations and variability among operators while being time-consuming and requiring training to develop the skill and competence to conduct the assessment analysis.

$$DRI = \frac{\sum 0.25 \times CCA + 2 \times (OCA + OCA_{RP} + DAP) + 3 \times (CCP + CCP_{RP} + Debon)}{Number\ of\ analyzed\ 1\ cm^2\ squares} \times 100cm^2 \qquad \text{Eq. 9.1}$$

where CCA is the total number of closed cracks in the aggregates; $OCA\ and\ OCA_{RP}$ are the total numbers of open cracks in the aggregates without and with reaction product, respectively; DAP is the total number of disaggregated/corroded particles; $CCP\ and\ CCP_{RP}$ are the total numbers of cracks in the cement paste without and with reaction product, respectively, and $Debon$ is the total number of debonded aggregates.

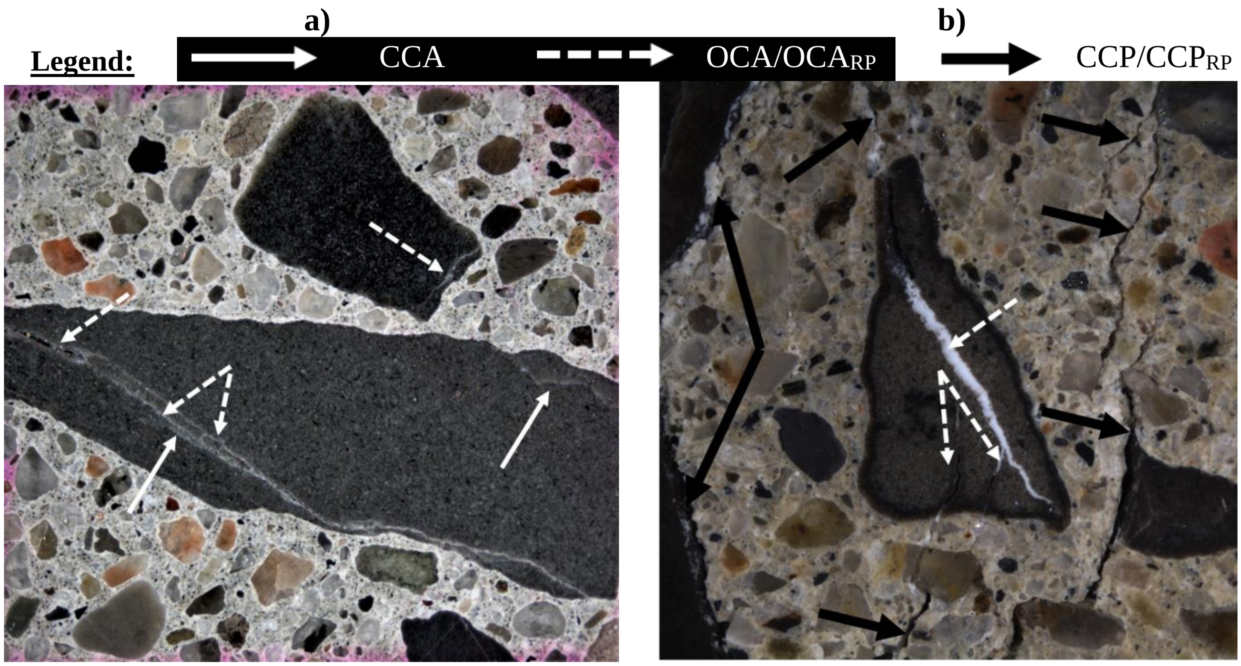

Figure 9.2. Micrographs of 1 cm^2 of the various damage features as per the DRI where a) the smaller aggregate particle contains an OCA/OCA_{RP} type crack, and the larger aggregate particle contains both CCA and OCA/OCA_{RP} type cracks and b) several OCA_{RP} type cracks in the middle aggregate and an extension of damage into the cement paste are shown.

Furthermore, the extended version of the DRI, as proposed by [3,4], considers unweighted counts of distress features as counts per 100 cm^2 and percentages, the crack density as the total of open cracks in both the aggregate and the cement paste—with and without reaction products (counts/cm^2)—along with the maximum crack widths and lengths. An increase in these distress characteristics correlates with a rise in the expansion and deterioration of internal swelling reactions (ISR) overall [15–19]. Nevertheless, the DRI methodology provides a wide range of analyses beyond counts of distress features when not restricted to manual assessment operations.

9.2.3. Technology applied to ASR damage quantification

Over the past few decades, various techniques have been developed to enhance the understanding of the implications of cracks and how they propagate within the material at a larger scale (i.e., mesoscale). Although all flaws and cracks compromise concrete performance, it is essential to distinguish between distress features and cracks that represent measurable mechanical damage to make informed decisions about mitigation, repair, and rehabilitation. Consequently, techniques that employ image analysis to quantify the characteristics of observed cracks at the mesoscale (e.g., extent, orientation, density, etc.) have proven effective in providing insight into the extent of the damage. However, these techniques necessitate the use of products such as fluorescent dye impregnated into the concrete surface being analyzed to highlight the cracks and provide contrast for more efficient analysis. Sample preparation of concrete specimens and cores with large surfaces is time-consuming, as it requires grinding and polishing to a certain degree, followed by applying resin. This process is followed by careful removal to avoid excessive grinding that could damage the impregnated cracks. Furthermore, the availability of open-source software such as ImageJ, Fiji, and NIH Image [20,21] can reduce analysis time by creating subroutines to eliminate unwanted artifacts (e.g., voids filled with dye or fluorescent material when analyzing cracks). Nevertheless, image analysis has begun quantifying the deterioration based on observed or selected parameters.

In 2000, Rivard et al. [22] quantified ASR damage on laboratory-made specimens measuring 75 by 75 by 300 mm. They used crack lengths and orientations as indicators of the extent of damage at 20x magnification, employing uranyl acetate to enhance contrast and highlight the reaction product (i.e., silica gel) under UV light. The researchers discovered that the damage indicator is influenced by the aggregate, aligning with the type of damage, as ASR primarily represents an aggregate distress mechanism. Similarly, in 2012, Lindgård et al. [23] developed the ‘cracking intensity’ metric for measuring crack widths and lengths. This parameter is calculated as the proportional area occupied by cracks over the total area under analysis (i.e., 70 mm by 280 mm), which is revealed under UV light due to epoxy-impregnated fluorescent dye. The entire specimen was considered, and the larger surface area provided characteristics such as the extent and pattern of cracking without requiring magnification, thus eliminating the need for a microscope during analysis [23]. However, both studies mentioned controlled the type of damage that causes expansion. Conversely, Li et al. [24] correlated crack characteristics from freezing and thawing, such as crack length density (i.e., total length over the analyzed area) and crack area density (similar to the 'cracking intensity' as the proportion of cracked area), with a damage degree calculated from the loss in modulus of elasticity for both air-entrained and non-air-entrained concrete mixtures using image analysis at 40x magnification. Others have further employed the DRI methodology to present crack patterns through heatmaps and annotated images to visualize damage heterogeneity within a specimen [17,25–27], along with preferential crack direction [28,29]. Image analysis can capture the extent of a known distress mechanism; however, it remains limited in diagnosing its nature. These studies emphasize the need to understand the spatial distribution of damage at a scale representative of the material mesoscale.

Digital images have facilitated computer vision and machine learning (ML) in detecting cracks in concrete, which were previously time-consuming tasks, particularly when accounting for sample preparation time. Consequently, automated surface cracking detection has increased over the last decade [30–43]. Meanwhile, applications of microscopy in concrete are limited and primarily focused on model development rather than damage quantification [7,44–47]. The feasibility of automating the DRI was previously explored [48], yet the techniques used to evaluate the machine's performance were confined to categorizing different crack types. While DRI is ideal for automation as an object segmentation task, research into automating the quantification of damage to concrete remains limited [48–50].

9.3. Scope of the work

The DRI is a microscopy tool used for quantifying and classifying concrete cracks while evaluating concrete distress mechanisms, such as internal swelling reactions (ISR). It can also be identified as an object detection and segmentation problem common in ML applications. To address current limitations in test procedures (e.g., time consumption and variability), this study aims to propose a methodology for assessing the machine's ability to estimate the location and type of distress features through classification, as well as the count of distress features, compared to the results from an operator (ground truth), based on previous research integrating DRI and ML. This work developed two models to detect and classify cracks based on the pre-determined distress features that contribute to DRI calculations (i.e., a crack detector/classifier and a crack counter). The distress features were produced by ASR originating from a highly reactive coarse aggregate (Springhill – Greywacke), chosen for its dark appearance, which aids in detecting distress features. They were evaluated at various damage levels (0.05%, 0.12%, 0.20%, and 0.30%) to understand the model's capability to collect the required data automatically.

9.4. Materials and methods

9.4.1. Specimen fabrication and damage exposure

A Greywacke reactive aggregate was selected for this study due to its fine-grained nature and dark colour, which aid in distinguishing between the aggregate and the cement paste and identify cracks within the aggregate. Fifteen concrete cylinders (i.e., 100 x 200 mm in size) were manufactured in the laboratory using the reactive coarse aggregate combined with a local non-reactive fine aggregate (Table 9.1). The concrete specimens were mix-proportioned according to the Concrete Prism Test (CPT) standard as outlined by ASTM C1293 [51] (Table 9.2). The mixture employed conventional Portland cement (CSA Type GU, ASTM type 1) with a high alkali content (0.88% $Na_2O_{eq.}$). The total alkali content was raised to 1.25% $Na_2O_{eq.}$ by cement mass using reagent-grade sodium hydroxide pellets.

Table 9.1. Aggregates used in this study.

Aggregate	Location	Rock Type	Specific Gravity	Absorption (%)
Reactive coarse (Springhill–SPR)	Fredericton, New Brunswick (Canada)	Greywacke	2.71	0.70
Non-reactive natural sand	Ottawa, Ontario (Canada)	Derived from Granite	2.60	0.82

Table 9.2. CPT standard mix-design.

Cement (kg/m^3)	Water (kg/m^3)	Non-Reactive Fine Aggregate (kg/m^3)	Reactive Coarse Aggregate (kg/m^3)		
			4.75–9.5 mm	9.5–12.5 mm	12.5–19 mm
420	189	823	308	308	318

The specimens were moist-cured at 20ºC for 24 hours after fabrication. Holes measuring 8.5 mm in diameter and 19 mm in length were drilled into the centre of both flat ends of the specimens. After cleaning the holes with compressed air, stainless-steel gauge studs were installed using a fast-setting cement paste slurry. The samples were then moist-cured for another 24 hours at 20ºC. Initial readings were taken with a digital micrometre, using the studs as reference points. The concrete specimens were subsequently stored under accelerated exposure conditions (i.e., 38°C and 100% RH) to promote ASR. Specimens were monitored over time, and once they reached the targeted expansion levels (i.e., 0.05%, 0.12%, 0.20%, and 0.30%), the concrete specimens were further prepared for analysis.

9.4.2. Sample preparation

One specimen from each targeted expansion level was chosen for this study. The specimens were continuously cut lengthwise using a masonry saw equipped with a 14-inch diamond blade and water as a coolant. The surfaces were ground flat and polished with an 18-inch diameter mechanically rotating thick steel plate and magnetic laps using grits of 30, 60, 140, 280 (80-100 microns), 600 (20-40 microns), 1200 (10-20 microns), and 3000 (4-8 microns) to achieve a reflective finish. This setup was selected to create a flat and even surface for image acquisition.

The surface preparation procedure is akin to sections prepared for petrography, as described in [52].

9.4.3. Image acquisition

For the specimens in this study, images were captured manually using a 12-megapixel digital camera attached to the stereomicroscope. The microscope's magnification was set to 8x, producing a field of view of 1 cm by 1 cm displayed on the accompanying image acquisition software. Two oblique goose-neck lights illuminated the regions of interest, eliminating shadows created by topographical features such as voids and cracks. The light brightness was adjusted arbitrarily based on the visibility of the cracks, particularly to analyze them in the cement paste through the computer screen and to ensure sufficient contrast between the aggregate and the cement paste. Binning was set to 1x1, and auto-exposure was selected to reduce acquisition time when adjacent images exhibited significant colour variations due to the heterogeneous nature of the concrete material. To preserve image quality, the images were saved in Portable Network Graphic (PNG) format. Each image was linked to a region of interest (ROI) by combining the names of rows and columns (where rows were classified by letters and columns by numbers); for example, the image labelled A1 refers to row A and column 1.

Several configurations were used to optimize the image acquisition of the 1 cm^2 squares. Originally, the 1 cm^2 squares were drawn directly on the finished concrete's surface using a fine-tipped permanent marker; however, Figure 9.3a shows the marker grid line within the 1 cm^2 boundary. To overcome such issues, a 3D-printed grid was then created by modifying the layout to ensure that the inner boundaries of the grid remained at 1 cm by 1 cm (Figure 9.3b).

a) b)

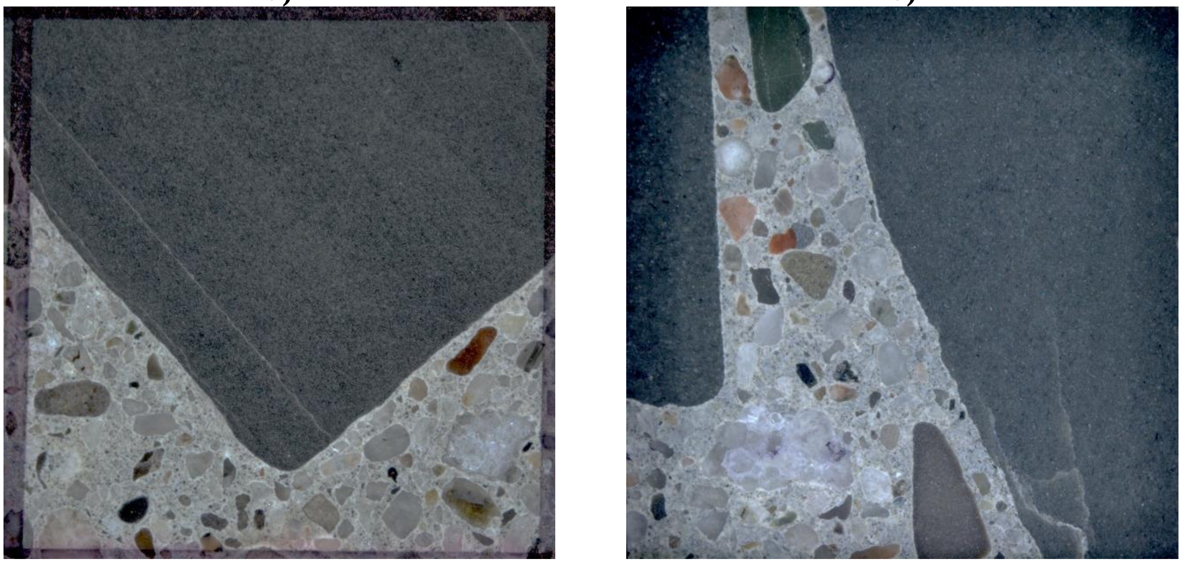

Figure 9.3. Field-of-view configurations where a) the grid marked by hand onto the concrete's surface is included and b) the view for the inner portions of the 3D-printed grid is shown.

Notably, the first configuration (Figure 9.3a) was employed for the training set of images. In contrast, the second configuration was utilized for testing, as the shadowed edges did not interfere with the method. Subsequent images were captured using a programmable motorized stage, which defined the grid thickness, ensuring that the ROI viewed under the microscope during manual operations was comparable to the images. When surfaces are not completely flat, the working distance may vary; thus, adjusting the focus stepwise may be necessary, either through auto-focus or manual adjustment. Table 9.3 presents the total number of images used in this study for training and testing the machine-learning model. The 0.30% expansion specimen was selected for training due to its prevalence in various crack types.

Table 9.3. Specimens used in this study including their expansion level, the number of 1 cm by 1 cm images analyzed and the role of the specimen image dataset.

Specimen expansion level	0.05%	0.12%	0.20%	0.30%
Number of images	163	169	155	141
Role	Test	Test	Test	Annotated for training and validation (50/50)

9.4.4. *Ground truth data collection*

In this study, it was essential to maintain the same ROI for the image annotations as for the operator generating the ground truth data and to compare the machine's performance to the operator's. The DRI was calculated by observing each 1 cm² square at 16x magnification using a stereomicroscope. The surface was illuminated with oblique goose-neck lights at a comfortable brightness level for the operator, allowing for clear visibility of the cracks. The operator began with the first square and counted the cracks according to the DRI (CCA, OCA+OCA_{RP}, and CCP+CCP_{RP}), which were tabulated. This process was repeated with the same combing configuration until all squares were analyzed. All cracks, regardless of size, were recorded to increase the number of detectable features for training the ML model. The tabulations included the squares' labels in the first column, the number of CCA in the second column, and so on. The files were saved in comma-separated values (.csv) and Text (.txt) formats for training and model analysis. This data collection procedure was applied to all four expansion levels of the study: 0.05%, 0.12%, 0.20%, and 0.30%.

9.4.5. *Segmentation and annotation of crack types*

After recording the features observed under the microscope, the annotator traced the counts onto the images from the 0.30% expansion specimen (which showed significant damage) using the colour codes outlined in Table 9.4. The first column of the table indicates the colour codes for red, blue, and green (i.e., RGB colours), followed by the intensity of each colour/channel on a scale from 0 to 255. Because there were only a few cracks in the cement paste with reaction product

(CCPRP), this category was combined with those lacking reaction product ($CCP+CCP_{RP}$), henceforth referred to as CCP. The table below also includes the number of features identified in the 0.30% expansion specimen, which was used to train the detector and classifier before data augmentation. Additionally, while the annotations for OCA and OCA_{RP}, henceforth referred to as OCA, were generated separately, their final results were combined because preliminary findings indicated better performance when merged and to prevent misinterpretation stemming from the removal of the reaction product (i.e., silica gel) during the sample preparation process [48]. Three files were then generated per ROI: 1) the raw image, 2) the annotated image displaying all annotations, and 3) the mask of those annotations. The total number of cracks across all images is presented to highlight the unbalanced dataset. For ASR, cracks typically occur within the aggregate particles, referenced as CCA, OCA, and OCA_{RP}, while a smaller proportion of $CCP+CCP_{RP}$ becomes more prevalent at expansion levels of 0.20% beyond.

Table 9.4. Colour codes for the crack types and the corresponding number of cracks.

Crack type	**CCA**	**OCA**	**OCA_{RP}**	**$CCP+CCP_{RP}$**
Colour code	Yellow	Blue	Green	Red
Red	255	0	0	255
Green	255	0	255	0
Blue	0	255	0	0
Number of cracks in total	702	356		154

9.4.6. Crack recognition and classification through Machine Learning (ML)

The algorithm employed in this study was originally developed for a previous feasibility study [48] and is based on deep neural networks, a category of universal function approximators. The behaviour of deep neural networks is determined by their internal weights, which are adjusted during the training process to approximate an objective function, thus minimizing the error or loss between the network outputs (i.e., gradient descent). In the specific context of this project, the developed algorithm takes raw images of concrete as inputs. It generates pixel-level masks that indicate whether a pixel belongs to a crack and, if so, the type of crack it represents. This approach is known as supervised learning, where the ground truth labels of the images are known and utilized during training. In this implementation, the model is trained to identify the three main types of damage features present in concrete specimens, including closed cracks in the aggregate (CCA), open cracks in the aggregate both with and without reaction product ($OCA+OCA_{RP}$), and cracks in the cement paste with and without reaction product ($CCP+CCP_{RP}$). Convolutional neural networks (CNN) are frequently used to convert images into a sequence of features (i.e., numbers) that machines can interpret. To create a one-to-one correspondence between the pixels in the input image and the output predictions, over 55,000 ASR-related distress features from 142 images, including augmentation, originating from a concrete specimen incorporating the Springhill aggregate at 0.30% of expansion (damage degree) were used during training. The following sections outline the various models employed in this study, including the detector and classifier, the classification predictions, and the crack counter.

9.4.6.1.Development of crack detector and classifier

The crack detector and classifier were developed using the U-Net architecture [53] and applied at the pixel level. This approach identifies whether a pixel is part of a crack and subsequently classifies it according to the type of crack (Figure 9.4). U-Net is widely employed for segmentation problems, such as those encountered in DRI. The process begins with the encoder receiving a greyscale image of 224 by 224 pixels. The bottleneck is reached at the bottom of the diagram, measuring 56 by 56 pixels. Subsequently, the decoding process starts with two levels of bilinear upscaling to increase spatial dimensions by interpolating the four nearest pixel values. The output image then comprises three channels, where the cracks are classified and masked using identification colours (yellow - Y, red - R, and blue-green - BG, respectively), as indicated in Table 9.4.

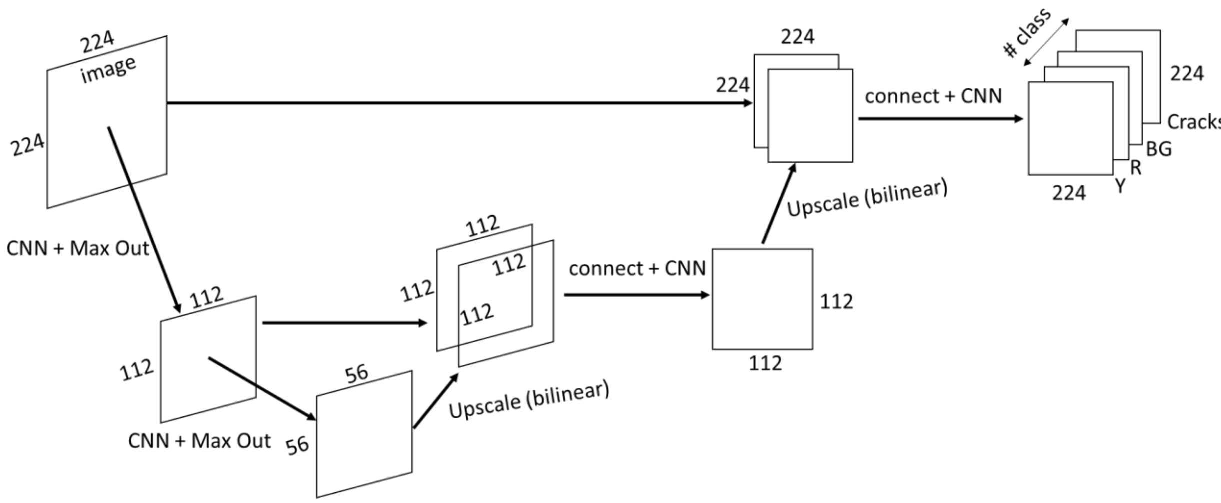

Figure 9.4. Model architecture for crack detector and classifier using U-Net where a 224x224 single channel input image is condensed to a 56x56 by strides of 2, followed by two levels of bilinear upscaling to produce the three-channel RBG image of classified cracks.

The machine was trained based on the types of cracks observed by the microscope operator, which were recorded and tabulated per ROI image and their locations according to the annotations. When given an image input, the ML algorithm makes two predictions: 1) detect cracks, and 2) assign probabilities to each pixel based on whether it belongs to one of the three types of cracks (yellow - Y, red - R, and blue-green - BG), as illustrated in Figure 9.5. Notably, the output colours do not yet match the classification colours (Figure 9.5b).

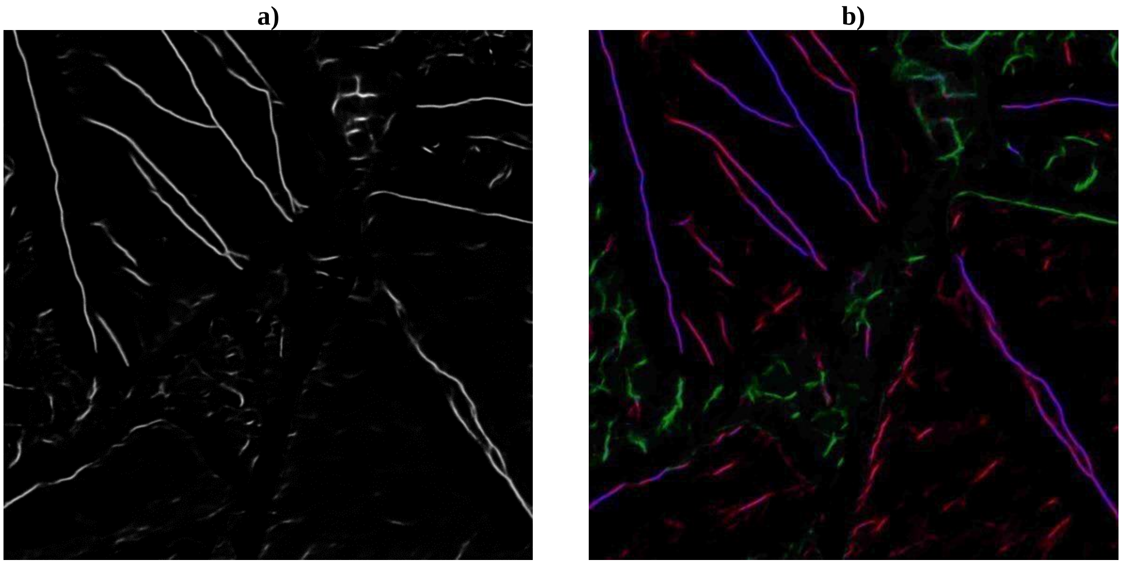

Figure 9.5. The predictions made by the detector and classifier are a) the location of pixels belonging to any crack and b) the pixel classification.

Computer vision techniques are further applied to enhance prediction quality by initially removing weak pixels and low-level white noise, and then identifying connected pixels as components (Figures 9.6a and b, respectively). Components with a diagonal length of less than 300 pixels (equivalent to 1 mm) were deemed artifacts and discarded (Figure 9.6c).

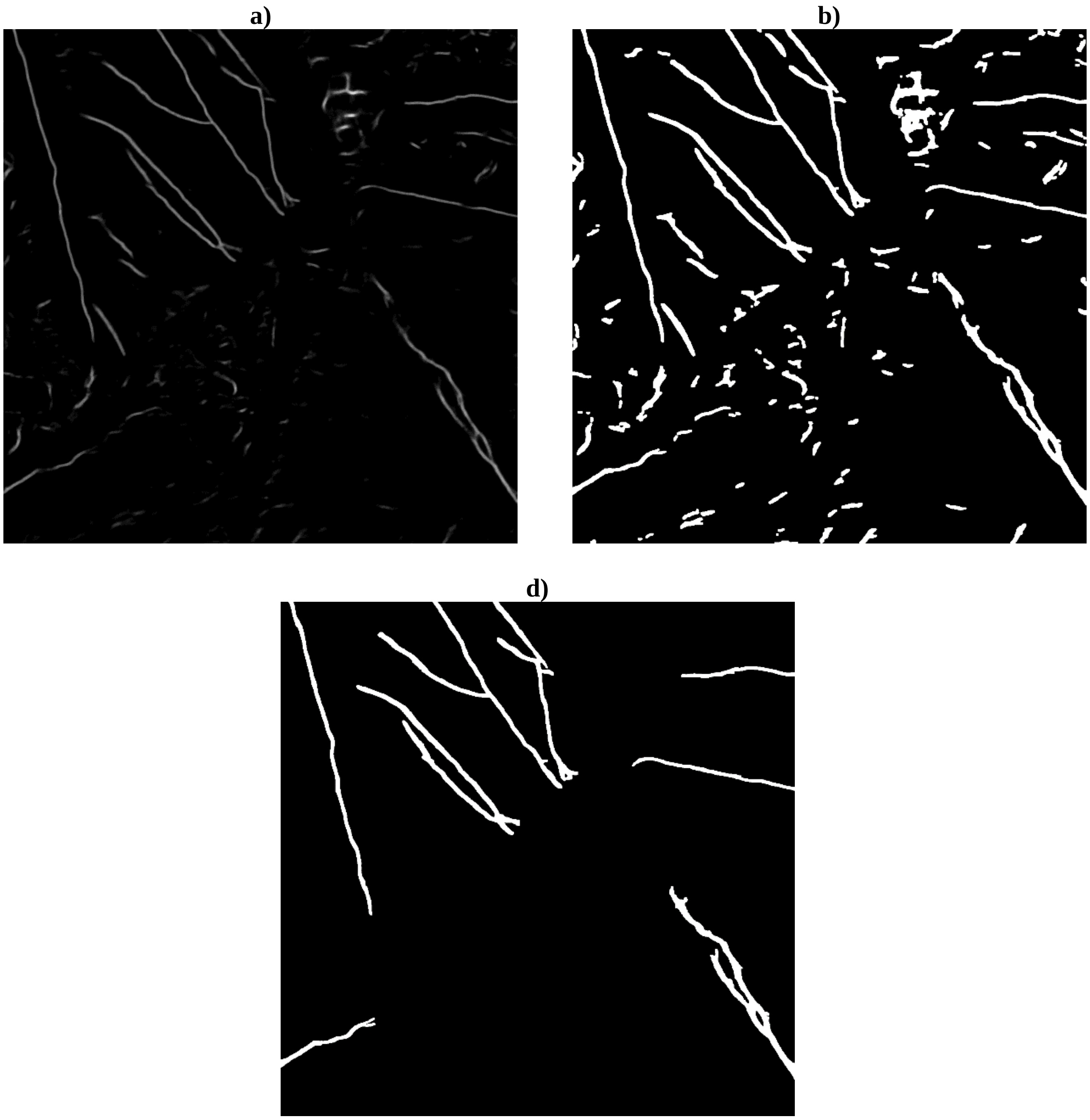

Figure 9.6. Computer vision techniques a) removing weak pixels and weak white noise, b) connection of the pixels, and c) removal of small components.

Considering the majority voting rule (Figure 9.7a), the component is completely coloured based on the prevalent crack type (Figure 9.7b). The colours were then adjusted to match those of the annotated masks for visual comparison (Figure 9.7c). The boundary between the aggregate particle and the cement paste was identified as CCP (indicated by the green arrow). In contrast, one of the CCPs (indicated by the red arrow) was not captured. It is important to note that while all cracks were highlighted in the masked image to assist in identification, small cracks (less than 1 mm) were not counted or tabulated.

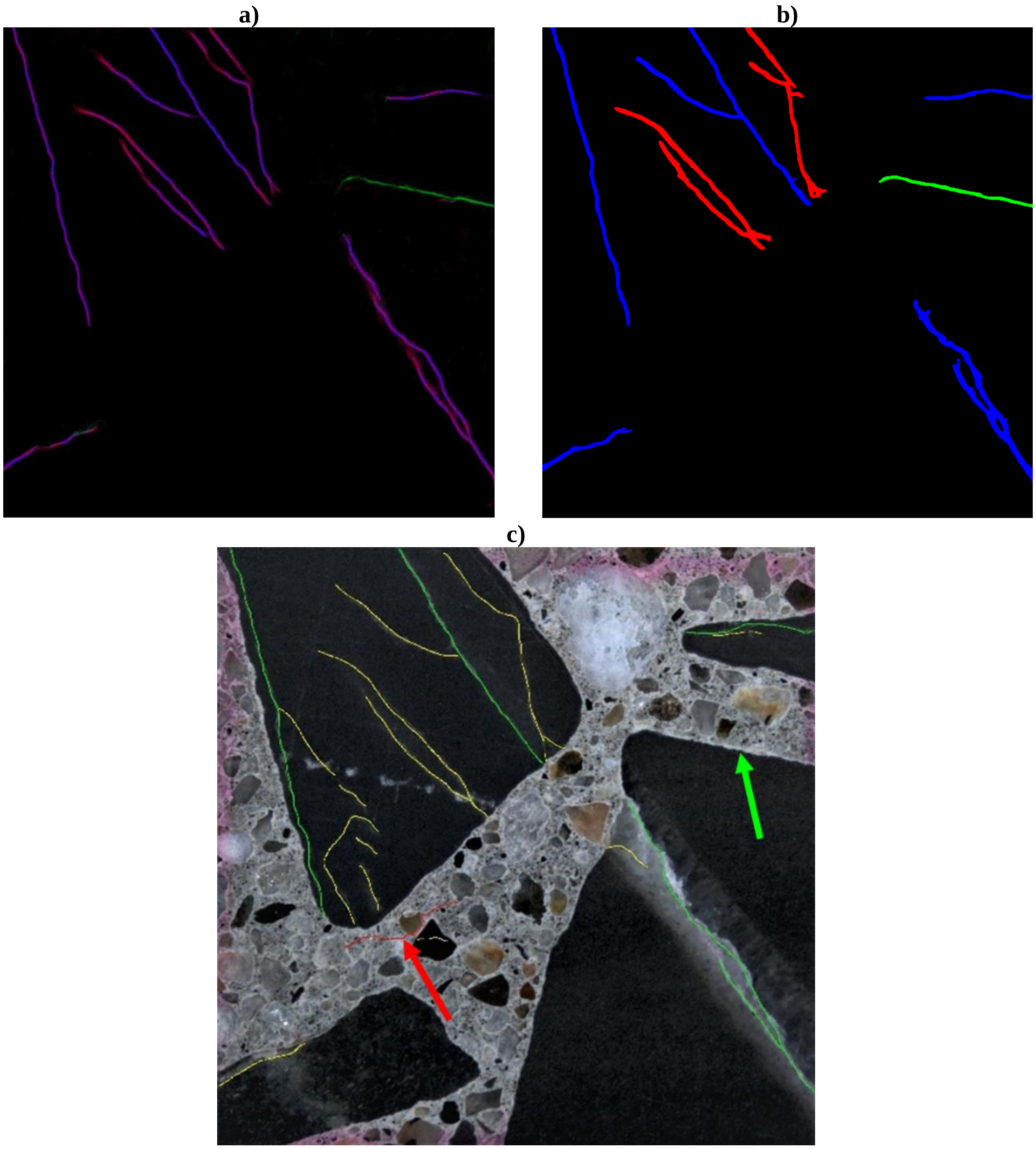

Figure 9.7. Classification based on probability of belonging to a crack type: a) adapted figure indicating only the cracks under investigation, b) the colouring based on the major probability and c) the manually annotated image for comparison.

9.4.6.2.Development of crack counter

Some detected cracks are connected and cannot be treated as single elements; therefore, a counter was required for the DRI application. Practically, the counting procedure, when conducted by an operator, is performed by selecting a starting point at the tip of one of the cracks and progressing through each crack segment until another tip is reached. When met with an intersection referred to as a node, the crack may divide into two or more segments. The number of cracks can also be calculated as per Eq. 9.2 and illustrated in Figure 9.8.

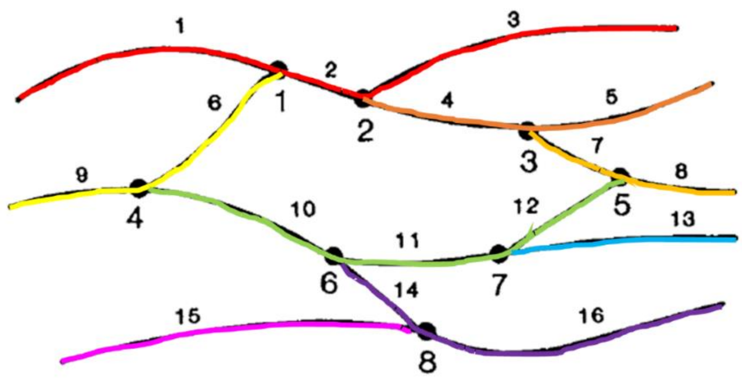

Figure 9.8. Point-count method using nodes and segments in a crack network. Colours highlight counts of segments used in practice during point counts for the DRI (Adapted from Sims et al. 1992).

To simplify the work by overlapping what has already been developed and overcoming the machine's inability to recognize crack tips, the counter counted nodes and calculated the number of cracks in each image as per Eq. 9.3. An example is shown in Figure 9.9 and Table 9.5.

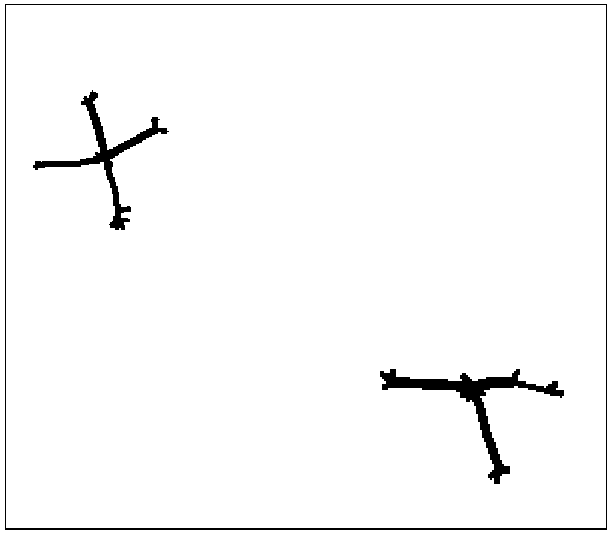

Figure 9.9. Example of two types of nodes in one ROI image of 1 cm by 1 cm.

Table 9.5. Sample calculation for crack counts using both equations 2 and 3.

Sample calculation	Equation
$Number\ of\ cracks = (number\ of\ segments) - (number\ of\ nodes)$ Example: Number of cracks $= 7 - 2 = 5$	Eq. 9.2
$$Number\ of\ cracks = \left(\frac{1}{2}\right)\left[N_1 + \sum_{i=3}^{\infty}(i-2)N_i\right]$$ Where N_1 is the number of crack segments with 2 tips (degree-1 nodes) and N_i is the number of nodes for a degree-*i* node for degree-3, -4, and -5. Example: $$Number\ of\ cracks = \left(\frac{1}{2}\right)\left[7 + \big((3-2)(1)\big) + \big((4-2)(1)\big)\right] = 5$$	Eq. 9.3

Synthetic data was generated to develop the crack counter for scenarios involving multiple node types (Figure 9.10a), while noise was added to the segments to simulate naturally occurring cracks in concrete. The synthetic data included node types of degree-1 (presence of a crack/edge), degree-3, degree-4, and degree-5 node types, which correspond to the number of cracks connected to a specific node. The counter was trained using 10,000 synthetic images, with 1,000 set aside for validation and another 1,000 for testing. Initially, degree-1 nodes were detected to indicate whether an unconnected crack was present, followed by the detection of degree-3, -4, and -5 nodes (Figure 9.10b). It should be noted that a degree-2 node would represent a crack with an angle, counted as a single crack. This process is similar to the crack classifier detailed in the previous section, except for the output indicating the node type for connected cracks.

a)

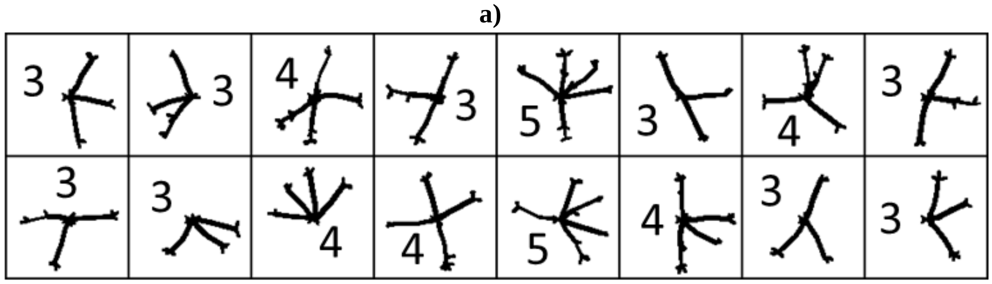

b)

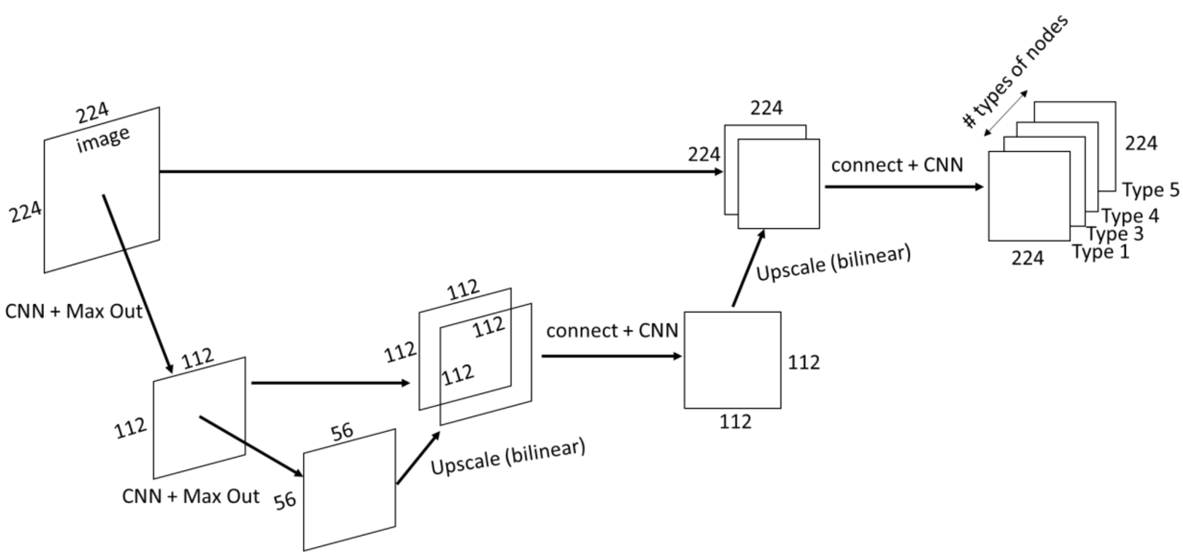

Figure 9.10. Crack counter development: a) examples of synthetic data including the type of degree-node and b) detection of node types using U-Net where a 224x224 single channel input image is condensed to a 56x56 by strides of 2, followed by two levels of bilinear upscaling to produce the node type output.

Additional information is required to evaluate Eq. 9.3 numerically, as practical applications may impose constraints that result in a finite sum. Moreover, dividing odd numbers in half yields fractional crack counts that are not included in DRI calculations. Although the model achieved an accuracy of 0.988, further analysis suggests that the U-Net-based network is inadequate since the node type is not derived from pixel-wise features. Consequently, a model that combines pixel-wise and standard classification would be more effective for crack detection counting.

9.5. Results

9.5.1. Classification predictions

A confusion matrix in Table 9.6 illustrates the detected and classified crack types represented by their colour codes. The results indicate an accuracy of 0.744. Following this, Table 9.7 outlines additional classification model performance metrics, such as F1 (which measures the performance of a binary classification model by combining precision and recall into a single metric), precision (the accurate prediction of the crack type), and recall (the rate at which the crack type is correctly predicted). These metrics were chosen due to the imbalanced dataset, which has a limited number of cracks in the cement paste (CCP – Red) compared to the cracks in the aggregates (CCA – Yellow and OCA – Blue-green), as indicated in Table 9.4. The model's yellow (CCA) classification demonstrates good precision and recall of 0.724 and 0.787, respectively, indicating that it detects most yellow (CCA) cracks, although it could improve its false positive rate. The red (CCP) classification boasts the highest precision (0.814), 12% and 7% higher than that of CCA and OCA, respectively. As a result, it accurately classifies cracks as red (CCP) when they are red, leading to a low rate of false positives. However, the model misses some of these cracks, resulting in lower recall. Meanwhile, the blue-green (OCA) cracks exhibit the lowest recall (0.707) compared to

CCA and CCP, showing differences of 10% and 1%, respectively; however, its F1 and precision scores fall between the other classes.

Table 9.6. Confusion matrix for classification of crack types.

		Predicted		
		Yellow	Red	Blue-green
Actual	Yellow	20029	441	4988
	Red	531	3125	723
	Blue-green	7119	271	17828

Table 9.7. Performance metrics such as F1, Precision and Recall for each crack type.

Metric	Yellow	Red	Blue-green
F1	0.754	0.761	0.731
Precision	0.724	0.814	0.757
Recall	0.787	0.714	0.707

9.5.2. Damage quantification through the DRI

Figure 9.11 shows that the estimated DRI calculated from the machine yields higher values, differing by 14% to 42% from the operator (Table 9.8), indicating an overestimation. While the DRI figures collected by the operator fall outside the typical range as proposed by [5] for the 0.20% and 0.30% expansion specimens, the crack propagation and extension align with those of [4]. The Springhill aggregate has a flaky nature, resulting in numerous cracks in the aggregates.

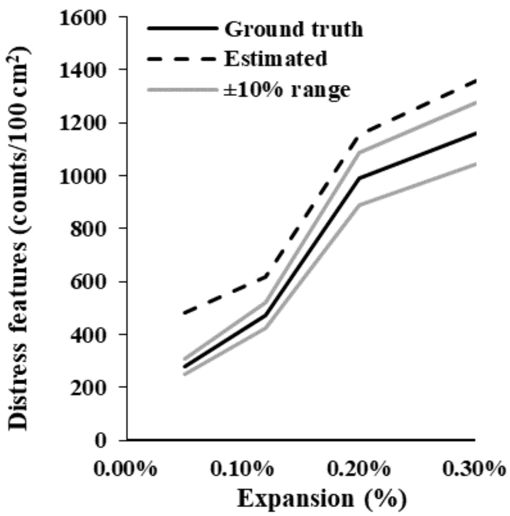

Figure 9.11. DRI results comparing the operator's ground truth and machine estimation. The grey lines indicate the ±10% lower and upper bounds from the ground truth.

Table 9.8. Comparison between DRI calculation and estimation performed.

Expansion level (%)	DRI number		
	Typical range [5]	Operator	Machine (% diff.)
0.00	100-155	-	-
0.04 ± 0.01	210-400	280	481 (42%)
0.11 ± 0.01	330-500	472	616 (23%)
0.20 ± 0.01	500-765	989	1156 (14%)
0.30 ± 0.01	600-925	1160	1357 (14%)

Figure 9.12a presents the extended version of the DRI, illustrating counts per 100 cm², as proposed by [4]. Figure 9.12b shows how the categorized bar charts differentiate the counts per feature. The counts of closed cracks in the aggregates (CCA) are underestimated at expansion levels of 0.05% and 0.12%. In contrast, they are overestimated at 0.20% and 0.30% expansion, with respective counts of -9%, -26%, 22%, and 14% (averaged at 17.75%). An opposite trend is observed for open cracks in the aggregate (OCA) at 8%, 1%, -34%, and -12% (averaged at 13.75%) for each increasing expansion level. An overestimation of cracks in the cement paste (CCP) is clearly noted; however, this decreases with the expansion level, dropping from 725% to 80%. This may indicate that the machine was trained on the 0.30% expansion specimen. During manual operations, evaluating a new operator's performance as within ±10% of an experienced operator is standard practice. Figure 9.13 illustrates the residuals of each distress feature and expansion level for the number of squares analyzed (ground truth) and images processed (estimated). The difference between the ground truth counts, and the predictions were used to compute the residuals, all indicating count differences within ±15 counts. Unlike the other distress features, the CCA

residuals exhibit wider variation with increasing expansion (from -13 to 14 count differences), suggesting the software's tendency to underestimate the actual counts (marks above the null line). Regarding OCA, results are underestimated for expansion levels of 0.05% and 0.20%, as evidenced by the data points concentrating above the null line. The cracks are less dispersed and more evenly distributed for expansion levels of 0.12% and 0.30%, with residuals ranging from -14 to 10 and -9.5 to 14, respectively. Additionally, as expansion increases, the CCP is overestimated for each level and becomes more dispersed around and below the null line; nonetheless, CCP has the smallest dispersion overall (-10.5 to 4.5) counts).

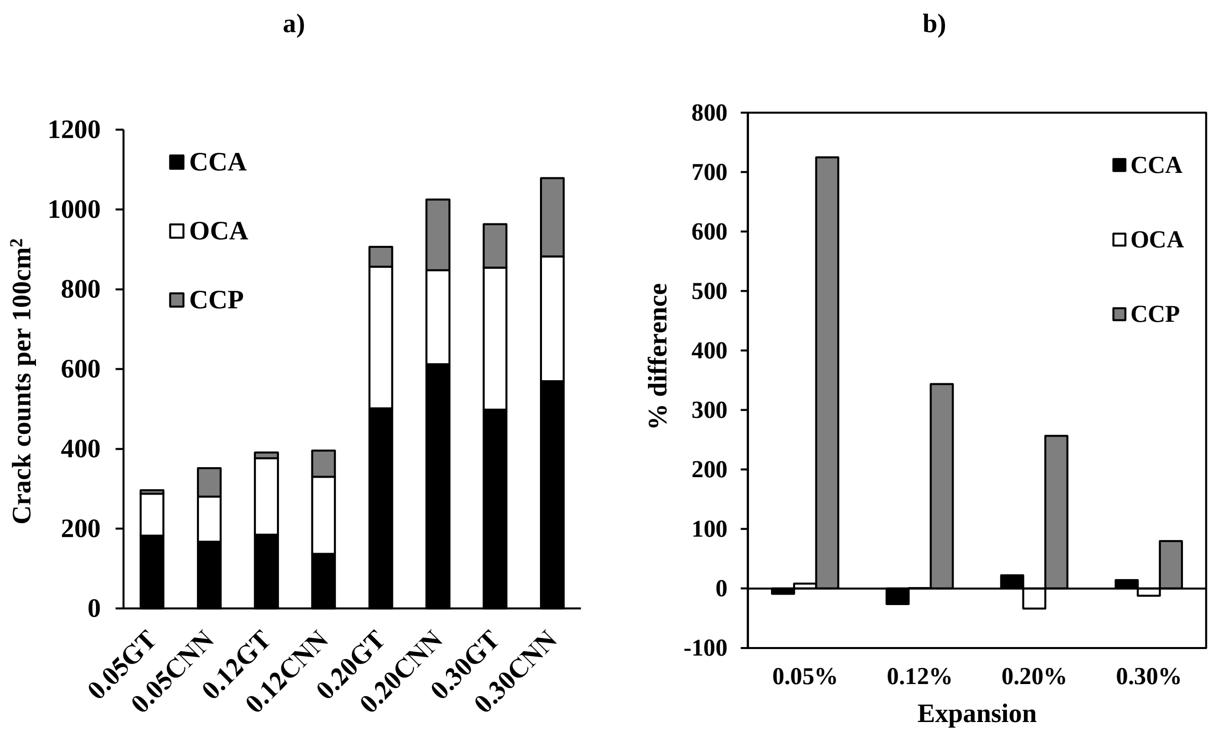

Figure 9.12. Bar charts of a) stacked crack counts/100 cm^2 and b) % differences for each expansion level.

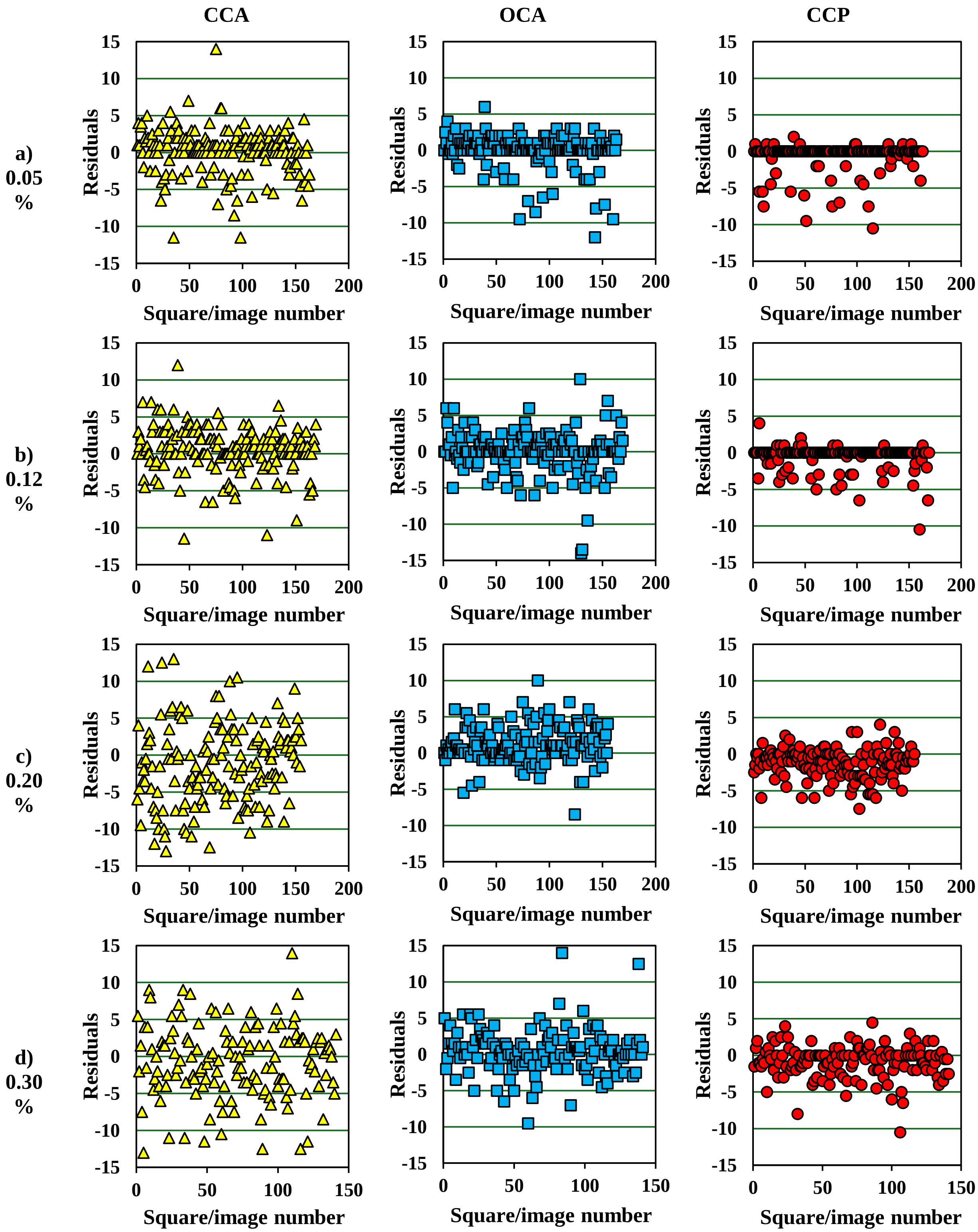

Figure 9.13. Residuals of each square (ground truth) and image (estimated) were analyzed for the various distress features and expansion levels.

9.5.3. Describing the data distribution

From the ML perspective, these models demonstrate distinguishable and acceptable performance. However, when used in combination to calculate the DRI, differences arise. In a previous feasibility study [48], performance was compared to a line of equality. Yet, the data collected using the DRI methodology consists of count data, which does not follow a normal distribution. Consequently, the underlying assumptions of linear regression do not apply to count data. Figure 9.14 illustrates the relationship between the count category and the frequency of ground truth and estimations per distress feature, along with the expansion level, revealing the non-normality of the data. Overlap in the data points indicates that the results from the machine are similar to those of the ground truth, which is typically the case in the tails for count categories greater than 5. The greatest discrepancies are observed at 0.05% and 0.12% for the closed cracks in the aggregates (CCA) and open cracks in the aggregates (OCA), respectively, where the machine overestimates the zero counts. Additionally, the zero counts of cracks in the cement paste (CCP) are underestimated throughout the expansion levels, with the largest difference occurring for the 0.30% and 0.20% expansion levels.

The boxplots further summarise the parameters, as demonstrated in Figure 9.15. Differences between the ground truth (GT) and the estimate (EST) are observed. The means of the GT and EST are closest at 0.05% expansion (i.e., 1.828 vs 1.761 for CCA and 1.049 vs 1.196 for OCA) and 0.12% expansion (i.e., 1.852 vs 1.462 for CCA and 1.911 vs 2.036 for OCA). At the same time, overestimation is noted in the CCP means (i.e., 0.086 vs 0.742 for 0.05% of expansion and 0.148 vs 0.710 for 0.12% of expansion). The means at 0.20% and 0.30% expansion for the CCA (i.e., 5.013 vs 6.394 and 4.979 vs 5.950, respectively) and CCP (i.e., 0.497 vs 1.955 and 1.092 vs 2.212, respectively) are overestimated. At the same time, values for the OCA are estimated lower (i.e., 3.555 vs 2.561 and 3.560 vs 3.348, respectively). The medians for the ground truth tend to be closer to the means throughout than the estimates; however, the medians and means follow a more similar trend at expansion levels of 0.20% and 0.30%. Nevertheless, a general overview of the distribution of results can be compared, but further investigation into the similarities between the ground truth and the estimates is still required.

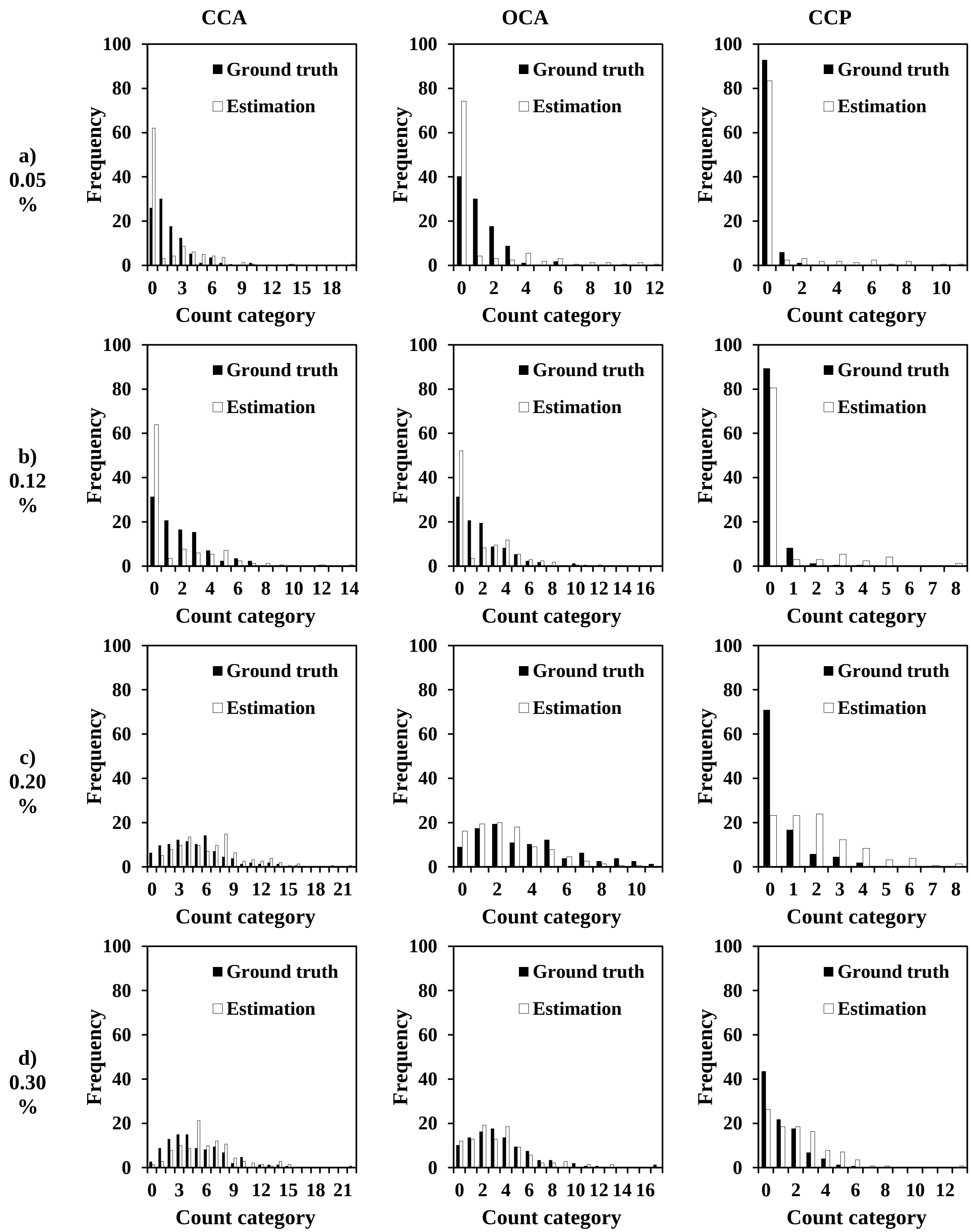

Figure 9.14. Data distribution for ground truth and estimations from the machine per distress feature and expansion level.

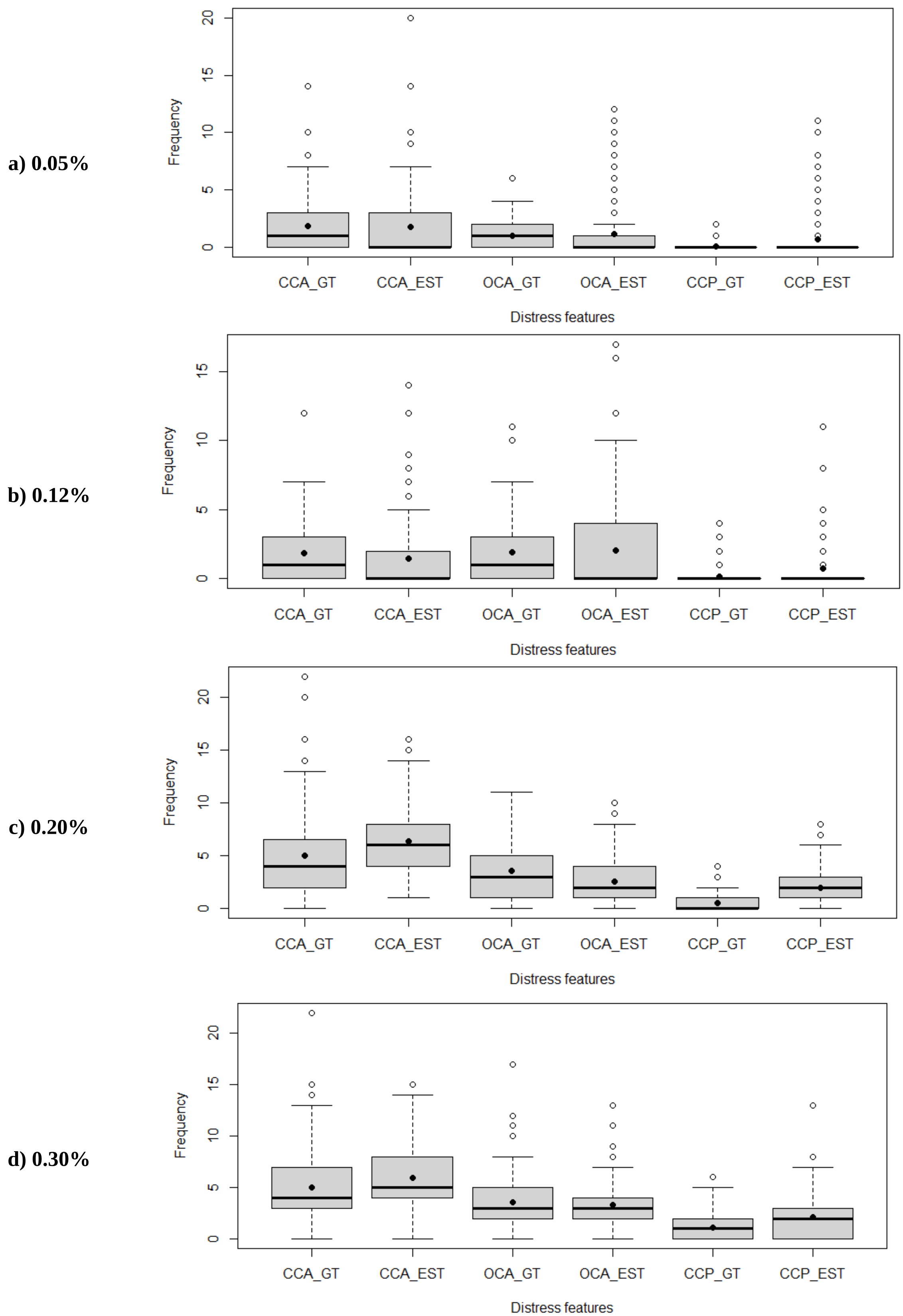

Figure 9.15. Boxplots of the distress feature for each expansion level comparing the ground truth (GT) with the estimations (EST).

9.5.4. *Validation of the estimations*

The distributions can then be compared through the goodness of fit (Chi-squared) to determine whether the data are similar, as per Eq. 9.4. Similar distributions are indicated by a check mark (☑). In contrast, different distributions are indicated by a cross (☒). The expected frequency was taken from the operator – GT, while the observed frequency represents the data obtained from the machine's estimations - EST. Cumulative frequencies were used in this application since the test requires proportional data with the same number of count categories (k, as per Eq. 9.4).

$$\chi^2 = \sum_{i=0}^{k} \frac{(o_i - e_i)^2}{e_i} \qquad \text{Eq. 9.4}$$

Where o_i and e_i are the observed and expected counts for the *i*th count category, and k is the total number of count categories.

Table 9.9 displays the goodness of fit results for each distress feature (crack type) at different expansion levels. Overall, the goodness of fit test results aligns with the overlapping data points and boxplots (see Figure 9.14 and Figure 9.15). For the 0.05% expansion, the CCA and OCA show different results between the operator (GT – EST) and the machine (estimation – observed values), primarily due to an overestimation of zero counts (refer to Figure 9.14a and Figure 9.15a). In contrast, the CCP shows consistent results between the operator and the estimate. An improvement is noted at 0.12% expansion, where only the CCA indicates different results between the operator and the machine, while the OCA and CCP appear similar. However, all distress features at 0.20% do not exhibit significantly similar results, even though the distributions visually suggest overlap (see Figure 9.14c), particularly for the CCA and OCA. At 0.30% expansion, only the OCA demonstrates significant similarities despite the visually overlapping results observed throughout (Figure 9.14d).

Table 9.9. The goodness of fit results for the operator vs estimation.

Crack_type	Degrees of freedom, υ	χ^2 test statistic	χ^2 critical	p-value ($\alpha = 0.05$)	Decision
			0.05%		
CCA	20	86.51	10.85	3.00E-10	☒
OCA	12	57.22	5.23	7.21E-08	☒
CCP	11	19.45	4.57	0.053	☑
			0.12%		
CCA	14	66.57	6.57	8.03E-09	☒
OCA	17	26.88	8.67	0.06	☑
CCP	8	9.39	2.73	0.31	☑
			0.20%		
CCA	22	74.73	12.33	1.17E-07	☒
OCA	11	36.60	4.57	1.34E-04	☒
CCP	8	94.50	2.73	5.66E-17	☒
			0.30%		
CCA	22	61.81	12.34	1.20E-05	☒
OCA	17	2.75	8.67	1	☑
CCP	13	36.80	5.89	4.45E-04	☒

9.6. Discussion

9.6.1. Ability to capture the significance of damage

The DRI is described as a semi-quantitative technique, suggesting that the interpretation of the results may be unclear. Although ranges of expected DRI values for a certain level of damage (expansion and mechanical) were adopted through the multi-level assessment [5], there remains hesitation about using the DRI as a companion diagnostic tool. Limitations regarding the DRI's subjectivity and variability may be addressed by understanding how to compare the observed data statistically. This work presents an initial attempt to statistically compare DRI data collected by an operator and the estimate. Table 9.10 presents the goodness of fit test results using Chi-squared to compare the distress features per expansion level. From 0.05% to 0.12% of expansion, the distributions of CCA and CCP are similar, while OCA differs. The increase in damage from 0.12% to 0.20% is captured through each crack type. The cracks in the aggregate, both closed and open, remain similar from 0.20% to 0.30% of expansion, while the CCP shows a significant difference. These results reflect the descriptive crack propagation model for OCA and CCP proposed by [54]. The most common feature for ASR is open cracks in the aggregates, which begin early at 0.05% of expansion and continue to increase in number and length (as indicated by crossing multiple 1 cm^2 grids). Meanwhile, CCP usually appears at 0.20% of expansion (as validated through the boxplots in Figure 9.15), extending from the OCA and indicating higher levels of damage for ASR. The machine detected this increase in OCA and CCP when the total counts were presented (Figure 9.12a). The machine's ability to distinguish levels of damage aligns with that of the operator (Table 9.10), except for OCA and CCP at 0.20% to 0.30% of the expansion. The goodness of fit test shows a significant difference for OCA, while the CCP presents similar results. Although it was established that further training was required for better identification of CCP, such discrepancies could lead to a misclassification of the level of damage and potentially indicate that the type of concrete is affected by a combined mechanism. Nevertheless, this approach allows for a statistical comparison across the results for each distress feature instead of relying solely on the DRI number or visual/subjective assessments through the bar charts.

Table 9.10. The goodness of fit results between levels of damage.

	Crack type	**0.05% to 0.12%**	**0.12% to 0.20%**	**0.20% to 0.30%**
Ground truth	CCA	☑	☒	☑
	OCA	☒	☒	☑
	CCP	☑	☒	☑
	Crack type	**0.05% to 0.12%**	**0.12% to 0.20%**	**0.20% to 0.30%**
Estimation	CCA	☑	☒	☑
	OCA	☒	☒	☒
	CCP	☑	☒	☑

As proposed by [54], the descriptive crack propagation model is illustrated in Figure 9.16 to demonstrate further the varying degrees of damage stages in ASR-affected concrete. According to the goodness of fit test, the CCA count frequencies are similar between 0.05% and 0.12% expansion; however, they differ between 0.12% and 0.20% expansion, likely due to the formation of OCA at this stage [54]. A similarity in CCA is observed from 0.20% to 0.30% expansion. Moreover, the goodness of fit test identifies the creation of OCA from 0.05% to 0.12% and from 0.12% to 0.20% expansion, as indicated by the crack propagation model. Similarly, the frequency distributions reveal that CCP is uncommon for ASR between 0.05% and 0.12% expansion. However, beyond 0.12% expansion, CCP penetrates into the cement paste and significantly increases in frequency, as demonstrated by the varying count distributions. Nonetheless, for the DRI to serve as a reliable diagnostic tool for ASR in concrete, ML models must be capable of capturing and identifying these distinct levels of damage.

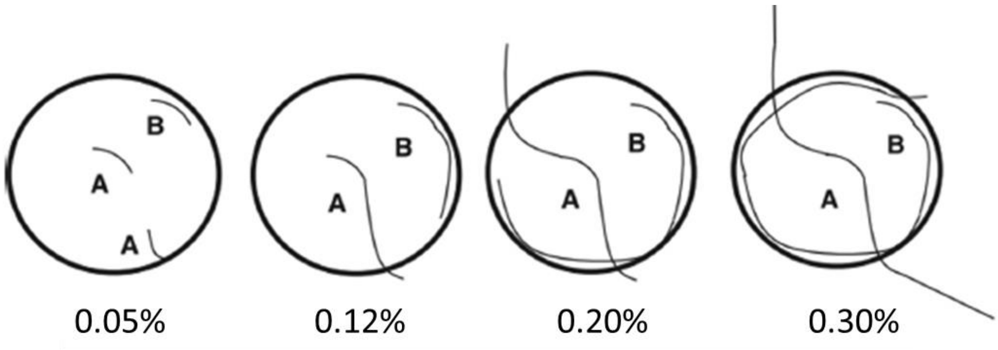

Figure 9.16. Descriptive crack propagation model for concrete affected by ASR [42].

These results reflect those obtained from one specimen at each expansion level; therefore, additional empirical data from a broader range of aggregate types, distress mechanisms, and environmental conditions could help identify underlying trends in quantifying crack propagation and patterns.

9.6.2. Visualizing and interpreting the training dataset

Problems involving a multi-disciplinary solution present certain constraints in determining the readiness of a measurement tool for specific applications. In ML, the metrics used to evaluate performance may not always align with those used to quantify damage due to ASR in concrete. In this context, visualizing outcomes from both the operator and the estimator facilitates the efficient selection of the next annotated training images. Indeed, analyzing each obtained output, where the machine locates and segments different crack types in each image, is the most suitable approach and necessitates expert intervention. However, this verification is time-consuming; therefore, plots with overlapping areas under the curves, as demonstrated in Figure 9.17, can be used to highlight similarities and enhance the goodness of fit test (Table 9.9). In the Chi-square test, cumulative counts are used for comparison; however, understanding differences in data distributions may aid in refining the model and EST outputs, especially considering it is a “new operator.” Overlapping areas under the curve indicate similarities in the overall data distribution, such as the CCP for

0.05% and 0.12% expansion and the OCA for 0.12% and 0.30% expansion. In instances where differences were noted by the Chi-squared test, such as for 0.05% and 0.12% expansion, the zero counts are overestimated, followed by an underestimation of the number of one-counts (i.e., the instances where 1 crack was counted) and a long right tail. The CCA zero counts are underestimated for 0.20% and 0.30% expansion, shifting the curve to the right and overestimating counts above 7 and 5, respectively. The OCA counts are overestimated up to 4 counts, after which they are underestimated for the 0.20% expansion. The CCP at 0.20% and 0.30% expansion presents underestimated zero counts until 1 and 2 counts, respectively.

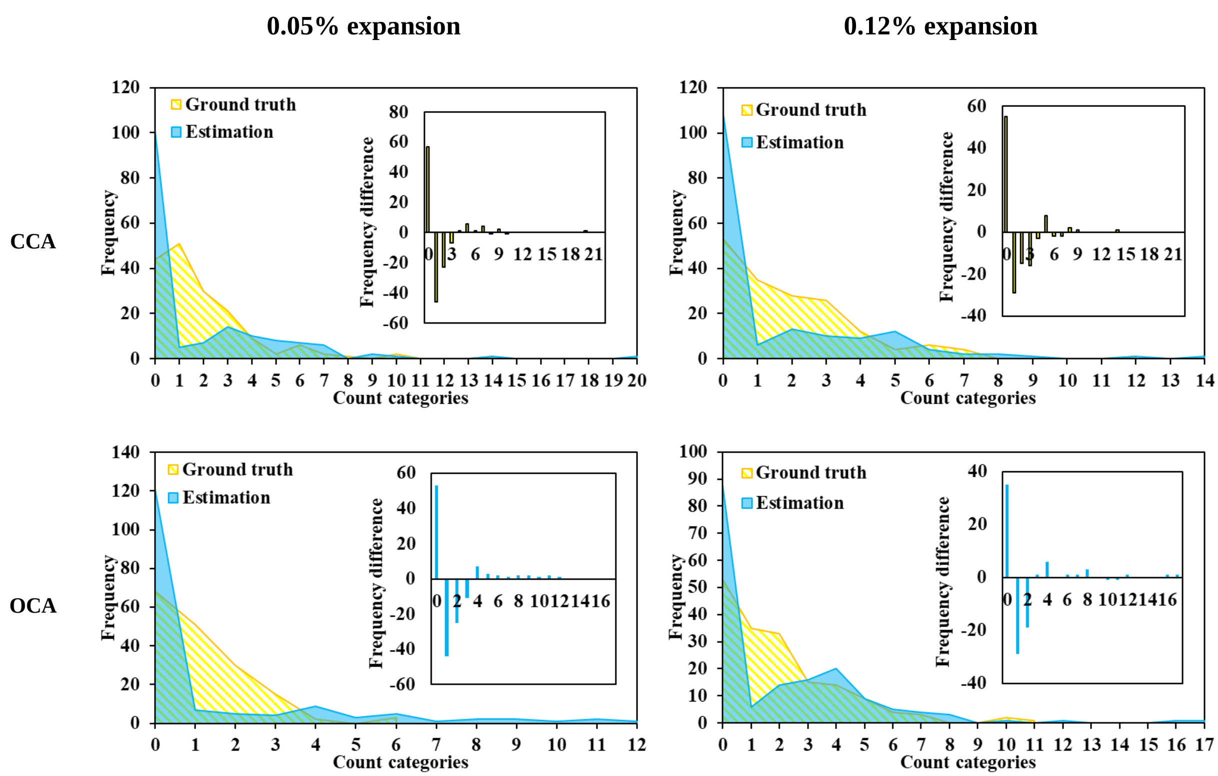

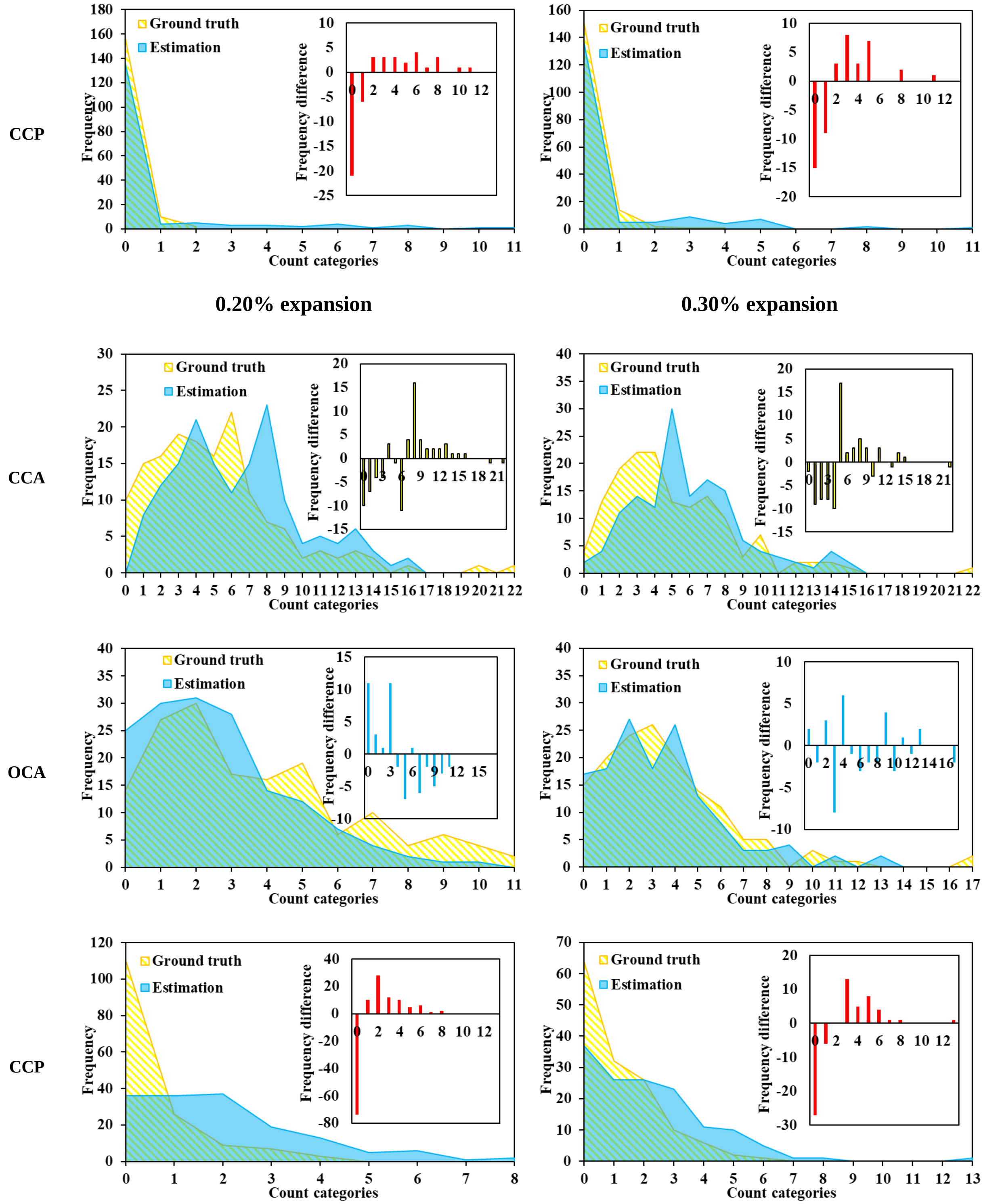

Figure 9.17. Comparison of distribution by area under the curve.

9.6.3. Future perspectives in automation of image diagnostics applied to concrete

The DRI can be seen as an image analysis technique that counts objects (distress features) to quantify damage to concrete. Image analysis is considered quantitative when its outputs can be correlated to a measurable property (i.e., expansion). Therefore, understanding the application and desired outputs is crucial to grasping the diagnostic capabilities of the tool used to assess concrete distress. Image analysis is limited to measuring crack length, area, widths, simple counts (analyzed as particles), and orientation. However, acquiring such characteristics through manual operations is impractical. Thus, image analysis could be applied to automatically annotated output images alongside DRI calculations, necessitating the support of AI. This combination can capture the full profile of the damage (i.e., crack extension/propagation, patterns, orientations, etc.) at a scale representative of the concrete material. Interestingly, the crack counter interpreted the crack counts within a network where multiple cracks are interconnected. In this context, graph theory, developed by Euler in 1736 to address the Königsberg bridge problem, offers insights into constructing a circular walking path without interference from the river [55]. Graphs consist of configurations of nodes and connections (edges) forming a structure. They are frequently employed in civil engineering applications through network analysis, such as designing roads, planning construction work sequences, and establishing hierarchies and relationships among employees. Therefore, networks serve as tools that can assist in decision-making. Trees, defined as “a connected graph that has no cycles” [56], represent one type of graph that can depict cracks in concrete since cracks generally have a starting and ending point and may branch out at intersections. Figure 9.18 illustrates a few examples of trees, including the number of nodes and segments (connections).

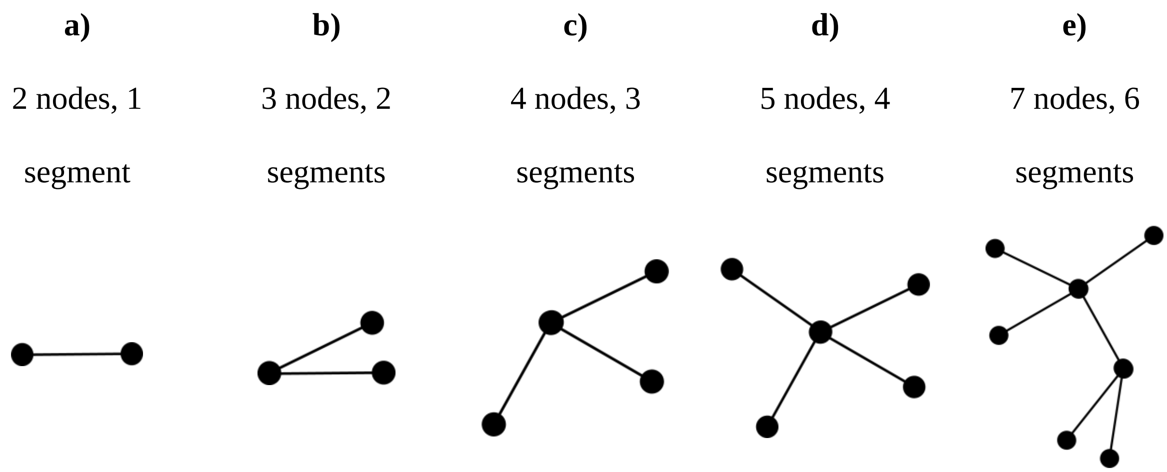

Figure 9.18. Some examples of tree graphs with the number of nodes and segments.

The visual output data used for DRI calculation provides an opportunity to explore the feasibility of applying network analysis to digital images. Gaining further insight into the damage patterns concerning aggregate location may uncover critical information that contributes to a more reliable diagnosis of damage to concrete due to internal swelling reactions, including ASR. Furthermore, this approach may extend beyond internal concrete, as similar patterns (e.g., map cracking and polygonal cracking) have been observed on the concrete surface.

9.7. Conclusion

This study proposes a method for evaluating the feasibility of automating the damage rating index (DRI), a procedure that involves point-count stereomicroscopy for data collection. The objects of focus in the segmentation challenge were cracks in concrete resulting from an alkali-silica reaction (ASR). The study's multidisciplinary approach presented certain challenges regarding the metrics used to assess the machine's performance in relation to its practical application by operators. These challenges were addressed by focusing on the methodology for statistically evaluating the machine's performance, which involved several models. The key conclusions are:

- To identify and categorize cracks according to their DRI types and to calculate the number of cracks per picture, two models (a crack detector/classifier and a counter) were developed. The accuracy of the detector/classifier was measured at 0.744, while the counter achieved an accuracy of 0.988. Compatibility issues arose because the detector/classifier operated at the pixel level, whereas the counter used image patches to count the nodes and determine the number of cracks based on the node type. The combined performance of the models was found to overestimate the damage due to ASR.
- In light of the hesitance to use the DRI as an ASR damage assessment tool, the data gathered through point counts showed that the distribution of data from the histograms of counts per square analyzed generally follows similar patterns. This facilitated the visualization of empirical data through a theoretical framework that can be statistically compared. Further work is needed to validate the type of distribution based on a larger sample dataset.
- Using the data collected from the histograms to create distributions of the observed frequencies from the operator as ground truth and the machine's estimations enabled the application of the goodness of fit test (Chi-squared) for each crack type. This concept was used to validate whether the machine can accurately capture this distribution while providing visuals of its performance. It was determined that, at low levels of expansion, only the distribution of the cracks in the cement paste was estimated well, due to the excess of zero counts. In contrast, the distributions of open cracks in the aggregate and cracks in the cement paste were deemed similar when comparing the ground truth to the machine's results for the moderately damaged concrete. No similarities in the count distribution were observed for the high level of damage, and only the distribution of open cracks in the

aggregate was considered similar to the ground truth. Therefore, these visuals assist the operator and annotator in selecting specimens/images for further research training.

- The DRI has the potential to serve as an objective assessment tool for engineering practitioners when evaluating damage from ASR. The fundamental concept behind the DRI, as a point-count method that collects frequency data and provides distributions, should be re-evaluated and regarded as an image analysis technique rather than solely petrography. Automating the procedure can also enhance the dataset and improve the results, aiding in the understanding of the DRI's outputs concerning the quantification of damage. Furthermore, the image parameters can be more easily controlled due to the nature of the procedure (1 cm by 1 cm images) compared to other microscopy techniques, which facilitates the creation of a standardized dataset.
- The machine's visual outputs can also be used to investigate crack propagation patterns, which may indicate various types of internal swelling reaction (ISR) damage, the extent of damage, anisotropic damage behaviour, areas of interest to reduce analysis time, and other unexplored aspects possibilities.

9.8. References

[1] I. Sims, A. Poole, eds., Alkali-aggregate reaction in concrete: a world review, CRC Press, Taylor & Francis Group, a Balkema book, Boca Raton London New York Leiden, 2017.

[2] P.E. Grattan-Bellew, A. Danay, Comparison of laboratory and field evaluation of alkali-silica reaction in large dams, in: Collection / Collection : NRC Publications Archive / Archives des publications du CNRC, 1992: pp. 1–25.

[3] L.F.M. Sanchez, B. Fournier, M. Jolin, J. Duchesne, Reliable quantification of AAR damage through assessment of the Damage Rating Index (DRI), Cement and Concrete Research 67 (2015) 74–92. https://doi.org/10.1016/j.cemconres.2014.08.002.

[4] L.F.M. Sanchez, B. Fournier, M. Jolin, M.A.B. Bedoya, J. Bastien, J. Duchesne, Use of Damage Rating Index to Quantify Alkali-Silica Reaction Damage in Concrete: Fine versus Coarse Aggregate, ACI Materials Journal 113 (2016). https://doi.org/10.14359/51688983.

[5] L.F.M. Sanchez, T. Drimalas, B. Fournier, D. Mitchell, J. Bastien, Comprehensive damage assessment in concrete affected by different internal swelling reaction (ISR) mechanisms, Cement and Concrete Research 107 (2018) 284–303. https://doi.org/10.1016/j.cemconres.2018.02.017.

[6] L.F.M. Sanchez, T. Drimalas, B. Fournier, Assessing condition of concrete affected by internal swelling reactions (ISR) through the Damage Rating Index (DRI), Cement 1–2 (2020) 100001. https://doi.org/10.1016/j.cement.2020.100001.

[7] Y. Song, Z. Huang, C. Shen, H. Shi, D.A. Lange, Deep learning-based automated image segmentation for concrete petrographic analysis, Cement and Concrete Research 135 (2020) 106118. https://doi.org/10.1016/j.cemconres.2020.106118.

[8] F. Azzam, T. Blaise, B. Brigaud, Automated petrographic image analysis by supervised and unsupervised machine learning methods, Sedika 2 (2024). https://doi.org/10.57035/journals/sdk.2024.e22.1594.

[9] V.E. Saouma, ed., Diagnosis & Prognosis of AAR Affected Structures: State-of-the-Art Report of the RILEM Technical Committee 259-ISR, Springer International Publishing, Cham, 2021. https://doi.org/10.1007/978-3-030-44014-5.

[10] V. Villeneuve, Détermination de l’endommagement du béton par méthode pétrographique quantitative, Master’s Thesis., Université Laval, 2011.

[11] V. Villeneuve, B. Fournier, J. Duchesne, Determination of the damage in concrete affected by ASR – the damage rating index (DRI), in: 14th International Conference on Alkali-Aggregate Reaction, Texas, USA, 2012.

[12] P.E. Grattan-Bellew, D. Mitchell, Quantitative petrographic analysis of concrete : the damage rating index (DRI) method, a review, in: CANMET International Conference on Recent Advances in Concrete Technology, Natural Resources Canada, Ottawa, Canada, 2006.

[13] L. Powers, F.H. Shrimer, Quantification of ASR in concrete: an introduction to the Damage-Rating method, in: 29th International Conference on Cement Microscopy, Québec, Canada, 2007.

[14] P. Rivard, G. Ballivy, Assessment of the expansion related to alkali-silica reaction by the Damage Rating Index method, Construction and Building Materials 19 (2005) 83–90. https://doi.org/10.1016/j.conbuildmat.2004.06.001.

[15] M.-A. Bérubé, B. Fournier, T. Côté, Using the damage rating index for assessing the expansion of concrete affected by freeze-thaw, sulphate attack, or ASR, in: 14th International Conference on Alkali-Aggregate Reaction, Austin, Texas, USA, 2012.

[16] L.F.M. Sanchez, T. Drimalas, B. Fournier, Assessing condition of concrete affected by internal swelling reactions (ISR) through the Damage Rating Index (DRI), Cement 1–2 (2020) 100001. https://doi.org/10.1016/j.cement.2020.100001.

[17] A. Zahedi, L. Saliba, L.F.M. Sanchez, A.J. Boyd, Reliability of the damage rating index to assess the condition of concrete affected by external sulfate attack, Magazine of Concrete Research 75 (2023) 135–148. https://doi.org/10.1680/jmacr.22.00061.

[18] P. Rivard, B. Fournier, G. Ballivy, The Damage Rating Index Method for ASR Affected Concrete—A Critical Review of Petrographic Features of Deterioration and Evaluation Criteria, Cement, Concrete, Aggr. 24 (2002) 11228. https://doi.org/10.1520/CCA10531J.

[19] A. Zahedi, A. Komar, L.F.M. Sanchez, A.J. Boyd, Global assessment of concrete specimens subjected to freeze-thaw damage, Cement and Concrete Composites 133 (2022) 104716. https://doi.org/10.1016/j.cemconcomp.2022.104716.

[20] C.T. Rueden, J. Schindelin, M.C. Hiner, B.E. DeZonia, A.E. Walter, E.T. Arena, K.W. Eliceiri, ImageJ2: ImageJ for the next generation of scientific image data, BMC Bioinformatics 18 (2017) 529. https://doi.org/10.1186/s12859-017-1934-z.

[21] J. Schindelin, I. Arganda-Carreras, E. Frise, V. Kaynig, M. Longair, T. Pietzsch, S. Preibisch, C. Rueden, S. Saalfeld, B. Schmid, J.-Y. Tinevez, D.J. White, V. Hartenstein, K. Eliceiri, P. Tomancak, A. Cardona, Fiji: an open-source platform for biological-image analysis, Nat Methods 9 (2012) 676–682. https://doi.org/10.1038/nmeth.2019.

[22] P. Rivard, B. Fournier, G. Ballivy, Quantitative Petrographic Technique for Concrete Damage Due to ASR: Experimental and Application, Cement, Concrete and Aggregates 22 (2000) 63–72. https://doi.org/10.1520/CCA10465J.

[23] J. Lindgård, M. Haugen, N. Castro, M.D.A. Thomas, Advantages of using plane polished section analysis as part of microstructural analyses to describe internal cracking due to alkali-silica reactions, in: Austin, Texas, USA, 2012.

[24] S. Li, G. Chen, G. Ji, Y. Lu, Quantitative damage evaluation of concrete suffered freezing–thawing by DIP technique, Construction and Building Materials 69 (2014) 177–185. https://doi.org/10.1016/j.conbuildmat.2014.07.072.

[25] M. Champagne, Applying the damage rating index for the spatial damage assessment in concrete specimens affected by alkali-silica reaction (ASR), Master's Thesis., Université Laval, 2020.

[26] O.D. Olajide, M.R. Nokken, L.F.M. Sanchez, Influence of Temperature on the Microstructural Properties of ASR-Affected Concrete, in: L.F.M. Sanchez, C. Trottier (Eds.), Proceedings of the 17th International Conference on Alkali-Aggregate Reaction in Concrete, Springer Nature Switzerland, Cham, 2024: pp. 185–194. https://doi.org/10.1007/978-3-031-59349-9_22.

[27] D.J. De Souza, L.F.M. Sanchez, Understanding the efficiency of autogenous and autonomous self-healing of conventional concrete mixtures through mechanical and microscopical analysis, Cement and Concrete Research 172 (2023) 107219. https://doi.org/10.1016/j.cemconres.2023.107219.

[28] A. Zahedi, C. Trottier, L.F.M. Sanchez, M. Noël, Microscopic assessment of ASR-affected concrete under confinement conditions, Cement and Concrete Research 145 (2021) 106456. https://doi.org/10.1016/j.cemconres.2021.106456.

[29] A. Zahedi, C. Trottier, L.F.M. Sanchez, M. Noël, Condition assessment of alkali-silica reaction affected concrete under various confinement conditions incorporating fine and coarse reactive aggregates, Cement and Concrete Research 153 (2022) 106694. https://doi.org/10.1016/j.cemconres.2021.106694.

[30] İ. Akgül, Mobile-DenseNet: Detection of building concrete surface cracks using a new fusion technique based on deep learning, Heliyon 9 (2023) e21097. https://doi.org/10.1016/j.heliyon.2023.e21097.

[31] Y. Bai, H. Sezen, A. Yilmaz, End-to-end Deep Learning Methods for Automated Damage Detection in Extreme Events at Various Scales, in: 2020 25th International Conference on Pattern Recognition (ICPR), IEEE, Milan, Italy, 2021: pp. 6640–6647. https://doi.org/10.1109/ICPR48806.2021.9413041.

[32] U.H. Billah, A. Tavakkoli, H.M. La, Concrete Crack Pixel Classification Using an Encoder Decoder Based Deep Learning Architecture, in: G. Bebis, R. Boyle, B. Parvin, D. Koracin, D. Ushizima, S. Chai, S. Sueda, X. Lin, A. Lu, D. Thalmann, C. Wang, P. Xu (Eds.), Advances in Visual Computing, Springer International Publishing, Cham, 2019: pp. 593–604. https://doi.org/10.1007/978-3-030-33720-9_46.

[33] P.S. Chakurkar, D. Vora, S. Patil, S. Mishra, K. Kotecha, Data-driven approach for AI-based crack detection: techniques, challenges, and future scope, Front. Sustain. Cities 5 (2023) 1253627. https://doi.org/10.3389/frsc.2023.1253627.

[34] Y. Chen, Z. Zhu, Z. Lin, Y. Zhou, Building Surface Crack Detection Using Deep Learning Technology, Buildings 13 (2023) 1814. https://doi.org/10.3390/buildings13071814.

[35] V.P. Golding, Z. Gharineiat, H.S. Munawar, F. Ullah, Crack Detection in Concrete Structures Using Deep Learning, Sustainability 14 (2022) 8117. https://doi.org/10.3390/su14138117.

[36] Md.M. Islam, Md.B. Hossain, Md.N. Akhtar, M.A. Moni, K.F. Hasan, CNN Based on Transfer Learning Models Using Data Augmentation and Transformation for Detection of Concrete Crack, Algorithms 15 (2022) 287. https://doi.org/10.3390/a15080287.

[37] S. Katsigiannis, S. Seyedzadeh, A. Agapiou, N. Ramzan, Deep learning for crack detection on masonry façades using limited data and transfer learning, Journal of Building Engineering 76 (2023) 107105. https://doi.org/10.1016/j.jobe.2023.107105.

[38] J.-H. Kim, J. Lee, Efficient Dataset Collection for Concrete Crack Detection With Spatial-Adaptive Data Augmentation, IEEE Access 11 (2023) 121902–121913. https://doi.org/10.1109/ACCESS.2023.3328243.

[39] X. Meng, Concrete Crack Detection Algorithm Based on Deep Residual Neural Networks, Scientific Programming 2021 (2021) 1–7. https://doi.org/10.1155/2021/3137083.

[40] M. Padsumbiya, V. Brahmbhatt, S. Thakkar, Automatic Crack Detection Using Convolutional Neural Network, J. Soft Comput. Civ. Eng. 6 (2022). https://doi.org/10.22115/scce.2022.325596.1397.

[41] P. Palevičius, M. Pal, M. Landauskas, U. Orinaitė, I. Timofejeva, M. Ragulskis, Automatic Detection of Cracks on Concrete Surfaces in the Presence of Shadows, Sensors 22 (2022) 3662. https://doi.org/10.3390/s22103662.

[42] S. Shim, Self-training approach for crack detection using synthesized crack images based on conditional generative adversarial network, Computer Aided Civil Eng (2023) mice.13119. https://doi.org/10.1111/mice.13119.

[43] C. Tello, S. Jabari, L. Waugh, M. Masry, J. McGinn, Improving Crack Detection on Concrete Structures Using Real-World Data Augmentation for Deep Learning Convolutional Neural Networks, in: Springer International Publishing, Moncton, NB, 2023.

[44] P. Bajcsy, S. Feldman, M. Majurski, K. Snyder, M. Brady, Approaches to training multiclass semantic image segmentation of damage in concrete, Journal of Microscopy 279 (2020) 98–113. https://doi.org/10.1111/jmi.12906.

[45] A.P. Bajcsy, S. Feldman, M. Brady, K. Snyder, Semantic SEM Image Segmentation of Concrete with Contextual Labels, Microsc Microanal 25 (2019) 144–145. https://doi.org/10.1017/S1431927619001454.

[46] S.S. Bangaru, C. Wang, M. Hassan, H.W. Jeon, T. Ayiluri, Estimation of the degree of hydration of concrete through automated machine learning based microstructure analysis – A study on effect of image magnification, Advanced Engineering Informatics 42 (2019) 100975. https://doi.org/10.1016/j.aei.2019.100975.

[47] A.N. Beskopylny, E.M. Shcherban', S.A. Stel'makh, L.R. Mailyan, B. Meskhi, I. Razveeva, A. Kozhakin, N. Beskopylny, D. El'shaeva, S. Artamonov, Method for Concrete Structure Analysis by Microscopy of Hardened Cement Paste and Crack Segmentation Using a Convolutional Neural Network, J. Compos. Sci. 7 (2023) 327. https://doi.org/10.3390/jcs7080327.

[48] A. Bezerra, The Use of Artificial Intelligence for Assessing Damage in Concrete Affected by Alkali-Silica Reaction (ASR), Master's Thesis., University of Ottawa, 2020.

[49] A. Bezerra, C. Trottier, L.F.M. Sanchez, B. Fournier, The use of artificial intelligence for assessing an overpass affected by Alkali-Silica Reaction (ASR), in: Bridge Safety, Maintenance, Management, Life-Cycle, Resilience and Sustainability, CRC Press, London, 2022: pp. 354–361. https://doi.org/10.1201/9781003322641-40.

[50] A. Dehghan, P. Zhang, E. Ossetchkina, D. Sloan, K. Peterson, Digital Microscopy Applied to Damage Rating Index for Alkali-Silica Reaction in Concrete, in: D. Cong, D. Broton (Eds.), Advances in Cement Analysis and Concrete Petrography, ASTM International, 100 Barr Harbor Drive, PO Box C700, West Conshohocken, PA 19428-2959, 2016: pp. 105–125. https://doi.org/10.1520/STP161320180003.

[51] ASTM C1293-18a, Test Method for Determination of Length Change of Concrete Due to Alkali-Silica Reaction, (2018). https://doi.org/10.1520/C1293-18A.

[52] A. Poole, I. Sims, Concrete Petrography: A Handbook of Investigative Techniques, 2nd ed., CRC Press, Taylor & Francis Group, a Balkema book, London, UK, 2016. https://doi.org/10.1201/b18688 (accessed June 21, 2023).

[53] O. Ronneberger, P. Fischer, T. Brox, U-Net: Convolutional Networks for Biomedical Image Segmentation, (2015). https://doi.org/10.48550/ARXIV.1505.04597.

[54] L.F.M. Sanchez, B. Fournier, M. Jolin, D. Mitchell, J. Bastien, Overall assessment of Alkali-Aggregate Reaction (AAR) in concretes presenting different strengths and incorporating a wide range of reactive aggregate types and natures, Cement and Concrete Research 93 (2017) 17–31. https://doi.org/10.1016/j.cemconres.2016.12.001.

[55] D. Jungnickel, Graphs, networks, and algorithms, 4. ed, Springer, Berlin, Heidelberg, 2013.

[56] J.L. Gross, J. Yellen, M. Anderson, Graph theory and its applications, Third edition, CRC Press, Taylor & Francis Group, Boca Raton, 2019.

Chapter 10: Conclusions and research recommendations

10.1.Summary

Concrete durability, while not the industry's primary focus in the sustainability roadmap towards Net Zero 2050, remains one of the most crucial strategies to decrease carbon footprint by reducing consumption. As infrastructure ages, whether due to natural processes or premature deterioration from issues like internal swelling reactions (ISR), preserving these concrete structures must become a priority. However, it is well understood that when the cause of deterioration is unknown—let alone its extent and implications from an engineering perspective—solutions for preservation will remain elusive and challenging.

The development and implementation of accessible, practical, and reliable tools are crucial for better understanding the effects of ISR-induced deterioration in concrete. Microscopy is a discipline rarely adopted in engineering practice, where mechanical testing is consistently the preferred method for obtaining quantitative outputs to compare with reported levels of deterioration. However, ISR impacts mechanical responses in distinct ways that cannot be captured by numerical outputs alone. Incorporating microscopy into engineering practices to explore the relationship between the types of distress features observed and their respective patterns enhances the comprehension of the extent of ISR-induced deterioration. The multi-level assessment was developed to provide a holistic approach to determining the cause and extent of ISR-induced deterioration. While the stiffness damage test (SDT) and the loss of mechanical properties are well accepted in engineering practices, there remain hesitations regarding using the damage rating index (DRI) due to operator variability in distinguishing levels of deterioration and the subjectivity involved in result interpretation. The DRI is a powerful and universal tool that enables an operator to gather information that mechanical testing may overlook. It allows operators to connect observed deterioration patterns to mechanical responses, allowing a deeper understanding of the concrete deterioration. Data collected during the analysis includes the DRI number, bar charts that display weighted or unweighted counts of distress features, proportions of these counts, lengths and widths of distress features, heat maps to visualize deterioration distribution (as DRI numbers or by distress feature), count data for histograms and boxplots, assessing anisotropy based on distress feature angles, and propagation counts when cracks extend across various concrete components, along with overall deterioration profiles. Throughout this research program, it became clear that the potential for utilizing the DRI as a methodology and versatile tool is gradually evolving; however, its perception and implementation remain limited. Since the inception of this program, the DRI has not been standardized, but currently, the Canadian Standards Association (CSA) and the American Society for Testing and Materials (ASTM) are taking steps toward standardizing it. Addressing the uncertainties surrounding the DRI is more crucial than ever.

This work, therefore, focused on the main components as a starting point towards the standardization of the DRI: its adaptability to distinguish delayed ettringite formation (DEF), understanding the contributions of the distress features to the mechanical responses for various ISRs; hence, its subjectivity, controlling operator variability to determine the extent of deterioration given the ISR (in this context, only alkali-silica reaction – ASR, due to its widespread presence), and unlocking the DRI's full potential through an automated version. The main contributions of this research program will henceforth be presented in an objective-based manner, along with corresponding future research recommendations:

10.2. The adaptability of the DRI to DEF

This work was divided into two parts. First, the procedure counting technique was examined to understand how it could be modified without altering the weighting factors or distress features. It focused on the Debon-type feature, encompassing cracks in the aggregate-cement paste interface. The original method states that for ASR, when a crack in its interface surrounds 50% of an aggregate, the crack is categorized as Debon. However, uncertainty remained regarding aggregates that span multiple squares. As such, the counting method proposed increasing the proportion of interface cracking to 75% (i.e., easily identifiable during the analysis) to avoid misclassifying other types of cracks, such as mechanical cracks interfered with by an aggregate. Moreover, the analysis was conducted on all aggregates where the operator considered adjacent squares to categorize a crack as Debon. Furthermore, during the sample preparation of severely DEF-affected concrete, dislodged aggregates are frequent and should be counted as Debon. While this methodology highlights the type of ISR compared to other types, the second part of this work aimed to validate the counting method with mechanical responses. The proposed counting method resulted in better correlations with expansion (i.e., R^2 increasing from 0.45 to 0.78), modulus of elasticity (i.e., R^2 increasing from 0.38 to 0.70), and the stiffness damage index (SDI) (i.e., R^2 increasing from 0.24 to 0.67). Additionally, using the extended version of the DRI against expansion, the proposed counting method distinguishes an increase in Debon-type cracks as expansion increases, thus validating the ability to capture the most representative distress feature DEF. A visual summary of the findings is illustrated in Figure 10.1.

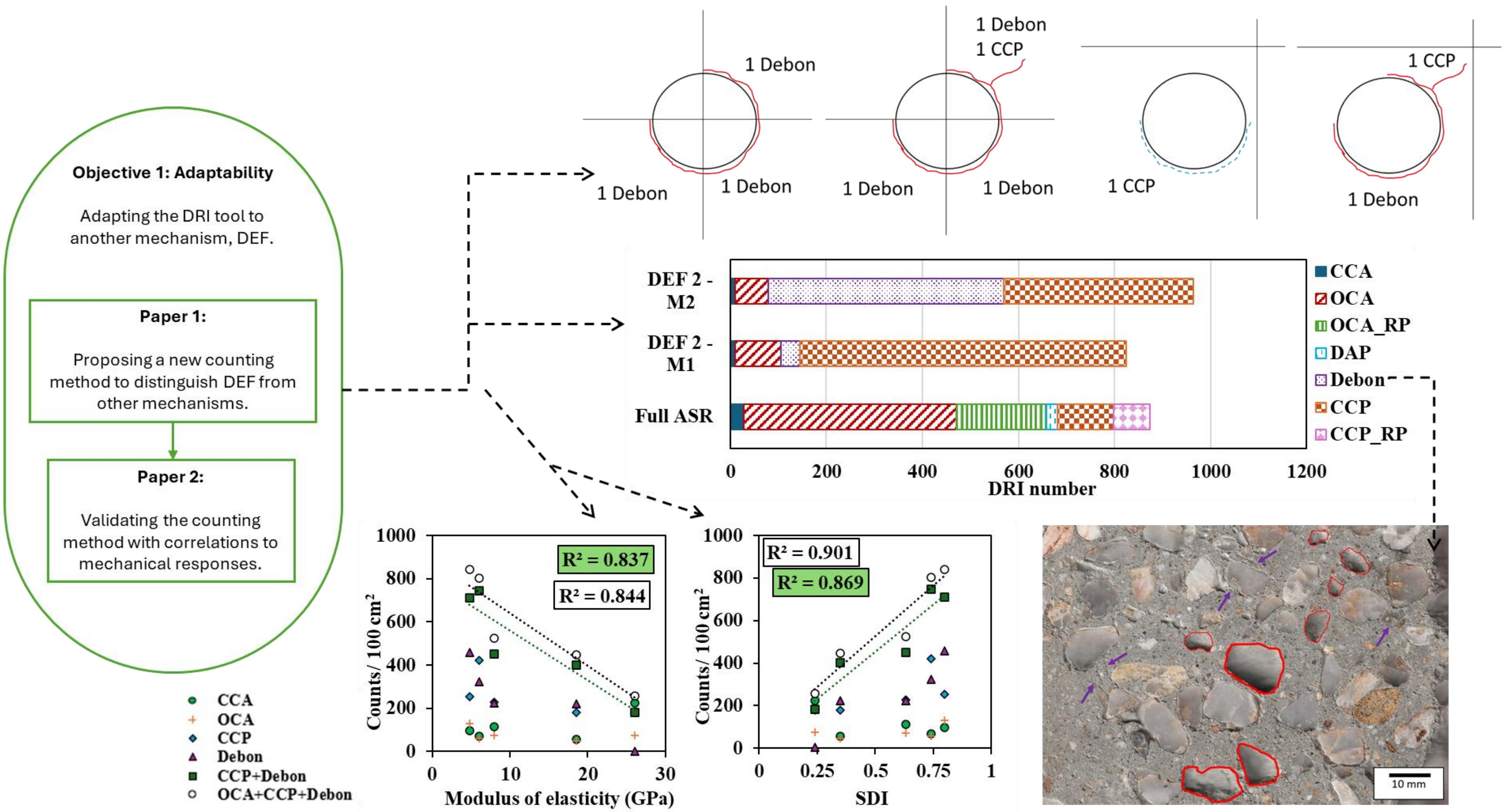

Figure 10.1. A visual summary of objective 1: Adaptability to DEF.

Research recommendations

It is, however, recommended to verify the proposed counting method with linear models and other mechanical responses (tensile and compressive strengths and plastic deformation index – PDI), while employing a wider variety of expansion levels, particularly lower ones, to understand how the DRI will capture DEF at its early onset. Additionally, this counting method can be used to establish a crack initiation and propagation descriptive model. Nevertheless, the DRI captures the current level of deterioration, and re-evaluation using the DRI after residual expansion testing is strongly recommended. Cases of ISR in which the current conditions have not yet been triggered can be better understood by using the DRI post-mortem to validate that the residual expansion accurately reflects the concrete deterioration.

10.3. The subjectivity of the DRI when applied to various ISR

The subjectivity in interpreting results arises from using the DRI number and bar charts to determine the cause and extent of ISR-induced deterioration. Extensive previous research and applications of the DRI to ASR have shown that the DRI number can be correlated to expansion. However, similar DRI numbers can be achieved by two different ISRs, yet they represent two different levels of deterioration due to the types of distress features observed and recorded. While the DRI over-expansion or other mechanical responses reflecting various levels of deterioration represents a two-dimensional construct, understanding the role of each distress feature regarding the expansion or mechanical response remains crucial for enhancing our understanding of the implications of ISR-induced deterioration in concrete. In this work, ASR, DEF, and freezing and thawing (FT) were incorporated into the study. It was determined that modifications to the DRI weighting factors are no longer necessary, as these modifications only slightly improve the correlations (i.e., most with an R^2 above 0.70, with the exception of two instances out of 48). The crack density (counts/cm²) using the distress features reflecting a progression of deterioration (open cracks in the aggregate and cracks in the cement paste) as a function of expansion showed an R^2 of above 0.71, while the behaviours of the trends varied as a function of the ISR. This led to the breakdown of the distress features as proposed in the extended version of the DRI, grouped as closed cracks in the aggregate, open cracks in the aggregate (with and without reaction product), cracks in the cement paste (with and without reaction product), and debonded aggregates. This study revealed the importance of closed cracks in the aggregates regarding mechanical responses due to the sliding effect of the crack planes compared to expansion while not producing an opening. As such, closed cracks in the aggregate remain a significant distress feature influencing mechanical responses. Predicting expansions based on open cracks in the aggregates and cracks in the cement paste resulted in an R^2 of 0.881 when using the distress mechanism as a categorical variable. However, the comparison of the predicted versus observed expansions proved inefficient. In the same context, the tensile and compressive strength, modulus of elasticity, hysteresis area (HA), SDI, and PDI included the closed cracks in the aggregate, the debonded aggregates, and interactions between the terms to obtain R^2 values of 0.43, 0.83, 0.85, 0.85, 0.80, and 0.88, respectively, when using the distress mechanisms as categorical variables. However, a total of 19 estimates were used to obtain these predictions. Analyzing crack propagations made it evident that expansions and mechanical responses need to be observed per distress mechanism, rather than as a categorical variable describing a change in response. Thus, expansion remains the metric that best describes deterioration and can be seen as a damage category with respect to a certain ISR; hence, determining the extent of deterioration given a specific ISR is crucial. Following the concept of what constitutes a sample and the convergence of the DRI number as the sample size increases using the law of large numbers, the counts were represented as boxplots alongside descriptive statistics. The interquartile ranges (IQR) along with the average counts of distress features were used to predict expansion for each ISR. This resulted in improved performance, with R^2 values of 0.96, 1 (due to limited data), 0.83, 0.95, and 1.00 for ASR, FT, FT&ASR, DEF, and DEF&ASR, respectively. Moreover, the concept of convergence of the DRI number as the sample size increases revealed that a larger sample size is required for a higher degree of damage; yet, for laboratory-made specimens, 75±25 cm^2 remains sufficient. Furthermore, while decomposing the DRI data into count data, the bootstrap method could be applied with 1000 iterations to ensure stability, with the mean as the parameter of interest and confidence intervals (CI) produced for each configuration used (distress mechanism, expansion level, aggregate type, and distress feature), thus establishing a range of expected values through the DRI. A visual summary of the findings is illustrated in Figure 10.2.

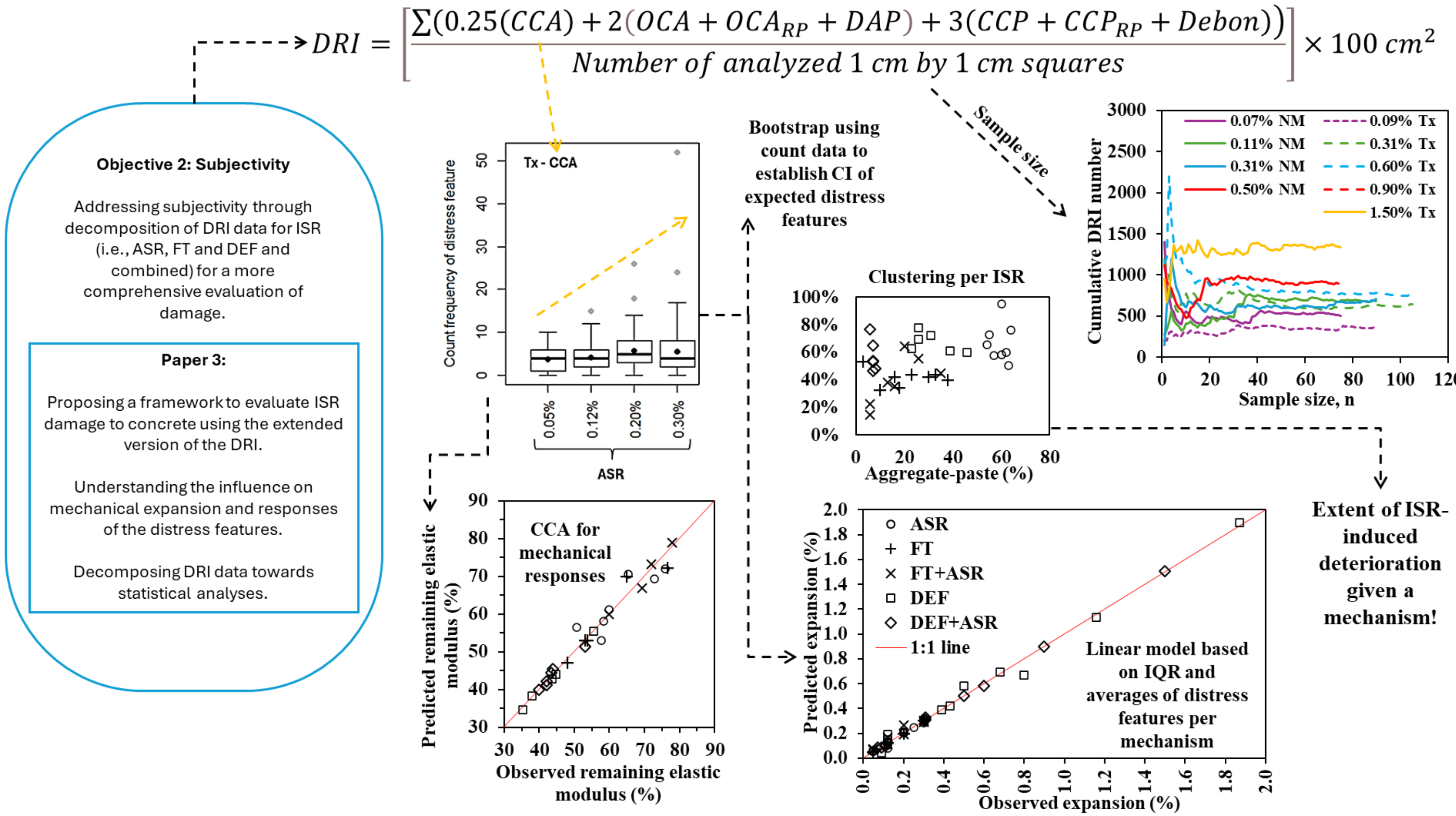

Figure 10.2. A visual summary of objective 2: Reducing subjectivity when evaluating ISR.

Research recommendations

This work was the first to decompose DRI data into count data, allowing for the visualization of 1 cm by 1 cm squares as a sample. This approach revealed the potential of the DRI data beyond mere DRI numbers and bar charts. Recommendations to apply this approach to a previous study incorporating a wide range of reactive aggregates and compressive strengths may help refine the linear model for ASR and enhance understanding of the role of aggregate type and concrete strength.

The application of the DEF counting method, as proposed in the scope of this research program, aims to further refine the linear models for DEF-induced deterioration. Given the influence on expansion, SDI, and modulus of elasticity explored in the previous topic, it is evident that further decomposing the DRI data, including Debon-type cracks as identified through the proposed counting method, will yield better predictions of mechanical responses.

Decoupling the combined DEF+ASR and FT+ASR mechanisms using this proposed approach may reveal patterns that lead to improved diagnoses. However, as indicated above, some mechanisms may remain untriggered before testing. It is highly recommended to include post-mortem DRI analysis following residual expansion or degradation tests to consider all possible scenarios in the field. Decoupling can likely only be implemented following such analyses, especially when interactions between the mechanisms favour or hinder the development of one another mechanism.

10.4. Reducing operator variability during investigations of the deterioration extent

Operator variability is one of the most discussed issues related to the DRI. While extensive previous research has addressed variability in distinguishing petrographic and distress features, uncertainties persist regarding the extent of deterioration indicated by an ISR. As a result, operator variability can be managed through rigorous training and resources available to support this training. Understanding how new operators engage with the tool during learning was crucial in this research. The ability to conduct the DRI develops the skill to draw conclusions based on observations. Therefore, the observations needed to be quantified intuitively and without biases to reach similar conclusions. This work considered DRI results from six operators for two types of reactive aggregates, all using the concrete prism test (CPT) mixture proportions and specimen fabrication. The combined unreactive aggregates varied, as did the sample preparation, reflecting the variables encountered in different laboratory settings. Resources to assist during the training include tabulated cumulative distress feature counts, which can be plotted as curves for visual interpretations. This approach was chosen based on familiarity with cumulative tables. It was also determined that the sample size in 1 cm by 1 cm squares needed to increase with the extent of deterioration. Thus, convergence curves of cumulative DRI were produced to help the operator achieve convergence during analysis. A visual summary of the findings is illustrated in Figure 10.3.

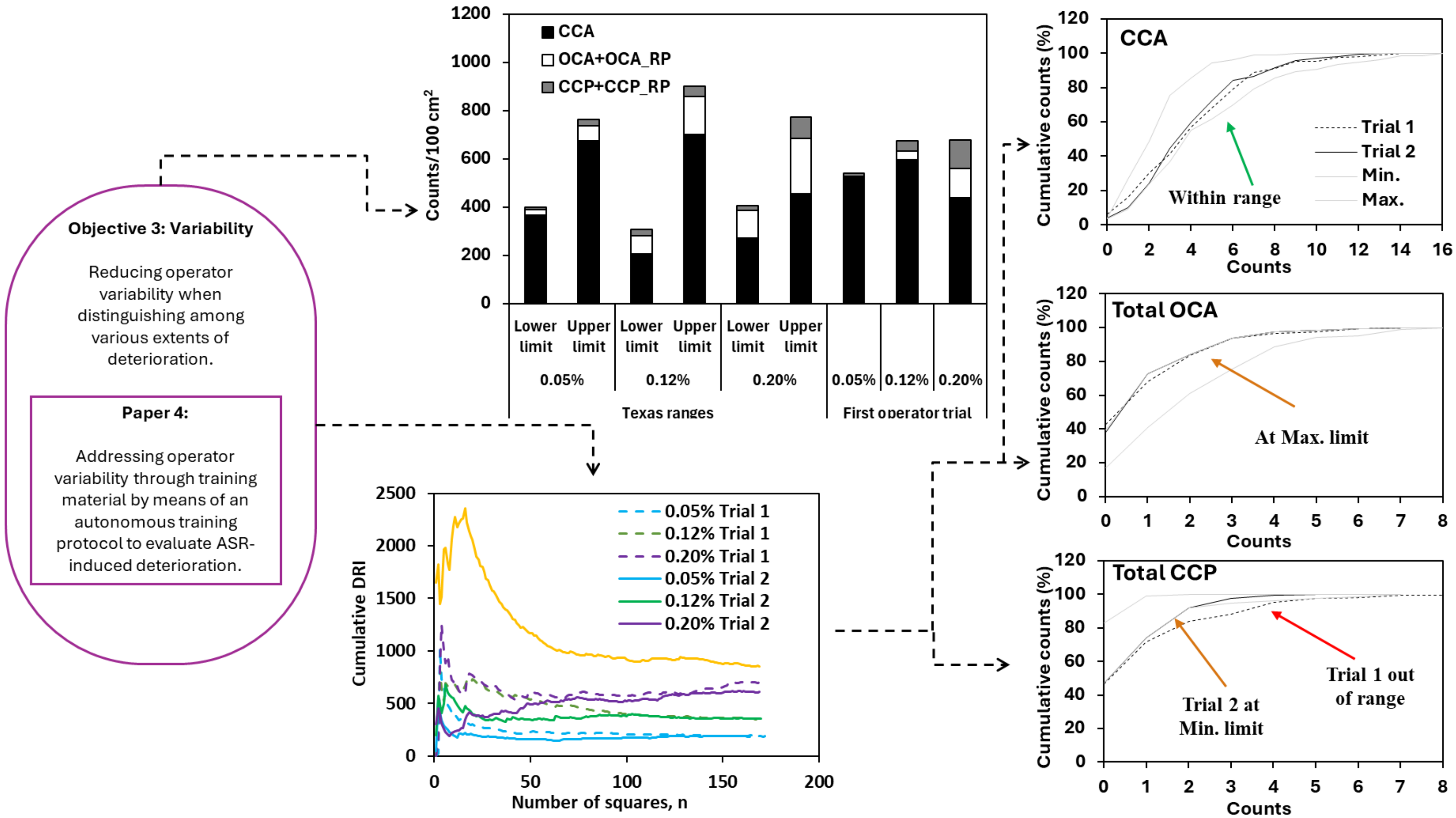

Figure 10.3. A visual summary of objective 3: Addressing variability by operator training.

Research recommendation

While this approach serves as a starting point, such a guide is anticipated to be necessary for all ISRs. As these guides continue to develop skills to identify the extent of damage associated with an ISR, the ranges of expected values will be refined, and datasets will be created to establish ranges based on statistical analyses. Therefore, it is advisable to document results from training iterations to understand better how to adapt the guide according to the needs of new operators. Calibration of new operators could be based on these results to ensure that less experienced operators can reliably conduct the analysis. Linking these calibrations to mechanical responses and expansion can help determine the certainty of the result and the allowable margin of error.

10.5. Effectively and efficiently using the DRI

In this final objective, the limitation of time was among the primary drivers for developing the automated version of the DRI. Although the time consumption of the DRI was not discussed in this thesis, as it reflects an economic aspect of conducting the analysis, it undoubtedly prompted its automation. However, while these topics are incredibly trendy, they should be considered carefully. This research focused on the performance metrics that evaluate the outputs from the automated DRI. It could be viewed as a new operator, thus requiring training and intervention. Machine learning (ML) outputs may converge to suitable values from an ML perspective, as was observed in the previous feasibility study. However, it is vital to understand the outputs from the application point of view and to question what the machine is doing to achieve its suitable metrics (i.e., an accuracy of 0.74 for the crack classifier-detector and 0.99 for the crack counter). In the first iteration of the model (i.e., Model 1), which employed a pixel-based approach, the outputs were adjusted to reach a targeted DRI number by augmenting counts where none existed. While the first model excelled in crack identification and classification tasks, compatibility with the crack counter caused these discrepancies. To resolve this, the model required an impractical number of annotated images for its dataset, prompting a new iteration of an automated DRI model (Model 2). In this version, instance segmentation was employed to consider the encountered distress features instead of determining whether a pixel belongs to a crack. The model loss served as a metric to compare the predictions to the ground truths for the second model iteration. The model loss achieved as work progressed (i.e., after training on 450 annotated images) was found to be 0.28, 0.08, and 0.19 for the classifications, locations of cracks, and accuracy in the predictions of the annotations, respectively, marking an improvement from the results presented in Chapter 8 (i.e., 0.80 during preliminary training). Distress features for ASR indicate an imbalance in the dataset, where a limited quantity of $CCP+CCP_{RP}$ is observed. However, additional training of Model 2 with only this type of crack (i.e., 50 annotated images out of 240 in the second training round) led to improved performance, resulting in a model loss of 0.13, 0.05, and 0.17 for the classifications, locations of cracks, and accuracy in the predictions of the annotations, respectively, achieving better performance with a smaller dataset. It is worth noting that this model does not combine OCA and OCA_{RP} into a single category and is the first to detect CCP_{RP}. The work accomplished in this research program's objective validates the automation of the DRI, where this version can be seen as a new operator in training. Figure 10.4 compares both models, the ground truth and the operator training curves from Chapter 7. The implementation of various aggregate types, representing a wider range of lithotypes along with different ISR mechanisms, is suggested as the next step. Furthermore, incorporating image analysis—such as crack lengths and widths, crack networks, Debon-type cracks, and crack orientations—would fully integrate this automated DRI. These additional crack characteristics may facilitate the incorporation of fracture mechanics into the analysis, thereby enhancing the overall impact of the DRI.

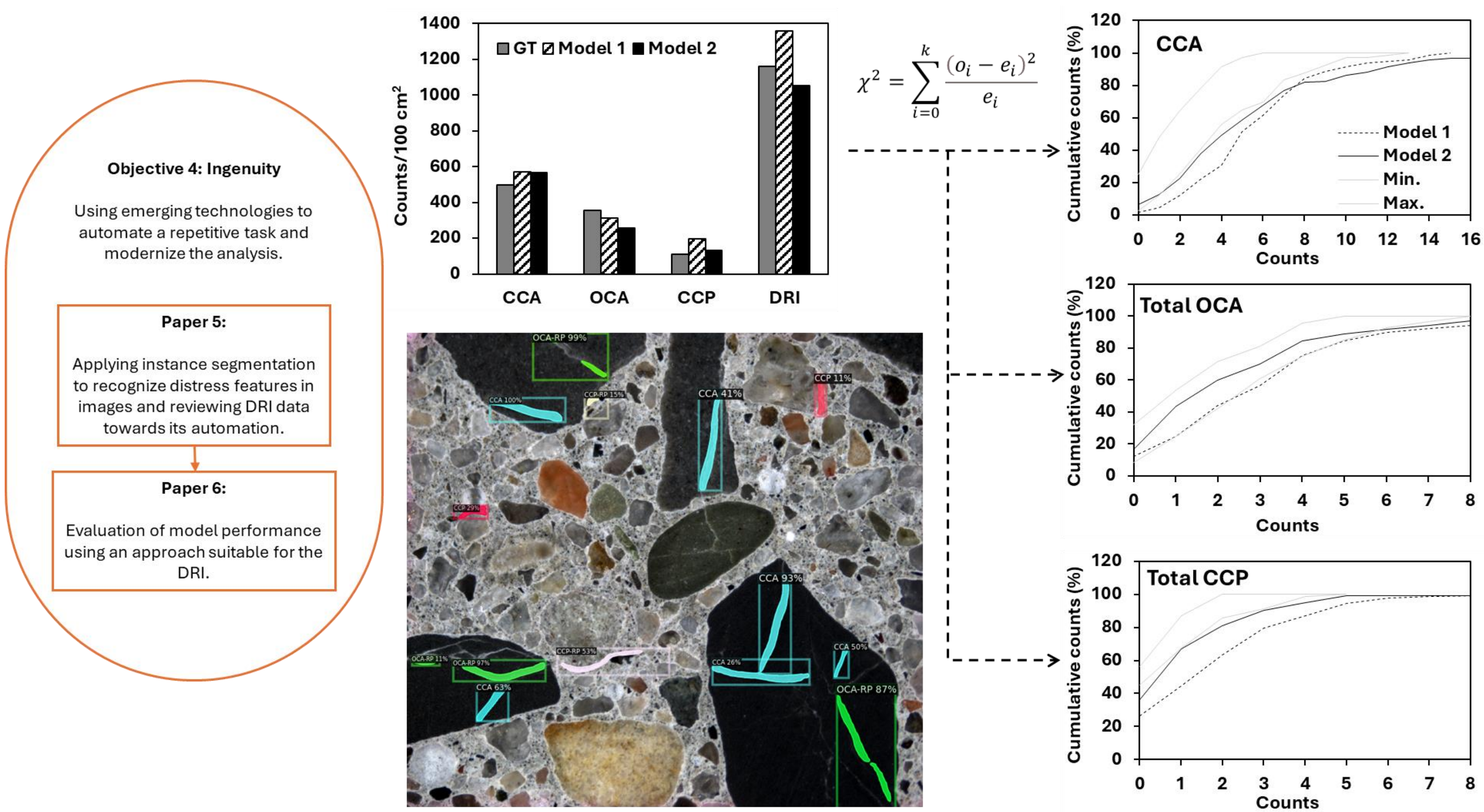

Figure 10.4. A visual summary of objective 4: Evaluating the automated version of the DRI.